HORST-HOLGER BOLTZ

SEMIFLEXIBLE POLYMERS IN DISORDERED POTENTIALS

technische universität
dortmund

Dissertation zur Erlangung des Grades eines Doktors der Naturwissenschaften.

Der Fakultät Physik der Technischen Universität Dortmund vorgelegt von Horst-Holger Boltz aus Dortmund.

Datum der Verteidigung: 30. September 2015

Contents

Zusammenfassung

Im ersten Teil dieser Arbeit betrachten wir das Verhalten semiflexibler Polymere in ungeordneten Potentialen. Zunächst untersuchen wir den statischen Lokaliserungsübergang steifer gerichteter Linien, linearer elastischer Mannigfaltikeiten mit Biegeenergie, in kurzreichweitigen Zufallspotentialen. Wir zeigen, dass es oberhalb der unteren kritischen Dimension mit steigender Unordnung einen Übergang in eine unordnungsdominierte Phase gibt, der numerisch direkt zugänglich ist. Wir analysieren die Eigenschaften dieser Phase und motivieren einen Zusammenhang zwischen der Lokalisation steifer gerichteter Linien und der gerichteter Linien in einer höheren Dimension und unterstützen dies mit numerischen Resultaten. Dieser Zusammenhang manifestiert die Bedeutung von Replikapaarwechselwirkungen für die Lokalisation in Unordnung. Dies hat unmittelbare Auswirkungen für das kritische Verhalten der Kardar-Parisi-Zhang-Gleichung (KPZ-Gleichung). Desweiteren führen wir das Konzept der unordnungsinduzierten Persistenzlänge ein und quantifizieren die Reduktion in der effektiven Steifigkeit durch die Unordnung. Sodann befassen wir uns mit der Entbindungsdynamik solcher Linien unter Kraft, die auch durch den Übergang im statischen Problem von besonderem Interesse ist. Die relevante Bewegungsgleichung ist die (eingefrorene) Herring-Mullins-Gleichung, die außerdem oberflächendiffusionsdominiertes Oberflächenwachstum beschreibt. Mit Hilfe analytischer Betrachtungen und numerischer Simulation bestimmen wir die kritischen Exponenten und vergleichen unsere Ergebnisse mit Vorarbeiten und Resultaten aus funktionaler Renormierung.

Im zweiten Teil widmen wir uns der Deformation einer elastischen Kapsel ob ihrer Bewegung in einer viskosen Flüssigkeit. Wir präsentieren ein iteratives auf der Lösung des hydrodynamischen Problems mittels Randintegralgleichungen und des elastischen Problems mittels Formgleichungen aufbauendes Lösungsschema und bestimmen die stationäre achsensymmetrische Form sowie die Geschwindigkeit einer elastischen Kapsel, die sich in einem Newtonschen viskosen Fluid bei sehr niedrigen Reynoldszahlen bewegt. Wir nützen diesen Ansatz, um systematisch die dynamischen Formübergänge einer sedimentierenden Kapsel zu ermitteln. Wir zeigen, dass die Lösungsbifurkationen in der Kraft-Geschwindigkeitsbeziehung aufgelöst werden können. Ferner erörtern wir die andere Formen des Antriebs, etwa durch eine Punktkraft oder einen aktiven Schwimmmechanismus.

Im dritten Teil präsentieren wir einen ereignisbasierten Monte-Carlo-Algorithmus zum Behuf der Simulation statistischer Systeme mit sterischen Wechselwirkungen. Am Beispiel des zweidimensionalen Gases harter (undurchdringlicher) Scheiben führen wir eine parallelisierte Version des Ereignisablaufalgorithmus' (event chain algorithm) ein und analysieren den Performanzgewinn. Das Wechselspiel aus notwendiger räumlicher Partionierung und paralleler Berechnung bedingt ein optimales Maß an Parallelisierung. Wir erweitern den Anwendungsbereich ereignisablaufbasierter Algorithmen auf Polymersysteme und diskutieren die Simulation netzwerkbildender semiflexibler Polymere sowie athermaler Schmelzen flexibler Polymere. Wir zeigen, dass unser Algorithmus nicht nur das korrekte Gleichgewichtsverhalten beinhaltet sondern auch in der Lage ist, die Dynamik auf hinreichend großen Zeitskalen widerzugeben. Weiterhin diskutieren wir für die Schmelze den Performanzgewinn durch systemspezifische, verschränkungsauflösende Austauschzustandsänderungen (swap move) und zeigen, dass wir insgesamt in der Lage sind, mit direkter Molekulardynamik vergleichbare Simulationsgeschwindigkeiten zu erreichen.

Abstract

In the first part we consider the behaviour of semiflexible polymers in disordered potentials. First, we investigate the static localisation transition of stiff directed lines, linear elastic manifolds with a bending energy, in short-ranged random potentials. We show that a stiff directed line above its lower critical dimension undergoes a localisation transition with increasing disorder. We demonstrate that this transition is accessible numerically and analyse the properties of the disorder dominated phase in detail. We propose a relation between the localisation of stiff directed lines and that of directed lines under tension in higher dimensions, which is strongly supported by our numerical findings. This shows that pair interactions in the replicated Hamiltonian determine the nature of directed line localisation transitions with consequences for the critical behaviour of the Kardar-Parisi-Zhang (KPZ) equation. Furthermore, we quantify how the persistence length of the stiff directed line is reduced by disorder. Second, we explore the dynamics under a driving force, which is particularly interesting as there is a localisation transition in the static problem. Their equation of motion is the (quenched) Herring-Mullins equation, which also describes surface growth governed by surface diffusion. We employ analytical arguments and numerical simulations to determine the critical exponents and compare our findings with previous works and functional renormalisation group results.

The second part deals with the deformation of an elastic particle due to its motion in a viscous fluid. We introduce an iterative solution scheme which couples hydrodynamic boundary integral methods and elastic shape equations to find the stationary axisymmetric shape and the velocity of an elastic capsule moving in a viscous fluid at low Reynolds numbers. We use this approach to systematically study dynamical shape transitions of spherical capsules sedimenting under the influence of gravity or centrifugal forces. All shape bifurcations can be resolved in the force-velocity relation of sedimenting capsules. Additionally, we study capsules pushed or pulled by a point force, where we always find capsule shapes to transform smoothly without bifurcations.

In the third part we present algorithmic improvements for the (statistical) simulation of systems with steric interaction. We present a parallelised event chain algorithms. We analyse the performance gains for the parallelised event chain and find a criterion for an optimal degree of parallelisation. We discuss first applications of the event chain algorithm to dense polymer systems, i.e., bundle-forming solutions of attractive semiflexible polymers and dense athermal melts. Our implementation of this algorithm produces the correct ideal behaviour of polymer chains in the dense melt in equilibrium. Moreover, the event chain Monte Carlo algorithm captures the inter- and intrapolymer diffusion, i.e., essential features of the polymer dynamics in melts correctly. Event chains also allow for an efficient preparation of initial configurations in the dense limit. We introduce additional local topology-changing moves to further increase simulation speeds in melts. We show that these event chain Monte Carlo algorithms achieve simulation speeds comparable to optimized molecular dynamics simulations.

Preface

I honestly appreciate the time you as a reader invest in reading this work and hope that my writing though inevitably factual in style for the vast majority of the text justifies this to some extent. I realise that I might be asking for a rather large amount of time due to the girth of this thesis and I will therefore not dwell on a lengthy global introduction or acknowledgements that are undoubtedly better given in personal manner. I will however give you some information on the structure of the following: this thesis is separated into three parts that are independent enough to justify individual introductions, conclusions, bibliographies and such. I chose this way of parallel presentation instead of meticulously constructing bridges and I still think this makes the core aspects of the text more accessible. Some parts might be familiar to you because they already have been published. The respective publications are listed on the following page and are appropriately cited at the beginning of the parts. This thesis closes with lists of more frequently used abbreviations and symbols.

Horst-Holger Boltz in July of 2015

Publications

A predominant share of the content of this thesis as been subject of prior publications or is in process of submission by the time of writing. We give a list of these publications in the following in the order of usage in the text and comment on relevant copyright issues in the prefaces of the afflicted parts.

Horst-Holger Boltz and Jan Kierfeld
Localization transition of stiff directed lines in random media
Physical Review E 86: 060102(R) (2012)

Horst-Holger Boltz und Jan Kierfeld
Stiff directed lines in random media
Physical Review E 88: 012103 (2013)

Horst-Holger Boltz and Jan Kierfeld
Depinning of stiff directed lines in random media
Physical Review E 90: 012101 (2013)

Horst-Holger Boltz and Jan Kierfeld
Shapes of Sedimenting Soft Elastic Capsules in a Viscous Fluid
Physical Review E 92: 033003 (2015)

Tobias A. Kampmann, Horst-Holger Boltz and Jan Kierfeld
Parallelized event chain algorithm for dense hard sphere and polymer systems
Journal of Computational Physics, 231: 864 (2015)

Tobias A. Kampmann, Horst-Holger Boltz and Jan Kierfeld
Monte Carlo Simulation of Dense Polymer Melts Using Event Chain Algorithms
Journal of Chemical Physysics, 143: 044105 (2015)

Part I

SEMIFLEXIBLE POLYMERS IN DISORDERED POTENTIALS

Preface to this part

There are some remarks on my behalf in order. First, parts of the following chapters have already[1] been published in Refs. 1–3. The variational analysis of the localisation transition within the replica method has been the subject of a prior thesis, see Ref. 4, and will therefore only be covered to a minimal extent, but an introduction into the replica formalism is necessary. The same goes for the transfer matrix algorithm used in the numerical simulations. However, the numerical data presented here are without exception from simulations that were performed during the work on this thesis. Due to the closeness in topic some similarities to Ref. 4 in the presentation are hardly avoidable, especially in the introductory sections, but the actual results are original findings of this thesis.

Second, this part of my thesis deals with two closely related but essentially independent problems that can be subsumed under the this part's title *Semi-flexible Polymers in Disorder*. Thus, there is a short exposition of the common concepts on the following pages, which might resemble a *cold open* in other media. The two following chapters then have individual introductions and motivations specific to the presented problems. However, the presentation here takes a linear approach and the chapters are meant to be read in order.

[1] These parts are ©2012-14 American Physical Society

HB

Preliminaries

We want to start at the very beginning. If we turn back some pages[2] we will notice the literal beginning, the title, of this part being *Semiflexible Polymers in Disordered Potentials*.

The term *polymer* could very well be defined as "[a] substance composed of macromolecules"[5], with the term macromolecule meaning "[a] molecule of high relative molecular mass, the structure of which essentially comprises the multiple repetition of units derived, actually or conceptually, from molecules of low relative molecular mass"[5].

[2] Advanced readers may feel free to remember this without actually turning pages.

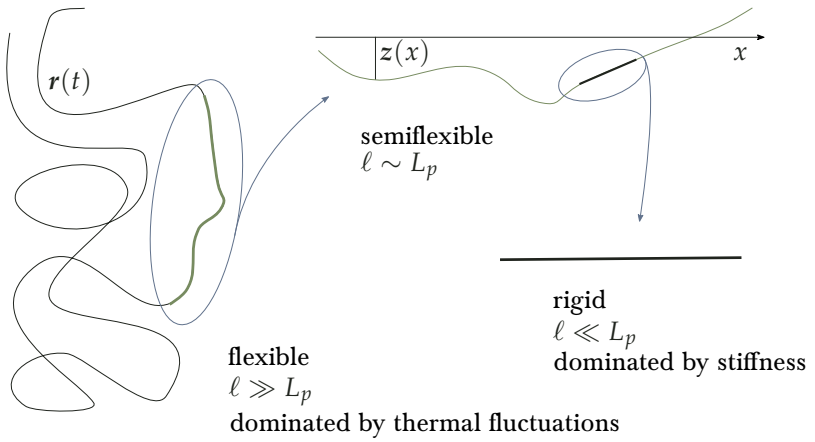

Figure 1: Schematic appearance of a semiflexible polymer with persistence length L_p on different length scales ℓ. In the semiflexible regime, $\ell \sim L_p$ the competing contributions to the free energy of the polymer, the configurational entropy (dominating for $\ell \gg L_p$) and the internal energy due to bending (dominating for $\ell \ll L_p$) are of the same order, giving rise to a directed line that can thermally fluctuate around its preferred axis. Adapted from Ref. 17.

The way of seeing polymers that this part of this work – highly non-exclusively – uses is more abstract, but identical in one aspect: above all polymers are large objects. Their size gives one dominating length scale. The way we model this is by virtue of a *line*, a space curve $\boldsymbol{r}(t)$ parametrised in some fashion by $t \leq 0 \leq L$. In this approach the shape of the line contains the complete information, especially the energy of the polymer[3]. The relation between shape and energy is where the word *semiflexible* comes into play. A flexible polymer would be one where every conformation of the polymer, every shape of the line, with the same contour length L_c has the same energy, whereas a "inflexible" (rigid) polymer would only allow for a small set of shapes (straights without curvature). Qualitatively, a semiflexible polymer has a rigidity towards bending, which creates an additional length scale, the persistence length L_p, above which the polymer is dominated by thermal fluctuations and, thus, rather flexible and below which the internal bending stiffness is dominating, rendering the polymer rather rigid. In Fig. 1 we try to visualise this dependence of the observed polymer behaviour on the length scale one is interested in. In the crossover region, that is on length scales $\ell \sim L_p$, the polymer is rather straight, or directed, but is fluctuating around this straight shape. This allows for a treatment in so-called Monge

[3] This neglects for example kinetic energies, but for the static considerations the velocity degree of freedoms would decouple nonetheless and later on we explicitly assume overdamped motion.

parametrisation, simplifying the $1+d$-dimensional space-curve $\boldsymbol{r}(t)$ to the graph of a d-dimensional function $\boldsymbol{z}(x)$, i.e. $\boldsymbol{r}(t) = (x,\boldsymbol{z}(x))^T$. This will be the way semiflexible polymers are treated throughout this work, as *stiff directed lines*. In the upcoming section this will be introduced more rigorously.

Going back to the title we can infer that this line will be subject to some *disordered potential*. A potential here means that we introduce a direct position-dependence of the energy: there are regions more and regions less favourable for the line. For a disordered potential, the actual value of this potential at some point $V(x,\boldsymbol{z})$ is a random variable that is *not thermally fluctuating*, but frozen or *quenched*. As a consequence thermodynamic averages are computed in a single realisation of the disorder and then an additional average over these realisations is needed.

These are the common ingredients for the two problems we will study in more detail below: The static localisation in a disordered potential and the depinning from this localisation due to a pulling force.

Elastic Manifolds in Monge parametrisation

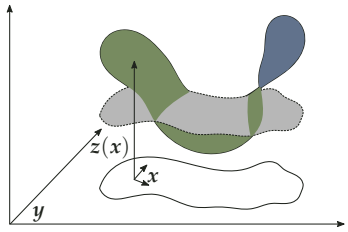

Figure 2: Sketch to explain the Monge parametrisation $(x,\boldsymbol{z}(x))$ of a manifold that is originally defined by some parametrisation $\boldsymbol{y}(s)$. This figure is adapted from Ref. 7.

Figure 3: The Monge parametrisation does not allow for neither loops (left side) nor overhangs (right side) as both would ask for a multi-valued displacement field $\boldsymbol{z}(x)$.

In very general terms we want to study elastic manifolds in external potentials. We will limit ourselves to manifolds which deviate only weakly from their preferred flat state. This restriction allows us to employ a Monge parametrisation[6], cf. Fig. 2, that is we separate the $D+d$ spatial dimensions into D internal or lateral dimensions and d transversal dimensions. Thus the manifold can be written in the form $(\boldsymbol{x},\boldsymbol{z}(\boldsymbol{x}))$ with $\boldsymbol{x}\in\mathbb{R}^D, \boldsymbol{z}\in\mathbb{R}^d$ where $\boldsymbol{z}$ gives the displacement of the manifold from its energetical ground-state, the D-dimensional hyperplane $\boldsymbol{z}\equiv 0$. Within this approach we neglect all shapes of the manifold that cannot be the image of a function $\boldsymbol{z}(\boldsymbol{x})$, in the simplest case of a line, $D=1$, this means forbidding loops and overhangs, see Fig. 3.

Demanding translational invariance of the $D+d$-dimensional space the elastic energy cannot directly depend on $\boldsymbol{z}$ or $\boldsymbol{x}$, but only on derivatives of $\boldsymbol{z}(\boldsymbol{x})$. Furthermore, we also demand inversion symmetry, meaning that the energy should be invariant under a change of sign of the displacement, $\boldsymbol{z}\to-\boldsymbol{z}$, which rules out all odd powers of $\boldsymbol{z}$ and its derivatives. Thus, it is very reasonable to start with an elastic energy[4]

$$\mathcal{H}_{\mathrm{el},\mathfrak{z}} \propto \int \mathrm{d}^D\boldsymbol{x}\ (\nabla_{\boldsymbol{x}}^{\mathfrak{z}}\boldsymbol{z})^2\,. \tag{1}$$

We omitted an elastic constant, which is needed to give the right hand side the dimension of an energy. The order of the derivative, given by the parameter $\mathfrak{z}$, characterises the type of elasticity, as we will see below. We assume that the manifold's internal coordinates $\boldsymbol{x}$ are bounded to the D-dimensional hypercube $[0,L]^D$ and call L the size of the manifold.

Thermal noise as well as disorder will in general lead to a rough manifold, by which we mean that the typical scale of displacement[5] z is diverging in the thermodynamical limit, $L\to\infty$. The statistics of displacements $\boldsymbol{z}$ is characterised by the *roughness exponent* ζ, which is defined by

$$z^2(L) \sim L^{2\zeta}$$

The geometric property related to ζ is the *self-affinity*[8] of the lines. This refers to the notion that the line $(\boldsymbol{x},\boldsymbol{z}(\boldsymbol{x})$ and the image of the anisotropic[6] affine transformation

$$\boldsymbol{x}\to b\boldsymbol{x},\quad \boldsymbol{z}\to b^{\zeta}\boldsymbol{z}$$

[4] It suffices to include one term, because for large system sizes L the elastic energy, scaling as $\sim z^2 L^{D-2\mathfrak{z}}$ (see below for a more gentle introduction to scaling arguments), is always dominated by the lowest relevant derivative.

[5] We will use the root mean square of the displacements with respect to averaging over thermal noise, disorder realisations or both.

[6] For $\zeta=1$ the transformation is isotropic and the line is not only self-affine but self-similar.

are statistically identical, in the sense hat they have identical distributions.

One way to rationalise the thermal value of the roughness exponent is the following scaling argument: If we rescale the internal coordinates by their typical size L and the displacements by their typical size, which we call z, we see that the elastic energy of eq. (1) scales as

$$\mathcal{H}_{\text{el}} \sim L^{D-2\mathfrak{z}} z^2. \tag{2}$$

The typical size of energy fluctuations is the temperature[7] T, which implies $T \sim L^{D-2\mathfrak{z}} z^2$ or by definition of ζ

$$\zeta_{th,\mathfrak{z}} = \max\left(\frac{2\mathfrak{z}-D}{2}, 0\right).$$

For $D > 2\mathfrak{z}$ the manifold is thermally flat, the fluctuations of the displacement remain finite even on large scales, which corresponds to $\zeta = 0$.

From the scaling argument associated with eq. (2) we see that a roughness exponent other than the thermal value will lead to an additional length dependence in the elastic energies. This is a sign of (free) energy[8] fluctuations which we will describe by the *energy fluctuation exponent* ω with

$$\Delta F \sim L^{\omega}$$

which is given by the difference between the roughness exponent and the thermal value

$$\omega = 2(\zeta - \zeta_{th}) = 2\zeta - 2\mathfrak{z} + D.$$

We are mostly interested in lines[9], $D = 1$, and the cases $\mathfrak{z} = 1$ and $\mathfrak{z} = 2$. The former will be referred to as the *directed line* (DL) and the latter as the *stiff directed line*. In the following we will elaborate on the model of the stiff directed line, comment on its relevance in the modelling of semiflexible polymers and then return to the directed line to examine the connection between these two types of elasticity.

[7] We use here and throughout the following energy units with $k_B \equiv 1$ or, equivalently, $\beta = T^{-1}$.

[8] In equilibrium all energy contributions should show identical scaling behaviour.

[9] In our nomenclature the difference between a polymer and a (directed) line is that a line uses Monge parametrisation.

Stiff directed lines

The main model of this work is the *stiff directed line (SDL)*, which corresponds to $D = 1$ and $\mathfrak{z} = 2$. Hence, each configuration of SDL is associated with a bending-type elastic energy[10]

$$\mathcal{H} = \int_0^L \mathrm{d}x \, \left[\frac{\varkappa}{2}(\partial_x^2 z(x))^2 + V(x, z(x))\right] \tag{3}$$

with a *bending rigidity* $\varkappa$. In the following, we call the size L, its fixed projected length, the length of the line. The *contour length* of the line is given by

$$L_c = \int_0^L \mathrm{d}x \, \sqrt{1 + z'(x)^2} \approx L + \frac{1}{2}\int_0^L \mathrm{d}x \, (\partial_x z(x))^2$$

(to leading order in z); it is not fixed and always larger than the length L. For later use, we included a potential[11] $V(x, z(x))$, which incorporates the coupling of the line to its exterior.

The value of the bending rigidity sets the length-scale on which deflections from the flat elastic ground-state become important, the so-called *persistence length*. We introduce the *tangent orientation*

$$v = \partial_x z$$

[10] In the context of the bending of stiff rods, also called beams, the elastic energy of an SDL corresponds to the Euler-Bernoulli theory[9] neglecting the orientation of the beam's cross-section. See also below the relation to the worm-like chain and its relation to Kirchhoff rods.

[11] It would be more in line with point mechanics to refer to the energy contribution $\int_0^L \mathrm{d}x \, V(x, z(x))$ as the potential (energy), but this would bloat up our discussion by having to speak of the "potential energy per length".

which scales as $v \sim L^{\zeta-1}$. Using the thermal roughness exponent (see below), we find linearly increasing fluctuations $v^2 \sim L$. We can therefore define the (thermal) persistence length by demanding that these fluctuations become of the order of one,

$$\langle v^2 \rangle (L_p) = 1.$$

Here we explicitly limit ourselves to averaging over thermal fluctuations, indicated by $\langle \ldots \rangle$. However, we will employ a completely analogous definition to introduce a disorder-induced persistence length later on. Following the same scaling argument as before including the bending rigidity we see that $z^2 \sim L^3/(\beta\varkappa)$ or $v^2 \sim L/L_p$ with

$$L_p \sim \beta\varkappa.$$

The thermal, $V \equiv 0$, behaviour of a stiff directed line is characterised by a roughness exponent

$$\zeta_{th} = \frac{3}{2}.$$

This high value, $\zeta > 1$, indicates that the stiff directed line is *super-rough*. One consequence of super-roughness is that a truly self-affine line has a diverging contour length. However, we always (often implicitly) assume that there is a (ultraviolet) cut-off at short length-scales (or high wave-vectors) and on this short lengths the line is described by the matching condition between the displacements and the tangent orientations, $\boldsymbol{z}(x + \Delta x) = \boldsymbol{z}(x) + \Delta x \boldsymbol{v}(x)$, which corresponds to a *locally* linear growth.

Relation to worm-like chains

As already mentioned in the introductory part of this chapter one motivation for the SDL model, eq. (3), is that it is the weakly bent limit[12] of the fundamental model for semiflexible polymers. The fundamental model for semiflexible polymers is the so-called worm-like chain (WLC) or Kratky-Porod model[10, 11]

$$\mathcal{H}_{\mathrm{WLC}} = \int_0^{L_c} \mathrm{d}s \left[\frac{\varkappa}{2} (\partial_s^2 \boldsymbol{r}(s))^2 + V(\boldsymbol{r}(s)) \right],$$

which models a semiflexible polymer as an inextensible rod with bending modulus $\varkappa$. The chain is parametrised in arc length, $0 \leq s \leq L_c$, and has a *local inextensibility* constraint $|\partial_s \boldsymbol{r}(s)| = 1$, which is hard to account for, both numerically and analytically[12, 13].

The WLC describes inextensible semiflexible polymers, such as DNA or cytoskeletal filaments like F-actin[14] on all length-scales. The microscopy images in Fig. 4 show nicely that the three fundamental regimes of a worm-like chain as a function of its length in units of its persistence length that we already covered in the introductory part of this chapter, see Fig. 1, are present in the cytoskeletal filaments.

The energy per length in the WLC is a pure bending energy proportional to the square of the curvature, which is the classic result[15] for elastic bending of a thin elastically isotropic rod[13].

For thermally fluctuating semiflexible polymers, the energy functional (3) is only a valid approximation for a weakly bent semiflexible polymer on

[12] If the polymer given by $\boldsymbol{r}(s)$ with $0 \leq s \leq L$ has no loops or overhangs, we can parametrise its shape in the form $(x,z(x))$. In this representation the squared curvature is given by $(z'')^2/(1+z')^3 \approx (z'')^2$ as the line is virtually inextensible and we find the connection to the SDL model.

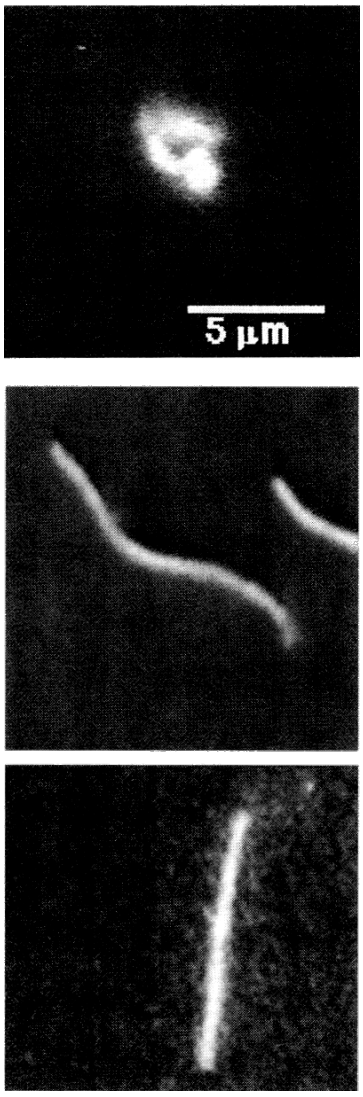

Figure 4: Fluorescence microscopy images of the three different persistence length regimes (cp. Fig. 1) in cytoskeletal filaments. From top to bottom: flexible intermediary filament, semiflexible F-actin and stiff microtubule. Reprinted with slight alterations from (Ref. 14) Biophysical Journal, 70(2), J. Käs et al., 609-625, Copyright (1996), with permission from The Biophysical Society.

[13] The Kirchhoff elastic rod also accounts for stretching, which we neglected because semiflexible polymers are virtually inextensible, and twisting, which is negligible as we are not interested in loadings with torsional stress. It is noteworthy, that this result for the bending energy can be achieved without any assumption on the elastic law of the material.

length scales below its persistence length[14] which is[12, 16, 17]

$$L_p = \frac{2}{D'-1}\frac{\varkappa}{T} = \frac{2}{d}\frac{\varkappa}{T}.$$

in $D' = 1 + d$ spatial dimensions.

Above the persistence length, a semiflexible polymer loses orientation correlations and starts to develop overhangs. Therefore, in a quenched random potential the SDL model describes semiflexible polymers in heterogeneous media, only as long as tangent fluctuations are small such that overhangs can be neglected, which is the case below a *disorder-induced* persistence length, which we will derive below. We will study the SDL in disordered potentials in the thermodynamic limit, that is on length scales exceeding the persistence length, nonetheless because the model is interesting in its own right, for example we are able to test analytical techniques for the analysis of elastic manifolds in disorder such as the functional renormalisation group approach, and because it will give a new method to gain insight into the physics of directed lines, for there is a close relation, which we will explore now.

[14] Here one would use a different definition of the persistence length than for a directed line. The persistence length of a worm-like chain is the length scale over which tangent correlations decay, that is $\langle \boldsymbol{t}(s)\boldsymbol{t}(s')\rangle = \mathrm{e}^{-|s-s'|/L_p}$ with $\boldsymbol{t} = \partial_s \boldsymbol{r}(s)$. However, these definitions are closely related: We define an angle ϑ by $\boldsymbol{t}(L)\boldsymbol{t}(0) = \cos(\vartheta)$ then the tangent direction $v(L)$ in the corresponding directed model is $v(L) \propto \sin(\vartheta)$ and, thus for sufficiently large L_p we have $\langle v^2(L)\rangle \sim L/L_p$.

Relation to directed lines

The difference between SDLs and DLs as we introduced them at the beginning of this section is the order of derivative in the elastic energy, see eq. (1): the SDLs have a bending type energy given by the second derivative ($\mathfrak{z} = 2$), whereas the DLs have a stretching type ($\mathfrak{z} = 1$) energy

$$\mathcal{H}_{\mathrm{DL}} = \int_0^L \mathrm{d}x \left[\frac{\tau}{2}(\partial_x z(x))^2 + V(x, z(x))\right]$$

of DLs with a line tension[15] τ. This energy functional is (up to prefactors) identical to the free energy (and thus the entropy) of a random walk in the d transversal dimensions (in this interpretation the internal coordinate x takes over the role of a time).

[15] We note that τ has the dimension of a force.

Thus we can employ the central limit theorem (or the general result for the roughness exponent derived before) to find that the thermal roughness exponent is $\zeta_{th,\mathrm{DL}} = 1/2$ for DLs. Here and in the following we use an explicit subscript DL when referring to the directed line. The roughness exponent is not only notable smaller than the SDL value $\zeta_{th} = 3/2$ indicating smaller excursions from the preferred axis, but it is also smaller than one.

Therefore typical configurations of SDLs and DLs will appear quite different, but looking for a connection we notice that the elastic parts of two energy functionals become identical in the free ($V \equiv 0$) case if we write the SDL energy (cp. eq. (3)) as a functional not of the line's displacement but of its tangent directions $v = \partial_x z(x)$:

$$\mathcal{H}[z] = \int_0^L \mathrm{d}x \left[\frac{\varkappa}{2}(\partial_x^2 z(x))^2\right] = \int_0^L \mathrm{d}x \left[\frac{\varkappa}{2}(\partial_x v(x))^2\right] = \mathcal{H}_{\mathrm{DL}}[v].$$

This simply manifests the difference of one in the two thermal roughness exponents. However, operating in the space of tangents usually becomes a lot less attractive in the presence of a position-dependent external potential, because a potential term $V(x, z(x))$ becomes $V(x, \int_0^x \mathrm{d}y v(y))$. If we dealt with potentials that depended solely on the tangent directions, $V(x, v(x))$, this part would definitely be too long, because we could simply take the DL result for say the roughness exponent and add one to make it an SDL result.

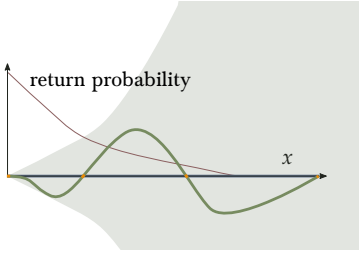

Figure 5: Schematic for the binding of a SDL (green line) in a short-ranged potential (blue line). The passages through zero are highlighted (orange), their statistic is given by the return probability (red line) which in turn is closely related to the typical width explored by thermal fluctuations (shaded area).

This goes to show that different things usually are different and for a general potential there is no mapping of the energy functionals onto another. Nonetheless, there is a connection[18, 19] between these two in *binding problems*, by which we mean the problem of a line[16] adsorbing to a short-ranged attractive potential around the preferred axis. We can write this as an additional energy contribution of the form $\mathcal{H}_{\text{bind}} \propto -\int_0^L \mathrm{d}x\, \delta_\lambda(z)$ with some omitted (positive) strength and δ_λ a short-ranged function, decaying on the length λ (the range of the potential), which we assume to be very small. But more important than this formal notation is its interpretation: we can realise that the binding energy is (for $\lambda \approx 0$) counting the number of times the line passes the axis $z = 0$.

[16] This is equivalent to the actual binding of two lines, which interact via a pair potential $f(|z_1 - z_2|)$. Separating the centre of mass and relative degrees of freedom, we find that the centre of mass interacts with a static attractive potential at $z_{CM} = 0$.

The key quantity for the binding of line is therefore[17] the probability that a line of length L starting at the preferred axis, $z(0) = 0$, "returns" to origin, that is ends at $z(L) = 0$. This *return probability* is characterised by the *return exponent* χ, defined by its decay behaviour

$$\text{Prob}(z(L) = 0) \sim L^{-\chi}.$$

[17] On a more rigorous basis the governing role of the return exponent follows, for example, directly from a necklace model treatment.[20]

The *critical properties* of the binding transition are governed by the value of χ for a free line. For DLs, which are essentially random walks[20] in d transverse dimensions, the return exponent is $\chi_\tau = d/2$, whereas it is $\chi = 3d/2$ for a SDL (after integrating over all orientations of the end)[21]. More generally, we can argue that ending points of a line with length L having a width $\sim L^\zeta$ are typically spread over the d-dimensional volume $\sim L^{\zeta d}$ from which we deduce that the probability that the line ends in an area around the preferred axis scales like $\sim L^{-\zeta d}$. Therefore the roughness and return exponent are related[19] by $\chi = \zeta d$. We summarise this in Fig. 5. The return exponent χ governs the critical properties of the binding transition to a short-range attractive potential or, equivalently, of the binding transition of two lines interacting by such a potential [18, 19].

The relation $\chi_\tau(3d) = \chi(d)$ implies that the binding transition of two DLs in $3d$ dimensions maps onto to the binding transition of two SDLs in d dimensions[18] and vice-versa.

This will become important because we will motivate below (and later on more rigorously using the so-called replica method) that in a certain sense the localisation of a directed elastic line in a disorder potential corresponds to a binding of the line to copies of itself.

[18] More generally, we can infer that two manifolds with $(d,D,\mathfrak{z})$ and $(d',D',\mathfrak{z}')$ whose energy is of the form of eq. (1) show *identical binding criticality*, if

$$d' = \frac{2\mathfrak{z}' - D'}{2\mathfrak{z} - D} d$$

Disordered potentials

The last missing piece from the title are the *disordered potentials*. In general, disorder here refers to anything that depends on the value of a random variable. This includes thermal fluctuations and therefore we should refer to the kind of disorder we are interested in here as *quenched disorder* as opposed to annealed disorder that is thermally fluctuating. To elucidate this difference, let us consider the computation of the canonical partition function for a system whose energy $\mathcal{H}_\mathcal{V}$ depends on the random variable[19] $\mathcal{V}$

$$Z_\mathcal{V} = \int \mathrm{d}\Gamma\, \mathrm{e}^{-\beta \mathcal{H}_\mathcal{V}}$$

[19] To keep notation simple we consider a scalar disorder variable for now, but the generalisation is straightforward.

where $\int \mathrm{d}\Gamma$ has to be replaced by an appropriate integration over all states of the system[20]. Any result, e.g. the free energy $F_\mathcal{V} = -\beta^{-1} \ln Z_\mathcal{V}$ or the thermal average $\langle X \rangle_\mathcal{V}$ of an observable X, computed using this partition

[20] For a (stiff) directed line this would mean a functional integration over the line shape $z(x)$ that is $Z = \int \mathcal{D}z(x)\, \mathrm{e}^{-\beta \mathcal{H}[z(x)]}$.

function $Z_\mathcal{V}$ depends on the realisation $\mathcal{V}$ of the disorder. We see that this is the correct answer to the wrong question, we are not interested in the results for a specific realisation of the disorder[21], but in general results for a given amount or strength of disorder. We therefore consider *disorder averages* over realisations. Here, we have to commit ourselves to the type of disorder (cp. Fig. 6): annealed disorder fluctuates thermally, that is the realisation of the disorder $\mathcal{V}$ just adds to the phase space that is explored through thermal fluctuations and we therefore should compute the partition function as[22]

$$Z_{\text{annealed}} = \overline{Z} = \int \mathrm{d}\Gamma \int \mathrm{d}\mathcal{V}\, P(\mathcal{V})\, \mathrm{e}^{-\beta \mathcal{H}_\mathcal{V}}$$

which gives rise to an annealed free energy $F_{\text{annealed}} = -\beta^{-1} \ln \overline{Z}$; or quenched disorder that is frozen on thermally relevant time scales, where we have to compute any quantity for each disorder realisation and then compute the average over disorder, a procedure that leads to the *quenched free energy*

$$F_{\text{quenched}} = \int \mathrm{d}\mathcal{V}\, P(\mathcal{V}) F_\mathcal{V} = -\beta^{-1} \int \mathrm{d}\mathcal{V}\, P(\mathcal{V}) \ln Z_\mathcal{V} = -\beta^{-1} \overline{\ln Z}.$$

In the former the disorder thus disappears because we can introduce an *annealed* energy functional $\mathcal{H}_{\text{annealed}}$ that is defined to reduce the annealed disordered partition function to a conventional, deterministic partition function, that is $\overline{\mathrm{e}^{-\beta \mathcal{H}_\mathcal{V}}} = \mathrm{e}^{-\beta \mathcal{H}_{\text{annealed}}}$. Thus the quenched case appears to be more interesting in that it seems to be more difficult (and it usually is). In this part we only deal with quenched disorder and therefore no longer dwell on this differentiation, any occurrence of the term disorder or disorder(ed) potential refers to quenched disorder in the potential with certain characteristics that we will introduce below, but before we go into technicalities, it might be helpful to take a visual approach to integrate this concept, because it is fundamental for everything that follows.

In Fig. 7 we show a somewhat artistic rendition of a line subject to a potential that is represented by an energy landscape. In line with the general experience of the gravitational potential the energy contribution at a site is proportional to its height. The line that is subject to this energy landscape fluctuates at finite temperatures, but the background does not. In each landscape we can observe the behaviour of the line (e.g. its shape or its energy) and then we have to perform an average over all landscapes. Had we considered annealed disorder the landscape in the picture would be flat (assuming that the distribution of the disorder is isotropic).

We are going to work with a *Gaussian distributed quenched random potential* $V(x,z(x))$ with zero mean[23] $\overline{V} = 0$ and *short-ranged correlations*[24], which in the most abstract form can be written as

$$\overline{V(\boldsymbol{x},z)V(\boldsymbol{y},z')} = g^2 \delta^d(z-z')\delta^D(\boldsymbol{x}-\boldsymbol{y})\,. \tag{4}$$

We refer to the parameter g as the strength of the disorder[25]. With respect to the notation we reiterate that the quenched disorder average over realisations of V of some quantity X is denoted as $\overline{X}$, whereas $\langle X \rangle$ denotes thermal averaging. In the most typical case we consider the full quenched average of an observable $\overline{\langle X \rangle}$. For *fluctuations* the two averaging procedures allow for three combinations

$$\Delta X_1^2 = \overline{\langle X^2 \rangle - \langle X \rangle^2}, \quad \Delta X_2^2 = \overline{\langle X \rangle^2} - \overline{\langle X \rangle}^2 \quad \text{and} \quad \Delta X_3^2 = \overline{\langle X^2 \rangle} - \overline{\langle X \rangle}^2$$

[21] If we were, we would simply use this realisation of the potential and not care to write a section about disordered potentials.

[22] We introduce here the over-bar notation, $\overline{\ldots}$, for averages over disorder realisations. This average makes use of the distribution $P(\mathcal{V})$ of the disorder.

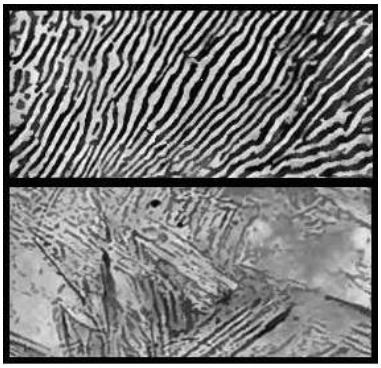

Figure 6: The terminology of annealed and quenched disorder originates from the heat treatment of materials where the distribution of disorder (impurities, for steel: mostly carbon) in a previously heated material depends on the rate of cooling. The pictures show photomicrographs of steel that has been cooled slowly (annealing, top) and fast (quenched, bottom). The annealed steel shows a lamellar structure of iron (dark) and iron-carbide (light), whereas the carbon impurities are distributed throughout the material in the quenched case. This Figure is an altered version of a figure from 22.

[23] This constitutes a choice of the energetical zero level and simply removes a constant contribution to the average energies.

[24] Correlations of the form of eq. (4) though conceptually intriguing will be ill-suited to work with for different reasons at some point both in analytical considerations as well as in numerical simulations. We will then use a contextually appropriate form of finite correlations that decay on a (short) typical length-scale λ (one example is the lattice constant in Fig. 7). Their important feature remains that there are no long-ranged correlations neither in transversal nor in longitudinal direction.

[25] The disorder is distributed with zero mean, but from the correlations, eq. (4), one sees that g controls the magnitude of typical values of the disorder potential, $\mathcal{O}(V) \sim \mathcal{O}(g)$.

which are not independent, which is why we can ignore the third form $\Delta X_3^2 = \Delta X_1^2 + \Delta X_2^2$. We call the first form, the disorder average of the thermal variance, the thermal fluctuations and the second form, the variance with respect to the disorder averaging, the sample-to-sample fluctuations (another sensible nomenclature[23] is internal and ensemble fluctuations).

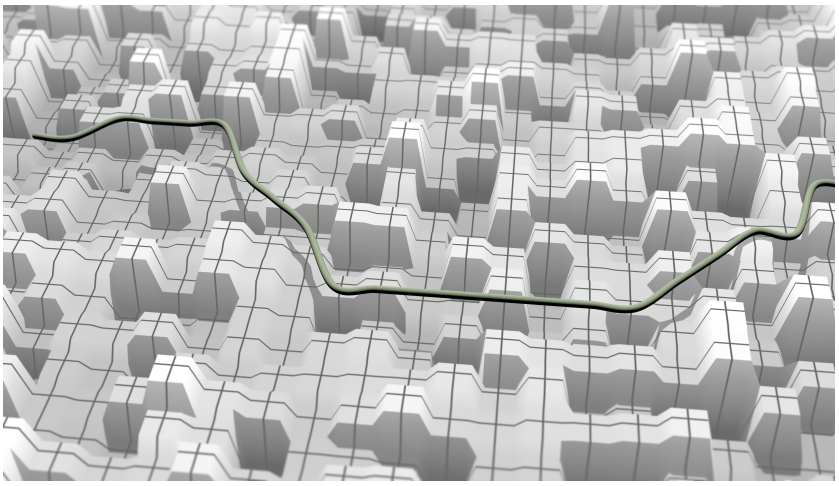

Figure 7: Visualisation of a stiff directed line in a disordered potential. The value of the disorder energy at a site is given by the height of the corresponding "column" (the cross-sectional area of which corresponds to the square of the correlation length of the disorder) building the energy landscape. The disorder contribution to the line's energy therefore favours the line to pass over deep valleys, whereas the elastic contribution favours straight segments. Also shown in this picture are the boundary conditions, the line starts on the left with a straight segment and has a free end on the right. The SDL is represented by a cubic spline, the height and width of which are aesthetic choices. A very similar depiction has been used in Ref. 4.

To support our previous motivation of the study of stiff directed lines in disordered potentials relating this to directed lines by virtue of a mapping that is rooted in binding problems let us now consider (also depicted in Fig. 8) the following[26]: The computation of the partition function for a specific disorder realisation consists of the evaluation of all paths of the line in this disorder. Now we concentrate on two typical line configurations in a disorder potential of sufficient strength such that it dominates over thermal fluctuations (e.g. $T = 0$, $g > 0$) and it appears plausible at least that there is a pronounced probability for these lines to "visit" the same energetically favourable disorder sites.

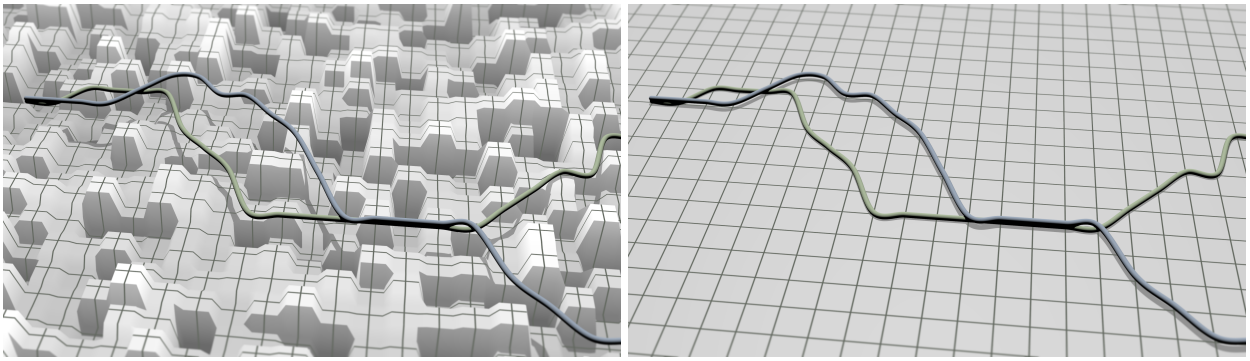

Figure 8: Simplified visual explanation of the effective attraction of two replicas in disordered potentials. The left picture shows the same energy landscape as Fig. 7, but with two copies of the line. Both lines explore independently the same energy landscape and have therefore an increased to probability to be at the same sites. This tendency to meet each other persists as an effective attraction after averaging (represented by the flat landscape in the picture on the right). A very similar depiction has been used in Ref. 4.

This holds in every disorder realisation and therefore the average effect of the disorder on the two copied lines we wanted to concentrate upon is the same as an *effective attractive binding interaction* between the lines in that there will be a finite fraction of length be spent[27] on the same sites in the thermodynamical limit, $L \to \infty$.

It is important to stress that this is a hand-waving argument that is severely flawed but allows for an intuitively accessible presentation of the relation of a disorder-dominated phase and the adsorbed phase in a binding problem.

[26] This is meant as an accessible introduction and not as a mathematically sound justification. Most importantly, there is a better reason to consider the interaction of copies of the line, which is rooted in the replica method that will be introduced later.

[27] This does not hold for two thermally fluctuating lines with $\zeta > 1/d$, as the probability to meet at length L decays as $L^{-d\zeta}$ and the cumulated quantity then scales as $L^{1-d\zeta}$.

Statics – Localisation of a stiff directed line in a random potential

Figure 9: Paths with lowest energy for given ending states for a stiff directed line in one realisation of the disorder. Here, the line grows from the left to the right. The chosen ending states where chosen under the aspect of visibility with the exception of the thicker green line that shows the globally optimal line. Thus, this is the state the system would be in for vanishing temperature, $T = 0$. The dots mark especially favourable spots of the Gaussian random potential V. This is a slightly altered version of a figure used in Ref. 4.

Introduction

Elastic manifolds in random media, especially the problem of a directed line (DL) or directed polymer in a random potential (DPRM), are one of the most important model systems in the statistical physics of disordered systems [24]. DLs in random media are related to important non-equilibrium statistical physics problems such as stochastic growth, see Fig. 10, in particular the Kardar-Parisi-Zhang (KPZ) equation [25–27], Burgers turbulence, or the asymmetric simple exclusion process (ASEP, see Fig. 11)[28]. Furthermore, there are many and important applications of DLs in random media such as kinetic roughening [28], pinning of flux lines in type-II superconductors [29, 30], domain walls in random magnets, or wetting fronts[24].

The energy of DLs such as flux lines, domain walls, wetting fronts is proportional to their length; therefore, the elastic properties of directed lines are governed by their line tension, which favours the straight configuration of shortest length. Both thermal fluctuations and a short-range random potential (point disorder) tend to roughen the DL against the line tension, see Fig. 12.

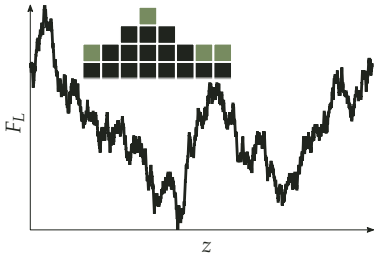

Figure 10: Height profile of an interface grown using a restricted solid-on-solid (RSOS) random deposition model[32] that is within the KPZ universality class. The model is sketched in the upper part: in each time-step one site is chosen and its height is increased $h_i \to h_i + 1$, if the height differences of the new interface satisfy the constraint $|h_i - h_{i+1}| \leq 1$. This allows for deposition on the green sites in the sketch.

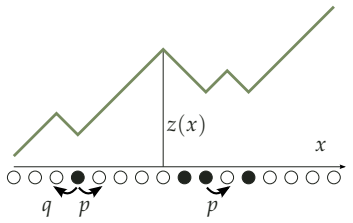

Figure 11: The asymmetric exclusion process and its relation to surface growth. The particles (full circles) can move to unoccupied (hollow circles) neighbouring sites with rates p,q. The effective interface is generated by translating sequences of un-/occupied sites to positive/negative slopes. After subtraction of the deterministic slope generated by the asymmetry, a rough interface remains, which can be related to the problem of a directed line in a random medium.

[28] The restricted partition function (see below) of the DL in a random medium is given by

$$\partial_L Z_L(z) = \Delta_z Z_L + V(x,z) Z_L$$

which is related to the KPZ-equation by means of the standard relation between partition function $F_L = -\beta^{-1} \ln Z_L$ (Cole-Hopf transformation).

As a result of the competition between thermal fluctuations and disorder, DLs in a random media in $D = 1 + d$ dimensions exhibit a *disorder-driven localisation transition*[31] above a critical dimension $d_c = 2$. Below this critical dimension the disorder is at all non-zero strengths dominating over thermal fluctuations and the line is localised to the random potential, whereas above it there is a high-temperature phase where the line is thermally fluctuating (unlocalised) and disorder is irrelevant. Obviously, the lowest integer dimension where such a transition is observable is $d = 3$.

These transitions have been studied numerically for dimensions up to $d = 4$ [33–43]. At low temperatures, the DL is in a disorder dominated phase and localises into a path optimising the random potential energy and the tension energy. Within this disorder dominated phase, the DL roughens, there are macroscopic energy fluctuations and a finite pair overlap between replicas [44–46]. At high temperatures, the disorder is an irrelevant perturbation, and the DL exhibits essentially thermal fluctuations against the line tension. It has been suggested that the critical temperature for the localisation transition of a DL in a random medium and the binding of two DLs by a short-range attractive potential coincide [36, 39].

DLs in a random medium (cf. Fig. 12) map onto the dynamic KPZ equation for nonlinear stochastic surface growth with the restricted free energy of DLs in $1 + d$ dimensions satisfying the KPZ equation[28]

$$\partial_L F_L(z) = \nu \Delta_z F_L + \frac{\lambda}{2} (\nabla_z F_L)^2 + V(x,z)$$

of a d-dimensional dynamic interface. The localisation transition of DLs with increasing disorder corresponds to a roughening transition of the KPZ interface with increasing nonlinearity. In the context of the KPZ equation, it is a long-standing open question[47] whether there exists an upper critical dimension, where the critical behaviour at the localisation transition is modified. Therefore, the critical behaviour of lines in random media can eventually also shed light onto the critical properties of the KPZ equation.

In the replica formulation of line localisation problems, the random potential gives rise to a short-range attractive pair interaction (see below). Therefore, pairwise interactions of DLs play a prominent role also for the physics of a single DL in a random potential. Furthermore, the critical temperature $T_{c,DL}$ for a DL in a random potential is believed to be identical to the critical temperature $T_{2,DL}$ for a system with two replicas [36, 39]. We will show numerically that this equality, $T_c = T_{2,}$, also holds for SDLs in a random medium. The important role of *pairwise interactions* suggests that not only the binding transition of two DLs in $3d$ dimensions maps onto to the binding transition of two SDLs in d dimensions but that the same *dimensional relation holds for the localisation transitions* of DLs and SDLs in a short-range random potential.

One aim is to support this conjecture by providing strong numerical evidence that the $d \to 3d$ analogy between DLs and SDLs in a random potential holds for the *entire free energy distributions* for DLs in $1 + 3$ and SDLs in $1 + 1$ dimensions. Because this analogy is rooted in the binding transition of replica pairs, we can conclude that critical properties of the localisation transition are determined by pair interactions in the replicated Hamiltonian, which has been previously suggested[48, 49].

It has been proposed that pair interactions can be used to formulate an order parameter of the disorder-driven localisation transition[44–46]: the pair overlap q, i.e., the average number of sites per length that two lines in the

same realisation of the disorder have in common. This coincides with the binding energy that characterises binding of two polymers by a pair potential.

We study the localisation transition of SDLs. We defined SDLs as directed lines with preferred orientation and no overhangs with respect to this direction, but with a different elastic energy as compared to DLs: SDLs are governed by bending energy, which penalises curvature, rather than line tension, which penalises stretching of the line. This gives rise to configurations which are locally curvature-free, i.e., straight but straight segments can assume any orientation even if this increases the total length of the line. For lines in disorder this gives rise to a different geometry of energetically favourable states (see Fig. 9 and Fig. 12 for comparison): large perpendicular displacements z of SDLs as shown in Fig. 9 are not unfavourable as long as their "direction" does not change, i.e., as long as their are locally straight and, therefore, do not cost bending energy. Such configurations increase, however, the length of the line and are suppressed for DLs by the tension or stretching energy.

There are a number of applications for SDLs in random media. SDLs describe semiflexible polymers smaller than their persistence length, such that the assumption of a directed line is not violated. Our results apply to semiflexible polymers such as DNA or cytoskeletal filaments like F-actin in a random environment as it could be realised, for example, by a porous medium [13]. Moreover, SDLs are closely connected to surface growth models for molecular beam epitaxy (MBE)[50, 51]. In the presence of surface diffusion, MBE can be described by a Herring-Mullins linear diffusion equation[52, 53], which is equivalent to the overdamped equation of motion of an SDL[29]. As a result, SDLs exhibit the same super-roughness as MBE interfaces. More generally, the zero temperature problem of a SDL in disorder can be formulated as a generic optimisation problem for paths in an array of randomly distributed favourable "pinning" sites (as indicated by points in Fig. 9), which minimise their bending energy at the same time as maximising the number of visited favourable pinning sites.

We investigate the disorder-induced localisation transition of SDLs for a short-range random potential and the scaling properties of the disordered phase. SDLs exhibit a localisation transition already in $D = 1{+}1$ dimensions, which is easily amenable to numerical transfer matrix studies, whereas it requires numerical studies in $D = 1{+}3$ dimensions to investigate the localisation transition of DLs. Therefore, we can verify several concepts that have been proposed or found for the localisation transition of DLs, e.g., the pair overlap as order parameter or the multifractality of the localisation transition, by simulations of SDLs in $D = 1{+}1$ dimensions. Notably, we will show that the pair overlap indeed provides a suitable order parameter for the localisation transition.

In the next section we will use a range of analytical methods to establish the existence of a localisation transition for the SDL in all accessible dimensions $d \geq 1$. Furthermore, we will infer expressions for the nontrivial roughness exponent in the disorder-dominated phase. Sadly, these analytical methods will turn out to be little fruitful, which is why we present the results of extensive numerical simulation. In the literal conclusion of this chapter we will summarise our findings and comment on the transfer of these to other models for semiflexible polymers in disorder.

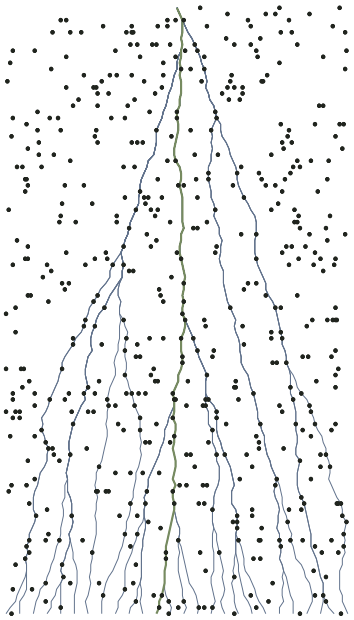

Figure 12: The same as in Fig. 9 but for a directed line. The difference in elastic energies leads to a drastic difference in the geometry of the optimal paths. The disorder realisations in here and in Fig. 9 are not the same. These two realisations were chose because the characteristics of the two line-types become apparent. This is a slightly altered version of a figure used in Ref. 4.

[29] This dynamic behaviour of an SDL is the subject of the second half of this part, starting on page 59.

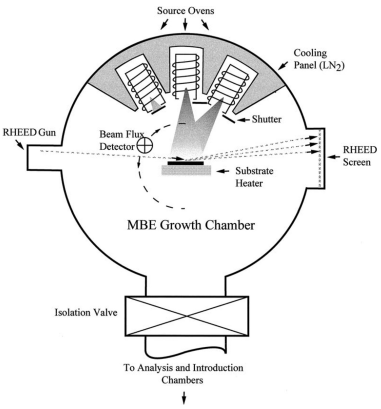

Figure 13: Scheme of a MBE chamber. The material from the source ovens is deposited onto the substrate (middle) which can be imaged using Reflection high-energy electron diffraction (RHEED). Reprinted from (Ref. 51) Surface Science, 500(1), J. R. Arthur, 189-217, Copyright (2002), with permission from Elsevier.

Analytical approaches

Scaling analysis

Lower critical dimension

We start with a scaling analysis by a Flory-type argument. We already argued before that for displacements $\sim z$ the bending energy in eq. (3) scales as $E_b \sim z^2 L^{-3}$. The disorder energy scales as $E_d \sim \sqrt{L z^{-d}}$, as can be seen from the correlations, eq. (4). Plugging the unperturbed thermal roughness $z \sim L_{th}^{\zeta}$ into the disorder energy estimate we get $E_d \sim L^{1-\zeta_{th} d/2}$, from which we conclude that the disorder is always relevant below a *lower critical dimension* d_c which can be defined by the criterion that the thermal return exponent becomes unity,

$$\chi(d_c) = \zeta_{th} d_c = 1,$$

which for the SDL with $\zeta = 3/2$ implies

$$d_c = \frac{2}{3}.$$

Above this critical dimension and, thus, in all physically accessible integer dimensions, the SDL should exhibit a transition from a thermal phase for low $g < g_c$ (high temperature $T > T_c$) to a disorder dominated phase above a critical value of the disorder g_c (low temperature $T < T_c$).

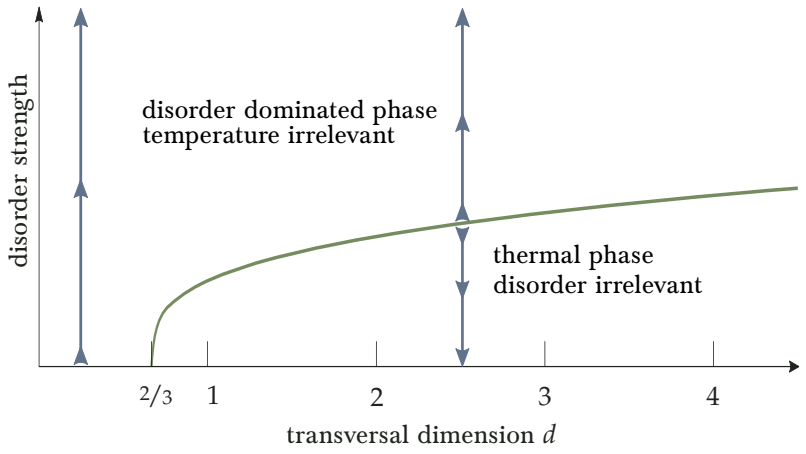

Figure 14: Qualitative phase diagram of the stiff directed line as gathered from the scaling analysis. There is a critical transversal dimension $d_c = 2/3$ below which the SDL is in the disordered phase for any nonzero disorder strength. Above this dimension there is a transition at a finite critical disorder strength (here and in the plot's labelling, we mean the relative strength with respect to thermal fluctuation, that is g/T, when referring to the disorder strength). The arrows indicate a simple renormalisation flow picture, where a phase transition would be expected to manifest itself in a repulsive fixed-point. However, as we will see below, the problem of an elastic line asks for a functional renormalisation and a renormalisation of the parameters does not suffice. This is a slightly altered version of a figure used in Ref. 4.

We can also infer that the lower critical dimension for DLs is $d_{c,DL} = 2$, which is in accordance with the proposed relation between DLs in $1+3d$ dimensions and SDLs in $1+d$ dimensions as is the mere dependence of the critical dimension on the value of the return exponent which also governs binding criticality.

With $d_c = 2/3 < 1$ the localisation transition of SDLs can be studied numerically in 1+1 (or higher) integer dimensions, whereas for DLs with $d_{c,DL} = 2$, the localisation transition is only accessible in simulations in $1+3$ (or higher) integer dimensions. Our numerical study of the line localisation transition presented below focuses on SDLs in $1+1$ dimensions, which are computationally better accessible using transfer matrix techniques as compared to a $1+3$-dimensional system of DLs.

Balancing the Flory estimates, $E_b \sim E_d$, gives a roughness estimate[30] $z \sim L^{\zeta_{Fl}}$. When disorder is relevant, this leads to

$$\zeta_{Fl} = \frac{7}{4+d} \qquad \text{for } d < d_c = \frac{2}{3}.$$

[30] For the DL the roughness in $1+1$ takes the rather pleasing value $\zeta_{DL,1+1} = 2/3$. This is a consequence of a fluctuation-dissipation-theorem[54] that holds for the KPZ-equation leading to Gaussian fluctuations, in our notation $\zeta_{DL,1+1}/\omega_{DL,1+1} = 2$. As $\omega_{DL} = 2\zeta_{DL} - 1$, we see $\omega_{DL,1+1} = 2/3$. As we are not aware of an analogous relation for the SDL (or the DL in higher dimensions), we should not expect the roughness exponent to be "simple", say a rational number.

Roughness

This result is only applicable below the critical dimension $d < d_c$, where $\zeta_{Fl} > \zeta_{th}$. Above the critical dimension, the Flory result would give $\zeta_{Fl} < \zeta_{th}$, which contradicts our expectation that the SDL roughens as it adjusts to the random potential. Furthermore, the sample-to-sample fluctuations of the free energy $\Delta F^2 \equiv \overline{(F - \overline{F})^2}$ for which we remind the reader of our definition of the *energy fluctuation exponent* ω by

$$\Delta F \sim L^{\omega}$$

would show an unphysical behaviour with a negative value of ω. This is rooted in the general scaling relation[31]

$$\omega = 2\zeta - 3\,. \tag{5}$$

An exponent $\omega < 0$ contradicts the existence of large disorder-induced free energy fluctuations in the low-temperature phase [37, 55], for which there is also strong numerical evidence[34–36]. We conclude that this kind of argument is not applicable above the critical dimension. Therefore, the same problems occur in Flory arguments for the DL for $d > d_{c,DL} = 2$, where one finds $\zeta_{Fl,DL} = 3/(4+d)$. The Flory approach *underestimates* the roughness exponent for all dimensions both for DLs and SDLs, i.e., $\zeta > \zeta_{Fl}$ as it features only one length scale on which the line can adjust to the disorder.

The Flory result ζ_{Fl} should provide a lower bound for the roughness exponent, i.e.

$$\zeta > \zeta_{Fl}\,.$$

Also, the thermal roughness $\zeta_{th,DL} = 1/2$ for DLs and $\zeta_{th} = 3/2$ for SDLs should provide another lower bound for the disorder-induced roughness, i.e.

$$\zeta > \zeta_{th}$$

because of the existence of disorder-induced free energy fluctuations in the low-temperature phase which require a positive energy fluctuation exponent $\omega > 0$. From the previous section we see that the former bound is the more restrictive one for $d < d_c$ whereas the latter is the relevant one for $d > d_c$.

Additionally, we can also give an upper bound for the roughness exponent in the disorder-dominated phase. In fact, we find two motivations leading to the same upper bound. We start with an argument that relates the line to the zero-dimensional problem of a single particle[56].

We consider a straight line and divide the line in its middle into two straight and rigid segments[32] separated by the mid-point $(L/2, z)$. The mid-point displacement z describes the restricted shape fluctuations of the two-segment line. Thus, we have simplified the one-dimensional problem of a line $z(x)$ to a *zero-dimensional* problem of a single coordinate z. The energy associated with this coordinate has two contributions: the bending of the shape fluctuations that are encoded in z which is

$$\mathcal{H}_{el}(z) = \frac{1}{2}(\varkappa/L^3)z^2,$$

and the disorder energy of the two straight segments is

$$\mathcal{H}_d(z) = V(z)$$

with an effective disorder potential that still has vanishing mean $\overline{V(z)} = 0$ and *length-dependent* correlations

$$\overline{V(z)V(z')} = (g^2 L)\delta^d(z - z').$$

[31] This scaling relation follows from the scaling of the bending energy $E_b \sim z^2 L^{-3} \sim L^{2\zeta-3}$ and the assumption $\Delta F \sim E_b$ that bending and free energy have the same scale dependence. The analogous scaling relation for the DL is $\omega_{DL} = 2\zeta_{DL} - 1$.

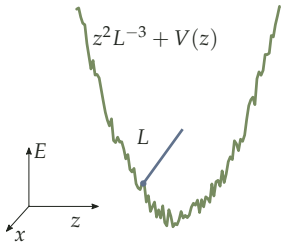

Figure 15: A sketch of the effective zero-dimensional energy landscape we use to find an estimate for the roughness exponent ζ. For this single-particle problem we can use the solution of Ref. 56.

[32] The division into two segments might appear arbitrary. One a more rigorous basis, we could start from a discretized line with N segments and then perform a real-space renormalisation, wherein each renormalisation step consists of the replacement of two neighbouring segments by a single new one. Computing the roughness in this scheme[57], we would then notice that the roughness is dominated by contributions from the last renormalisation step, that is by the longest scales. Therefore we can limit ourselves to the last step.

The prefactor of L in the last line originates from the fact that the effective disorder fluctuations come from two line segments of length $L/2$. So our reduced model consists of a single particle in a parabolic confinement and an additional Gaussian disorder potential.

In Ref. 56, a roughness

$$\overline{\langle z^2 \rangle}_0 \sim \frac{(g^2 L)^{1/2}}{\varkappa / L^3} \sim L^{7/2}$$

(plus logarithmic corrections) has been obtained for this zero-dimensional problem (see also Fig. 15) with the single degree of freedom z by an Imry-Ma argument and a more detailed replica calculation. From this roughness we find a roughness exponent

$$\zeta_0 = \frac{7}{4}$$

for the stiff two-segment line. For the directed line, an analogous argument[33] (including a parabolic potential with prefactor $\sim L^{-1}$) gives $\zeta_{0,DL} = 3/4$.

[33] This is also the result of the real-space renormalisation analysis of Ref. 57.

Using the scaling relation, see eq. (5), we can transfer this roughness to a corresponding energy fluctuation exponent

$$\omega_0 = \frac{1}{2}$$

for two-segment lines, which holds for SDLs and DLs[34]. The zero-dimensional nature of this computation suggests that it should be exact in $d = 0$, which is also supported by the notion that this upper bound then coincides with the lower bound from the Flory calculation.

[34] More generally, this result is independent of the elasticity type, which we indicated by the order of derivative $\mathfrak{z}$ in eq. (1). Going through the steps we find $\zeta_0 = {}^{-1+4\mathfrak{z}}/_4$ and $\omega = 2\zeta - (2\mathfrak{z} - 1) = 1/2$

As stated before this upper bound to the energy fluctuation exponent can also be found in a different way. The energy fluctuations stem from the disorder part of the energy, thus the largest fluctuations possible for a line or manifold are realised, if one ignores the trivial case of summing up random numbers along the internal dimension or dimensions. In this case the free energy performs a random walk whose step distribution is given by the disorder distribution and we can conclude that the adaptation of a D-dimensional elastic manifold to a disorder potential must not lead to fluctuation exponents larger than

$$\omega_0 = D/2.$$

In anticipation of the functional renormalisation group treatment introduced below we introduce the distance to the upper critical internal dimension

$$\varepsilon = (4\mathfrak{z} - D)$$

which allows us to write the corresponding roughness exponent, which is an upper bound to the actual exponent, in a compact form for all values of $\mathfrak{z}$

$$\zeta < \zeta_0 = \frac{\varepsilon}{4}.$$

Using $\varepsilon = 8 - D$ for the SDL and $\varepsilon = 4 - D$ for the DL we see that this does indeed reproduce the same roughness exponent bounds that we found before. The upper bound $\zeta < \varepsilon/4$ also holds within the functional renormalisation group calculation[58], where $\zeta = \varepsilon/4$ is found to correspond to the trivial fluctuation of the zero mode of the effective disorder correlation.

All in all, we have obtained bounds

$$\max(\zeta_{th}, \zeta_{Fl}) < \zeta < \zeta_0,$$

which apply both for SDLs and DLs. For SDLs, this gives a relatively small window, see also Fig. 16, of possible roughness exponents,

$$\max\left(\frac{3}{2}, \frac{7}{4+d}\right) < \zeta < \frac{7}{4},$$

which, for example, limits $\zeta_{\varkappa}$ for SDLs in $1+1$ dimensions to $1.5 < \zeta < 1.75$.

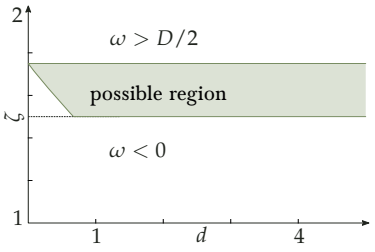

Figure 16: The range of possible values of the roughness exponent ζ. Roughness exponents lower than the thermal value are excluded by demanding a positive value for the energy fluctuation exponent, which also cannot become larger than the trivial "Brownian" limit, $\omega < D/2$.

Variation in replica space

A rather natural approach to broaden the analytical insight beyond scaling arguments is to apply the already mentioned replica technique[59]. This means creating a theory of multiple interacting particles, solving this for arbitrary particle number n and finally continuating this result to the rather peculiar case of vanishing particle number, $n \to 0$. As is often the case with interacting many particle systems a closed solution is usually not feasible for elastic manifolds in disordered potentials, with the one notable and very prominent exemption of then exact solution[60] of the directed polymer in $1+1$ dimensions.

In this section we will follow the conceptually identical treatment of directed manifolds by Mezard and Parisi, see Ref. 65. As the bulk of this work has been presented before[4] the treatment here will remain limited and we refer to that prior work for any omitted details. In an attempt to not obfuscate things unnecessarily we restrict ourselves to one transversal dimension, $d = 1$, for the time being and comment later on how to adapt this to higher dimensions.

The very basis of replica approaches to disordered systems is the following representation[35] of the logarithm of a number Z

$$\ln Z = \lim_{n\to 0} \frac{Z^n - 1}{n}.$$

This identity is often referred to as the *replica trick*. Its importance for the statistical physics of disordered systems is that it offers a means to compute the quenched average of the free energy

$$\overline{F} = -\beta^{-1}\overline{\ln Z}$$

in a manner that performs the actual averaging procedure before the evaluation of the partition function. We will briefly dwell on this point to elucidate the appeal of the replica method. The partition function of an elastic line in a particular realisation $\mathcal{V}$ of the disorder is given as the integral over phase space[36] of the Boltzmann weights

$$Z_{\mathcal{V}} = \int \mathcal{D}z(x)\ \mathrm{e}^{-\beta\mathcal{H}_{\mathcal{V}}[z(x)]}$$

where we introduced subscripts to emphasise the explicit dependence on the disorder realisation. Then the quenched average of the free energy is given by integration over disorder realisations[37]

$$\overline{F} = -\beta^{-1}\int \mathcal{D}\mathcal{V}\, P(\mathcal{V}) \ln Z_{\mathcal{V}}.$$

In the replica approach the relevant computation[38] is the *replicated partition function*

$$Z_{\mathrm{rep}} = \overline{Z^n} = \prod_{\alpha}\left(\int \mathcal{D}z_\alpha\right)\overline{\mathrm{e}^{-\beta\sum_\alpha \mathcal{H}[z_\alpha]}} = \prod_{\alpha}\left(\int \mathcal{D}z_\alpha\right)\mathrm{e}^{-\beta\mathcal{H}_{\mathrm{rep}}}$$

[35] The proof of this is very straightforward when done in the right direction. Application of L'Hospital's rule to the right hand side yields $\lim_{n\to 0}\frac{Z^n-1}{n} = \lim_{n\to 0}\frac{Z^n \ln Z}{1} = \ln Z$.

[36] The phase space consists here of all possible conformations $z(x)$ of the line and thus a functional integration.

[37] Each realisation contributes with some statistical weight $P(\mathcal{V})$.

[38] This is also the step where the effective attractive replica interaction is generated. Before averaging over the disorder we have an n-particle system with a factorising partition function Z^n indicating statistical independence and therefore no interaction.

where the replica index[39] α goes over the n system replicas and the last term introduces the *effective replica Hamiltonian*. This is generated by interpreting the disorder averaged Boltzmann weight as the Boltzmann weight of a new effective energy functional.

The elastic part of the initial energy functional is independent of the disorder which leaves us at evaluating[40] the disorder contribution to the replicated Hamiltonian

$$\begin{aligned}\overline{\mathrm{e}^{-\beta\sum_\alpha \int_0^L \mathrm{d}x\, V(x,z_\alpha(x))}} &= \mathrm{e}^{\beta^2/2\sum_{\alpha,\beta}\int_0^L \mathrm{d}x\, \int_0^L \mathrm{d}y\, \overline{V(x,z_\alpha(x))V(y,z_\beta(y))}} \\ &= \mathrm{e}^{\beta^2 g^2/2\sum_{\alpha,\beta}\int_0^L \mathrm{d}x\, \delta(z_\alpha(x)-z_\beta(x))}\,.\end{aligned}$$

In its entirety the replica Hamiltonian[41] thus reads

$$\mathcal{H}_{\mathrm{rep}} = \sum_\alpha \int_0^L \mathrm{d}x\, (\partial_x^2 z_\alpha)^2 - \frac{\beta g^2}{2}\sum_{\alpha,\beta}\int_0^L \mathrm{d}x\, \delta(z_\alpha(x)-z_\beta(x)).$$

And there we have it, the second term is nothing but an attractive short-range pair interaction of two replicated lines. However, we have to keep in mind that there are n interacting lines and n ultimately is going to zero. Thus, it is unclear a priori how much knowledge of binding problems of two lines can be transferred. Nevertheless, the replica method enabled us to study the average behaviour of a disordered system using one effective, deterministic system.

Alas, we are not aware of a way computing the partition function exactly. We therefore make use of a variational approach in Fourier space, but before we can do that, we have to take of some calamities of the replica Hamiltonian.

For one the bending energy introduces infrared singularities $\sim k^{-4}$, k being the wave number in Fourier space, in the Green's function, which have to be regularised. The method we choose is to introduce a parabolic potential (or "mass" term) $\int \mathrm{d}x \mu z^2(x)$. This effectively confines the system to a finite size in the transversal dimension and we are then ultimately interested in taking the limit $\mu \to 0$ an unbounded system.

Secondly, an infinitely small disorder correlation length in the transversal dimension, just as a point interaction in a binding problem, is problematic. We therefore introduce a finite correlation length λ, that is we write

$$\overline{V(x,z)V(x',z')} = g^2 f_\lambda((z-z')^2)\delta(x-x'),$$

where f_λ is a sufficiently fast decaying function[42] depending on the length λ that gives the original δ-correlator (see eq. (4)) in the limit $\lambda \to 0$. So, we are really using the following replica Hamiltonian in Fourier space

$$\mathcal{H}_{\mathrm{rep}} = \frac{1}{2L}\sum\sum_k (\varkappa k^4 + \mu) z_\alpha^2 - \frac{\beta g^2}{2}\sum_{\alpha,\beta}\int_0^L \mathrm{d}x\, f((z_\alpha - z_\beta)^2). \tag{6}$$

We use Feynman variation[63, 64] in replica space with the one kind of trial Hamiltonian we are confident will lead us to solvable realms: a Gaussian functional, i.e. one that is quadratic in the fields z_α, $\mathcal{H}_\mathcal{V} = (2L)^{-1}\sum_k \sum_{\alpha,\beta} z_\alpha G^{-1}_{\alpha\beta} z_\beta$ with $G^{-1}_{\alpha\beta} = (\varkappa k^4 + \mu)\delta_{\alpha\beta} + \sigma_{\alpha\beta}$ and the self-energy matrix σ providing variational parameters. Extremising[43] the free energy estimate[44] $n\mathcal{F} \equiv F_\mathcal{V} + \langle \mathcal{H}_{\mathrm{rep}} - \mathcal{H}_\mathcal{V}\rangle_\mathcal{V}$ with respect to the self-energy matrix σ gives (in the continuum limit $L^{-1} \approx 0$) a self-consistent equation

[39] Every occurrence of small Greek letters as summation index is a replica index going over $1,\ldots,n$. These limits are therefore omissible.

[40] Suppose we have a random quantity X which we write as $X = \mathrm{i}kY$ with known cumulants $\overline{X^n}_c$, then we find[61]

$$\begin{aligned}\ln \overline{\mathrm{e}^{-\mathrm{i}kY}} = \ln \overline{\mathrm{e}^X} &= \sum_{n=1}^\infty \frac{(-\mathrm{i}k)^n}{n!}\overline{Y^n}_c \\ &= \sum_{n=1}^\infty \frac{(-\mathrm{i}k)^n}{n!}\left(\frac{\mathrm{i}}{k}\right)^n \overline{X^n}_c = \sum_{n=1}^\infty \frac{1}{n!}\overline{X^n}_c\end{aligned}$$

and therefore

$$\overline{\mathrm{e}^X} = \mathrm{e}^{\sum_{n=1}^\infty \frac{(-1)^{n+1}}{n!}\overline{X^n}_c}.$$

[41] For the directed line we would have a first derivative in the first term. Then, by variation (for a more detailed presentation see for example Ref. 4) we see that the restricted partition function $Z(x,z)$ obeys a differential equation that essentially is the Schrödinger equation for the Lieb-Liniger (LL) model[62]

$$\mathcal{H}_{LL} = -\sum_{j=1}^N \partial_{x_j}^2 + 2c \sum_{1\le i<j\le N}\delta(x_i - x_j)$$

of interacting bosons. Thus the replicated partition function is given by the ground state energy[60, 62]

$$E(n) = E_1 n + E_3 n^3$$

of this quantum model, which implies $\omega = 1/3$.

[42] We use the Gaussian $\sqrt{2\pi} f_\lambda(x^2) = \lambda\, \mathrm{e}^{-x^2/(2\lambda^2)}$, which does in deed give a representation of the Dirac delta-distribution for $\lambda \to 0$ as it converges to zero everywhere but for $x = 0$ and is normalised for every λ.

[43] In standard statistical physics the variational estimate is an upper bound to the free energy, which means that the variational free energy has to be minimised. However, we are interested in the limit of *vanishing particle number*, $n \to 0$, which demands that the variational free energy has to be maximised.

[44] All quantities that are subscripted $\mathcal{V}$ are to be computed using $\mathcal{H}_\mathcal{V}$.

for the self-energy matrix [65]

$$\sigma_{\alpha\gamma} = \begin{cases} -\sum_{\alpha'\neq\alpha} \sigma_{\alpha\alpha'} & \alpha = \beta \\ -2\beta g^2 \tilde{f}' \left(\int \frac{\mathrm{d}k}{2\pi\beta} (G_{\alpha\alpha} + G_{\gamma\gamma} - 2G_{\alpha\gamma} \right) & \alpha \neq \gamma \end{cases}$$

with $\tilde{f}_\lambda(x) \equiv \int \mathrm{d}y \, \sqrt{2\pi}^{-1} e^{-y^2/2} f_\lambda(y^2 x) = \sqrt{2\pi}^{-1} \sqrt{\lambda^2 + x}^{-1}$.

Following Mezard and Parisi we choose a one-step hierarchical replica symmetry breaking Ansatz for σ. In $d = 1$, the variation[45] of the free energy estimate yields two self-consistent equations

$$u_c \propto S_1(\Sigma)(\lambda^2 + S_1(\Sigma))^{-1} \quad \text{and} \quad \Sigma \propto (\beta^{20} g^{16} \varkappa^3 u_c^{20})^{-1}$$

for u_c and Σ, where we omitted numerical constants. We are not able to give a closed solution, because combining these two equations, we find that the solutions would require finding the root of a polynomial of degree 15 which in general cannot be expressed in terms of radicals,

$$\Sigma^{1/20} \sim \frac{\lambda^2 + \Sigma^{-3/4}}{\Sigma^{-3/4}} \sim \lambda^2 \Sigma^{15/20} + \text{const.}$$

Nonetheless, using the condition $u_c < 1$, we can show that there is no solution unless the potential strength g and correlation length λ are above finite values.

Although variation in replica space is known[65] to fail in reproducing the exact solution[60] for the problem of the DL in disorder in finite dimensions, we interpret this as an indication for the existence of a critical disorder strength or, correspondingly, a critical temperature. The variational replica approach leads, however, to the thermal roughness exponent also in the low-temperature phase, which should come to little surprise as there is Gaussian energy statistics involved just as in the thermal case without (relevant) disorder, cp. Fig. 33 on page 54.

[45] We refer to our earlier in-detail presentation in Ref. 4 for explanations, the actual calculation and the definition of the variables used here.

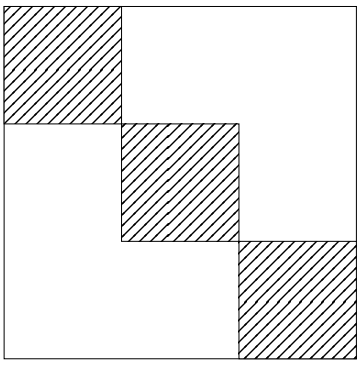

Figure 17: Matrix with one-step breaking. Within the equally marked areas the matrix elements are identical. This is the first step to the iterator hierarchical breaking of replica symmetry[66]. This figure is taken from and the reader for more explanation referred to Ref. 4.

Functional renormalisation group

There has been some success studying elastic manifold problems in disordered potentials using functional renormalisation group (FRG) analysis [58, 67–71]. Here, the idea is to incorporate the fluctuations on all length scales into an effective disorder correlator, which is then determined by demanding invariance under renormalisation.

This method can be adapted to generalised elastic energies of the kind we are interested in $\mathcal{H}_\mathfrak{z} \propto \int \mathrm{d}^D x \, (\nabla_x^\mathfrak{z} z)^2$ for D-dimensional elastic manifolds with d transverse dimensions[46].

The case $\mathfrak{z} = 1$ corresponds to elastic manifolds which already have been extensively studied [58, 67–71], whereas $m = 2$ corresponds to manifolds dominated by bending energy.

Additional to this elastic energy there is of course still the usual disorder energy contribution

$$\mathcal{H}_V = \int \mathrm{d}^D \boldsymbol{x} \, V(\boldsymbol{x}, \boldsymbol{z}).$$

However, we can no longer assume the disorder to have the simple, short-ranged correlations as before, because we are looking for the *effective disorder correlations*. Therefore, in the FRG approach we take the random disorder potential to have zero mean and a correlator of the general form[47]

[46] Within the FRG literature, the number of transverse dimensions is frequently denoted by N.

[47] This is of the form considered in the variational replica calculation with $g^2 f_\lambda \to R$.

$$\overline{V(\boldsymbol{x},z)V(\boldsymbol{x}',z')} = R(z-z')\delta^{(D)}(\boldsymbol{x}-\boldsymbol{x}'),$$

where the whole function $R(z)$ is renormalized.

After replication this gives an effective energy functional (in suitable units)

$$\beta\mathcal{H}_{FRG} = \int \mathrm{d}^D\boldsymbol{x}\left(\frac{1}{2T}\sum_\alpha\left[(\nabla_{\boldsymbol{x}}^{\mathfrak{z}}z_\alpha)^2+\mu z_\alpha^2\right]-\frac{1}{2T^2}\sum_{\alpha,\beta}R(z_\alpha-z_\beta)\right)$$

where we again introduced a mass term. For the following it is important to realise the constraints to the function $R(z)$. The energy should be symmetric under permutation of the replicas, which implies an inversion symmetry, $R(z) = R(-z)$. Furthermore, we are interested in short-ranged disorder, in $d = 1$ this implies a monotonously exponentially fast decaying shape of $R(z)$.

The basic idea of renormalisation in physics can to some extent always be trivialised[48] to change nothing and then demand that nothing has changed. In this spirit we perform an infinitesimal scale-change (SC) by a factor $b = e^{\mathrm{d}l}$ of all lengths in the lateral dimension. For this scale-change to be consistent with the definition of the roughness exponent ζ the lateral dimensions have to be scaled by a factor b^ζ, yielding

$$x \to bx \quad \text{and} \quad z \to b^\zeta z.$$

Linearising $e^{\mathrm{d}l} = 1+\mathrm{d}l$ we see that $\beta\mathcal{H}$ remains invariant under this scale-change, if we additionally change the temperature and the disorder correlator

$$T \to T+\mathrm{d}l\frac{\mathrm{d}T}{\mathrm{d}l} \quad \text{and} \quad R \to R+\mathrm{d}l\frac{\partial R}{\partial l}.$$

This leads to the following FRG flow equations[49]

$$\left.\frac{\mathrm{d}T}{\mathrm{d}l}\right|_{\mathrm{SC}} = 2(\zeta_{th}-\zeta)T = -\omega T \tag{7a}$$

$$\left.\frac{\partial R}{\partial l}\right|_{\mathrm{SC}} = (\varepsilon-4\zeta)R+\zeta(z\cdot\boldsymbol{\nabla}_z)R \tag{7b}$$

with the distance from the upper critical lateral dimension

$$\varepsilon = 4\mathfrak{z}-D$$

and the thermal roughness exponent[50]

$$\zeta_{th} = (2\mathfrak{z}-D)/2.$$

The flow equation (7a) for the temperature is believed to be exact due to a Galilean invariance[51] of the Hamiltonian. Thus we can conclude that for a disorder dominated phase with $\zeta > \zeta_{th}$, corresponding to relevant energy fluctuations and $\omega > 0$, the system is characterised by a $T = 0$ FRG fixed point, at which we want to determine the roughness exponent ζ. The other way to stabilise the temperature flow would be $\zeta = \zeta_{th}$, which is a solution on this level for every temperature T. Thus, there seems to be no direct way for this kind of analysis to capture the transition[52] from $\zeta > \zeta_{th}$ to $\zeta = \zeta_{th}$ at a finite temperature. Hence, we (for now) abandon all hopes of gaining insight into the nature of this transition, but we might still learn something about the disorder dominated phase. In the following, we work[53] with $T = 0$, as this is the fixed point we are interested in and this neglect of thermal fluctuations

[48] The author acknowledges the questionable thickness of the ice he is figuratively standing on here.

[49] We subscript these flow equations with SC to emphasise that these follow from scale-change.

[50] For $D \geq 2\mathfrak{z}$ the thermally fluctuating manifold does not have a macroscopic roughness and ζ_{th} can no longer be interpreted as thermal roughness exponent.

[51] The replicated energy functional depends only on derivatives and differences and, thus, a tilt of the line $z(x) \to z(x)+fx^{\mathfrak{z}}$ simply adds a contribution $\sim f^2L^D$ to the free energy. This contribution is only affected by the scale-change part of the renormalisation program and therefore the scale-change gives the exact flow of the temperature[68, 72].

[52] In sufficiently high transversal dimensions, $d > d_c$.

[53] That is, we only consider terms of the lowest in T, which obviously are terms of order $\mathcal{O}(T^{-2})$.

simplifies the flow-equations. As a consequence, we can make no statement about the transition at a finite temperature within this approach.

Upon inspecting the second flow equation (7b), we see that (as stated before) the trivial case of $R \equiv \text{const}$ does indeed imply $\zeta = \varepsilon/4$, the upper bound we found in a different manner before[54].

In the proper renormalisation, we integrate out short wavelength fluctuations in the lateral dimensions in a shell $\Omega(b)$, defined by[55] $\Lambda/b < |\boldsymbol{q}| < \Lambda$, in momentum space and perform the scale-change afterwards. As argued before this only involves the disorder part of the replicated energy as the scale-change considered before is exact for the elastic energies. We isolate the short scale fluctuations, $\boldsymbol{s}$, by splitting up the displacement field

$$\boldsymbol{z} = \tilde{\boldsymbol{z}} + \boldsymbol{s}$$

and can then in principle eliminate them by computing their contribution to the replicated partition function. The latter can at this point be written as

$$\overline{Z^n} = \left(\prod_\alpha \int \mathcal{D}\boldsymbol{z}_\alpha\right) \mathrm{e}^{-\beta \mathcal{H}_{FRG}[\{\boldsymbol{z}_\alpha\}]} = \left(\prod_\alpha \int \mathcal{D}\tilde{\boldsymbol{z}}_\alpha\right) \mathrm{e}^{-\beta \mathcal{H}_{FRG}[\{\tilde{\boldsymbol{z}}_\alpha\}]} \left(\prod_\alpha \int \mathcal{D}\boldsymbol{s}_\alpha\right) \mathrm{e}^{-\beta \mathcal{H}_0[\{\boldsymbol{s}_\alpha\}]}\, \mathrm{e}^{-\beta \mathcal{H}_{dis}[\{\boldsymbol{s}_\alpha\}]}$$

The second half of this can be expressed[56] in terms of thermal averages[57]

$$\overline{Z^n} \propto \left(\prod_\alpha \int \mathcal{D}\tilde{\boldsymbol{z}}_\alpha\right) \mathrm{e}^{-\beta \mathcal{H}_{FRG}[\{\tilde{\boldsymbol{z}}_\alpha\}]}\, \mathrm{e}^{\sum_j \frac{(-1)^j}{j!} \langle \beta \mathcal{H}_{dis}[\{\boldsymbol{s}_\alpha\}]^j \rangle_{c,0}}\,, \tag{8}$$

i.e. using the *free propagator* $G(\boldsymbol{q})$, which we define in Fourier space[58] by

$$\langle \boldsymbol{z}_\alpha(\boldsymbol{q}) \boldsymbol{z}_\beta(\tilde{\boldsymbol{q}}) = (2\pi)^D \delta^D(\boldsymbol{q} + \tilde{\boldsymbol{q}}) G(\boldsymbol{q})$$

and has the form $G(\boldsymbol{q}) = \frac{T}{q^{2\mathfrak{z}} + \mu} \delta_{\alpha,\beta}$. In this computation we have to keep in mind that by definition of $\boldsymbol{s}$ we only have to consider contributions from wave-vectors that are within the momentum shell $\Omega(b)$.

The averaged disorder energy $\langle \beta \mathcal{H}_{dis}[\{\boldsymbol{s}_\alpha\}]^j \rangle_0$ does not renormalise the disorder correlator[68]. This term includes the renormalisation of the disorder by thermal fluctuations (which is of the order T^{-1} and thus neglected for the $T = 0$ fixed-point) and, naturally, the renormalisation of the free energy. The higher terms can be systematically computed using a diagrammatic approach. The diagrams that have to be evaluated are *independent* from the type of elasticity used (as indicated by $\mathfrak{z}$), which only enters in the definition of the propagator. We could therefore skip the more tedious combinatorial aspects and directly adapt the results[59] of Ref. 58 to SDLs. It is however instructive to present the one-loop calculation here as this demonstrates the mechanism and it will become clear in the process why the one-loop equations do not depend on the elasticity type but the two-loop[58, 69–71] equations do. For this purpose it is sufficient to limit ourselves to the case of $d = 1$.

In Fig. 18 we present the main ingredients of the one-loop calculation. We are interested in the term $\sim \langle \beta \mathcal{H}_{dis}[\{\boldsymbol{s}_\alpha\}]^2 \rangle_{c,0}$ and therefore have to compute integrals with two instances of R in it, which in terms of the diagrammatics means that we consider diagrams with two vertices. Note that we only need to consider connected diagrams[60] as we compute cumulants. There is a momentum conservation rule for each loop (in the unsplit diagram) and a vertex with k outgoing lines corresponds to the k-th derivative (after k Wick contractions). Additionally, a disorder vertex with lines outgoing at both replicas ("saturated" vertex) means that the argument of the correlator

[54] In the scale-change equations we see that $\zeta = \varepsilon/4$ is an upper bound because $R > 0$ and also $(z \cdot \boldsymbol{\nabla}_z) R < 0$ (R should be a non-negative, monotonously decreasing function of $|\boldsymbol{z}|$).

[55] Here Λ is the ultraviolet cut-off.

[56] cf. the remark in sidenote 40 on page 32

[57] The two subscripts shall indicate that here cumulants (c) are to be calculated using (0) $\mathcal{H}_0$.

[58] Here the lateral dimensions are to be Fourier transformed, i.e. $\boldsymbol{z}(\boldsymbol{x}) \to \boldsymbol{z}(\boldsymbol{q})$.

[59] In Ref. 58 a dimensional regularisation instead of ultraviolet cut-off as presented here was used, evaluating all integrals to first order in $\varepsilon = 4\mathfrak{z} - D$ instead of limiting the integration domain to a shell in momentum space. This is a technical difference and of no further importance.

[60] Also, a disconnected diagram with m connected parts would have an additional combinatorial factor of n^{m-1} as the replicas indices would be independent and thus not contribute in the replica limit of $n \to 0$.

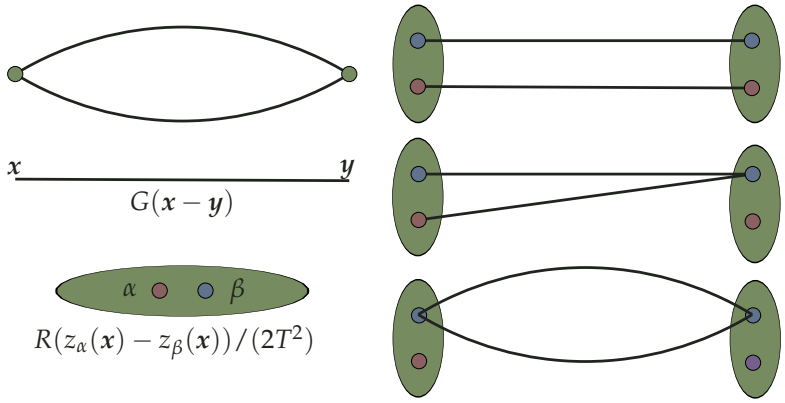

Figure 18: Sketch for the diagrammatic approach to the computation of the renormalisation flow equations following Ref. 58. The constituents of any diagram are the propagator (lines) and disorder vertices (green circles/ellipses) as shown in the lower left corner. There is one (top left) fundamental diagram to one-loop order, i.e. with two vertices. However, there are two replica indices involved at each vertex, which is the reason this diagram has to be "split" into the three topologically distinct diagrams on the right side. The three replica diagram (bottom) is of order T^{-1} as any loop connecting identical replicas contributes an additional factor T. The other two are contributing to the zero temperature equations (two vertices give T^{-4} and two lines give T^2). This figure is necessarily close to the figures of Ref. 58.

(respectively its derivative) is zero. Finally, we have to sum over all occurring replica indices.

Following these rules the two relevant diagrams lead to a renormalisation contribution

$$\delta R_1 = \int_{\boldsymbol{x},\boldsymbol{y},\boldsymbol{q},\boldsymbol{k}} \cdots \int \frac{\mathrm{e}^{-\mathrm{i}\boldsymbol{q}\cdot\boldsymbol{x}-\mathrm{i}\boldsymbol{k}\cdot\boldsymbol{y}}}{2!4T^4} \sum_{\alpha,\beta} G(\boldsymbol{q})G(\boldsymbol{k})\delta(\boldsymbol{q}+\boldsymbol{k})R''(z_\alpha(\boldsymbol{x})-z_\beta(\boldsymbol{x}))\left[N_{\mathrm{up}}R''(z_\alpha(\boldsymbol{y})-z_\beta(\boldsymbol{y}))+N_{\mathrm{middle}}R''(0)\right]$$

where the first term in brackets stems from the upper diagram on the right hand side of Fig. 18 and the second from the middle one. The pre-factor of $\frac{1}{2!}$ is the same as in (8). The factors N_{up} and N_{middle} are the combinatorial factors for the two diagrams. In the upper diagram we can switch the meaning of "blue" and "red", giving $N_{\mathrm{up}} = 2$, and in the middle diagram we can additionally choose at which colour there are two outgoing lines, giving $N_{\mathrm{middle}} = 4$. The momentum conservation leads to $\boldsymbol{x} = \boldsymbol{y}$ and the propagator contributions give in the limit of a shell as integration domain[61]

$$\int_{\Omega(b)} \cdots \int \frac{\mathrm{d}^D\boldsymbol{q}}{(2\pi)^D}\frac{T^2}{q^{4\mathfrak{z}}} = C_D T^2 \mathrm{d}l$$

where C_D is a prefactor that depends on the dimension D and the cut-off Λ. Collecting everything we end up with the one-loop renormalisation flow equations[62]

$$\left.\frac{\partial R}{\partial l}\right|_{\text{one loop}} = (\varepsilon - 4\zeta)R + \zeta z R' + C_D\left(\frac{1}{2}R''^2 - R''R''(0)\right)$$

where C_D can be eliminated by rescaling $R \to C_D^{-1/2}R$

$$\left.\frac{\partial R}{\partial l}\right|_{\text{one loop}} = (\varepsilon - 4\zeta)R + \zeta z R' + \frac{1}{2}R''^2 - R''R''(0).$$

This last step clears all dependence from the elasticity, but this means we have chosen a scale for R and in two-loop order there will be $\mathfrak{z}$-dependent factors. This is the form in which this equation has been presented before in Refs. 58, 67, 70 for $d = 1$ and Refs. 68, 71 for general d.

For general d and $\mathfrak{z}$, the two-loop contribution has not been calculated, but as already mentioned we can infer the two-loop level from Ref. 58 for

[61] We set $\mu = 0$ as we are only interested in high momenta.

[62] All omitted arguments of R and its derivatives are z.

general $\mathfrak{z}$ and $d = 1$, where

$$\left.\frac{\partial R}{\partial l}\right|_{\text{two loop}} = (\varepsilon - 4\zeta)R + \zeta z R' + \frac{1}{2}R''^2 - R''R''(0) + \frac{X_\mathfrak{z}}{2}\left[R'' - R''(0)R'''^2 - R'''(0^+)^2 R''\right] \tag{9}$$

has been found. The third derivative in the last term has to be evaluated as $R'''(0^+)$ because the correlator flows to a *non-analytic* solution with a *cusp*, that is a jump in the third derivative at zero. The elasticity type dependent prefactor $X_\mathfrak{z}$ is[70] to leading order in ε given by[63]

$$X_\mathfrak{z} = \int_0^1 \frac{\mathrm{d}t}{t}\,\frac{1 + t^\mathfrak{z} - (1+t)^\mathfrak{z}}{(1+t)^\mathfrak{z}} + \psi(2\mathfrak{z}) - \psi(\mathfrak{z})$$

The two relevant values here are $X_1 = 1$ and $X_2 = -1/6$. As we do not know the value of ζ a priori this equation does not suffice to formulate a closed problem. However, we are not interested in any solution of the flow equation, but only in the *one solution* that can reasonably be interpreted as an effective disorder correlator. Thus, the exponent ζ is determined from the FRG equation by requiring a fixed point solution for short-range disorder to be positive and vanish exponentially fast for large z. Therefore, in one-loop order results for the roughness exponent ζ depend on $\mathfrak{z}$ only through the dimensional expansion parameter $\varepsilon = 4\mathfrak{z} - D$.

For $d = 1$, we can adapt the final results achieved in Ref. 67 in one-loop, which have been extended in Refs. 58, 70 to two loops,

$$\zeta_{\text{FRG}} = 0.20830\varepsilon + 0.00686\, X_\mathfrak{z}\, \varepsilon^2. \tag{10}$$

For an SDL ($D = 1$, $\mathfrak{z} = 2$, $\varepsilon = 7$) with $d = 1$ transverse dimensions, we obtain on the one-loop level a roughness exponent[64]

$$\zeta_{\text{FRG, one loop}} \approx 1.4571,$$

which is close to the Flory estimate $\zeta_{Fl} = 3/5$ but also violates the lower bound set by the thermal roughness, $\zeta_{\text{FRG}} < \zeta_{th} = 3/2$. On the two-loop level, we find a negative prefactor $X_2 < 0$ and, thus, still $\zeta_{\text{FRG}} < \zeta_{th} = 3/2$.

The existence of an upper critical dimension d_u, above which $\zeta < \zeta_{th}$ applies, has been discussed, in particular for DLs (D=1, $\mathfrak{z}$=1) and as a candidate for the upper critical dimension of the KPZ equation to which the DL problem can be mapped. Our above finding $\zeta_{\text{FRG}} < \zeta_{th} = 3/2$ in two-loop order indicates that for SDLs with $\mathfrak{z} = 2$, $d = 1$ could be interpreted such that $d = 1$ is already above the upper critical dimension d_u, i.e., $d_u < 1$.

Using the one-loop result for general d, we can estimate this upper critical dimension d_u for SDLs. Solving the FRG fixed point equation for $R(z)$ numerically[65], we find $d_u \approx 0.84 < 1$ using the one-loop equations[66] and the numerical methods outlined in Ref. 58 . The two-loop result for the critical dimension is lower because, analogously to the DL results of Ref. 71, the two-loop corrections are negative for $d > d_u$. We will present numerical results which show that there exists a disorder dominated phase with $\zeta > \zeta_{th} = 3/2$ for SDLs in $d = 1$ below a critical temperature, which shows that the FRG results are questionable for lines with $D = 1$ and, correspondingly, large values for the expansion parameter ε. This could hint[67] towards a fundamental problem with this renormalisation group approach. One reason might be that it uses expansions in terms of $\varepsilon = 4\mathfrak{z} - D$. At $\varepsilon = 0$ one is at large

[63] Evaluation of the integral yields

$$X_\mathfrak{z} = \frac{2^{-\mathfrak{z}}(1+\mathfrak{z})\Gamma(1+\mathfrak{z})\Gamma(2+\mathfrak{z})^{-1}}{m} \times {}_2F_1(\{1,1\},2+\mathfrak{z},-1) - m\,{}_3F_2(\{1,1,1+\mathfrak{z}\},\{2,2\},-1) + \psi(2\mathfrak{z}) - \psi(\mathfrak{z}).$$

The special functions[73–75] used here are in ascending obscurity the Gamma function

$$\Gamma(x) = \int_0^\infty \mathrm{d}t\, t^{x-1}\,\mathrm{e}^{-t},$$

the Digamma function

$$\psi(x) = \frac{\Gamma(x)}{\Gamma'(x)}$$

and the generalised hypergeometric function

$${}_pF_q(\{a_1,\dots a_p\},\{b_1,\dots,b_q\},x) = \sum_{n=0}^\infty \frac{(a_1)_n \dots (a_p)_n}{(b_1)_n \dots (b_q)_n}\frac{z^n}{n!}.$$

The definition of the latter makes use of the Pochhammer symbol (or rising factorial)

$$(x)_0 = 1$$
$$(x)_n = x(x+1)\dots(x+n-1) \quad n \geq 1.$$

[64] This value is based upon a naive evaluation at $\varepsilon = 7$. Evaluation to two loops and Pade approximants give reasonably close values. We can use an argument following the lines of our scaling argument where we actually computed ζ in a zero-dimensional system to estimate the $D = 0$ value $\zeta_{D=0} = \mathfrak{z}$, which effectively allows us to determine a third order in ε. This way we find more physical estimates for the roughness exponent of $\zeta \approx 1.6 \pm 0.1$, where we obtain the errors by comparison of different extrapolation schemes. This will turn out to be in good agreement with the actual numerical result.

[65] The approximate solution for the roughness exponent (using one-loop terms)

$$\zeta_{\text{app}} \approx \frac{\varepsilon}{4+d}\left[1 + \frac{2^{-d+2/2}}{4e}\frac{(d+2)^2}{d+4}\right]$$

from Ref. 68 gives a critical dimension $d_u = 0.937669 < 1$.

[66] We use Taylor expansions up to order 12, which allows us to determine ζ to four digits. As this is the same method by which eq. (10) has been obtained, there is some value for the reader to present more detail in the appendix starting on page 81. The result $d_u < 1$ remains valid using the two-loop equations, where the additional two-loop terms contain the same factor $X_\mathfrak{z}$ as for $d = 1$.

[67] There is, of course, the more technical explanation that $\varepsilon = 7$ might demand higher terms.

transversal dimension $D = 4\mathfrak{z} > 2\mathfrak{z}$. This means that the expansion is done starting from a manifold that is thermally flat[68] and thus fails to incorporate thermal fluctuations.

[68] In the sense that $\langle z^2 \rangle$ remains finite on arbitrarily large length scale; hence, the thermal roughness exponent is $\zeta_{th} = 0$, see also note 50 on page 34.

Another interesting question is how the flow changes with thermal fluctuations. To study the influence of a finite temperature let us consider the lowest level on which this is possible, that is the first term of higher order in T we neglected, the one in the zero-loop correction (from $\langle \beta \mathcal{H}_{dis}[\{s_\alpha\}^j] \rangle_0$). If we include this and the scale-change contribution we find at *fixed temperature* in suitable units that the stationary solution of the flow equation is given by

$$0 = (\varepsilon - 4\zeta)R + \zeta R' u + R'' = R + \zeta_{th} u R' + R''.$$

We used that a solution at fixed temperature can only exist at the thermal roughness. This equation can be solved[69] and one finds[70]

$$R_{\zeta_{th}}(z) = \mathrm{e}^{-\zeta_{th} z^2/2}\, M(-\frac{1-\zeta_{th}}{2\zeta_{th}}, \frac{1}{2}, \frac{\zeta_{th}}{2} z^2).$$

[69] Here, we are using the initial conditions $R(0)=1$ (arbitrary), $R'(0)=0$ (symmetry).

[70] Kummer's confluent hypergeometric function[73] $M(\alpha,\beta,\gamma)(x)$ is a special case of generalised hypergeometric function introduced earlier in sidenote 63, namely $M(\alpha,\beta,\gamma)(x) = {}_1F_1(\alpha,\beta,\gamma)(x)$.

The Gaussian envelope guarantees a sufficiently fast decay. However, this solution could pass through zero. From Refs. 74, 75 we learn that $R_{\zeta_{th}}$ has no positive real roots, if $\zeta_{th} > 1$, and[71] $\lceil -\frac{1-\zeta_{th}}{2\zeta_{th}} \rceil$ positive real roots, if $\zeta_{th} < 1$. Thus, the simplified flow equations studied here allow for a solution with thermal roughness only above the lower critical dimension, that is $d > d_c$ or $d\zeta > 1$. This is a rather surprising agreement with our scaling analysis before. We take this a hint that the FRG is in principle able to capture the transition and a high temperature phase. However, as this is a *functional renormalisation* procedure the manifestation of such a transition is more subtle than in standard renormalisation schemes, where we would expect a repulsive fixed-point of the flow as a trademark of the transition. The existence of two phases is linked to the question whether there are two distinct values of ζ for which the corresponding solution of the correlator flow equation is physically sensible. Ideally, one would like to reduce the complexity of this problem by finding a family $R_\varepsilon(z,\zeta)$ of correlators that solve the flow equations for any given ε,ζ and reduce the flow of the function $R(z)$ to one of ζ. However, this might very well be impossible.

[71] Here, $\lceil x \rceil$ is the smallest integer that is larger or equal to x (ceiling).

Summary of analytical efforts

We found through scaling analysis that the SDL in $d = 1$ undergoes a transition from a high temperature phase with $\zeta = \zeta_{th}$ to a disorder-dominated phase with $\zeta > \zeta_{th} = 3/2$. We also found an upper bound to the roughness exponent in the latter phase by mapping the SDL to a one-dimensional substitute problem, a procedure which overestimates the disorder. This way, we were able to deduce $\zeta < 7/4$. The variational replica calculation though ultimately fruitless provided further arguments for the existence of a disorder dominated phase. Finally, we presented a functional renormalisation group analysis that in its current form is not able to produce a reliable result for the roughness exponent. Yet, we were able to find hints of the transition within this framework by considering the temperature in the flow equations in the lowest order.

This is frankly quite unsatisfactory. The analytical treatment of elastic manifolds in disorder is difficult and this holds for the SDL as well. This should not be reason for deeper frustration as we still have one rather fail-safe option in our arsenal of problem-solving techniques: the numerical approach.

So[72], if this problem is unwilling, we will use force ...

[72] This is meant as an allusion and not as endorsement of violence or erlkings.

Numerical results

Returning from $(D+d)$-dimensional manifolds to the problem of $(1+d)$-dimensional SDLs in disorder, further progress is possible by numerical studies using the transfer matrix method [23, 24] both for $T=0$ (as seen in Fig. 9 (page 25)) and for $T>0$.

Previous numerical studies for DLs in 1+3 dimensions offer the opportunity for a comparison of the exponents ω (energy fluctuations), describing the low temperature phase, and ν (correlation length), describing the transition[73], in the low temperature phase to test the aforementioned analogy to an SDL in $1+1$ dimensions. The values found there are $\omega \approx 0.186$ [35, 36, 76, 77] and either $\nu \approx 2$ [33, 36, 39] or $\nu \approx 4$ [34, 36].

[73] To fully describe the behaviour at criticality an infinite number of exponents is needed, see Refs. [39, 49] and the section on the multifractal nature of the partition function starting on page 47.

Transfer matrix algorithm

We are going to use a transfer matrix algorithm, details of which can be found elsewhere[4]. For the sake of a closed presentation in this work we will present the basic concept in the following[74]. Instead of tackling the whole partition function we consider the restricted partition function

$$Z_L(z,v) = \int_{z(0)=v(0)=0}^{z(L)=z,v(L)=v} \mathcal{D}z\ \mathrm{e}^{-\beta\mathcal{H}}$$

where the subscript denotes the length. This gives the probability or weight $w_L(z,v)$ for the line to end at length L with a displacement z and a tangent orientation v via

$$w_L(z,v) \equiv \mathrm{Prob}(z(L)=z, v(L)=v) = Z_L(z,v)\Big(\sum_{z',v'} Z_L(z',v')\Big)^{-1}.$$

[74] We will explain the algorithm with the SDL in mind as we consider the transfer to a DL to be straightforward.

The probability distribution for the ending points at length L is directly related to the distribution at a shorter length $L-\Delta L$, because the total probability is a conserved quantity and, thus, w_L is given[75] by $w_{(L-\Delta L)}$ and the *transition probabilities* for the segment of length ΔL. This reasoning gives rise to the *Chapman-Kolmogorov equation*

$$w_L(z,v) = \int \mathrm{d}y\,\mathrm{d}u\, w_{L-\Delta L}(y,u) w_{\Delta L}(y,u|z,v)$$

[75] The evolution of $w_L(z,v)$ is a Markovian process (or Markov chain once x is discretised). If we tried to marginalise the tangent distribution $\tilde{w}_L(z) \propto \int \mathrm{d}v\, w_L(z,v)$ this would not hold because of the bending interaction that contains a second derivative.

where $w_{\Delta L}(y,u|z,v)$ is the probability of a line with length ΔL starting at (y,u) to end at (z,v) in the phase space spanned by displacements and tangent orientations. For a sufficiently small ΔL the line segment is straight and we can directly evaluate the needed path integral as it reduces to essentially one path. In this limit $w_{\Delta L}$ is given by the Boltzmann factor corresponding to the energy gain or loss on this straight segment. From a discretisation of the energy functional we conclude that a segment of an SDL with[76] length $\Delta L = 1$ starting at y with orientation $\mathrm{d}z/\mathrm{d}x = u$ and ending at z with orientation v contributes an energy $\Delta E_x(u-v,z) = \varkappa/2(u-v)^2 + V(x,z)$, where the additional causality condition $z = y+v$ applies which couples positions and tangents. The random potential breaks the translational symmetry in the x-direction, which introduces a direct dependence of this transition energy from the position. In summation, we can compute the restricted partition function by a *transfer matrix* method[77]

$$w_L(z,v) \propto \sum_{\substack{u \\ |u-v|\le\Delta_v}} \mathrm{e}^{-\beta\Delta E_L(u-v,z)}\, w_{L-1}(z-u,u)\,. \tag{11}$$

[76] This merely constitutes a choice of length units.

[77] We introduce here the cut-off Δ_v, exploiting that the energy is parabolic in the tangent difference. Additionally z and v are also limited to keep the dimension of the partition function and the transfer matrix finite, see Ref. 4 for details.

The proportionality constant is given by the normalisation condition[78] $1 = \sum_{z,v} w_L(z,v)$. The algorithm of eq. (11) can be used to compute the weights iteratively. We also discretise the z-direction, such that the line now is a piecewise linear spline on a (for simplicity) square lattice. The lattice constant coincides in our method with the correlation length of the disorder, which is drawn on each lattice site[79]. For the sake of simplicity and comparability we choose $g = 1$ and vary the temperature. The initial condition is given by $w_0(z,v) = \delta_{z0}\delta_{v0}$.

[78] For numerical stability reasons, the restricted partition function $Z_L(z,v)$ should not be evaluated directly but its normalised pendant $w_L(z,v)$. The cumulated normalisation constant is a useful quantity as it is the total partition function and therefore gives the free energy.

[79] The random potential $V(x,z)$ is represented by Gaussian random variables drawn using the Ziggurat method[78] with $\overline{V(x,z)} = 0$ and $\overline{V(x,z)V(x',z')} = g^2\delta_{xx'}\delta_{zz'}$

Zero temperature

For vanishing temperature $T = 0$ there are no entropic contributions to the free energy. Hence the line is always in its ground state and minimising the energy E_L^0, and the superscript is a reminder that these considerations are valid for $T = 0$. This can be done iteratively

$$E_L^0(z,v) = \min_u \left[E_{L-1}^0(z-u,u) + \Delta E_L(u-v,z)\right]$$

and all observables X are to be measured in the resulting (non-degenerate) ground state, i.e. $\langle X\rangle_{T=0} = X(z_{\min},v_{\min})$ with the ground state energy $E_L^0(z_{\min},v_{\min}) = \min_{z,v} E_L^0(z,v)$.

Finite temperature

At finite temperature the weight w_L, the normalised version of the restricted partition function Z_L, is used in the computation of thermal averages

$$\langle X\rangle = \Big(\sum_{z,v} Z_L(z,v)\Big)^{-1} \sum_{z,v} X(z,v)Z_L(z,v) = \sum_{z,v} X(z,v)w_L(z,v)$$

This averaging procedure is only correct for quantities X that are measured at the end of the line, moments of the energy (potential or total) are accumulated along the contour of the line and have to be computed in an iteration scheme[4, 23] very similar to eq. (11). Finally, for all observables the quenched average over realisations of the disorder has to be performed.

[80] The expectation being that a phase transition is associated with a divergence (or discontinuity) in derivatives of the free energy, which should be apparent in the free energy.

Free Energy

Existence and nature of the disorder dominated phase

Looking for a phase transition and with the free energy directly available it is rather straightforward[80] to look in the free energy for any evidence of a phase transition.

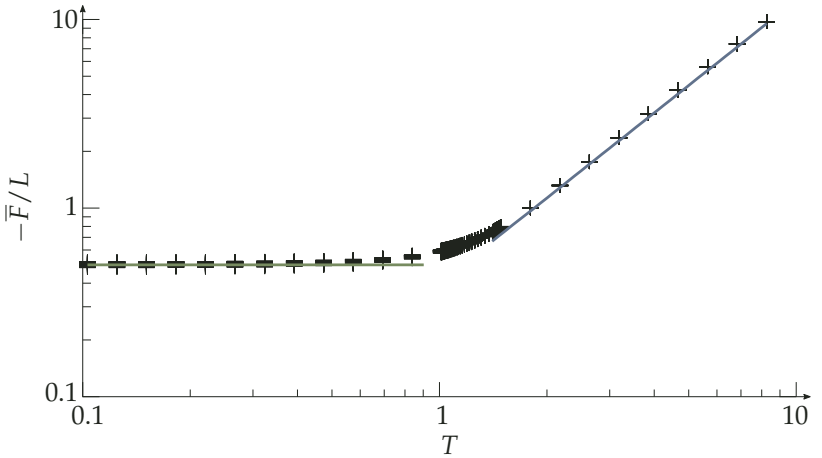

Figure 19: The disorder average of the free energy per length $\overline{F}/L$ as a function of the temperature shown as a log-log-plot. The clear change in the temperature dependence from $\sim T^0$ to $\sim T$ is strong evidence of a phase transition. We plotted these asymptotics as well. We show lengths $L = 50,60,\ldots,100$, so that the "scattering" of the symbols for one temperature indicates the deviation from extensivity $F \sim L$. For sufficiently high temperatures, $T \gtrapprox 2$, there is a very good agreement with the thermal scaling behaviour. The symbols spread in the low temperature phase, implying non-vanishing fluctuations due to the finite number of disorder realisations.

We know the free energy scales as $F \sim TL$ in the free, $g = 0$, system. This should be recovered for high temperatures, whereas temperature should be irrelevant in a disorder dominated phase, which should also feature large scale energy fluctuations giving rise to a finite value of the respective exponent ω, so we expect $\overline{F} \sim T^0 L$.

In Fig. 19 we show the free energy per length as a function of the temperature. This figure is rather boring in the good way in that it nicely matches our expectation[81] for the free energy in a system that undergoes a disorder-driven localisation transition. We can conclude that there is a transition and that it is very roughly[82] localised at $T_c \approx 1-2$.

To classify this disorder-dominated phase we can as directly as before look at the fluctuations around this mean free energy and determine the energy fluctuation exponent ω by fitting the sample-to-sample fluctuations

$$\Delta F(L,T) = (\overline{F(L,T)^2} - \overline{F(L,T)}^2)^{1/2} \propto L^{\omega}.$$

The result of this procedure is shown in Fig. 20. There is a clear evidence for a transition with a significantly non-vanishing value of ω at low temperatures which is of the order of $\omega \approx 0.15-0.16$. However, we see that this method of determining ω is biased due to the finite size of the system, which becomes apparent in the non-vanishing fluctuation exponent at high energies. Using this discrepancy $\Delta\omega \approx 0.02$ as an estimate for the error of this method we see that the value of ω determined from the free energy fluctuations is compatible to $\omega \approx 0.13-0.18$. The steep flank in $\omega(T)$ allows us to give a more precise estimate for the critical temperature of $T_c \approx 1.5$.

[81] Note that due to a clerical error the free energy has been misrepresented in Ref. 4, leading to the unphysical behaviour discussed therein.

[82] We will determine T_c in a more precise manner later on, which is not possible using the free energy alone.

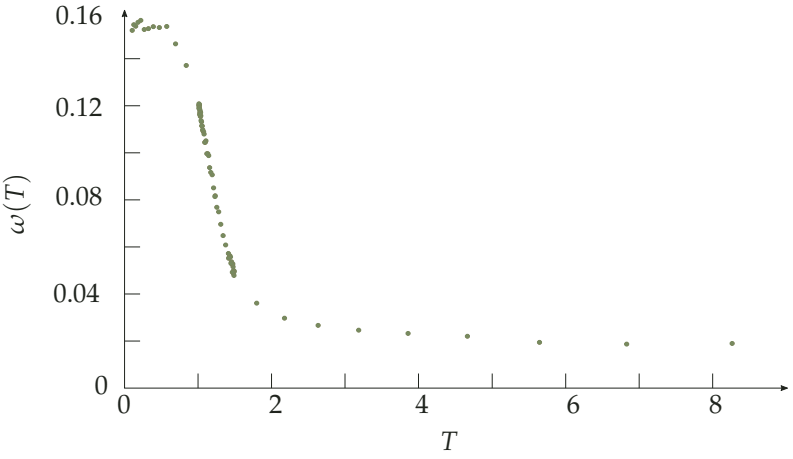

Figure 20: The energy fluctuation exponent ω determined from the sample-to-sample fluctuations of the free energy $\Delta F(L,T) = (\overline{F(L,T)^2} - \overline{F(L,T)}^2)^{1/2}$ by fitting the expected L^{ω}. The result is consistent with a phase transition around $T_c \approx 1.5$ and does indeed show a larger exponent for $T < T_c$. However, there is also a systematic error apparent in this determination of ω, leading to non-vanishing values of ω even at very high temperatures.

Roughness

The other natural observable to analyse looking for a localisation transition is the *roughness* $\overline{\langle z^2 \rangle}$. The expectation is that the two phases should manifest in a twofold manner, via a different scaling with length as we expect different roughness exponents and via a different temperature dependence. Thus the roughness should show two different regimes, a high temperature phase with the thermal roughness $\overline{\langle z^2 \rangle} \sim TL^3$ and a low temperature phase with $\overline{\langle z^2 \rangle} \sim T^0 L^{2\zeta}$ (with $\zeta > \zeta_{th}$.

In Fig. 21 we show the roughness $\overline{\langle z^2 \rangle}$ as a function of temperature and demonstrate that these expectations are met. The roughness as a function of the temperature T does indeed show the two regimes and there is also a good agreement to the free energy shown in Fig. 19.

In order to determine ζ we measure[83] a *local roughness exponent*[43]

$$2\zeta(L) = \log_5(\overline{\langle z^2 \rangle}(L) / \overline{\langle z^2 \rangle}(L/5)) \tag{12}$$

This method of determining ζ gives more sensible results than fitting $\overline{\langle z^2 \rangle}(L)$ directly as we did for the energy fluctuation exponent.

[83] The number 5 in this seems rather arbitrary, because it is. It is a compromise between the wish to compare two lengths as far apart as possible to see clearer scaling and the necessity to not include too small lengths which might display transient behaviour.

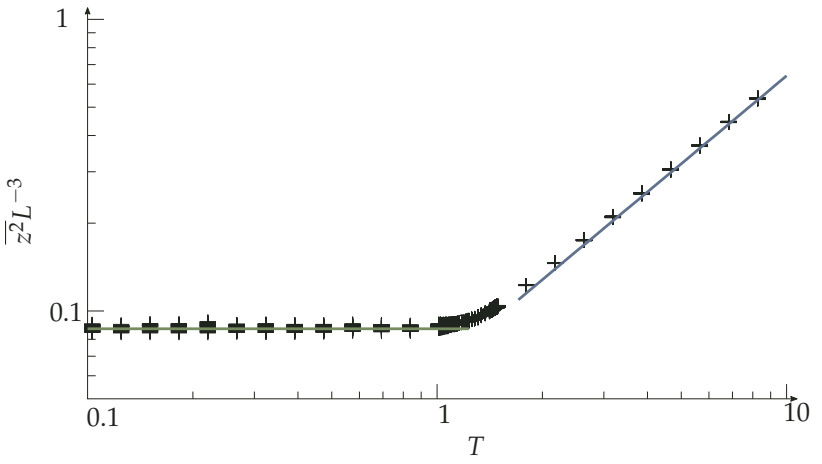

Figure 21: The roughness $\overline{\langle z^2\rangle}$ as a function of the temperature. There are two distinct regimes where the roughness scales as $\overline{\langle z^2\rangle} \sim T^0$ and $\overline{\langle z^2\rangle} \sim T$ respectively. We plotted these asymptotics as well. We show lengths $L = 50{,}60{,}\ldots{,}100$, so that the "scattering" of the symbols for one temperature indicates the quality of the rescaling with L^{-3}. Sufficiently deep in the high temperature phase, $T \gtrapprox 2$, there is hardly any broadening of the original cross symbols corresponding to good agreement with $\zeta = \zeta_{th} = 3/2$ scaling behaviour. Reversely, the symbols show a significant width in the deep temperature phase, with points for larger L showing higher rescaled roughness (not visible here) implying $\zeta > \zeta_{th}$. For a more rigorous analysis of the length scaling see the main text and Fig. 22.

The data for $\zeta_\varkappa$ as a function of temperature presented in Fig. 22 exhibit two distinct high and low temperature regimes and a significant "dip" of the local roughness exponent around $T \approx 1.4$.

Via the scaling relation (5), $\omega = 2\zeta - 3$, we obtain the exponent ω from the roughness exponent $\zeta_\varkappa$. As in the context of DLs[79], it can be argued that ω should vanish at the disorder-induced localisation transition, resulting in a roughness exponent $\zeta = 3/2$. This seems to hold, even though the numerical value for high temperatures is slightly above $\zeta = 3/2$. The origin of the slightly too large roughness exponents in the high temperature phase is not clear, with one possible explanation being that the lower length used in the computation of the roughness exponent is too small and therefore still influenced by the initial conditions.

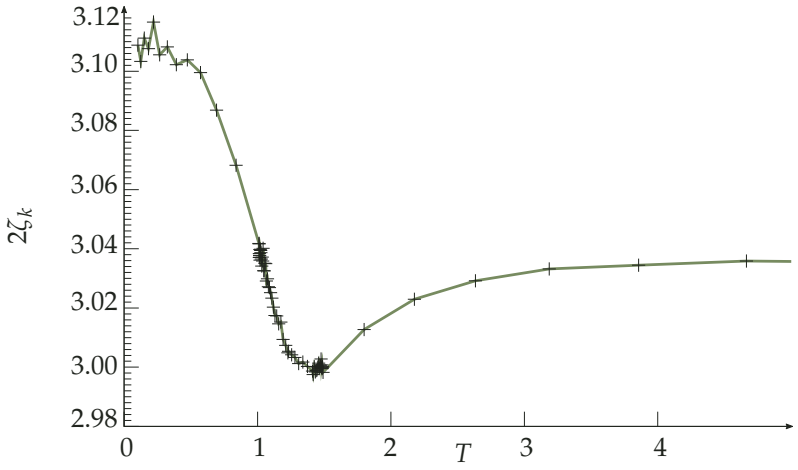

Figure 22: Roughness exponent $2\zeta_\varkappa$ for various temperatures, computed via (12). The deviation for high temperatures from the analytical value $2\zeta = 3$ indicates numerical shortcomings, nonetheless there is a clear "dip" at $T \approx 1.4$, which we identify as the critical temperature. For low temperatures, we find values consistent with $\omega \approx 0.11$.

This is strong evidence for a phase transition at $T_c \approx 1.4$. For low temperatures, the values $2\zeta \approx 3.11$ give $\omega \approx 0.11$ according to eq. (5), which is slightly lower than $\omega = 0.186$, which is the literature value for DLs in 1+3 dimensions [35, 36, 76, 77]. However, it is also clearly visible that these local estimates for the roughness exponents are still temperature dependent, which is an indication that the lengths used here are not large enough to suppress any next-to-leading order influences. What we can safely infer is that there is a transition to a rougher, disorder dominated phase, where temperature becomes irrelevant, and the transition temperature is $T_c \approx 1.4$.

Disorder-induced persistence length

The roughness, the displacement in the transversal dimension, is closely related to the averaged tangent directions $\overline{\langle v^2\rangle} \equiv \overline{\langle(\partial_x z)^2\rangle}$, which from

dimensional analysis should scale as

$$\overline{\langle v^2\rangle} \sim \overline{\langle z^2\rangle}/L^2 \sim L^{2(\zeta-1)} \sim L^{1+\omega}.$$

The tangent fluctuations do not only allow for a complementary determination of the roughness related exponents ζ and ω, but also to determine the length scale on which the line reorients, which we already introduced as the persistence length. We define[84] an effective *disorder-induced persistence length* $\tilde{L}_p$ for the SDL as the length scale at which the disorder averaged tangent fluctuations become equal to one,

$$\overline{\langle v^2\rangle}(\tilde{L}_p) = 1. \tag{13}$$

[84] This is apart from the disorder average completely identical to the way we introduced the persistence length in the first place.

In the low temperature phase, we expect a disorder dominated roughness and temperature-independent tangent fluctuations $\overline{\langle v^2\rangle}$, which result in a temperature-independent disorder-induced persistence length with $\tilde{L}_p \sim T^0$. The line roughens in the low temperature phase, which gives rise to a persistence length decrease as compared to the thermal persistence length that diverges for low temperatures, $L_p \sim \varkappa/T$. From the Flory result $z \sim (g/\varkappa)^{2/(4+d)} L^{7/(4+d)}$ at low temperatures, we expect $v \sim (g/\varkappa)^{2/(4+d)} L^{(3-d)/(4+d)}$ for the disorder-induced tangent fluctuations and find a Flory estimate for the parameter dependence of the effective persistence length

$$\tilde{L}_p \sim (\varkappa/g)^{2/(3-d)} \tag{14}$$

at low temperatures according to the criterion (13). For SDLs in $1+1$ dimensions, we therefore expect $\tilde{L}_p \propto g^{-1}$.

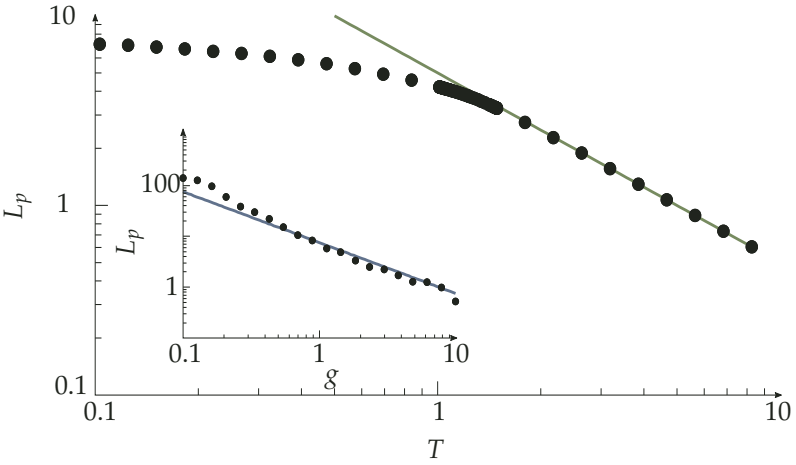

Figure 23: The generalised persistence length $\tilde{L}_p$ according to eqs. (13) and (16) as a function of the temperature T. $\tilde{L}_p$ matches its thermal value (solid line) for $T > T_c$ and is reduced and approximately constant for $T < T_c$. Our method of determining L_p allows for $L_p < 1$ even though the transfer matrix algorithm uses a discretised line built from segments of length $\Delta L = 1$. Inset: $\tilde{L}_p$ at $T = 0$ versus the potential strength g. The Flory result $\tilde{L}_p \sim g^{-1}$ (green line), see eq. (14) matches the data.

To determine the generalised persistence length from eq. (13) numerically, we used the *tilt symmetry* of the replicated Hamiltonian[80], according to which the value of the *internal fluctuations*

$$\overline{\langle v^2\rangle - \langle v\rangle^2} \approx L/\beta\varkappa$$

is independent of the disorder strength and always takes its high temperature phase value.[85] Therefore, we can separate the disorder independent and dependent contributions to the tangent fluctuations

$$\overline{\langle v^2\rangle} = \overline{\langle v^2\rangle - \langle v\rangle^2} + \overline{\langle v\rangle^2}$$

and use a fit to the latter of the form

$$\overline{\langle v\rangle^2}(T,L) = a(T) L^{1+\omega'(T)} \tag{15}$$

[85] This is due to the invariance of the replicated energy functional under tilts, as already exploited around footnote 51 on page 34. This is discussed in more detail in Ref. 4.

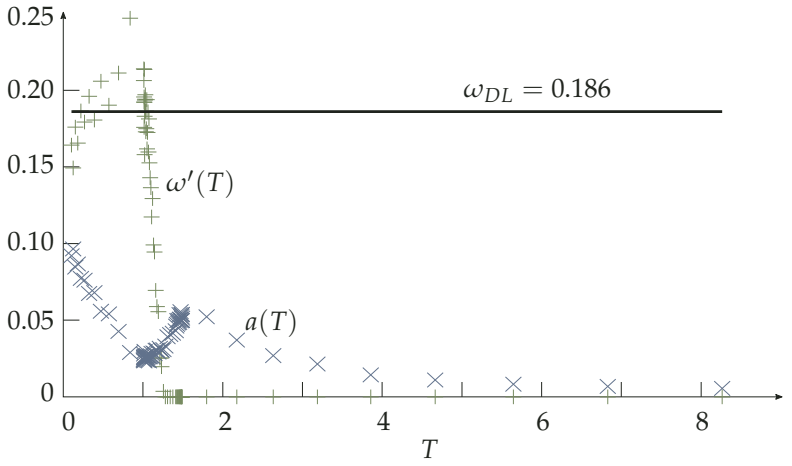

Figure 24: The parameters $a(T)$ (green, Greek crosses) and $\omega'(T)$ (blue, saltires) used in fitting the sample-to-sample fluctuations of the tangent directions, $\overline{\langle v \rangle^2}$, cf. eq. (15). The latter vanishes around $T = T_c$. Comparing this to the direct fit shown in Fig. 20 we see that the method used here gives more plausible results. The amplitude $a(T)$ is of lesser importance here and given for completeness, if we fix $\omega' = \omega = 0.186$, it vanishes around $T = T_c$. The horizontal line corresponds to the literature value for DLs in $1+3$ dimensions, $\omega = 0.186$.

with an amplitude $a(T)$ and an exponent $\omega'(T)$, which should agree with the free energy exponent ω. Then, we can rewrite $\overline{\langle v^2 \rangle}$ as[86]

$$\overline{\langle v^2 \rangle} = \frac{L}{\beta \varkappa} + a(T) L^{1+\omega'(T)}, \tag{16}$$

and determine $\tilde{L}_p$ using eq. (13). This allows for the isolation of the "non-trivial" contribution to the tangent fluctuations and, therefore, a more concise determination of the effective persistence length.

Our results for $\tilde{L}_p$ are shown in Fig. 23. In the low-temperature phase for $T < T_c \approx 1.4$, the persistence length becomes indeed disorder-induced, i.e., almost independent of temperature and our results are consistent with the above scaling result (14). In the high temperature phase, our results approach the standard thermal persistence length $L_p \sim \beta \varkappa$.

The results for the parameters, $a(T)$ and $\omega'(T)$, used in the fit of (16) to the data are shown in Fig. 24. For $T < T_c$ our results are consistent with $\omega \approx 0.186$, which is the literature value for DLs in $1+3$ dimensions [35, 36, 76, 77]. In fact, we get very similar results for L_p if we fix $\omega'(T) = \omega = 0.186$. Finally, the best fit for $a(T)$ is strictly positive, resulting in a decrease of the persistence length due to the disorder in accordance with the expectation.

Disorder-induced localisation and binding

The localisation transition temperature T_c equals the replica pair transition temperature T_2 for SDLs

The direct way to search for a relation to a binding problem is to study the associated binding problem. We have checked for the SDL via numerical transfer matrix calculations that the localisation temperature in disorder T_c equals the transition temperature T_2 for replica pair binding, $T_c = T_2$. As stated before, we use the same transfer matrix algorithm for the replica pair system with a short-range binding potential by exploiting that the binding of two SDLs can be rewritten as a binding problem of one effective SDL in an external potential using relative coordinates [82]. This SDL has a bending stiffness of $\varkappa' = \varkappa/2$ and the "potential energy" we are interested in (cf. eq. (6)) for the replica pair binding is $-\beta g^2 \int \mathrm{d}x\, \delta(z)$. For the interpretation of the simulation results one has to keep in mind that the energy functional is temperature dependent and, therefore, derivatives of the free energy with respect to the inverse temperature β are not given directly by cumulants of the internal energy. Using the notations

$$\mathcal{H}_{el} = \varkappa \int \mathrm{d}x\, (\partial_x^2 z)^2$$

[86] In the case of $\omega = \omega' = 0$ we find

$$\begin{aligned} \overline{\langle v^2 \rangle} &= L/\tilde{L}_p \\ &= L/L_{p,th} + L/L_{p,dis} \end{aligned}$$

allowing for a separation of disorder ($L_{p,dis}$) and thermal ($L_{p,th}$) contributions to the persistence length. This has been used in Ref. 81, but is strictly only valid for $\omega = 0$. For finite ω we find that $\tilde{L}_p$ is given as the solution of

$$1 = \tilde{L}_p/L_{p,th} + (\tilde{L}_p/L_{p,dis})^{1+\omega}.$$

Also, we can not directly infer the tangent correlations from v^2. In the thermal case we have $\langle \boldsymbol{t} \cdot \boldsymbol{t}' \rangle = \langle \cos\theta \rangle = {}^1/_2 \langle \mathrm{e}^{\mathrm{i}\theta} + \mathrm{e}^{-\mathrm{i}\theta} \rangle = \mathrm{e}^{-\langle \theta^2 \rangle/2}$ and with $v = \sin\theta \approx \theta$ we find a direct connection between the tangent correlations of a WLC and the tangent orientations of an SDL. However, this assumes *Gaussian* statistics of v which is incompatible with a finite ω.

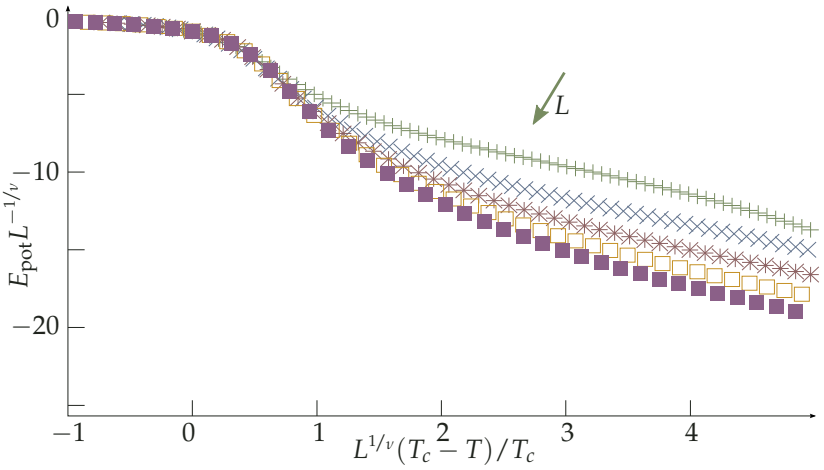

Figure 25: Finite size scaling for the SDL adsorption problem that corresponds to the two-replica binding, see text for detailed explanation. The scaling uses $T_c = 1.44$ and $\nu = 2$. As only one sample is needed for the calculation we used larger system lengths $L = 100$ (green, Greek crosses),200 (blue, saltires),...,500 mauve, full squares).

as before for the elastic part of the energy and

$$\mathcal{H}_{bind} = -g^2 \int \mathrm{d}x\, \delta(z)$$

for the reduced[87] binding energy the partition function is given by

$$Z = \int \mathcal{D}z\, \mathrm{e}^{-\beta\mathcal{H}_{el} - \beta^2 \mathcal{H}_{bind}}\,.$$

As always the free energy is computed via $F = -\beta^{-1} \ln Z$ implying that

$$\frac{\partial(\beta F)}{\partial\beta} = \langle \mathcal{H}_{el} + 2\beta\mathcal{H}_{bind}\rangle = U + \beta\langle\mathcal{H}_{bind}\rangle$$

where U is the total internal energy (treating $\beta\mathcal{H}_{bind}$ as a potential). Thus, the derivative of the difference of the free energies with and without the adsorption term with respect to the inverse temperature, which (assuming hyperscaling) should give the divergent correlation length $\beta\delta F = \beta(F_g - F_0) \sim L(T_c - T)^\nu$, is close to criticality identical to the "potential energy" $E_{pot} = -\beta\mathcal{H}_{bind}$ and usual finite size scaling should be applicable, as is shown in Fig. 25. We retain the known correlation length exponent $\nu = 2$ for the adsorption problem [82]. We see matching curves for the used system sizes $L = 100, 200 \ldots 500$ around $T - T_c \approx 0$ for $T_2 = 1.44$, which equals $T_c \approx 1.4$ for the SDL in disorder.

[87] Reduced in the sense that factors of T are missing

Pair overlap as order parameter

More importantly, we identify a binding-related order parameter for the localisation transition. For DLs, the disorder-averaged overlap

$$q = \lim_{L\to\infty} \overline{\frac{1}{L}\int_0^L \mathrm{d}x\, \delta(z_1(x) - z_2(x))}$$

of two replicas has been proposed as order parameter [44, 45]. Up to now, it has been numerically unfeasible to verify this order parameter for DLs in $d > 2$ dimensions where a localisation transition exists because the relevant $2d$-dimensional two replica phase space is too large. For SDLs, on the other hand, the transition is numerically accessible already in $1+1$ dimensions and we show that the overlap q is indeed a valid order parameter using an adaptation of the transfer matrix technique from Ref. 44, see Fig. 26.

This involves simulating *two* interacting SDLs, therefore[88] we have to compute the full overlap-distribution. That is we have to keep track for every point in the four-dimensional two-line phase-space (two displacements

[88] This is very similar to how energies are computed, see Ref. 4, but involves twice the number of degrees of freedom

and two tangent orientations) how much overlap weight has been accumulated by all paths ending there. This is done by iteratively computing the overlap-distribution $Q_L(z_1,v_1;z_2,v_2)$, whose transfer matrix equation reads

$$Q_L \propto \sum_{\substack{u_1,u_2 \\ |u_1-v_1|\leq\Delta_v \\ |u_2-v_2|\leq\Delta_v}} \mathrm{e}^{-\beta\Delta E_L(u_1-v_1,z_1)-\beta\Delta E_L(u_2-v_2,z_2)} \left[Q_{L-1}(z_1-u_1,u;z_2-u_2,u_2) + w_L(z_1-u_1,u_1)w_L(z_2-u_2,u_2)\delta_{z_1,z_2}\right].$$

The first term in the brackets represents the contribution from shorter lengths and the second term gives the current overlap at length L. We omitted the normalisation factor which is given by the square of the normalisation factor used in the normalisation of the weights. Using this we can directly compute the overlap at a given length as

$$q(L) = \frac{1}{L}\overline{\sum_{\substack{z_1,z_2 \\ v_1,v_2}} Q_L(z_1,v_1;z_2,v_2)}.$$

As this clearly is associated with a greater amount of computational effort, we only use lengths up to $L = 30$ and 10^3 samples.

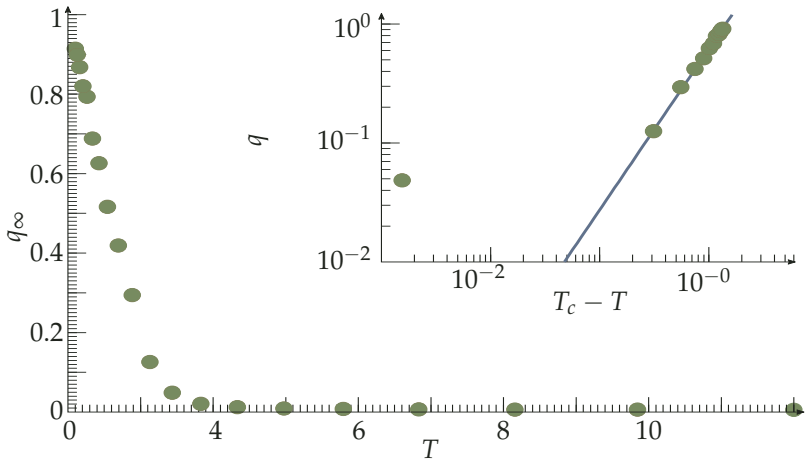

Figure 26: Two plots regarding the overlap order parameter q. Large: We estimate the value of q at infinite length, q_∞, from finite lengths using a fit that accounts for the first correction in L^{-1}

$q_T(L) = a(T)/L + q_\infty(T)$.

In the plot we show q_∞ as a function of the temperature T. Inset: Double-logarithmic plot of the overlap q (at the largest length considered, i.e. $L = 30$) versus $T_c - T$ (with $T_c = 1.44$), the solid line is given by $q \sim (T_c - T)^{-\beta'}$ with $\beta' \approx -1.36$.

For DLs, it has been found[45] that the overlap at criticality decays as $q \sim L^{\Sigma}$ with $\Sigma = -2\zeta = -(1+\omega)$ in $d = 3$. This has been extended to finite temperatures yielding $q \sim |T - T_c|^{-\nu\Sigma}$. Indeed, we find a qualitatively similar behaviour

$$q \sim |T - T_c|^{-\beta'}$$

with an exponent $\beta' \approx 1.3 - 1.4$. Our best estimate for Σ is $\Sigma \approx -0.75$, cf. Fig. 27. Because of small simulation lengths L we do not conclude this deviation to be a definite statement against the renormalisation group results presented in Ref. 45, but, interestingly, this would, unlike the DL renormalisation group result $\Sigma = -(1+\omega) < -1$, suggest[20] that two SDLs in a random potential are certain to meet eventually.

At this point it is noteworthy that our own renormalisation group analysis from before suggested that the effective disorder correlator R transforms under a scale-change $\boldsymbol{x} \to b\boldsymbol{x}$ like $R \to b^{-4\varepsilon+4\zeta}R$. This disorder correlator captures the effective disorder energy per length and it is therefore reasonable to assume that q should show identical scaling behaviour which would imply

$$q \sim L^{-4\varepsilon+4\zeta} \sim L^{-D+2\omega}$$

which is not directly dependent on the type of elasticity considered. By this reasoning, we can give a "scale-change" estimate for Σ

$$\Sigma|_{SC} \approx -0.628$$

which is close (considering the small system sizes) to the numerical value $\Sigma \approx -0.75$. For the correlation length exponent ν we find values $\nu \approx 2$ compatible with the corresponding problem of DLs [33, 36, 39]; such that our present results deviate from $\beta' = \nu\Sigma$. Nevertheless, the connection between DLs and SDLs provides the first system to test the proposed order parameter in a localisation transition numerically and to determine the otherwise inaccessible exponents β' or Σ.

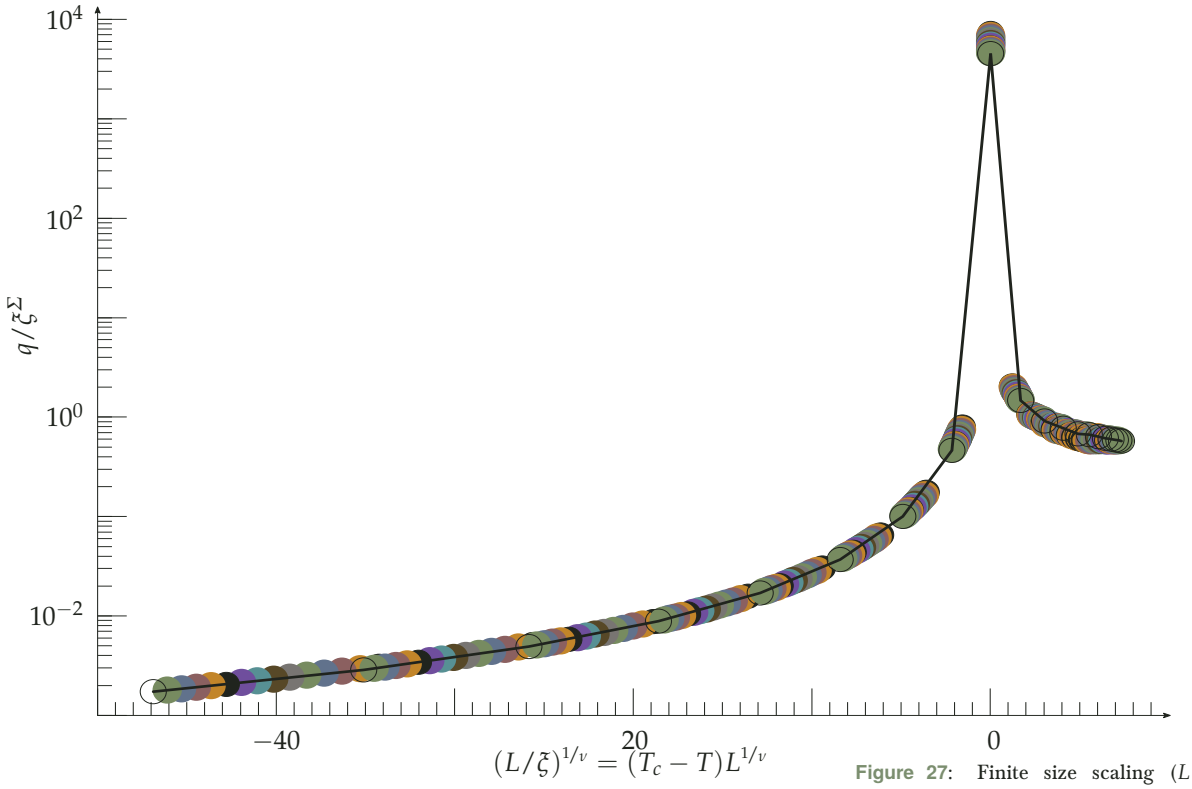

Figure 27: Finite size scaling ($L = 15,\ldots,30$) for the overlap order parameter. Our best results are $\Sigma \approx 0.75$ for the exponent related to the decay of the order parameter, and $\nu \approx 2$ for the correlation length exponent. As before, we used $T_c = 1.44$.

Geometry of the weight distribution in the disordered phase

One of the features expected in a disorder dominated phase are Derrida-Flyvbjerg singularities [40, 83]. These are features of the statistical weights[89]

$$w_L(z) = \sum_v w_L(z,v) = \overline{\langle\delta(z)\rangle}$$

function for the SDL to end at a specific point z. As the phase is disorder dominated, some characteristics of these weights should resemble random fragmentation[90] processes and origin from mere statistics and the distribution used for the random potential rather than details of the Hamiltonian involved. According to Derrida and Flyvbjerg the distributions $P_1(w_1)$ and $P_2(w_2)$ of the largest and the second largest weight, respectively, should exhibit singularities at $1/n$ ($n = 1,2,3,\ldots$) in a disorder dominated phase with a multivalley structure of phase space [83]. For SDLs in disorder, we calculated the distribution of the value of the largest and the second largest weight numerically as shown in Fig. 28 and indeed find singularities at 1 and

Derrida-Flyvbjerg singularities

There is a small motivation of these singularities in the appendix, see page 83.

[89] Here we use weights were we marginalised the dependency on the tangent directions in an effort to highlight the similarity to one-dimensional fragmentation processes and the previous study of the DL.

[90] The quantity to be fragmented here is the total probability $1 = \sum_z w(z)$.

$1/2$ for $T < T_c$. We are not able to clearly resolve higher singularities at $1/n$ with $n \geq 3$, which might be due to the underlying (Gaussian) distribution or the number of samples used. Analogous singularities can be found in the distribution of the information entropy $s = -\sum_z w \ln w$ at values $-\ln(1), -\ln(2), -\ln(3)$, whereas nothing similar can be observed at high temperatures, where the entropy distribution is Gaussian and the distribution of the (second) largest weight is sharply peaked around zero corresponding to a non-localised phase. We see this as a confirmation that the SDL indeed undergoes a transition to a disorder dominated phase at $T_c \approx 1.4$.

Multifractal structure of the weights

As before there is a near-to-minimal example for a very simple process in which multifractality arises in the appendix, see page 83.

For DLs in $1+3$ dimensions, some insight into the underlying structure of the transition has been achieved within the multifractal formalism [84–86]. As we conjecture the transitions for the DL and SDL to be essentially analogous, we expect to find similarities to the analysis that has been done before for DLs [39], but also deviations where the obvious geometrical differences become important. The idea is that different moments Y_q of the statistical weights

$$Y_q(L) = \sum_i \mathrm{Prob}(z(L) = z_i)^q$$

are dominated by different regions of the support and thus show a different scaling with the system size L. The probability is given by the ratio of restricted and unrestricted partition function $\mathrm{Prob}(z(L) = z_i) \equiv w_L(z_i) = Z_L(z_i)/Z_L$. The sum goes over all the possible ending points in the numerical simulation, whereas for the continuous analytical problem Y_q would be defined by an integral over z.

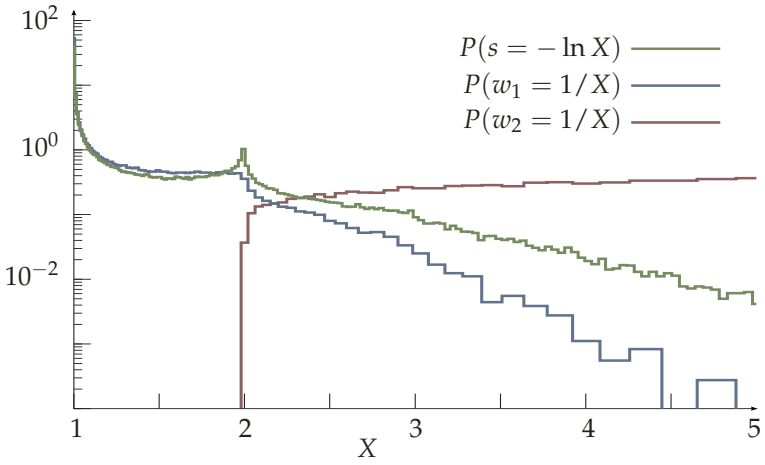

Figure 28: Distribution of the largest (w_1, blue line) and second largest (w_2, red line) statistical weight $w(z) = Z(z)/Z$ and the information entropy $s = -\sum_z w(z) \ln w(z)$ (green line) in the low-temperature phase, $T < T_c$. These singularities strengthen the picture of a disorder-dominated phase and show that the line localises with large weight at few sites. The distributions are plotted such that interesting features should occur on integer values of X (see key in the top right corner).

In the high temperature phase, the weights $w_L(z)$ obey the scaling form

$$w_L(z) = L^{-\chi} \Omega(z/L^{\zeta})$$

with the return exponent χ (defined by $w_L(0) \sim L^{-\chi}$ as introduced above). It is straightforward to see that the Y_q then scale according to

$$Y_q(L)\big|_{T>T_c} \sim L^{-(q-1)\chi} = L^{-(q-1)\zeta d}$$

in the high temperature phase. In the low temperature phase, the line is localised and therefore the Y_q remain finite as $L \to \infty$. At criticality the Y_q are diverging, but the quenched disorder is relevant, and it becomes important how the (necessary) average over realisations of the disorder is computed. This is closely related to the common question regarding systems with disorder is whether a certain quantity is self-averaging. If so its typical

and average values, the latter of which could be dominated by rare events, should be identical. For the Y_q a reasoning like this motivates the definition of two variants with respect to the disorder average. The straightforward *average* value which is

$$Y_q^{av} = \overline{Y_q}\big|_{T\approx T_c} \sim L^{-\tilde{\tau}(q)} = L^{-(q-1)\tilde{D}(q)} \tag{17a}$$

and the *typical* value[91] which is

$$Y_q^{typ} = \mathrm{e}^{\overline{\ln Y_q}}\Big|_{T\approx T_c} \sim L^{-\tau(q)} = L^{-(q-1)D(q)}. \tag{17b}$$

Here we also introduced the exponents τ and $D(q)$ (the version with a tilde corresponds to the average Y_q and the version without to the typical Y_q) describing the decay of the Y_q with the system length. The definition of $D(q)$ is such that it allows for an easy identification of "trivial", so-called monofractal behaviour where all moments have the same length dependence (as in the high temperature phase) and includes the obvious case of $q = 1$, where $Y_1 = 1$ and $\tau(1) = 0$ by definition. The $D(q)$ are referred to as generalised dimensions [84], and the function $D(q)$ discriminates between monofractal ($D(q) = const$ as for $T > T_c$) and multifractal behaviour ($D(q) \neq const$). The interpretation of the $D(q)$ as (fractal) dimensions of subsets is rather peculiar as we are dealing with a probability distribution or *measure*. Nonetheless it is useful as it requires $D(q)$ to be monotonically decreasing because none of the subsets can have a larger dimension than their union. There are at least two special values of $D(q)$ with an obvious meaning: $D(0)$ is the *Hausdorff dimension* of the support and, thus, directly related to the geometry of the system[92] and $D(1)$ is called the *information dimension* as it appears like a dimension in the Shannon information entropy

$$s = -\sum_z w_L(z) \ln w_L(z) = -\,\partial_q Y_q\big|_{q=1} \approx D(1) \ln L.$$

However, upon inspection of the definition of Y_q it is clear that $D(1)$ cannot be computed directly as $Y_1 \equiv 1$ by definition but only as an analytic continuation of $D(q)$. The same holds for $D(0)$ because $w_L(z)^0 \equiv 1$ and there is no length-dependence in Y_0. The measure $w_L(z)$ is called fractal iff $D(0) > D(1)$[87].

[91] We consider the following example to justify our nomenclature: Take a series of M values X with $X_1 = M$ and $X_i = 1$ for $i > 1$. This series has one outlying value and its average is $X_\infty^{av} = \lim_{M\to\infty} \overline{X} = 2$ in the limit of large M. Any reasonable definition of a typical value should give $X_\infty^{typ} = 1$ for large M and indeed we find $\overline{\log X} = 1/M \log M$ which yields $X_\infty^{typ} = \lim_{M\to\infty} \mathrm{e}^{\overline{\log X}} = 1$.

[92] The Hausdorff dimensions of the support for the measures related to DLs and SDLs with d transverse dimensions are $D_{DL}(0) = d$ and $D(0) = 2d$ (z and $v = \partial_x z$), respectively, which gives $D_{DL}(0) = 3$ for DLs in $1+3$ dimensions and $D(0) = 2$ for SDLs in $1+1$ dimensions.

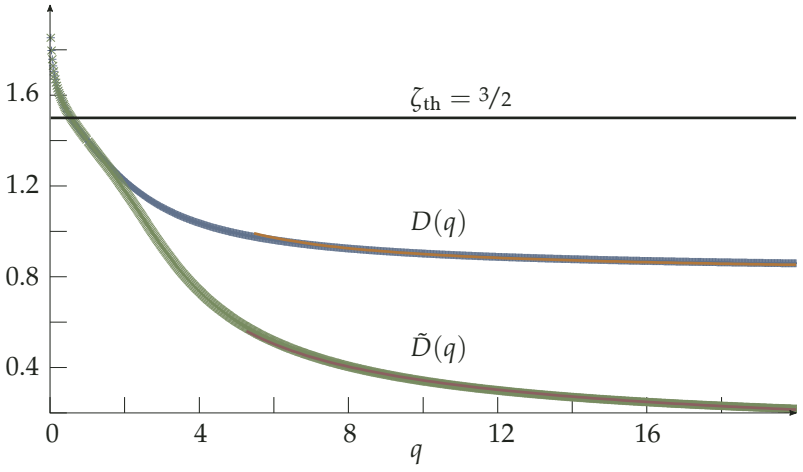

Figure 29: Generalised dimensions $D(q)$ (from the typical Y_q) and $\tilde{D}(q)$ (from the average Y_q) at criticality $T = T_c$. The dark line is $D_{T>T_c} = 3/2$. The data is marked by saltires that are superposed by solid lines which show monomial fits for large q, which we will use later on in the study of the associated singularity spectrum, see text. The two check-results $D(0) = \tilde{D}(0) = 2$ and $D(1) = \tilde{D}(1) = \zeta_{th}$ are reasonably well matched, although there are differences. The typical and average dimensions agree until $q = q^* \approx 1.5$. At large q large weights dominate and this therefore goes to show that the average is dominated by large, isolated ($\tilde{D} \to 0$) weights, as to be expected for a localised phase. The clear deviation between typical and average behaviour of Y_q is an indicator that this quantity is not self-averaging.

In Fig. 29, we present numerical results for $D(q)$ and $\tilde{D}(q)$ for an SDL in disorder at criticality. As a control for the numerics one can use the information dimension $D(1)$, which should coincide with its high temperature value

$D(1)|_{T>T_c} = \chi = \zeta d = 3/2$ at criticality. The data appears to resemble the Anderson transition-like scenario that has been reported for the DL [39] with matching dimensions[93] $D(q) = \tilde{D}(q)$ for $q < q^* \approx 1.5$. The separation of $D(q)$ and $\tilde{D}(q)$ indicates different behaviours of typical and average values of $Y_{q>q^*}$, from which one is tempted to conclude that these quantities are *not self-averaging*. Furthermore both Y_q^{av} and Y_q^{typ} are diverging faster than exponential for $q < 0$, which leads to $D(q < 0) = \tilde{D}(q < 0) = \infty$. The information dimension $D(1)$ is measured to be about $D(1) \approx 1.4$ and, therefore, does not coincide with the expected high temperature value $3/2$. However, this could be a numerical artifact from limited system sizes.

[93] For DLs the range of matching dimensions lasts[39] until $q^*_{DL} \approx 2$.

It is noteworthy that q^* is below two, meaning that the typical value of the *correlation dimension* $D(2)$ differs from its average value, both of which are below the DL value[39] in $1+3$ dimensions $D_{DL}(2) = \tilde{D}_{DL}(2) \approx 1.3$. As $Y_2 = \sum_z w_L(z)^2$ this quantifies the probability for the ends of a pair of lines to coincide. However, it is important that it does not provide insight into the question whether the localisation is related to a binding process of pairs of replicas. The reason for this is that Y_q is measured at the *end of the line*[94]. To detect an effective binding, we have to consider (as we did) an energy-like quantity, the pair overlap, that is accumulated along the length of the line.

[94] or to say it in song "It don't matter if you're by my side (at the end of the line)" (End of the line, Traveling Wilburys).

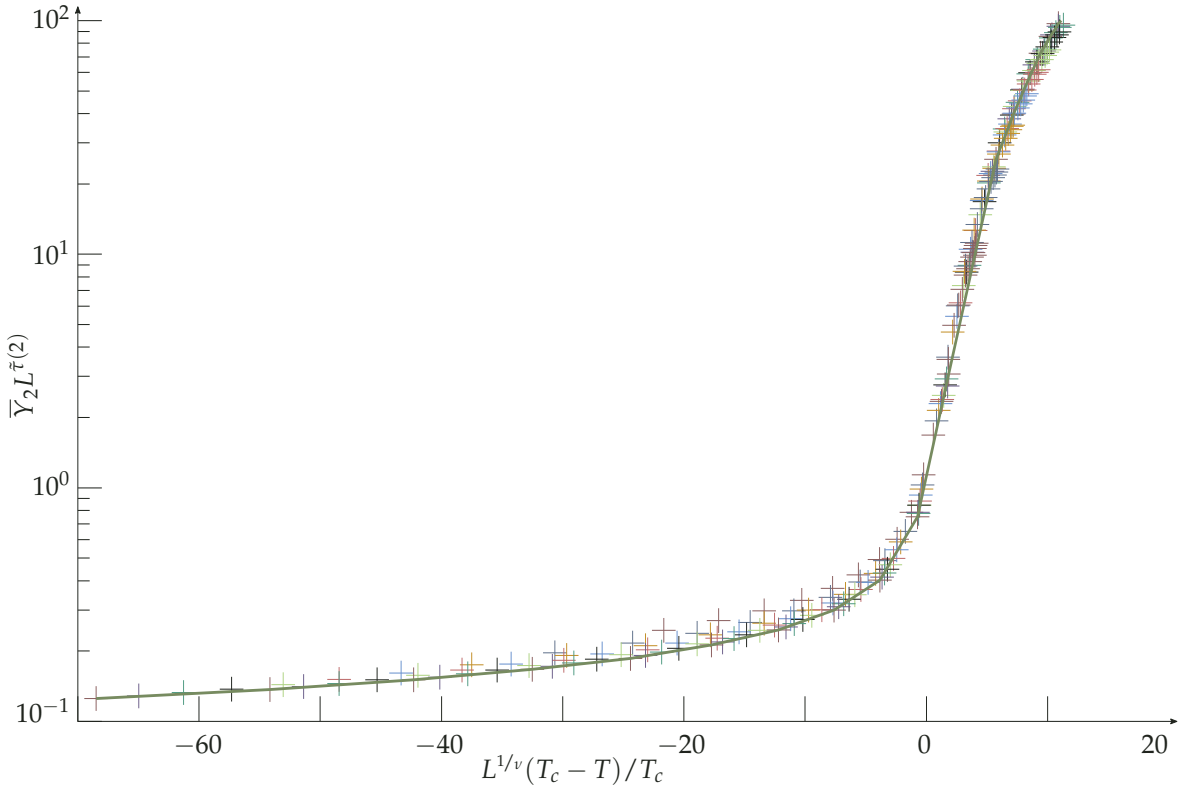

Figure 30: Finite size scaling $\overline{Y_2} L^{\tilde{\tau}(2)}((T_c - T)/T_c \cdot L^{1/\nu})$ giving $\nu = 2$ and $T_c = 1.41429$ for lengths $L = 20,30,\ldots,100$, the points for $L = 100$ are interconnected by a linear line as a visual guidance. The collapse does not work for the alternatively proposed value $\nu = 4$. For $T < T_c$, $\overline{Y_2}$ remains finite for large L and, therefore, the finite size scaling observable diverges as $L^{\tilde{\tau}(2)}$. The given value of T_c is the best fit[88] with the correlation length restricted to $\nu = 2$. The data available does not rule out $T_c \approx 1.44$.

For now, we realise that we have data available for some quantity, here Y_q, for a wide range of lengths L and temperatures T in a system with a phase transition. Thus, we might learn something about this phase transition from studying the finite-size scaling. Luckily enough, we know[36, 89, 90] that for Anderson transitions, the finite-size scaling of the Y_q at criticality does involve the multifractal spectrum but only the one standard correlation

length exponent ν,

$$\overline{Y_q} = L^{-\tilde{\tau}(q)} f((T_c - T)L^{1/\nu}).$$

Thus, it allows for a completely independent validation (cf. Fig. 30) of the critical temperature and the correlation length exponent, yielding a more exact value $T_c \approx 1.44$ compatible with our results from before (see the discussion of free energy and roughness starting on page 40) and unambiguously a value $1/\nu \approx 0.5$ for the correlation length exponent. The value for T_c will also turn out to be compatible with the critical temperature of a related effective binding problem, which we will explored before (page 44).

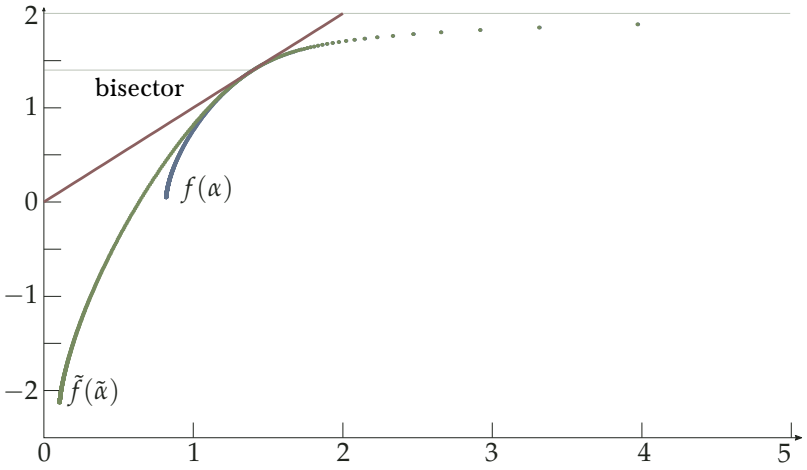

Figure 31: The singularity spectra $f(\alpha)$ and $\tilde{f}(\tilde{a})$, see eq. (19). For a better comparison with the expectations the plot also shows the lines corresponding to $f(\alpha) = D(2) = 2$, $f(\alpha) = D(1) \approx 1.4$ (both light green) and $f(\alpha) = \alpha$ (red), see text. The bisector and $f(\alpha)$ touch at an α that is slightly smaller than $\alpha = 1.5$. We consider this to be wrong, but at least it is consistent with the determined generalised dimensions, see also Figs. 29 and 32.

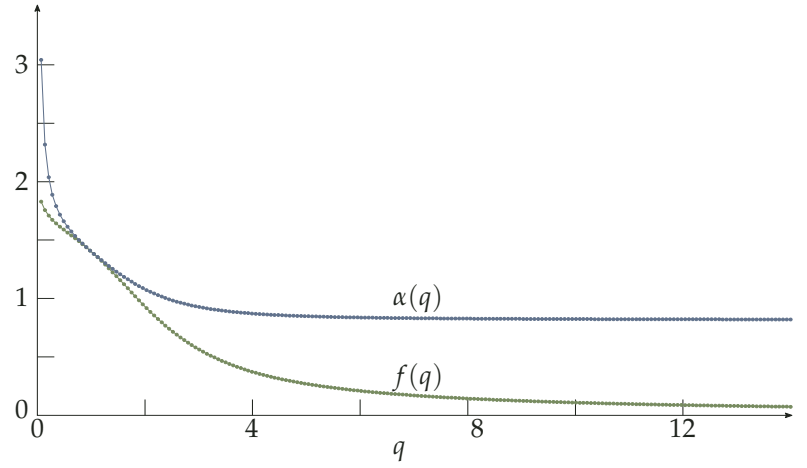

Figure 32: The directly measurable $\alpha(q)$ (blue) and $f(q)$ (green) from which Fig. 31 was created. The contact point is at $\alpha = f(\alpha) \approx 1.4 \approx D(1)$

An equivalent description of the multifractal nature is related to the Legendre transform $f(\alpha)$ of $\tau(q)$ given by

$$q = f'(\alpha) \tag{18a}$$

$$\tau(q) = \alpha q - f(\alpha). \tag{18b}$$

The function $f(\alpha)$ is called the *singularity spectrum*, because it gives the number $N(\alpha) \sim L^{f(\alpha)}$ of points z, where the weight $w(z)$ has a singularity $w \sim L^{-\alpha}$. A Legendre transform of the measured $\tau(q)$ and $\tilde{\tau}(q)$ would require an analytical continuation and, thus, be very error-prone. Fortunately, it is possible to directly measure $\alpha(q)$ and $f(q)$ [91] and, thus, the singularity

spectrum $f(\alpha)$ parametrically:

$$f(q) = -\lim_{L\to\infty} \overline{\sum_i \mu(q,z_i)\ln\mu(q,z_i)}/\ln L \tag{19a}$$

$$\alpha(q) = -\lim_{L\to\infty} \overline{\sum_i \mu(q,z_i)\ln w(z_i)}/\ln L \tag{19b}$$

with

$$\mu(q,z_i) \equiv w^q(z_i)/(\sum_j w^q(z_j)).$$

This method of computing $f(\alpha)$ gives the Legendre transform of $\tau(q)$, because eq. (18) implies (omitting the limits)

$$\tau(q) = \alpha(q)q - f(q) = -\overline{\ln\sum_i w^q(z_i)}/\ln L = -\overline{\ln Y_q(L)}/\ln L \tag{19c}$$

in agreement with eq. (17b), and, therefore, $f(\alpha)$ corresponds to typical values of Y_q. Note that $\alpha(q) = \tau'(q)$ is fulfilled by construction. This is the common definition of the (multifractal) singularity spectrum that is also applicable for non-disordered systems.

Here, disorder is relevant and we need to capture not only the typical, but also the (differing, cf. Fig. 29) average behaviour. Analogously to eq. (19) we derive the following computation of the Legendre transform[95] $\tilde{f}(\tilde{\alpha})$ of $\tilde{\tau}(q)$. We use eq. (17) and the inverse transform of (18)

[95] We distinguish between α and $\tilde{\alpha}$ to avoid ambiguities as both are directly measured.

$$\tilde{\tau}(q) = -\ln\overline{\sum_i w^q(z_i)}/\ln L \tag{20a}$$

$$\tilde{\alpha}(q) = \tilde{\tau}'(q) = -\overline{\sum_i w^q(z_i)\ln w(z_i)}/(\ln L\cdot\overline{\sum_i w^q(z_i)}) \tag{20b}$$

$$\tilde{f}(\tilde{\alpha}) = \tilde{\alpha}q - \tilde{\tau}(q) = -\overline{\sum_i w^q(z_i)(\ln w^q(z_i)/\overline{\sum_j w^q(z_j)} - 1)}/\ln L. \tag{20c}$$

The spectrum $f(\alpha)$ is shown in Fig. 31. Its shape matches the expectations that originate from general properties and the known results for the DL [39] and is consistent with the results for the Legendre transform $\tau(q)$. Our results show that $f(\alpha)$ is a monotonic function starting at a finite $\alpha_{\min} = D_{\min}(q) \approx 0.8$ which is close to the DL value $\alpha_\tau^{min} \approx 0.77$ and ending at $\alpha_{max} = \infty$, which corresponds to the infinitely large values $\tau(q)$ for $q < 0$. The maximum value of $f(\alpha)$ is $f(\alpha\to\infty) \to D(0)$ and it touches the bisector $f = \alpha$ around $\alpha = D(1) \approx 1.4$, thus confirming the previously found deviation $D(1) \neq 3/2$. We see no indication that $f(\alpha)$ becomes negative somewhere, which would describe rare events (number decreases exponentially in L), but this is to be expected as $f(\alpha)$ contains the *typical* behaviour and should not become negative[39]. The *average* behaviour that leads to $\tilde{f}(\tilde{\alpha})$ does include rare events and does not seem to have a finite α_{min}, implying $\tilde{D}(\infty) = 0$. We back this by noting that we can achieve a good fit of the data for $\tau(q)$ and $\tilde{\tau}(q)$ at large q (we used $5 < q < 20$) with a monomial Ansatz $f(q) = aq^b$. For an approximate analysis we round b to one decimal giving

$$\tau(q \gg 1) \approx aq \quad \text{and} \quad \tilde{\tau}(q \gg 1) \approx \tilde{a}q^{2/5}$$

with some constants a,$\tilde{a}$. We apply the Legendre transform and get for $q \gg 1$

$$\alpha(q) \approx a \approx 0.81 \qquad f(\alpha) \approx 0$$
$$\tilde{\alpha}(q) \sim q^{-3/5} \to 0 \qquad \tilde{f}(\tilde{\alpha}) \sim -\tilde{\alpha}^{-2/3} \to -\infty$$

In summary, we see a (Anderson transition-like) scenario in the multifractal analysis of the localisation transition of an SDL in 1+1 dimensions which is very similar to the findings in Ref. 39 for a DL in 1+3 dimensions despite obvious differences due to the different geometry. In particular, the multifractal structure of the statistical weights differs between typical and average values both for DLs and SDLs. This becomes apparent in the generalised dimensions $D(q), \tilde{D}(q)$, which differ for $q \gtrapprox 1.5$. We also find a matching critical correlation length exponent ν. Additionally, we showed that the average behaviour is significantly influenced by rare events, leading to negative values in $\tilde{f}$, the Legendre transform of $\tilde{D}(q)$. The significance of rare (extreme) events at criticality is in accordance with our findings for the energy distribution.

Free energy distributions of SDL in 1+1 and DL in 1+3 dimensions

We can go one step further than for the determination of the fluctuation exponent, cp. Fig. 20, and consider not only the second moment but the whole distribution of the free energy as shown in Fig. 33, which is obtained by computing the free energy for every sample and rescaling to zero mean and unit variance,

$$G_F(X) = \mathrm{Prob}((F - \overline{F})/\Delta F = X).$$

This rescaling should make G_F more robust against the influence of numerical details. For DLs in $d = 1$ it has been found that this distribution is of a universal form [92]. The asymptotic behaviour of the negative tail of the rescaled free energy distribution for low temperatures is of the form

$$\ln G_F(X) \sim -|X|^\eta \quad (X < 0, |X| \gtrapprox 1).$$

This allows us to determine the energy fluctuation exponent ω via the Zhang argument [24, 36, 38]: Let us consider the following rescaled moments of the partition function

$$Z_n \equiv \overline{Z^n} = \int \mathrm{d}F\, P(F)\, \mathrm{e}^{-\beta n(F-\overline{F})} \propto \int \mathrm{d}X\, G_F(X)\, \mathrm{e}^{-\beta n(X+\overline{F})\Delta F}$$

where we substituted $X = (F - \overline{F})/\Delta F$ and used that the partition function is the Laplace transform of the free energy. The last line is clearly dominated by the negative tail of $G_F(X)$ and we can write

$$Z_n \propto \int \mathrm{d}f\ \mathrm{e}^{-|X|^\eta - \beta n\, \mathrm{e}^{-\beta n(X+\overline{F})\Delta F}}.$$

Using $\Delta F \propto L^\omega$ we see that the argument of the exponential is extremal for $X_{\mathrm{opt}} = c_1(n,\beta) L^{\omega/\eta - 1}$ and a saddle point integration[96] gives

$$Z_n \sim \mathrm{e}^{c_2(n,\beta) L^{\omega\eta/\eta - 1}};$$

on the other hand, $\ln \overline{Z^n} \sim L$ should be extensive resulting in $\omega\eta/\eta - 1 = 1$ or

$$\eta = (1 - \omega)^{-1}. \tag{21}$$

We find $\eta \approx 1.23$ (dashed black line in Fig. 33) or $\omega \approx 0.18$. This is in agreement with the values reported for DLs in $1 + 3$ dimensions.

For a direct comparison of the rescaled free energy distributions of an SDL in 1+1 and a DL in 1+3 dimensions we simulated both systems (the DL up to lengths $L = 60$) and find that the rescaled free energy distributions in

[96] Along the same lines we find that $\ln \overline{Z^n} \sim -n\overline{F} + \mathrm{const} \cdot n^{1/\omega}$. Thus we have found an expression for leading orders in n of the ground state energy (cp. footnote 41 on page 32) of the replica problem. The next-to-leading order that goes as $\mathcal{O}(n^{\approx 5.3})$ does not raise confidence that the full solution is of a simply accessible form. This is in contrast to Lässig's[93] quantisation argument (assuming an operator product expansion for the height correlations of the KPZ equation) which predicts $\mathcal{O}(n^6)$ or $\omega = 1/6$.

the low temperature phases have to be considered *identical* within numerical accuracy. This could hint towards a new seemingly "universal" distribution for certain random systems, much like the Tracy-Widom distribution that is found for the DL in 1+1 dimensions and various other systems [92]. For finite system sizes this universal behaviour can only be expected for free energy fluctuations $|X|$ small compared to an upper threshold [94, 95]; we believe, however, that our simulation does not cover the very rare fluctuations that induce the non-universal part for very large $|X|$. In Fig. 34 we show the distributions for $T < T_c$ (DL and SDL) in a manner where the exponent η becomes more apparent. Here we introduce the exponent η', which is the analog to η for the positive tail

$$\ln G_F(X) \sim -|X|^{\eta'} \quad (X > 0, |X| \gtrapprox 1),$$

where the Zhang argument is not applicable. We find a value $\eta' \approx 1.84$.

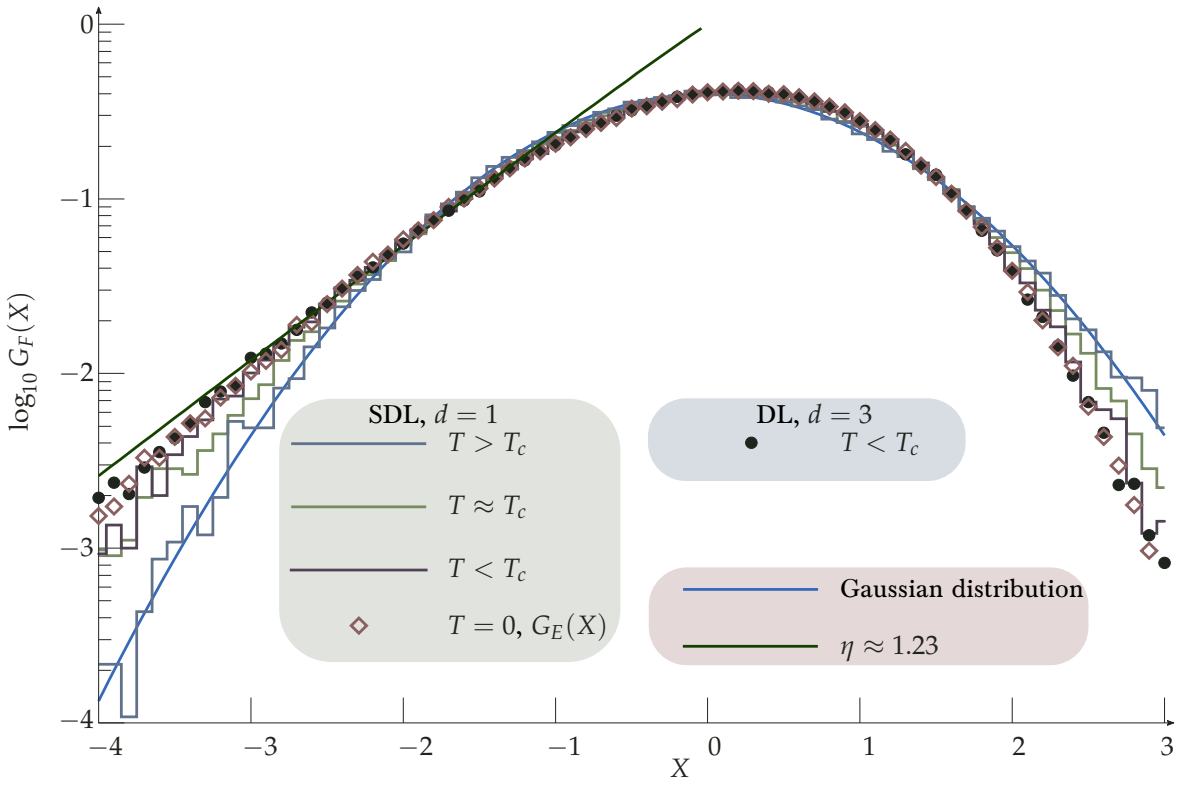

Figure 33: Rescaled free energy distribution $G_F(X) = P((F - \overline{F})/\Delta F)$ for a stiff directed line (SDL) in $1 + 1$ dimensions. We show distributions for $T = 0$ (hollow red diamonds, ground state energy) as well as for three finite temperatures $T < T_c$ (violet line), $T \approx T_c$ (green line) and $T > T_c$ (blue line). Results for a directed line (DL) in $1 + 3$ dimensions are shown (dark, full circles).

Based on an exact renormalisation on the diamond lattice [42] and an optimal fluctuation approach [95], it has been previously suggested for DLs that η' and ω are related via (cf. eq. (21))

$$\eta' = d_{\text{eff}}/(1 - \omega)$$

with $d_{\text{eff}} = 1 + d$ for the hypercubic lattice. This is found to be valid for the DL in $1 + 1$ dimensions, where[42] $\omega = 1/3$ and $\eta' = 3$. For the problem at hand, the literature value $\omega = 0.186$ for DLs in $d = 3$ would lead to $\eta' \approx 5$, which is far from the value $\eta' \approx 1.84$ we find; thus, the ratio η'/η does not match the prediction $\eta'/\eta = (1 + d)$. In Ref. 95 $\eta = 2$ and $\eta' = 3$ were found to be *superuniversal* (independent of d) for the DL in dimensions $d > 2 = d_c$ at temperatures $T > T_c$. We can neither confirm nor deny this result, as we are not able to cover the "most distant" part of the distribu-

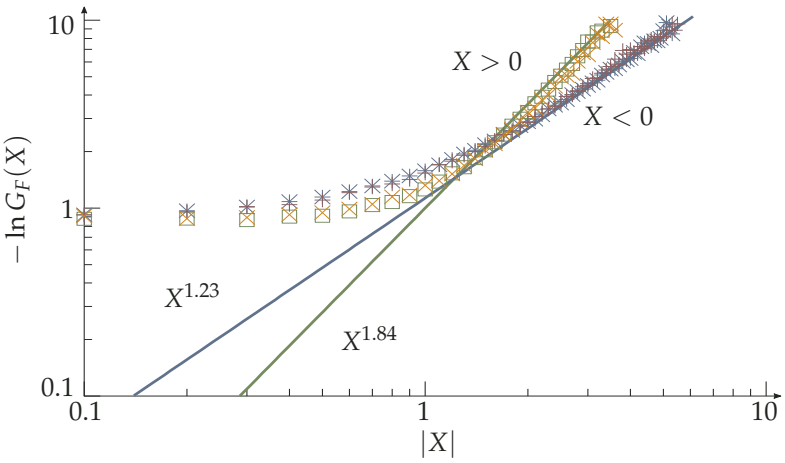

Figure 34: Double logarithmic plot of the negative logarithm of the rescaled free energy distribution $G_F(X)$ ($X = (F - \overline{F})/\Delta F$) at low temperatures $T < T_c$ for the DL (blue stars for $X < 0$ and hollow squares for $X > 0$) and the SDL (violet Greek crosses for $X < 0$ and orange saltires for $X > 0$). We see identical behaviour for SDL and DL consistent with exponents $\eta \approx 1.23$ and $\eta' \approx 1.84$, see text.

tion, but our interpretation that G_F is Gaussian for $T > T_c$ would lead to $\eta = \eta' = 2$.

The finite size corrections to the free energy[24, 96] should also scale as L^ω leading to $F/L \approx a + bL^{\omega-1}$. We did not succeed in determining a precise, consistent ω in this way, possibly because our systems are too small.

The free energy distributions in Fig. 33 seem to be identical for $T < T_c$ and $T \approx T_c$ (as it is also the case for the DL [36]), which suggests $\omega_{T=T_c} = \omega_{T<T_c} \approx 0.186$ contradicting the $\omega_{T=T_c} = 0$ argument [79], but one has to bear in mind that the saddle point integration in the course of the Zhang argument is only applicable if $\eta > 1$ or $\omega > 0$.

A more distinct difference between the behaviour at criticality and at low temperatures can be found in the distribution of the potential energy as shown in Fig. 35 (also the potential energy is rescaled using $X = (E - \overline{E})/\Delta E$ analogously to Fig. 33 for the free energy distribution). For the potential energy distribution, the behaviour at the critical temperature is clearly different from the behaviour both at $T > T_c$ and $T < T_c$ (which are not identical for the DL) and exhibits a decay $\ln G_E(X) \sim \mathrm{e}^{-|X|} (X < 0, |X| \gg 1)$ resembling extreme value distributions of the Gumbel type.

A tentative explanation might be that the transition occurs because of extreme values of the potential at which the otherwise thermally fluctuating line localises. The random potential has a Gaussian distribution, thus its extreme values are distributed according to a Gumbel distribution or Fisher-Tipett type I extreme value distribution[97] [97]

$$P^{\alpha,\beta}_{\text{Gumbel}}(X) = \beta^{-1} e^{-z(X)-e^{-z(X)}}.$$

The distribution of the potential energy at the critical temperature might be of a similar shape. As we are studying the rescaled distribution of the potential energy, which has zero mean and unit variance, we can use a one-parameter version of the Gumbel distribution

$$g_m(X) = \psi_1(m) m^m \Gamma(m)^{-1} \left(\mathrm{e}^{h_m(X) - \mathrm{e}^{h_m(X)}}\right)^m \tag{22a}$$

with the *shape parameter* m and the abbreviation[98]

$$h_m(X) \equiv (X + \psi(m))\psi_1(m) - \ln m. \tag{22b}$$

This distribution inherently features the correct decay at the tails, with $\ln g_m(X)$ decreasing faster than algebraic for $X < 0$ and linearly with slope $m\psi_1(m)$ for $X > 0$. However, our best approximation to the data with $m = 1.7$ deviates for $X > 0$.

[97] In our notation the Gumbel distribution depends on $z(X) = (X - \alpha)/\beta$, the location parameter α, and the scale parameter β (the parameters depend on the number of "trials").

[98] Here, we once again use the trigamma function[73] $\psi_1(x) = \mathrm{d}^2 \ln \Gamma(x)/\mathrm{d}x^2$.

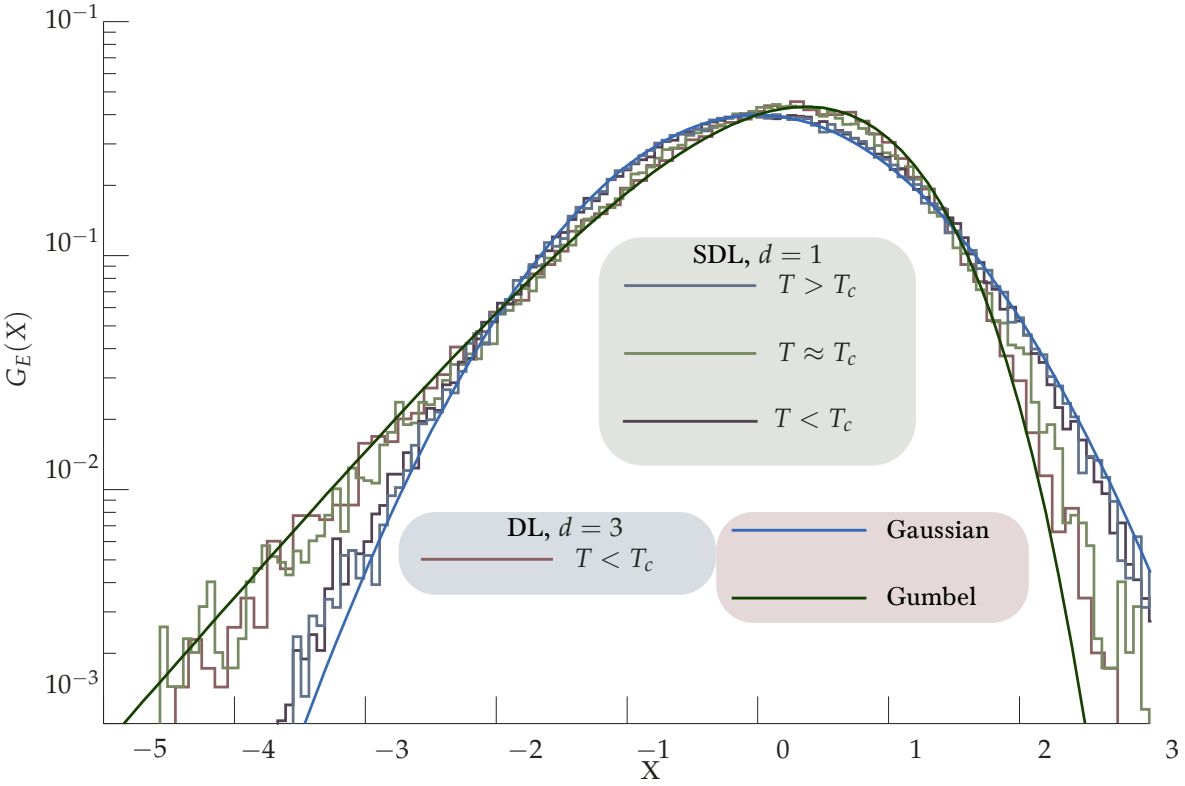

Figure 35: Rescaled potential energy distribution for an SDL in 1+1 dimensions. Plotted are distributions for three finite temperatures $T < T_c$ (dark line), $T \approx T_c$ (green) and $T > T_c$ (blue). Results for a DL in $1+3$ dimensions are shown in violet. Here, the dark green curve is an approximation using a one-parameter Gumbel distribution (cf. eq. (22a) with $m = 1.7$), whereas the blue curve is the normal distribution.

It is remarkable that the potential energy distribution is well described by an extreme value distribution only right at the transition at $T = T_c$, whereas it approaches a Gaussian not only for $T > T_c$ but also for $T < T_c$, see Fig. 35. The Gaussian distribution at low temperatures might stem from the Gaussian distribution used in the realisation of the disorder potential.

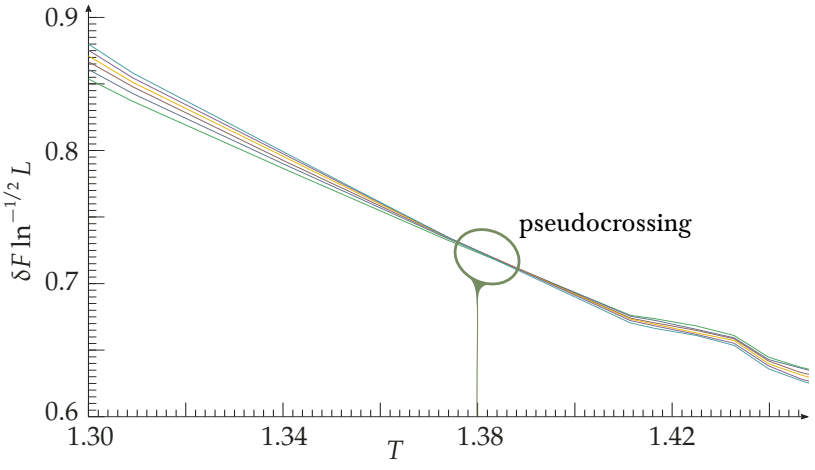

Figure 36: The reduced free energy $\delta F = \overline{F} - \overline{F}_{\text{ann}}$ rescaled by $\ln^{1/2} L$ for lengths $L = 50{,}60{,}\ldots{,}100$ as a function of the temperature T. There is a pseudo-crossing of the lines around $T \approx 1.38$.

At the critical temperature, where $\omega \approx 0$, the fluctuations of the free energy have been found to scale logarithmically with L, $\Delta F \sim \ln^{1/2} L$ [36]. We support this statement by studying the difference of quenched and annealed free energies $\delta F = \overline{F} - \overline{F}_{\text{ann}}$, which should as well scale as $\delta F \sim \ln^{1/2} L$ at the transition. As the annealed free energy directly depends on numerical details such as system size and neglected elements of the transfer matrix, we determine it by simulating a system without disorder and adding the contribution of the annealed potential, $\overline{F}_{\text{ann}} = F_{g=0} - Lg^2\beta/2$. This also

allows for an approximate determination of the critical temperature by finite size scaling, see Fig. 36. To verify this argument we tried also different scaling behaviours of the form $\delta F \sim \ln^c L$ and obtained a consistent pseudo-crossing only for $c \approx 1/2$. Furthermore the annealed free energy can be used to compute the temperature $T_{0,\varkappa}$, below which the annealed entropy is negative. This provides a lower bound on the actual critical temperature, whereas the replica pair binding temperature $T_{2,\varkappa}$ represents an upper bound [36]. We find $T_{0,\varkappa} \approx 0.4$, which is consistent with $T_c \approx 1.4$.

Conclusion

We studied stiff directed lines (SDLs) in $1{+}d$ dimensions subject to quenched short-range random potential analytically and numerically. Using Flory-type scaling arguments and a replica calculation we show that, in dimensions $d > 2/3$, a localisation transition exists from a high temperature phase, where the system is essentially annealed, to a disorder dominated low temperature phase. The low temperature phase is characterised by large free energy fluctuations with an exponent $\omega > 0$ and a roughness exponent ζ, which slightly exceeds the thermal value $\zeta_{th} = 3/2$ for an SDL. Flory arguments suggest $\zeta = 7/4{+}d$ for an SDL. Both exponents are related by $\omega = 2\zeta - 3$.

For the SDL in $1+1$ dimensions we performed extensive numerical transfer matrix calculations and find the existence of a localisation transition and an exponent $\omega \approx 0.18$ in the low temperature disorder dominated phase. The value for ω is close to the established value $\omega \approx 0.186$ for directed lines (DLs) under tension in $1+3$ dimensions. Moreover, the rescaled free energy distributions are *identical*. Both points suggest that the nature of the low-temperature phase is very similar, if not identical. The multifractal analysis reveals a very similar structure of the statistical weights at the critical temperature for DLs in $1+3$ dimensions and SDLs in 1+1 dimensions. It also allows for a determination of the correlation length exponent ν, for which we find, again in accordance with the findings for a DL in 1+3 dimensions, $\nu = 2$. Additionally, we find evidence for the relevance of rare events at criticality.

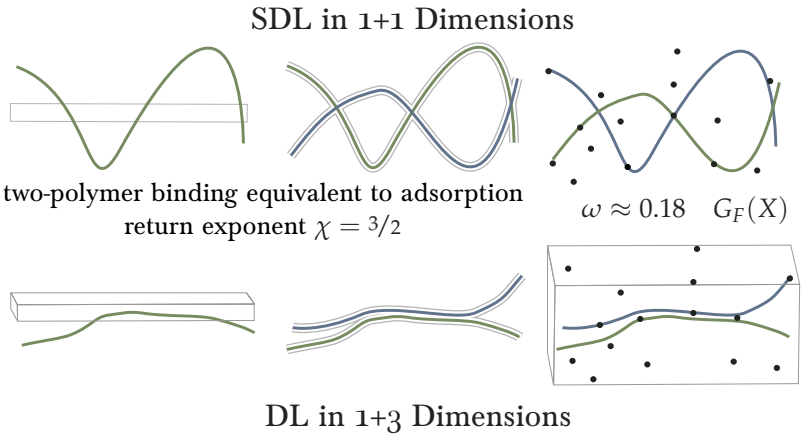

This strongly supports a relation between DLs in $1+3d$ and SDLs in 1+d dimensions based on identical return exponents χ for two replicas to meet. The validity of a relation based on properties of a single replica pair suggests that the critical properties of DLs in a short-range random potential are governed by replica pair interactions. The mapping can make DL transitions in high dimensions computationally accessible, which we demonstrated in

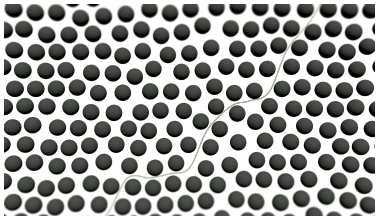

Figure 37: Sketch of a possible application of our study of SDLS in disorder to WLCs as considered in Ref. 81. A frozen configuration of hard disks is generated (using the event-chain algorithm, see final part of this work) in which a WLC (green) explores the free space (the disks are impenetrable), leading to an effective persistence length. Here, there is no direct way to quantify the strength of the disorder, but one can argue that the presence of the disorder forces the polymer to bend, which corresponds to a typical bending energy that is given by the size of the disks and the mean free path between them (cf. the final remark in Ref. 81). This way we bring this system into a form that is closer to ours, replacing confinement induced deflections with "disorder interactions". Thus, our predictions on the scaling level should (and do) hold. Adapting more complex quantities such as the roughness (or the decay of tangent correlations) is difficult. A transition has not been observed in this system, which is a consequence of the fact that the impenetrability of the hard disks is always relevant for sufficiently long. It is ongoing work to explore the annealed case of this model (thermally fluctuating disk positions)[98]. Another interesting adaptation would be to consider a finite potential for the disks.

Figure 38: Schematic summary of our findings for the relation between DLs and SDLs. Our results for the energy fluctuation exponent ω (introduced below in eq. (5)) and for the free energy distribution $G_F(x)$ are presented in sections I and I. The shaded area marks the range of the short-ranged (binding) potential. The effective binding interaction becomes apparent in the replica formalism (section starting on page 31); the importance of two-replica interactions for SDLs is one essential result of this work, see sections starting on pages 44 and 45.

showing that the two-replica overlap provides a valid order parameter across the localisation transition of SDLs in $1+1$ dimensions. Furthermore, the importance of pair interactions suggests that the critical temperature for DLs in random potentials is indeed identical to the temperature below which the ratio of the second moment of the partition function and the square of its first moment diverges, which implies that the localisation transition temperature T_c in a random potential equals the replica pair transition temperature T_2 for replica pair binding, which has been originally put forward and verified numerically for DLs in 1+3 dimensions [36, 39]. Using the numerical transfer matrix approach we could verify this conjecture also for SDLs in $1+1$ dimensions. Our findings are summarised schematically in Figs. 38 and 39.

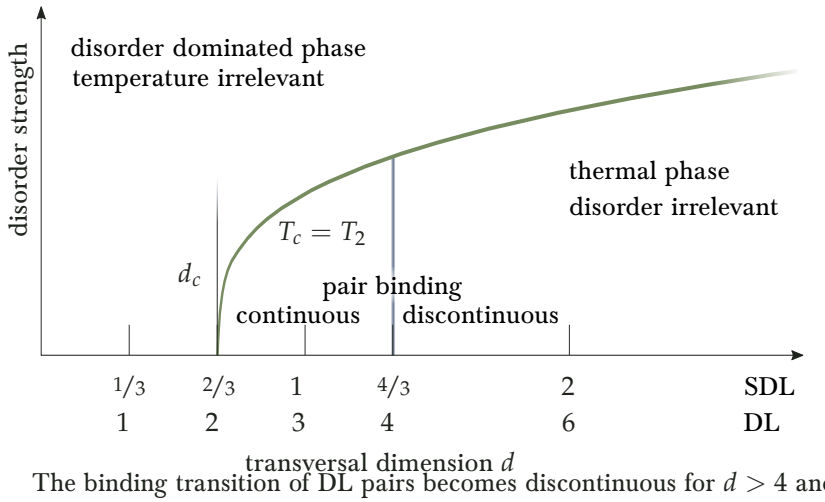

Figure 39: Schematic summary of our results supporting a relation between DLs in 1+3d and SDLs in 1+d dimensions and the importance of replica pair interactions for the localisation transition in a random potential.

The binding transition of DL pairs becomes discontinuous for $d > 4$ and, analogously, the binding of SDL pairs[19, 82] for $d > 4/3$. Because DLs in random potentials are equivalent to the KPZ equation [25], the validated relation to the SDL suggests that the roughening transition of the KPZ problem could acquire similar discontinuous features for $d > 4$ dimensions. Thus, $d = 4$ would remain a special dimension, although it is not the upper critical dimension [99]. We have performed simulations of the SDL in $d = 2 > 4/3$, but this leads to necessarily smaller system sizes[99] on which we were not able to observe clear thermodynamic scaling, thus we are in no position to shed light on this question from the SDL at this point.

Finally, we conclude with a remark on the application of our findings to the equilibrium behaviour of *polymers in disordered potentials* beyond the weakly bent limit that allows one to reduce a WLC to an SDL as discussed in the introduction. At small persistence lengths the polymer will be pinned at a single (or very few) disorder sites leading to compact, higher-dimensional polymer conformations (such as globules (three dimensional considering the way the size of the polymer scales with its length) or toroids (two-dimensional)) that have been explored in[100] Ref. 13. Our results are applicable, if the effective persistence length is of the same order as the contour length, which for example can be achieved[101] if the disorder is realised through spatial confinement[81], see Fig. 37, which can be motivated as a crowded environment. For this "entropic" disorder it is not straightforward to infer a strength of the disorder in our terms (see Fig. 37), but should be possible and then allow for a comparison at least on the scaling level. However, as partly discussed in sidenotes 14 (page 21) and 86 (page 44) the effective persistence length as key geometric quantity cannot be directly inferred from the decay of tangent correlations due to the invariant thermal contributions to the orientational fluctuations for $\omega > 0$.

[99] Any physical dimension adds two dimensions in the computations due to the tangent orientational degree of freedom.

[100] The "delocalized" classification in that work refers to states that stretch over a macroscopic portion of the medium, which includes the thermal and the localized phase in our nomenclature

[101] The mean free path between two crowder particles that are placed with density ρ is roughly $\lambda \sim \rho^{-1/2}$ which also sets the relevant scale for the disorder-induced persistence length. At small densities ($\lambda \gg L_c, L_p$) the polymer will coil up in one void and is hardly affected by the disorder (the disorder-induced persistence length cannot exceed the thermal one). At very large densities ($\lambda \ll L$) the polymer is effectively flexible again with a Kuhn length set by the disorder.

Dynamics – Depinning of a stiff directed line from a random potential

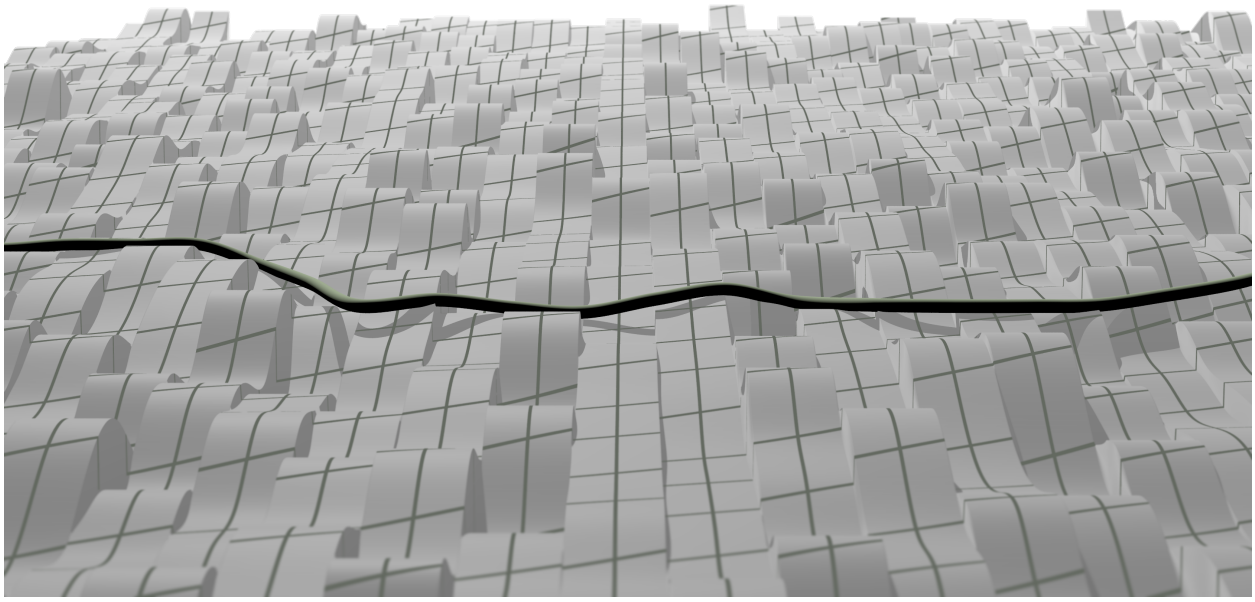

Figure 40: Artistic rendition of the depinning under force of a stiff directed line in a disordered potential. The force acts downwards in this depiction and is incorporated by a shift of the energy landscape. In our formulation the problem is discrete in the internal direction x and continuous in the transversal direction z, where we use a spline interpolation of the potential (as depicted, the knots of the splines used coincide with the knots of the shown grid). Here, the line is partially blocked (leftmost part of the line), these barriers will eventually be overcome due to elastic forces as the rest of the line moves in the direction of the force.

Introduction

Just as elastic manifolds in random, disordered media are one of the most important model systems in the statistical physics of disordered systems, which exhibit disorder-dominated pinned phases with many features common to glassy systems [24, 29], the depinning of an elastic manifold from a disorder potential under the action of a driving force is a paradigm for the non-equilibrium dynamical behaviour of disordered systems capturing the avalanche dynamics of many complex systems if they are driven through a complex energy landscape[100].

In particular, the problem of a directed line (DL) or directed polymer (i.e., an elastic manifold in $1+1$ dimensions) in a random potential and driven by a force has been subject of extensive study [70, 101–110]. At zero temperature, there is a threshold force, at which the manifold changes from a localised state with vanishing mean velocity to a moving state with a non-zero mean velocity.

The depinning transition has been treated within the framework of classical

critical phenomena by functional renormalisation group techniques starting from the more general problem of depinning of D-dimensional elastic interfaces (with $D = 1$ corresponding to lines). In $D = 4 - \varepsilon$ dimensions, "critical" exponents at depinning can be calculated by functional renormalisation using dimensional regularisation in an ε-expansion [111–113].

At finite temperature, there is experimental evidence for a creep motion at any non-vanishing driving forces which can be understood qualitatively as thermally activated crossing of energy barriers which result from an interplay of both elastic energies of the line and the disorder potential.

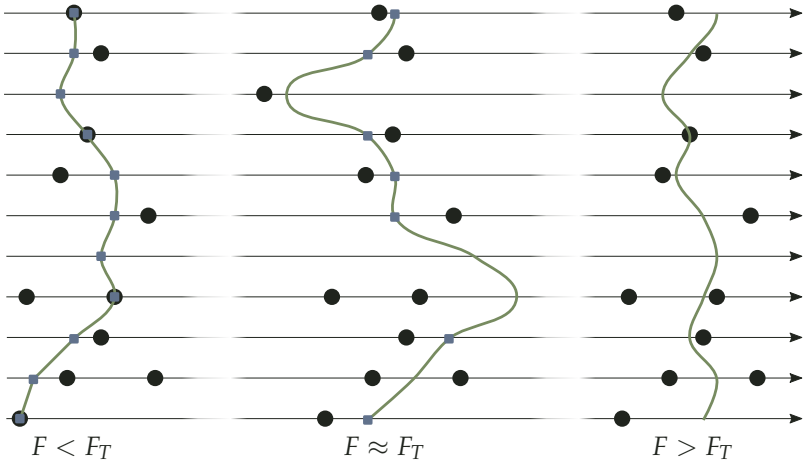

Figure 41: Schematic figure of typical SDL configurations below, at, and above the depinning transition (from left to right) in random-potential (RB) disorder. The black circles represent especially favourable locations within the random potential. Segments of the line that are currently not moving are marked with Gray squares.

Here, we again concentrate on stiff directed lines (SDLs), whose elastic energy is given by the curvature of the line and, thus, represents a bending energy. This gives rise to configurations which are locally curvature-free and straight but, in contrast to the DL, the straight segments of SDLs can assume any orientation even if this increases the total length of the line.

There are a number of applications and interesting general theoretical issues concerning SDLs in random media. The overdamped equation of motion of a SDL is the (fourth-order) Herring-Mullins linear diffusion equation [114, 115], which also describes surface growth governed by surface diffusion. The depinning dynamics of the Herring-Mullins equation in quenched disorder has been subject of a number of prior studies [116–119], whose findings (e.g., an unphysically small roughness exponent) differ in part significantly from ours as we will point out below. SDLs also describe semiflexible polymers with contour lengths smaller than their persistence length for bending fluctuations, such that the assumption of a directed line is not violated [120]. Our results can be applied to the depinning dynamics of semiflexible polymers such as DNA or cytoskeletal filaments like F-actin in a random environment, such as a porous medium, as long as the correlation length of the depinning transition is smaller than the persistence length. As in other semiflexible polymer phase transitions (such as adsorption) non-universal quantities such as the value of the depinning threshold itself will be governed by the bending elasticity. At the depinning transition, where the correlation length diverges, semiflexible polymers will exhibit a crossover to critical properties of effectively flexible lines (DLs) with a segment length set by the persistence length.

Moreover, we have seen that static SDLs in a random potential feature a disorder-driven localisation transition at finite temperatures already in $1 + 1$ dimensions[1, 2, 121]. Due to an interesting dimensional shift in the problem, an analogous transition occurs for DLs only in higher dimensions. In

principle, this offers an opportunity to observe new phenomena arising from an interplay of depinning and delocalisation for SDLs (the disorder used in Refs. [116–119] does not feature such a transition in the static problem). The localisation transition at a finite temperature also offers the opportunity to test the usage of static quantities in the treatment of creep motion, because the SDL is not pinned by disorder above the critical temperature.

A lot of the progress for the depinning theory of DLs has been based on two basic theorems due to Middleton [103], which essentially state that a forward moving DL can only move forward and will stop in a localised configuration, if such exists. This allows for an unambiguous time-ordering of a sequence of states. We will show that these theorems do not hold for the SDL, which can be seen as a consequence of the next-to-neighbour terms that are introduced by the bending elasticity.

As an external pulling force F intrinsically couples to only one transversal displacement component u, there is no substantial gain in treating more than one transverse dimension, and we will restrict our analysis to this case.

In suitable units, the overdamped equation of an elastic line with an elastic energy $\mathcal{H}_{\mathrm{el}}$ as in eq. (1) can be written as[102]

$$\frac{\partial u(x)}{\partial t} = -\frac{\delta \mathcal{H}_{\mathrm{el}}}{\delta u(x)} + \eta(x,u) + F \tag{23}$$

at zero temperature. The first term on the right hand side represents the elastic forces as obtained from variation of the elastic energy. The force F denotes a static, uniform pulling force[103], which tends to depin the line from the disordered medium, and $\eta(x,u)$ is a quenched force due to the disordered medium. For this quenched force we distinguish two cases in the following, random-field and random-potential disorder (see Fig. 42). For random-field (RF, sometimes also random-force) disorder, $\eta(x,u)$ is a random variable with zero mean and short-ranged correlations[104]

$$\overline{\eta(x,u)\eta(x',u')} \propto \delta(x-x')\delta(u-u') \quad \text{(RF)},$$

whereas for random-potential or random-bond (RB) disorder the force $\eta(x,u) = -\partial_u V(x,u)$ stems from a random potential $V(x,u)$, which features zero mean and short-ranged correlations. Hence, after a Fourier transformation in the transverse dimension, we can write

$$\overline{\eta(x,q)\eta(x',q')} \propto q^2\delta(x-x')\delta(q+q') \quad \text{(RB)}.$$

Within this work we will mostly focus on random-potential (RB) disorder; in particular, all our numerical results are for RB disorder. The analytical arguments, i.e., scaling relations and functional renormalisation group results will be applied to both types of disorder.

If thermal fluctuations at temperature T are included, an additional time-dependent white noise $\tau(x,t)$ with zero mean and correlations

$$\langle \tau(x,t)\tau(x',t')\rangle_T = 2T\delta(x-x')\delta(t-t')$$

is added on the right hand side of eq. (23). We introduce $\langle X\rangle$ to denote averages over time, $\langle \ldots \rangle_T$ for averages over thermal noise and $[\ldots]$ for spatial averages at a given time.

At zero temperature, there is a finite threshold value F_T at which the velocity

$$v(t) = \overline{[\dot{u}(x,t)]}$$

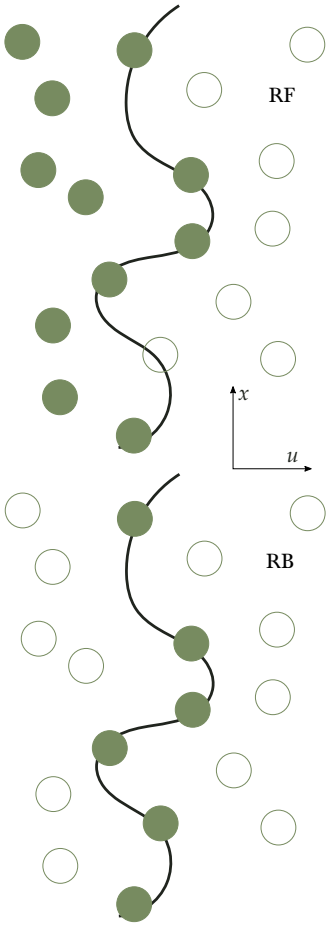

Figure 42: The two disorder types considered in this chapter. The nomenclature random field (RF) and random bond (RB) has its origin in magnetic problems (domain walls). Shown is an elastic line in a disorder represented by circles, here only the full circles contribute to the energy of the line. In the random potential case (bottom) these are only those that are in contact with the line (this is also the case we considered before for the static localisation), for a domain wall this would correspond to e.g. lattice defects (hence, random bond). In the random field case (top) the energy is afflicted by the all contributions from displacements that are (by choice) below the line (in the "domain" that is enclosed by the line). This figure is based on a similar sketch in Ref. 110.

[102] In this part some symbols change their meaning, especially z is no longer the displacement in the transversal direction, which is now u, but the dynamical exponent and F is no longer a free energy, but the pulling force. However, the author has the utmost confidence in the reader to handle this.

[103] We can interpret this in terms of the potential as a tilt of the energy landscape via $V \to V - Fu$, as in Fig. 40

of a driven elastic manifold in a pinning potential becomes nonzero in the limit of very large times t

$$\langle v(t)\rangle \begin{cases} = 0 & F \leq F_T \\ > 0 & F > F_T \end{cases}.$$

The shape of the driven line and its dynamics are usually characterised by the roughness exponent ζ and the dynamical exponent z, which describe how the roughness or width of the line,

$$w^2(t) = \overline{[u(x,t)^2 - [u(x,t)]^2]} = \overline{[u(x,t)^2]_c}, \tag{24}$$

scales with the system size L and the time t:

$$w^2(t) \sim \begin{cases} t^{2\zeta/z} & t \ll t_L \\ L^{2\zeta} & t \gg t_L \end{cases} \tag{25}$$

with the typical time scale $t_L \sim L^z$.

SDLs with $\mathfrak{z} = 2$ are closely related to surface growth models for molecular beam epitaxy (MBE) [50]. In the presence of surface diffusion, MBE has been described by a (quenched) Herring-Mullins linear diffusion equation[52, 53, 114, 115] for a surface described by a height profile $u(x,t)$,

$$\frac{\partial u(x)}{\partial t} = -\nabla^4 u(x) + \eta(x,u) + F. \tag{26}$$

In the Herring-Mullins limit, it is assumed that effects from a surface tension can be neglected as compared to surface diffusion effects[105]. Surface tension would give rise to additional $\nabla^2 u$-terms. In this context, the quantity F describes the constant flux of particles onto the surface and $\eta(x,u)$ random fluctuations in the deposition process.

In suitable units[106], the Herring-Mullins equation (26) is equivalent to the overdamped equation of motion (23) of the SDL. Without external forces ($\eta = 0$, $F = 0$) the exponents ζ and z take their thermal values $\zeta_{th} = 3/2$ and $z_{th} = 4$ [50]. The observation of the "super-rough" $\zeta = 3/2 > 1$ in tumour cells [122] hints towards further experimental relevance of the Herring-Mullins equation.

For the DL with $\mathfrak{z} = 1$, the equation of motion is the quenched Edwards-Wilkinson equation[123]

$$\frac{\partial u(x)}{\partial t} = \nabla^2 u(x) + \eta(x,u) + F,$$

and the thermal exponents are $\zeta_{th} = 1/2$ and $z_{th} = 2$. Generally, the thermal exponents[107] are given by $\zeta_{th} = \frac{2\mathfrak{z}-D}{2}$ and $z_{th} = 2\mathfrak{z}$.

Equilibrium properties

The equilibrium ($F = 0$) problem of a SDL in a $1+1$-dimensional medium with RB disorder features a localisation transition at a finite temperature T_c as we pointed out before. The roughness exponent is $\zeta_{\mathrm{eq,RB}} \approx 1.59 > 3/2$ in the disorder-dominated phase for $T < T_c$ and assumes the thermal value $\zeta = 3/2$ for $T > T_c$. In contrast to the SDL, the DL with one transverse dimension is localised for all temperatures with a roughness exponent[60] $\zeta_{\mathrm{eq,RB}} = 2/3$. This implies that the SDL in RB disorder offers the opportunity to study the dynamics of an unlocalised elastic manifold in disorder for

[104] As the forces are short-ranged random variables, the associated potential $V(x,u(x)) = -\int_0^{u(x)} \mathrm{d}y\eta(x,y)$ is essentially a random-walk with time u, from which we can infer that $\overline{V(x,u(x))V(x',u'(x'))} \sim |u-u'|$. In this way we see that the RF disorder is *long-ranged* in the potential.

[105] We derive the Herring-Mullins equation from this perspective in the appendix, see page 84.

[106] With a full set of parameters the equation would read $\lambda\partial u(x)/\partial t = -\varkappa\nabla^4 u(x) + g\eta(x,u) + F$, which reduces to the given form by rescaling $x = x/x_0$, $u = u/u_0$ and $t = t/t_0$ with x_0 given by the discretization, $u_0 = (g/\varkappa)^{2/3}x_0^3$ and $t_0 = \lambda x_0^4/\varkappa$.

[107] For a general elasticity energy of the type of eq. (1) (assuming positive, integer $\mathfrak{z}$ for simplicity) the equation of motion in $D+1$ dimensions is

$$\frac{\partial u(\boldsymbol{x})}{\partial t} = (-1)^{\mathfrak{z}+1}\nabla^{2\mathfrak{z}} u(\boldsymbol{x}) + \tau(\boldsymbol{x},u).$$

Rescaling $x \to bx$, $u \to b^\zeta u$, $t \to t^z t$ (and inferring the scaling behaviour of the thermal noise from its correlator) gives

$$b^{z+\zeta}\frac{\partial u(\boldsymbol{x})}{\partial t} = b^{\zeta+2\mathfrak{z}}(-1)^{\mathfrak{z}+1}\nabla^{2\mathfrak{z}} u(\boldsymbol{x}) + b^{-z+D/2}\tau(\boldsymbol{x},u)$$

from which we directly see $z = 2\mathfrak{z}$, $\zeta = \zeta_{th} = \frac{2\mathfrak{z}-D}{2}$.

$T > T_c$ and the interplay of the delocalisation transition at $T = T_c$ and a depinning transition at $F = F_T$.

For RF disorder, functional renormalisation group approaches [58, 69] using an expansion in $\varepsilon = 4 - D$ around the upper critical dimension $D_c = 4$ give a static roughness exponent $\zeta_{\mathrm{eq,RF}} = \varepsilon/3$ to at least two (and possibly all) orders in an expansion in ε and in good agreement with numerical results both for the DL [124, 125] and[108] the SDL[126].

The result $\zeta_{\mathrm{eq,RF}} = \varepsilon/3$ is the simple scaling or "Flory" result that follows from balancing the typical elastic energy of a line with displacement u, which scales as $\mathcal{H}_{\mathrm{el}} \sim L^D (u/L^3)^2$, with the typical disorder energy $\mathcal{H}_{\mathrm{dis}} \sim \sqrt{L^D u}$ as the disorder energy is picked up at L^D independent sites and its correlator is linear in u for sufficiently large u [67]. As we have seen, similar arguments fail to reproduce the non-trivial RB roughness exponent, but can provide bounds to it.

[108] In a discrete model that tried to directly implement surface diffusion and was proposed to correspond to the undriven quenched Herring-Mullins equation a differing exponent $\zeta_{\mathrm{eq,RF}} \approx 1.93$ was found for the SDL [116].

Previous work on the depinning of the quenched Herring-Mullins equation

There has been some previous work on the depinning of SDLs with RF disorder. From renormalisation group analysis it is expected that the critical exponents of the depinning transition are universal for all disorders with shorter ranged correlations than RF (including RB), although a different scenario is possible in principle [70]. For the DL the exponents do coincide for RF and RB disorder [109].

The roughness exponents previously found at the depinning of a SDL in RF disorder are $\zeta \approx 1.48 - 1.50$ and $\zeta = 1.48$ and a dynamical exponent $z \approx 1.77 - 1.78$ [117, 118]. Furthermore, in a discrete model [119] based on the quenched Herring-Mullins equation $\zeta = 1.35$ and $z = 1.60$ have been found at depinning. One obvious problem with these values for the roughness exponent ζ is that they are *smaller* than the thermal value $\zeta_{th} = 3/2$, i.e. disorder decreases the roughness of the line. We will comment below in more detail on similarities and differences in the findings of these studies to ours.

Analytical results

Critical exponents and scaling relations

In order to describe the depinning of driven elastic lines in a random medium within the framework of classic critical phenomena [111–113, 127], the roughness exponent ζ and dynamical exponent z introduced in eq. (25) are not sufficient but one additional exponent related to the control parameter, the driving force F, is needed. In the vicinity of the depinning threshold F_T we can introduce two exponents describing the *order parameter*, which is the velocity v of the centre of mass, and the *correlation length* ξ:

$$\begin{aligned} v &\sim (F - F_T)^{\beta} \\ \xi &\sim (F - F_T)^{-\nu}. \end{aligned} \tag{27}$$

The correlation length ξ gives the typical length of segments that rearrange during the avalanche-like motion close to the threshold; the typical time scale for this segment motion is $t_\xi \sim \xi^z$.

We can use one of these exponents, e.g. the correlation length exponent ν, to obtain from the equilibrium scaling relation

$$w(t,L) = t^{\zeta/z} g(t/t_L)$$

with a scaling function[109] $g(x)$, which underlies eq. (25), a corresponding scaling relation close to depinning,

$$w(t,F) = t^{\zeta/z} g(t/t_\xi) = t^{\zeta/z} f_\pm(t^{1/\nu z}(F - F_T)), \tag{28}$$

with scaling functions[110] $f_\pm(x)$ (for forces above (+) and below (-) the threshold).

There are two scaling laws relating the exponents β and ν to the roughness exponent ζ and the dynamical exponent z at the depinning transition. The first scaling law simply establishes a relation between β and ν using that velocity is displacement per time

$$v \sim w(t_\xi)/t_\xi \sim \xi^{\zeta - z}$$

(for $t \gg t_\xi$), which results in

$$\nu = \frac{\beta}{z - \zeta}. \tag{29}$$

This relation is valid independently of the form of the elastic energy, i.e., independent of $\mathfrak{z}$. As all exponents should be positive this also implies $z > \zeta$. The other relation comes from an additional tilt symmetry[111] of the equation of motion[113, 127], which leads to

$$\nu = \frac{1}{4 - \zeta} \tag{30}$$

for the SDL[112] ($\mathfrak{z} = 2$) or, for general elasticity, to

$$\nu = (2\mathfrak{z} - \zeta)^{-1}.$$

The relations (29) and (30) should hold both for RF and RB disorder at depinning.

For the analysis of simulation data it is convenient to infer exponents from the short time scaling properties of the velocity, which follows from the scaling (28) and $v \sim w/t$:

$$\begin{aligned} v(t,F) &\sim t^{\zeta/z - 1} f_\pm(t^{1/\nu z}(F - F_T)) \\ &\sim t^{-\delta} f_\pm(t^\gamma (F - F_T)) \end{aligned} \tag{31}$$

where we introduce two auxiliary exponents

$$\gamma = 1/\nu z \tag{32}$$

$$\delta = 1 - \zeta/z = \beta/\nu z = \beta\gamma, \tag{33}$$

for convenient data analysis (using the scaling relation (29) in eq. (33)).

There is a another exponent that is often referred to as ν or ν_{FS} describing the scaling of the sample-to-sample fluctuations of the threshold force

$$\Delta F_T \sim L^{-1/\nu_{\mathrm{FS}}} \tag{34}$$

in a system of finite size L. In general, ν and ν_{FS} do not have to coincide. For the DL, $\nu = \nu_{\mathrm{FS}} \approx 4/3$ has been confirmed [105, 128], whereas for the charge density wave problem (periodic potential), ν and ν_{FS} are distinct [129].

This might affect the scaling relations (29) and the auxiliary exponents γ and δ, see eqs. (32) and (33), which could read $\nu_{\mathrm{FS}} = \beta/(z - \zeta)$, $\gamma = 1/\nu_{\mathrm{FS}} z$, and $\delta = \beta/\nu_{\mathrm{FS}} z$. This happens if threshold force fluctuations by sample-to-sample disorder fluctuations on a scale L, $\Delta F_T \sim L^{-1/\nu_{\mathrm{FS}}}$, are larger than

[109] This scaling form follows directly from the notion that the relevant length scale in the lateral dimensions is the minimum of $L_t \sim t^{1/z}$ and L. Then the width has to be of the given form with the limits $g(0) \approx 1$ and $g(x) \sim x^{-\zeta/z}$ for $x \gg 1$.

[110] For this to be consistent with the equilibrium relation, $f \pm (x)$ has to have the following limits: $f_\pm(0) \approx 1$ and $f_\pm(x) \sim |x|^{-\zeta\nu}$ for $|x| \gg 1$.

[111] This time we do not tilt the line, but the energy landscape, that is we change the force $F \to F + \mathfrak{f}x$ with $\int \mathrm{d}x \mathfrak{f}(x) = 0$. Formally, we can compensate this by also tilting the line $u \to u - (-1)^{1+\mathfrak{z}} \nabla^{-2\mathfrak{z}}$. Thus, we see that in Fourier space we have a response to this tilt of the force

$$\frac{\partial u(q)}{\partial \mathfrak{f}(q)} \sim q^{-2\mathfrak{z}}.$$

By definition of the exponents the displacement $u(q)$ scales as L^ζ, the wavenumber q as L^{-1} and the force $\mathfrak{f}$ as $L^{-1/\nu}$ and the response is scale invariant, iff

$$\nu = \frac{1}{2\mathfrak{z} - \zeta}.$$

[112] The exponent values obtained previously in Ref. 117 are $\zeta \approx 1.50$ and $\nu \approx 1.01$ at the SDL depinning transition (for RF disorder). These values are problematic as they violate the scaling relation (30). One reason for this problem might be that the exponent ζ has been determined by direct measurement of the roughness $w(L)$ and its scaling for different system sizes L. However, such an approach is strongly influenced by the choice of the transverse system size (which should be $M \sim L^\zeta$) because the value for the critical force F_T depends also on the transverse system size. As Ref. 117 contains two other independently measured exponents, namely δ (see below) and β in our nomenclature, and scaling relations (29) and (30) imply $\zeta = 4\beta(1 - \delta)/(\delta + \beta(1 - \delta))$, we can give a resulting "scaling" roughness exponent $\zeta_{\mathrm{scaling}} \approx 2.4$, which strongly differs.

the excess to the threshold force necessary to depin a segment of length L, $F - F_T \sim L^{-1/\nu}$, see eq. (27). Therefore, we expect $\nu < \nu_{\mathrm{FS}}$ if ν and ν_{FS} are distinct.

Fluctuations in the depinning force F_T originate from the fluctuations in the disorder. The threshold force of a finite manifold of size L and width $w \sim L^\zeta$ occupying a volume $(\mathrm{Vol.}) \sim L^D w \sim L^{\zeta+D}$ should at least pick up the same fluctuations as the mean of a summation of i.i.d. random numbers (the forces on every site) which are $\sim (\mathrm{Vol.})^{-\frac{1}{2}}$. This results in a general lower limit for the depinning force fluctuations[130]

$$\Delta F_T \geq c(\mathrm{Vol.})^{-\frac{1}{2}} = \tilde{c} L^{-\frac{\zeta+D}{2}}$$

thus giving[113]

$$\nu_{\mathrm{FS}} \geq \frac{2}{\zeta + D}. \tag{35}$$

[113] This looks similar to our reasoning in the static case. However, it is important to realise that the trivial case of summing i.i.d. random numbers is an upper bound to fluctuations in the static case, whereas it is a lower bound here.

It has been argued that $\nu = \nu_{\mathrm{FS}}$ for an elastic line as long as the line continuously "explores" new regions of the disorder [127]. In this interpretation, distinct correlation length exponents ν and ν_{FS} for the charge density wave are a manifestation of the fact that the line "knows" the total potential at each point due to its periodicity. If $\nu = \nu_{\mathrm{FS}}$ holds, the bound (35) is equivalent to a lower bound to the roughness exponent ζ at depinning,

$$\zeta \geq \varepsilon/3 \quad \text{if } \nu = \nu_{\mathrm{FS}}, \tag{36}$$

which is valid for all elastic energies of the form (1), i.e., for all $\mathfrak{z}$. The *contraposition* is equally important[114]: if the roughness is less than $\varepsilon/3$, this implies that ν and ν_{FS} are distinct.

[114] This is also in line with the functional renormalisation group, as we will see below.

An upper bound to the roughness exponent comes from studying the line in the Larkin approximation with a constant (u-independent) random force acting on every segment of the line [29, 131]. The resulting Larkin roughness exponent is $\zeta_{\mathrm{Larkin}} = \varepsilon/2$. As the line can gather unbounded energy via large undulations in accordance with the force this represents an upper bound to the problem with finite potential range and, therefore,

$$\zeta \leq \varepsilon/2,$$

which holds for the roughness exponents ζ below, at, and above depinning.

Functional renormalisation group

It has originally been suggested that the roughness exponent ζ at the threshold force $F = F_T$ is independent of the type of disorder (RB or RF) and coincides with the static roughness of the line in a medium with RF disorder $\zeta_{\mathrm{eq,RF}} = \varepsilon/3$ to all orders of ε [127]. The discrepancy to numerical simulations [132] has been solved by means of the two-loop functional renormalisation group[115] (FRG) [70], which gives for the roughness exponent at depinning both for RB and RF disorder

$$\zeta = \zeta_1 \varepsilon + \zeta_2 \varepsilon^2 = \frac{\varepsilon}{3} + \frac{X_\mathfrak{z} \varepsilon^2}{27\sqrt{2}\gamma_{EM}} + \mathcal{O}(\varepsilon^3) \tag{37}$$

[115] To avoid repetition (with the static case) our discussion of the FRG here is rather minimal. We give some more details in the appendix, see page 85.

with the Euler-Mascheroni constant[116] γ_{EM} and the known constant $X_\mathfrak{z}$ that depends on the form of the elastic energy, especially $X_2 = 1$ and

[116] Using the previously defined Digamma function we can give[73] γ_{EM} by $\psi(1) = -\gamma_{EM}$. It might be more helpful simply state the numerical value $\gamma_{EM} \approx 0.57721$.

$X_4 = -1/6$. The FRG approach is based on a flow equation for the disorder force correlator[117] $\Delta(u)$ defined by

$$\overline{\eta(x,u)\eta(x',u')} = \delta(x-x')\Delta(u-u').$$

At two-loop order the FRG flow converges to the same fixed point disorder correlator (shown in Fig. 43) both for RB and RF disorder. Therefore, two-loop FRG predicts identical roughness exponents at depinning.

[117] This is the second derivative of the potential correlator $R(u)$, $\Delta(u) = -R''(u)$, we focused upon in the static case as can be easily seen using their Fourier transforms.

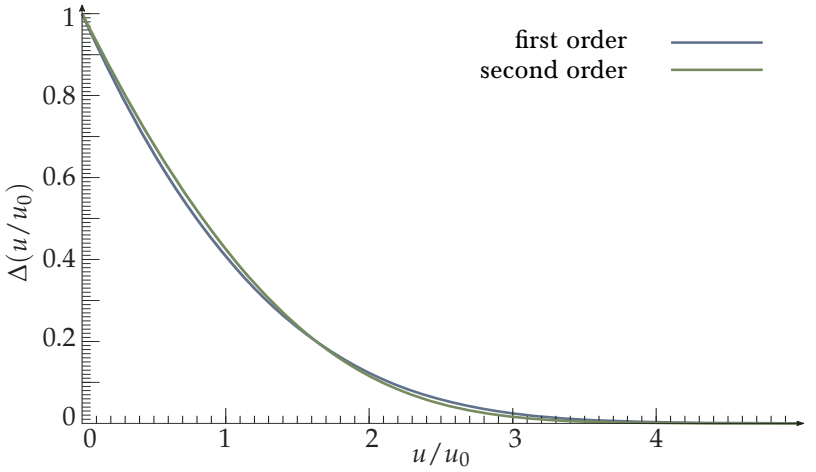

Figure 43: The fixed point solution to the functional renormalisation group flow equation of Ref. [70] for the disorder correlator $\Delta(u)$. The length scale u_0 is determined via $\int \mathrm{d}u\Delta(u/u_0) = 1$. The two-loop solution corresponds to a roughness exponent given by eq. (37). The small deviations between first and second order give rise to distinct roughness exponents, see eq. (38).

As $\varepsilon = 4\mathfrak{z} - d$ is rather large for the SDL, the two-loop contribution is important. This can be seen in the deviation of the two naive[118] results

$$\zeta_{1\text{-loop}} \approx 2.33 \quad \text{and} \quad \zeta_{2\text{-loop}} \approx 1.94 \tag{38}$$

using a direct evaluation of eq. (37). Thus the SDL roughness at depinning is expected to be above the static equilibrium value for zero external force $\zeta_{\mathrm{eq,RB}} \approx 1.59$ for RB disorder, but below the static result $\zeta_{\mathrm{eq,RF}} = 2/3$ for RF disorder. We note that any extrapolation of the results in eq. (37) necessarily violates the bound (36), which holds if $\nu = \nu_{\mathrm{FS}}$, as the negative two-loop contribution leads to $\zeta < \frac{\varepsilon}{3}$ for some finite ε. This is an indication for two distinct exponents ν and ν_{FS}.

In Fig. 43 we show the numeric solution of the FRG fixed point for the disorder correlator $\Delta(u)$ verifying that eq. (37) does indeed correspond to the unique non-negative faster than algebraically decaying (convex in double logarithmic plot) solution. We followed the numerical procedure outlined in Refs. [58, 70]. The new second order contribution y_2 giving the two-loop contribution in the Ansatz $\Delta(u) = \varepsilon/3 y_1(x) + \varepsilon^2/18 y_2(x) + O(\varepsilon^3)$ can be approximated by the Taylor series

$$\begin{aligned} y_2(x) \approx{}& 0.190021\,u - 0.1613u^2 + 3.37491\times10^{-2}u^3 + 3.21649\times10^{-3}u^4 - 4.32055\times10^{-4}u^5 \\ &- 2.55032\times10^{-4}u^6 - 4.7737\times10^{-5}u^7 + 1.0426\times10^{-6}u^8 + 3.44412\times10^{-6}u^9 + O(u^{10}). \end{aligned}$$

[118] Padé approximants give values $\zeta_{2\text{-loop}} \approx 1.9432$ to $\zeta_{2\text{-loop}} \approx 1.999$. As we will see below, the upper limit is closest to the value from numerical simulations, we therefore reproduce the corresponding approximant

$$\zeta(\varepsilon) \approx \frac{\zeta_1\varepsilon}{1-\frac{\varepsilon\zeta_2}{\zeta_1}}.$$

[119] The problematic part here is to evaluate

$$I_\eta^{(\mathfrak{z})} = \int_{q_1,q_2} \frac{1}{\left(q_1^2+m^2\right)^{\mathfrak{z}}\left(q_2^2+m^2\right)^{2\mathfrak{z}}} \times \frac{1}{\left(q_2^2+m^2\right)^{\mathfrak{z}} + \left(\left(q_1-q_2\right)^2+m^2\right)^{\mathfrak{z}}}$$

to leading order in ε for $\mathfrak{z} = 2$.

The FRG calculation[70] is in principle also capable of determining the dynamical exponent z and, thus, all exponents. However, to two loops this involves the evaluation (to leading order in ε) of the "correction to friction"[119] which remains an open task for $\mathfrak{z} = 2$. It is possible[120] to find bounds for the value of the dynamical exponent z in two-loop order[121]

$$1.86 \le z_{2\text{-loop}} \le 2.77 \quad . \tag{39}$$

[120] Details are given in appendix starting on page 86.

[121] These bounds are from a direct evaluation of z at $\varepsilon = 7$, one could try to employ a more sophisticated extrapolation method, but this would be of little value here. Also, it is noteworthy that the lower bound given here is most definitely not restrictive enough, as $z > \zeta$ must hold.

exponent	ζ	z	ν	ν_{FS}	β	δ	γ
FRG (one-loop)	7/3	22/9	3/5	3/5	1/15	1/22	22/15
FRG (two-loop)	1.97(3)	$\zeta \leq z < 2.77$	0.493(7)	2	eq. (29)	eq. (33)	eq. (32)
simulation Ref. [117]	1.50	1.78	1.01	–	0.289(8)	0.160(5)	0.55
simulation this work	2.00	2.15	0.50	2.00	0.29	0.07	0.56

Table 1: Critical exponents at the SDL depinning transition determined via one- and two-loop functional renormalisation group (FRG) [70] and numerical simulation results from Ref. [117] (this work does not attempt to measure ν_{FS}, but since there $\zeta \leq \varepsilon/3$ holds one would expect it to coincide with ν). The penultimate line uses the numerical values for β and δ and the scaling relations. We are not able to give a precise estimate for z in two-loop order and therefore give only the bounds, consequently there is little use in stating values for β, δ. We give the two-loop result and error as inferred from the biggest and smallest values found using Pade approximants of ζ.

The exponents at one- and two-loop order for the SDL are given in Table 1 together with the previous numerical findings.

An interesting question in the FRG analysis is the stability of the fixed point solution. It has been argued [70, 127] that the two previously defined correlation length exponents coincide, that is $\nu = \nu_{\mathrm{FS}}$, if the fixed point solution for the disorder correlator is stable. This is in agreement with the results for charge density waves (fixed point unstable [111, 112], $\nu \neq \nu_{\mathrm{FS}}$ [129]) and the DL (fixed point presumably stable [70], $\nu \approx \nu_{\mathrm{FS}}$ [105]). We did not try to perform a full stability analysis, but we note that the simple argument of Ref. 70 for the instability of the fixed point for charge density waves might also hold for SDLs: after integrating the FRG flow equation from $u = 0^+$ to $u = \infty$ it reads

$$-m\partial_m \int_0^\infty \Delta(u)\mathrm{d}u = (\varepsilon - 3\zeta) \int_0^\infty \Delta(u)\mathrm{d}u - X_4 \Delta'(0^+)^3. \tag{40}$$

The second contribution on the right hand side is negative because (to two loops)

$$\zeta = \frac{1}{3}\varepsilon - \frac{X_3 \Delta'(0^+)^3}{3\int \Delta} = \frac{\varepsilon}{3} + \zeta_2 \varepsilon^2 \tag{41}$$

and $\zeta_2 < 0$ (for the SDL, here and in the following we use the shorter notation $\int \Delta \equiv \int_0^\infty \mathrm{d}u \Delta(u)$). More importantly, this implies that $\zeta < \varepsilon/3$ and, thus, the FRG fixed point of $\int \Delta$ is unstable. Denoting the fixed point solution by Δ^* we find that the instability of the fixed point of eq. (40) leads to a flow of the form

$$\Delta_m(u) = \Delta^*(u) + c m^{-(\varepsilon - 3\zeta)}$$

with $c = m_0^{\varepsilon - 3\zeta} \int_0^\infty (\Delta_{m_0}(u) - \Delta^*(u))\mathrm{d}u$. Thus an additional constant (u-independent) contribution to the fixed point $\Delta^*(u)$ is generated, that grows as m goes to zero if $\zeta < \varepsilon/3$. This means that to two-loop order a random force of the Larkin-type is generated[122]. This random force generates the Larkin-like roughness $\zeta_{\mathrm{Larkin}} = \varepsilon/2$ which for the SDL with $\varepsilon = 7$ implies a separate correlation length exponent

$$\nu_{\mathrm{FS}} = \frac{1}{4 - 7/2} = 2 \tag{42}$$

according to the tilt-symmetry scaling relation, see eq. (30).

[122] SDLs subject to Larkin-like random forces have been one subject of Ref. 4.

Large force limit, crossover to single particle limit

For sufficiently large external forces we can generalise the perturbative arguments for DLs from Refs. [101, 102] to general elastic manifolds in $D+1$ Dimensions with an elastic energy of the form (1). Then, to second order in perturbation theory, the velocity of the centre of mass of the line is

$$v \approx F - \text{const} \times F^{\frac{D-2\zeta}{2\zeta}}$$

Here we assumed a short-ranged random potential that is completely uncorrelated along the internal dimensions. For the problem at hand ($D = 1$, $\mathfrak{z} = 2$) this implies that the first correction at large forces should scale as

$$1 - \frac{v}{F} \sim F^{-7/4}. \tag{43}$$

This is in agreement with our numerical results for not too large forces. The asymptotic behaviour for very large forces can be understood with the same perturbative reasoning that led to eq. (43), but neglecting the elastic forces and considering the effective single-particle (sp) equation $\frac{\partial u}{\partial t} = \eta(u) + F$. This leads to

$$\begin{aligned} v_{\mathrm{sp}} &= F - \mathrm{const} \times F^{-1} R_u^{-3} \\ 1 - \frac{v_{\mathrm{sp}}}{F} &\sim F^{-2} \quad . \end{aligned}$$

The crossover should happen, when the length scale $(\Delta_u/F)^{1/4}$ on which the elastic adjustments to the forced induced motion are relevant becomes significantly smaller than the lattice spacing Δ_x. This is the length scale that corresponds to the time scale Δ_u/F for a moving line to get to the next "disorder site" for the free dynamic exponent $z_0 = 4$.

Finite Temperature

At finite temperatures $T > 0$ there is a thermally activated motion, $\langle v \rangle > 0$, for any driving force F. For the DL this dynamical phenomenon has successfully been described via the thermal activation over barriers that are determined from a static consideration as the motion is expected to be very slow for low temperatures and forces [104, 133, 134]. For forces $F < F_T$ below depinning this involves activation over large energy barriers (diverging in the limit $F \approx 0$) and results in so-called creep motion. As a result of thermal activation, the sharp depinning transition at $F = F_T$ is rounded. For forces $F > F_T$ above depinning the line moves with finite velocity and additional thermal activation has only little effect.

For the SDL, there is an additional complication because of the disorder-induced localisation transition at a finite temperature T_c [1, 2]. For temperatures $T < T_c$, we expect the SDL to behave qualitatively similar to a DL, i.e., to exhibit creep for $F < F_T$, thermal rounding of the depinning transition at $F = F_T$, and only minor modifications of the flow behaviour for $F > F_T$. In order to derive the SDL creep law via a scaling argument, we consider the static equilibrium energy fluctuations, which scale as[123]

$$E_{\mathrm{eq}} \sim L^{\omega}.$$

[123] The exponent ω is still the equilibrium energy fluctuation exponent $\omega = D - 2\mathfrak{z} + 2\zeta_{eq}$.

In a static framework, a depinning force F simply tilts the energy landscape

$$U_F \sim F L^D w \sim F L^{D+\zeta_{eq}}.$$

Balancing these two contributions to optimise the total barrier energy $E_{\mathrm{barrier}} = E_{\mathrm{eq}} - U_F$, one gets the energy of the effective barriers scaling as

$$E_{\mathrm{barrier}} \sim F^{-\mu}$$

with the *barrier exponent*

$$\mu = \frac{D - 2\mathfrak{z} + 2\zeta_{eq}}{2\mathfrak{z} - \zeta_{eq}} = \frac{\omega}{2\mathfrak{z} - \zeta_{eq}}.$$

For lines with $D = 1$, this gives $\mu = 1/4$ for the DL and $\mu \approx 0.07$ for the SDL. The velocity follows from the Arrhenius law to be

$$v \sim \mathrm{e}^{-\mathrm{const} \times F^{-\mu}/T}.$$

For the DL this has been confirmed experimentally[135].

For temperatures $T > T_c$, on the other hand, the scenario is less clear. In the static problem, the SDL then depins already by thermal fluctuations. The roughness in the static problem is only larger than the thermal roughness, $\zeta_{eq} > \zeta_{th}$, for temperatures $T < T_c$ below the critical temperature [1, 2]. For $T > T_c$, the static SDL is thermally rough $\zeta_{th} = (4 - D)/2$, and there are no macroscopic energy fluctuations. Assuming that the static equilibrium physics is indeed relevant for low driving forces (as in the derivation of the creep law), the conclusion could be that there are only finite energy barriers of characteristic size $E_{\mathrm{barrier}} = C$, and the velocity is given by the so called thermally assisted flux flow (TAFF) [136, 137]

$$v_{\mathrm{TAFF}} \propto \frac{F}{T} \mathrm{e}^{-C/T}.$$

The treatment of Ref. 104 within the FRG suggests that (at least to one-loop order) the force-force correlator Δ is only affected by a finite temperature within the "thermal boundary layer" of width $\sim T$ (especially, there is only a "cusp" for $T = 0$). Within this layer the line assumes the static roughness ζ_{eq}, whereas on larger scales the dynamic roughness $\zeta > \zeta_{eq}$ becomes apparent (for finite $v > 0$). Thus, the FRG seems to be in line with our previous reasoning, that is $\mu = 0$ for $T > T_c$ and a TAFF-like velocity-force curve.

However, this comes with the substantial caveat that, to our knowledge[124], the FRG theory in its present form is not apt to describe the full temperature dependence and, in particular, the existence of a transition to thermal roughness (which should manifest itself in the emergence of a fixed point solution with roughness ζ_{th}) at finite temperature. One basic difficulty is that a disorder-induced localisation transition at a finite temperature T_c does only occur for low dimensions $D < 2$[3], whereas the FRG uses an expansion around an upper critical dimension $D = 4$[3]. Starting on page 77, we will present numerical evidence that the thermal rounding of the depinning transition at the threshold force F_T is very similar for DLs and SDLs. This surprising result suggests that the thermal depinning transition of the SDL in the absence of a driving force does *not* change the depinning by a driving force qualitatively.

[124] We discussed this in the static treatment. There are promising hints at the lowest possible order but any substantial progress seems to be difficult.

The numerical determination of the barrier exponent μ is an unsolved problem even with algorithms specifically designed to capture the creep dynamics [138]. The thermal rounding of the transition leads to a temperature dependent velocity at the (zero-temperature) threshold force, which, for the DL, has been found to follow a power-law

$$v_{F_T} = T^{\psi}. \tag{44}$$

It has been suggested that[125] $\psi = \beta/(1 + 2\beta)$ [104, 139]. Numerically and experimentally a value $\psi \approx 0.15 \approx \beta/(1 + 2\beta)$ ($\beta \approx 0.245$ [138]) has been found for the DL with RB disorder [140, 141].

[125] The perturbative argument in Ref. 104 is equally valid for the SDL.

Numerical results

Direct integration of the equation of motion

We make use of a recently presented implementation[109] for graphics processing units [126] (GPUs). The high number of parallelly executed computations

[126] Our simulations were performed on a Tesla C2070. We used the CUDA Toolkit, version 5.0.[142]. We slightly increased the performance by consequently using templated kernels.

becomes very advantageous for large lengths, with an effective speedup of two orders of magnitude for the DL [109]. As the different elastic force generates only little additional branching (the determination of the next-nearest neighbours with periodic boundaries), the GPU implementation is also favourable for SDLs.

Additionally, we implemented an equivalent simulation for CPUs. An Euler integration scheme is used for the benefit of computational simplicity.

In the numerical simulations we focus on random potential (RB) disorder (as opposed to Ref. 117). The random potential is implemented by drawing random numbers from a normal distribution on an $L \times M$ lattice where M is the transverse size of the system [143]. Between the lattice points the potential is interpolated by periodic, cubic splines[127] in u-direction. Disorder averages were performed over 10^3 samples. Our system is periodic in x- and u-direction and the simulation starts with a flat line $u(x) \equiv 0$.

We set the lattice spacing in both directions equal to one, $\Delta_x = \Delta_u = 1$, and approximate the fourth derivative by the central finite difference

$$\nabla^{(4)} u(x) \approx u(x-2) - 4u(x-1) + 6u(x) - 4u(x+1) + u(x+2),$$

which is of second order in space. A von-Neumann stability analysis[128] shows that (without external forces) the Euler integration scheme becomes unstable for $\Delta t/\Delta_x^2 > 2^{-3}$. Throughout this work we used time steps $\Delta t \leq 2^{-6}$, unless stated differently.

As the width of the line can be influenced by various effects on different length scales, it can be difficult and error-prone to infer ζ directly from the line width w. Therefore, it is helpful to study the structure factor[129]

$$S(q,t) = \overline{|u(q,t)|^2} \sim q^{-(2\zeta+1)} \tag{45}$$

where $u(q,t)$ is the Fourier transformation of $u(x,t)$.

For sufficiently large M the system is ergodic only above the threshold, when the line moves. Thus, for forces smaller than the threshold force (cp. Fig. 44) the line does not show the static roughness, but adjusts itself to the potential on short length scales leading to Larkin roughness $\zeta_{\text{Larkin}} = 1/2$, whereas the conformation on longer length scales depends on the initial conditions. Here and in the following we plot the structure factor as a function of $2\sin(q/2)$ to correct for lattice artifacts.

[127] The splines are efficiently computed by implementing Thomas' algorithm, see for example Ref. 144.

[128] We consider a disturbance $d(x,t) = e^{at}\, e^{ibx}$ whose time-evolution is given by

$$\begin{aligned} e^{a\Delta t} &= 1 - \Delta t \left(e^{-2ib} - 4\, e^{-ib} \right. \\ &\quad \left. + 6 - 4\, e^{ib} + e^{2ib} \right) \\ &= 1 - \Delta t\, (2\cos 2b - 8\cos b + 6)\,. \end{aligned}$$

The term in braces is $\in [0,16]$, which leads to an exponentially fast growth of disturbances for $\Delta t > 2^{-3}$.

[129] The scaling relation for the structure factor assumes self-affinity of the line.

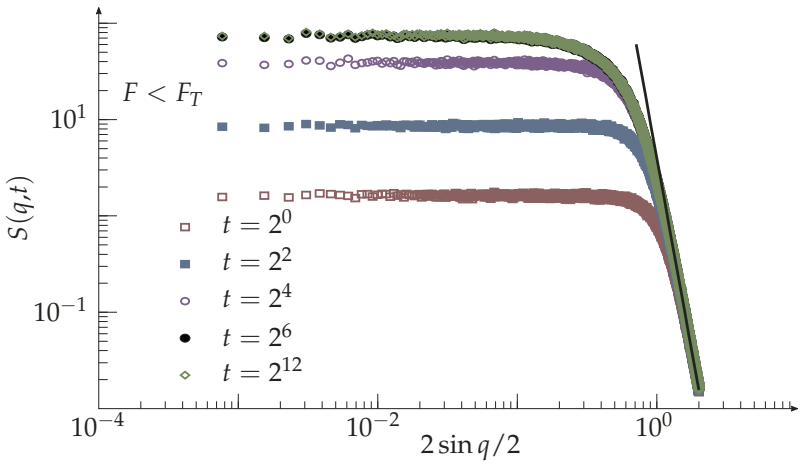

Figure 44: Disorder averaged structure factor $S(q,t)$ for a SDL with $F = 1.00 < F_T$ ($L = 8192$, $M = 16384$). The initial conditions (flat line) persist on long length scales and cross over to a regime with Larkin roughness ($\zeta_{\text{Larkin}} = 1/2$, solid line) on short length scales. After adjustment to the disorder till about $t = 2^6$ the conformation of the line does not change.

Short-time dynamics scaling

Alike previous studies [109, 117, 145] we employ short-time dynamics scaling to determine the critical exponents of the SDL at depinning. From eqs. (28) and (31) we know that, at $F = F_T$, velocity and line width scale as

$$v \sim t^{-\delta} \sim t^{-\beta/\nu z}$$
$$w \sim t^{1-\delta} \sim t^{\zeta/z} \quad .$$

These two observables contain the same information regarding the critical exponents. The behaviour for forces near the threshold can be used to extract the exponent $\gamma = 1/\nu z$ from rescaling the velocity according to eq. (31),

$$v(t,F)t^{\beta/\nu z} \sim f_{\pm}(t^{1/(\nu z)}(F - F_T)). \tag{46}$$

However, with actual data it turns out to be difficult to extract precise and unambiguous exponents from this finite-size scaling like procedure. Additionally, the roughness exponent ζ becomes apparent in the structure factor $S(q,t)$ for wave-numbers below some $q_t \sim L_t^{-1} \sim t^{-1/z}$, see eq. (45).

In Ref. 117, $\delta \approx 0.16$ has been found from studying $v(t)$ and $w(t)$ for RF disorder. In Fig. 45 we obtain the same result for RB disorder. Additionally, we show in Fig. 46 that the data can be nicely matched using the scaling of eq. (46) and $\gamma \approx 0.56$ in agreement with Ref. 117. By definition of δ and γ, this implies $\beta = \delta/\gamma \approx 0.29$ and by means of scaling relations $\zeta \approx 2.4 - 2.5$ as we already pointed out. We do not find any evidence (at any force) in the structure factor supporting this roughness. We do observe the emergence of a new roughness exponent $\zeta \approx 2$ at higher forces as can be seen from Fig. 48. We consequently conclude that this is a more plausible location of the threshold force and that $\zeta \approx 2$ is indeed the threshold roughness exponent.

The examination of $v(t)$ at higher forces and larger times reveals that the curves that do not saturate to a finite v for large times ($F > F_T$) or go to zero ($F < F_T$) seem to consist of two power-law segments, where only the first one for smaller times is consistent with $\delta \approx 0.16$, see Fig. 47. This is analogous to the most recent findings for the DL in Ref. 109. In Fig. 47 we show $v(t)$ for $F = 1.793$, which we believe to be close to the threshold force F_T for the system size we use. As the exponent δ in the second power-law segment is rather close to zero and we have no independent method to determine F_T (see also below on page 78) giving a precise value for δ is difficult. As the threshold roughness does not only influence the structure factor exactly at F_T, but also for deviating forces (given that the correlation length is still noticeably large), we think that we can rely on our value of $\zeta \approx 2$ even though we do not know F_T precisely. Additionally, we will support the claim of a roughness exponent $\zeta \approx 2$ with an independent method below, see page 74. In Fig. 47 we show that $F_T = 1.793$ is consistent with an exponent value $\delta \approx 0.07$ for larger times t, whereas $\delta \approx 0.16$ only at smaller times.

For $F_T = 1.793$ we obtain, based on the numerical results $\delta \approx 0.07$ and $\zeta \approx 2.0$, the following set of exponents:

$$F_T \approx 1.793\,, \qquad \delta \approx 0.07\,,$$
$$\zeta \approx 2.0\,, \qquad z = \zeta/(1-\delta) \approx 2.15\,,$$
$$\nu = \frac{1}{4-\zeta} \approx 0.5\,, \qquad \beta = \nu(z-\zeta) \approx 0.08\,,$$

To determine z we used the scaling relation (33). The value for ν then follows from the scaling relation (30) based on the tilt symmetry, the value for β from the scaling relation (33).

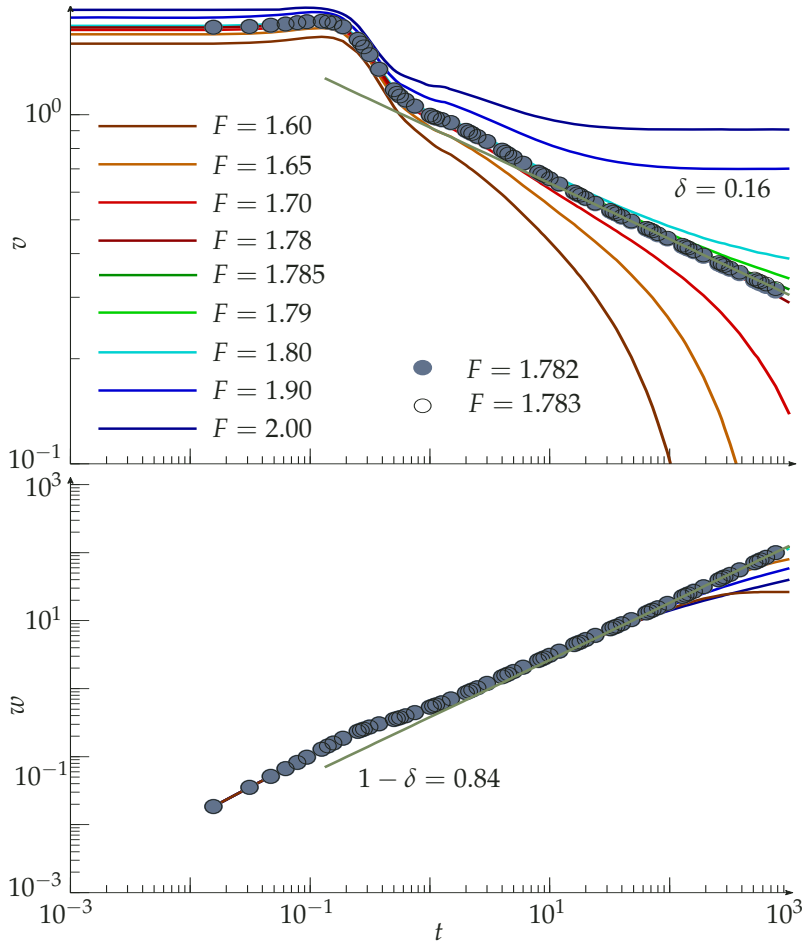

Figure 45: (upper two plots) The disorder-averaged centre-of-mass velocity $v(t)$ (top) and roughness $w(t)$ (bottom) in a system with $L = 8192$, $M = 16384$ for various forces and short times. Both quantities exhibit power-law regime consistent with $\delta = 0.16$ at $F \approx 1.782 - 1.783$. For clarity we plotted the data for these data as full ($F = 1.782$) and hollow ($F = 1.783$) circles and used lines for the rest (the key given in the upper figure holds for both). We note that the time-averaged roughness $\langle w(t) \rangle$ becomes maximal around $F \approx 1.782 - 1.783$.

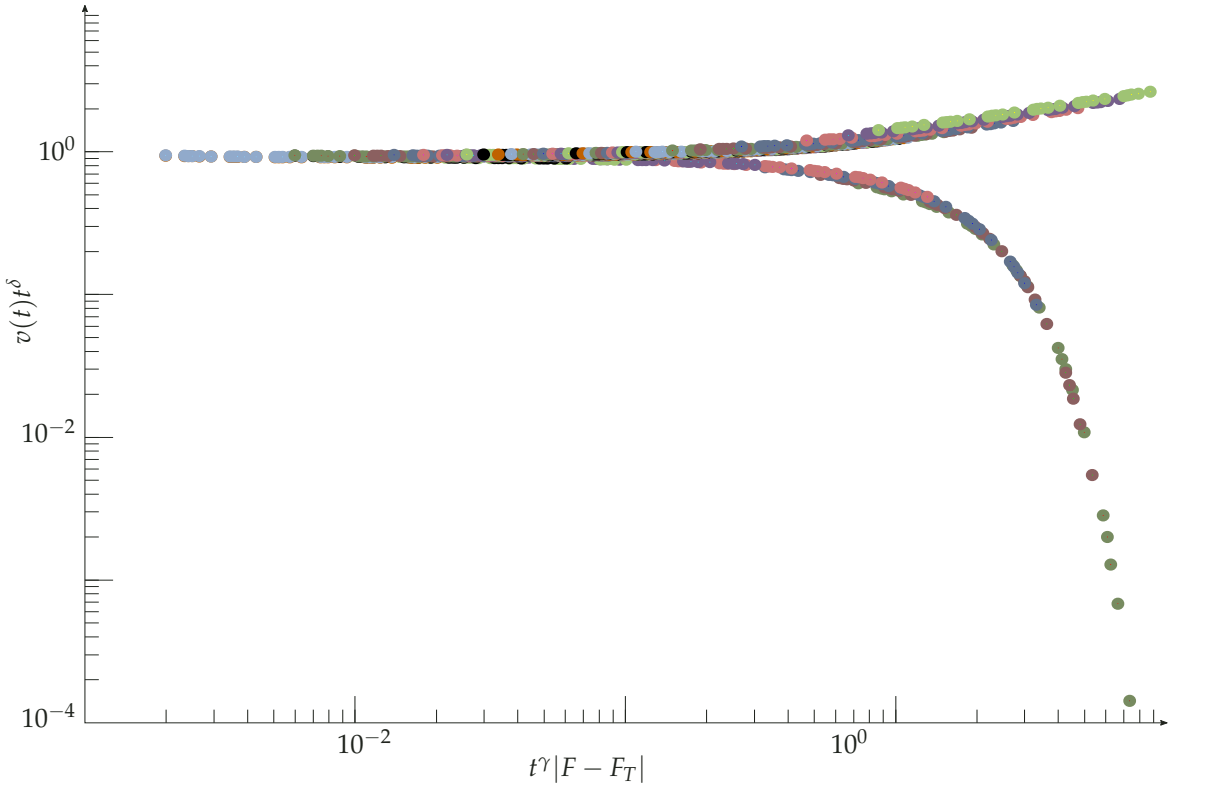

Figure 46: (lower, larger plot) Scaling plot of the velocity for different forces and times using eq. (46). The upper branch contains forces $F > F_T$ and the lower one forces $F < F_T$. Parameters are as for Fig. 45, but we used more force values ($1 < F < 2$). As scaling is not expected to hold for small times, we only considered $t > 10$. In agreement with Fig. 45, we used $F_T = 1.7825$ and $\delta = 0.16$. We see satisfying scaling for $\gamma \approx 0.56$, which coincides with the findings of Ref. [117].

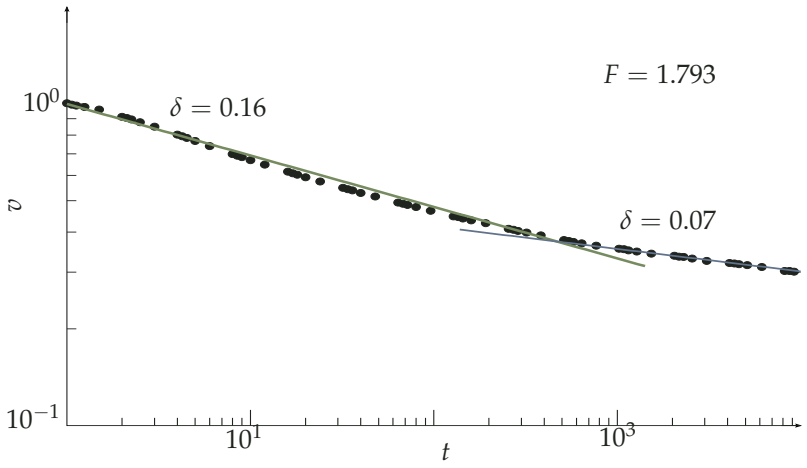

Figure 47: The disorder averaged centre-of-mass velocity for $F = 1.793$. The system parameters are as for Fig. 45, which suggested $F_T \approx 1.782 - 1.783$. The description by a power-law fits better in the "macroscopic" large time regime. Although we rather determined F_T by demanding a consistent δ as in Figs. 45 and 46, we note that, for $F = 1.793$, the second-power law fits particularly well.

We note, however, that the value for β is inconsistent with the value of $\beta \approx 0.28$ that we obtain numerically as explained in the next subsection. A value $\beta \approx 0.29$ implies $\nu = \beta/(z-\zeta) \approx 1.92$ with errorbars that are consistent with the exponent $\nu_{\mathrm{FS}} = 2$ introduced above to characterise sample-to-sample fluctuations of the free energy, see eqs. (34) and (42). Moreover, $\beta \approx 0.29$ is only consistent with the scaling relation $\delta = \beta/\nu_{\mathrm{FS}}\, z \approx 0.07$, see eq. (33), if we use $\nu_{\mathrm{FS}} = 2$. This suggests that the SDL in disorder is indeed characterised by two different exponents $\nu \neq \nu_{\mathrm{FS}}$ similar to charge density waves [129]. Therefore, we conclude that all our data are best represented by the following extended set of exponents (cp. Table 1):

$$\begin{aligned} &F_T \approx 1.793\,, && \delta \approx 0.07\,, \\ &\zeta \approx 2.0\,, && z = \zeta/(1-\delta) \approx 2.15\,, \\ &\nu = \frac{1}{4-\zeta} \approx 0.5\,, && \nu_{\mathrm{FS}} \approx 2\,, \\ &\beta \approx 0.29 \approx \nu_{\mathrm{FS}}(z-\zeta). \end{aligned} \tag{47}$$

We are not able to give sensible margins of errors and simulations of much larger systems (such that the ratio w/vt becomes constant) might be needed.

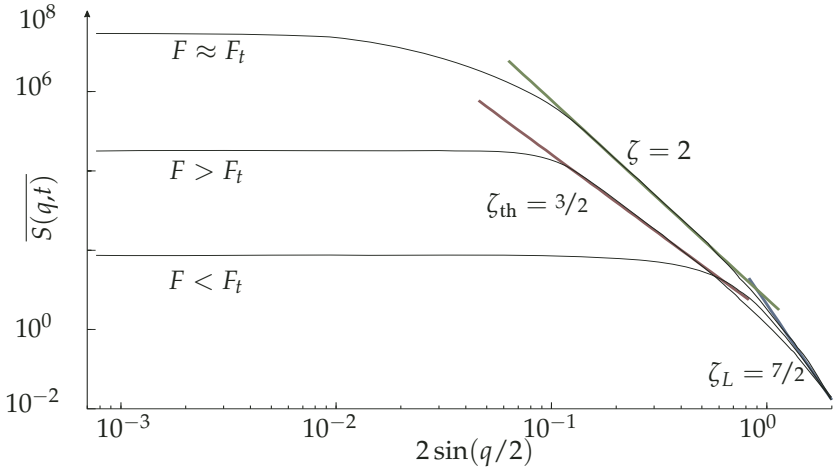

Figure 48: The disorder-averaged structure factor for a system with $L = 8192$, $M = 16384$ at time $t = 4096$ at three different forces representing the three regimes: under-critical, critical and over-critical. Although configurations are not strictly self-affine (pure power-law behaviour in the structure factor) there is a clear emergence of an exponent $\zeta = 2$ around the threshold force. We identify this as the "critical" roughness exponent. As in Fig. 45, the system shows maximal roughness at the threshold.

Velocity force relation

We also tried to determine the velocity exponent β directly. In the treatment of DLs, there is a significant discrepancy in the reported values of β, with

either $\beta \approx 0.33$ [105] or $\beta \approx 0.25$ [109]. These were determined by means of two slightly different approaches: one can either determine (as in [105]) the threshold force $F_{T,\text{sample}}$ for each sample and average $\overline{\langle [\dot{u}] \rangle (F - F_{T,\text{sample}})}$ or use $\langle v \rangle (F - \overline{F_{T,\text{sample}}})$ (as in [109]). We chose the first approach because $\overline{F_{T,\text{sample}}}$ cannot be clearly extracted from short-time dynamics scaling and, thus, the sample specific threshold force has to be determined anyway.

In Fig. 49 we show data for two single samples of sizes $L = 2048$ and $L = 8192$. We infer from our data

$$\beta \approx 0.28.$$

This agrees with the value $\beta \approx 0.29$ found in Ref. [117].

Large forces

We have successfully confirmed the perturbative results, cp. Fig. 50, for large driving forces. Additionally, we checked that the roughness exponent ζ of the SDL takes its thermal value $\zeta_{th} = 3/2$ for sufficiently large driving forces.

An interesting (and maybe counter-intuitive) result is that increasing the force leads to *a decrease in the effective temperature*. We show this in Fig. 51 using the time averaged width (cp. eq. (24)) of the line as function of the force[130].

[130] We expect the width w to scale as $w^2 \sim L_p^2 (L/L_p)^{2\zeta}$ with an effective persistence length L_p of the SDL.

For the dynamic depinning the simulation results in Fig. 51 show an increase of the SDL width at depinning, followed by a decrease $w \sim F^{-1}$ at high forces, where the roughness exponent assumes its thermal value $\zeta = \zeta_{th} = 3/2$ again. This is consistent with a behaviour $w^2 \sim L^3/L_p$ with $L_p \sim F$ and, thus, an "effective" temperature $T_{\text{eff}} \sim F^{-1}$ that *decreases* with driving force F. This can be rationalised from the FRG approach by noting that for high velocities the disorder contributes in form of an additional thermal noise corresponding to a temperature[104] $T_{\text{eff}} \sim v \int \Delta$. At high forces the line is far from the threshold and, thus, $\int \Delta$ should be close to the RB-disorder value of $\int \Delta = 0$. The observed behaviour $T_{\text{eff}} \sim F^{-1}$ implies $\int \Delta \sim F^{-2}$ because $v \sim F$.

Confinement in a moving parabolic potential

A different approach [106–108, 146] to compute the threshold force and, additionally, the effective disorder correlation functions is to pull the line very slowly with a spring. This means to introduce a parabolic potential acting on each line segment according to

$$V_{\text{par}}(u,t) = m^2 (u - w(t))^2$$

and move the centre $w(t)$ of the parabolic potential with a (small) constant velocity $\dot{w} = \text{const} > 0$. We call m^2 the strength of the potential. The underlying idea is essentially that the force $F(\dot{w})$ exerted by the parabolic potential on the line as it moves forward becomes the threshold force for $m \to 0$, $\dot{w} \to 0$. More precisely, it was found for the DL that

$$\langle w - [u(w)] \rangle m^2 = F_T + C m^{2-\zeta}$$

with some constant C (from now on, we assume that $\dot{w}$ is sufficiently small).

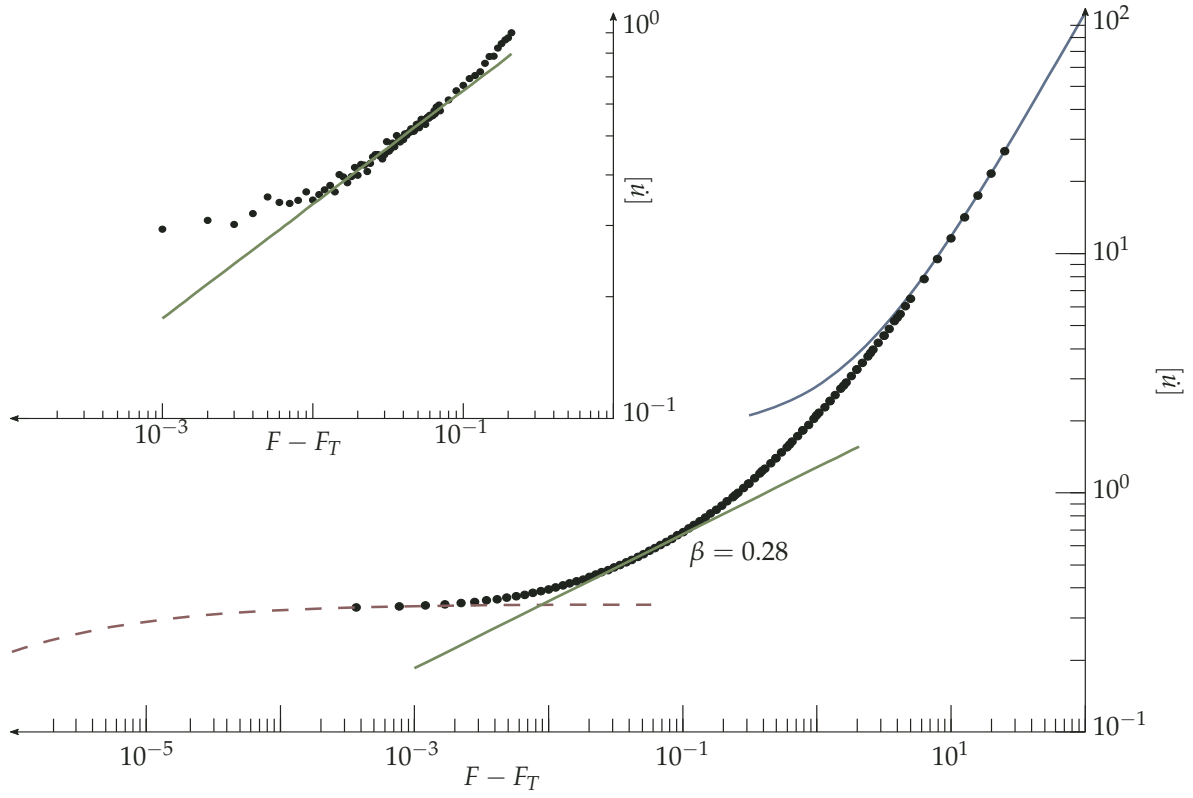

Figure 49: (upper figure) Velocity force relation for a sample of longitudinal size $L = 2048$ and transverse size $M = 8192$. The time average was computed over 10^{10} time steps $\Delta t = 2 \cdot 10^{-2}$. We interpret the smaller slope at very low force differences as the beginning of the "single particle"-behaviour $v^{-1} \propto \text{const} + (F - F_T)^{-1/2}$ that has been derived in Ref. [105], whereas at higher force difference the moving line with $v \sim F$ becomes apparent. The best value of β depends on the threshold force used (here and in the inset we used $F_T \approx 1.79$), but we found consistent values of $\beta \approx 0.28$ for various sizes and samples. Inset: velocity force relation for one larger sample with $L = 8192$ and $M = 16384$. The time average was computed over 2^{20} time steps $\Delta t = 2^{-6}$. There is a larger window with visible scaling.

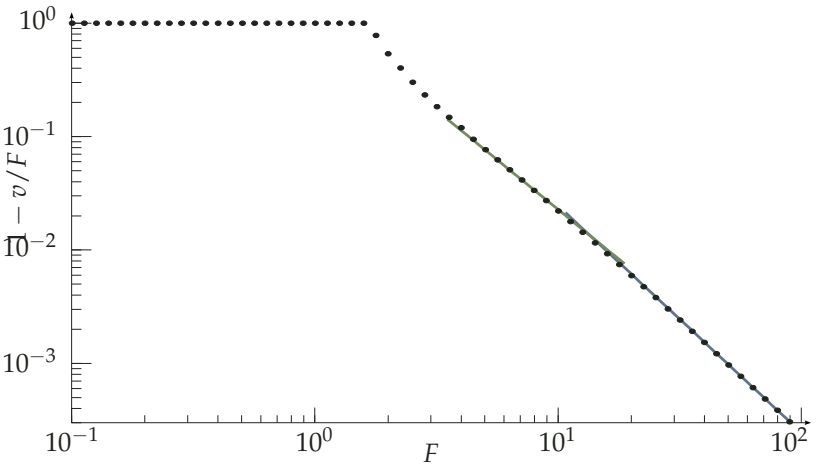

Figure 50: (lower figure) The deviation from the asymptotic $v \sim F$ for large forces in *one* sample. The green solid line is the perturbative result as given by eq. (43), the blue solid line is given by $1 - v/F \sim F^{-2}$. A similar cross-over to the single-particle behaviour has been observed for the DL [147]. We used 2^{20} small time steps $\Delta t = 2^{-10}$ to accurately simulate the system even for large forces. For steady state results the time average was performed only over the last 2^{19} time steps. The system has lateral size $L = 64$ and transverse size $M = 512$.

For general $\mathfrak{z}$, the expected corrections due to finite values of m have to be adjusted to account for the different elasticity. The length scale L_m at which the confinement through the parabolic potential becomes relevant follows from balancing the elastic and the potential energy per length

$$u^2/L^{2\mathfrak{z}} \sim m^2 u^2 \quad \text{with} \quad L_m^{\mathfrak{z}} \sim m^{-1}$$

L_m is the length of independently adjusting line-segments. Averaging over all w, i.e., averaging over disorder, typical displacements scale as $u_m \sim L_m^{\zeta}$. This leads to effective forces scaling as

$$F_m \sim m^2 u_m \sim m^2 L_m^{\zeta} \sim m^{2-\zeta/\mathfrak{z}},$$

which includes the aforementioned DL result ($\mathfrak{z} = 1$). A different approach [109] leading to the same result would be to use the known scaling of the finite-size corrections to the threshold force in one sample $F_T(L) - F_T \sim L^{-1/\nu}$ together with the notion that the relevant length scale is imposed by the parabolic potential and therefore given by $L_m \sim m^{-1/\mathfrak{z}}$.

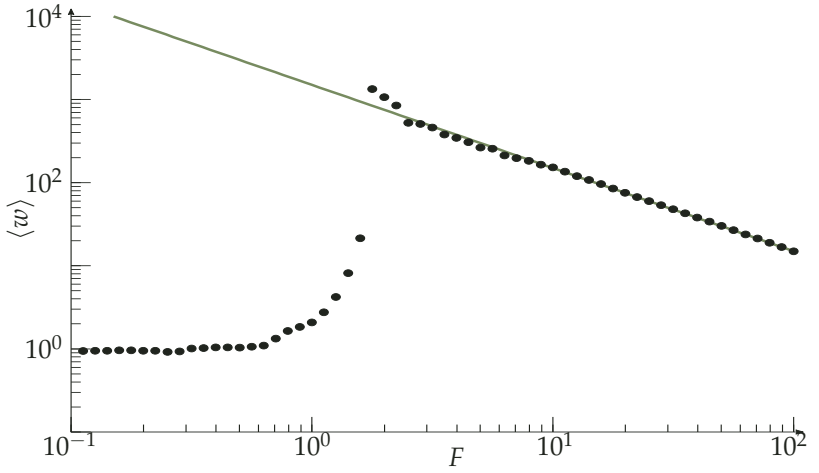

Figure 51: Time averaged width for a sample with $L = M = 512$. The time average was performed over 2^{30} time steps. The line is maximally rough at the threshold, which is consistent with a "shockwave" motion, where small segments of the line move whilst the rest is blocked. At higher forces the width reduces with the force, which could be interpreted as a decrease of the effective temperature or, analogously, an increase in the effective persistence length. The solid line is a guide to the eye showing the F^{-1} trend of the width.

The confinement splits the line into independent segments of length L_m and, therefore, one gets $F_m = F_T(L_M) - F_m m^{1/\nu_\mathfrak{z}}$. Using eq. (30) one finds $1/(\nu_\mathfrak{z}) = 2 - \zeta/\mathfrak{z}$ and, thus, the approaches are equivalent. Here, it is also clear that there will be deviations for very small $\mathfrak{z}$ when L_m exceeds L.

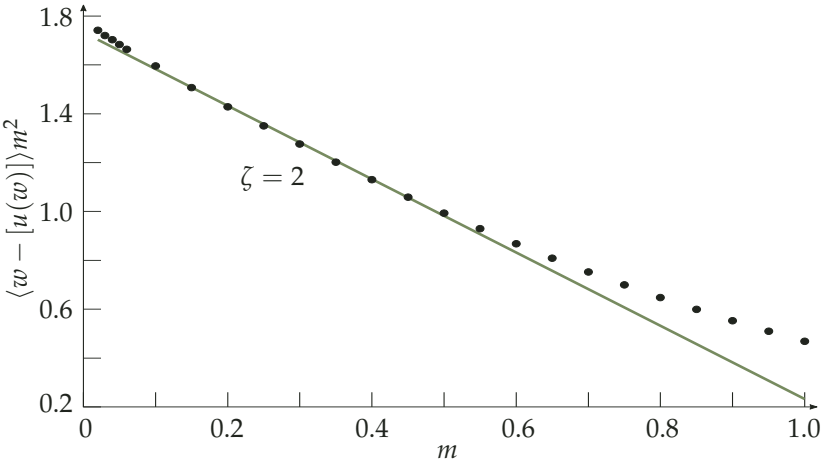

Figure 52: Time average of the net force that the parabolic potential exerts on the centre of motion of the line ($L = 256$, $M = 1024$). The solid line is a fit for $m \in [0.1,0.5]$ with $\zeta = 2$ yielding $F_T = 1.733 \pm 0.007$. The velocity of the parabolic potential was $\dot{w} = 10^{-6}$. The shape of the numerical results and their deviations from the analytical expectation resemble the findings for the DL in Ref. 107. The value $F_T = 1.733$ deviates from the value found above because of the differing system size.

As the line is constantly moved forward we chose to change the implementation of the potential. We still have a fixed amount M of potential values (knots for the cubic spline), but we update the potential "on-the-fly" as the line is moved forward. Every time a segment of the line reaches a new quarter of M, we update the quarter that has the greatest distance to the current location and compute the splines [in principle, this changes the spline at the current location of the line, but the change is negligibly small if M is large enough[131]. Our motivation for this scheme was to avoid finite-size-effects in the transverse direction and to be able to compute the disorder average as a time average. In Fig. 52 we show that our data are consistent with $\zeta \approx 2.0$.

[131] For the simulations presented here we used $M = 1024$.

Furthermore, this setup allows for a direct measurement of the effective force correlation function and hence a validation of the renormalisation group solution. This is achieved via the second cumulant of $u(t) - w(t)$ as

$$\langle (u(t) - w(t))(u(t') - w'(t')) \rangle_c m^4 \propto \Delta(w - w').$$

This contribution is closely related to the shape of the force correlation function [70], see eq. (41). The existence of a non-vanishing $\Delta'(0^+)$, often referred to as "cusp", is a sign of the non-analyticity of the correlation function. We show our results in Fig. 53, which demonstrate promising agreement with the functional renormalisation group fixed point function.

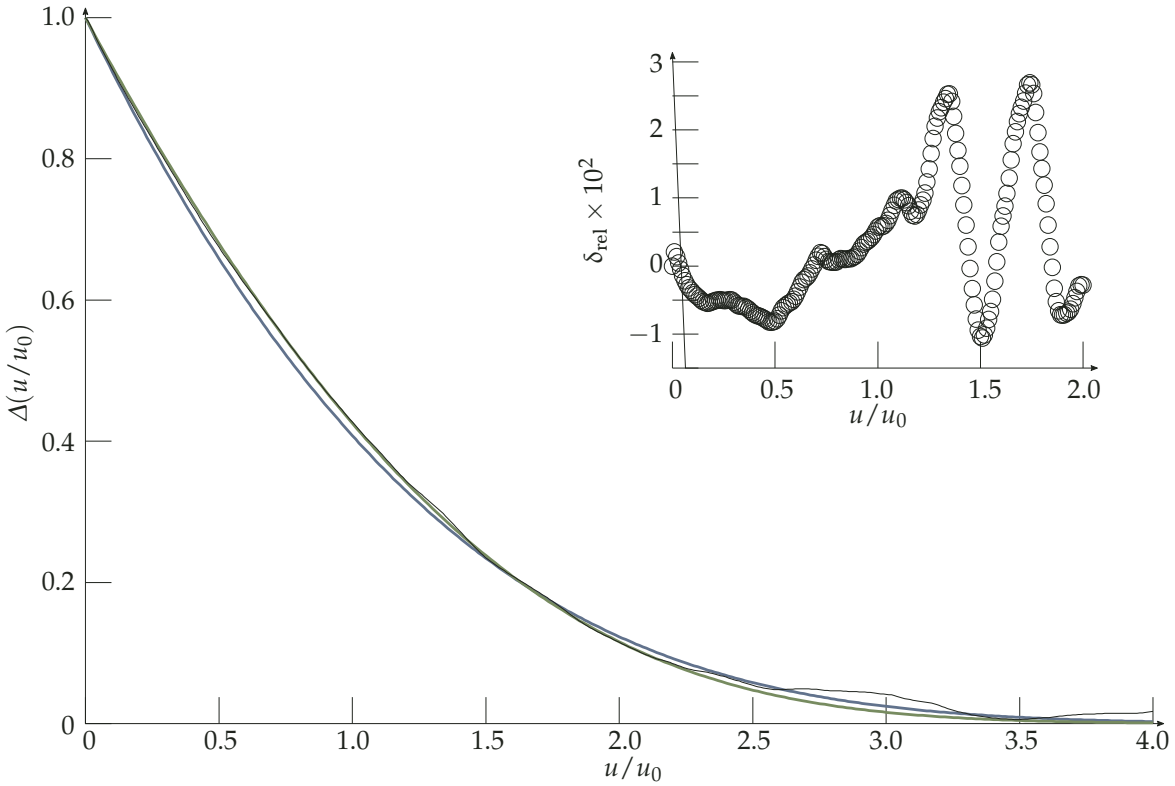

Figure 53: Numerical determination of the disorder correlator $\Delta(u)$ according to (I) with $m^2 = 10^{-2}$. The data are taken from the same simulation as for Fig. 52. The blue line is the one-loop solution and the green line is the two-loop solution, see Fig. 43 and Ref. [70]. The length scale u_0 is determined via $\int \mathrm{d}u \Delta(u/u_0) = 1$. The inset shows the relative difference between the two-loop solution Δ_{2L} and the numerically determined values Δ, i.e., $\delta_{\mathrm{rel}} = (\Delta - \Delta_{2L})/\Delta_{2L}$ for small u/u_0.

Finite temperatures – thermal rounding

The finite mean velocity at arbitrarily small non-zero temperatures is only visible for very long simulation times, Thus, the regime in which creep/TAFF behaviour should occur is not accessible for us.

The thermal rounding exponent ψ, as defined in eq. (44), can be interpreted in a slightly different way, that we feel is more apt for the interpretation of numerical data. Moving away from the threshold at $F = F_T$ and $T = 0$ the velocity scales as $(F - F_T)^\beta$ or T^ψ, respectively. Thus, a finite temperature at F_T can effectively be seen as a contribution to the pulling force with

$$F - F_T \sim T^\eta \quad \text{with} \quad \eta = \psi/\beta. \tag{48}$$

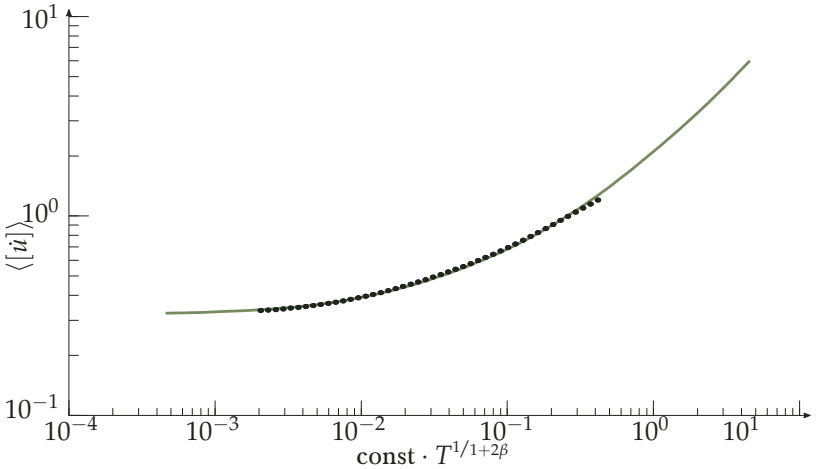

Figure 54: Time average of the velocity at the threshold force for finite temperatures. We used $\beta = 0.28$ or $\eta = 0.64$ in the rescaling of the temperature (black points). The data collapse with data for the velocity as a function of $F - F_T$ at $T = 0$ (green line) after rescaling using eq. (48). The data for the velocity as a function of $F - F_T$ at $T = 0$ and, thus, all system parameters but the temperature are the same as for Fig. 49.

Adapting our previous statements the perturbative conjecture would be $\eta = 1/(1 + 2\beta)$. In Fig. 54 we show that using this rescaling we can collapse

data for the velocity as a function of $F - F_T$ at $T = 0$ and for the velocity at the threshold $F = F_T$ as a function of temperature. The data collapse is consistent with $\eta = 1/(1 + 2\beta)$ and $\beta \approx 0.28$.

We compare our numerical results for the thermal rounding of the depinning transition for the DL and the SDL in Fig. 55. Surprisingly, we find *no* evidence for a qualitative change at a finite temperature that could be associated with the localisation transition in the static problem. This could either mean that the change is too subtle to be apparent within our numerics or that, in terms of the FRG, a finite velocity $v > 0$ implies that the relevant fixed point is one featuring $v > 0$ and $T = 0$, which would make the transition at finite temperature irrelevant for a moving line.

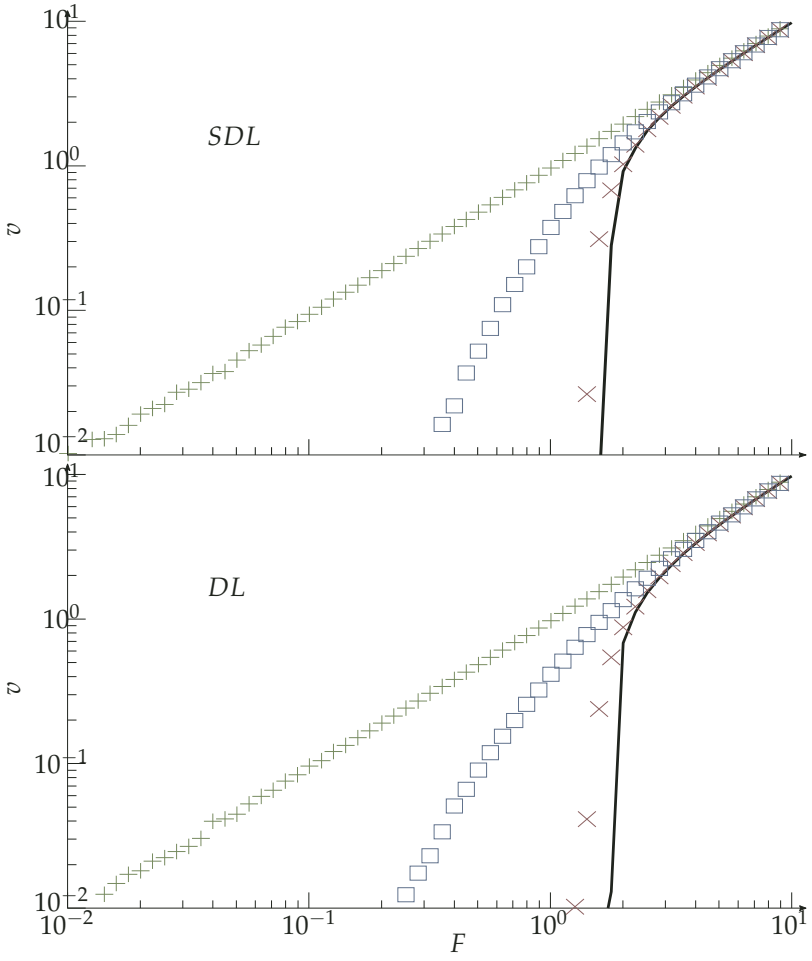

Figure 55: Velocity of the line as a function of the driving force at four different temperatures (solid line: $T = 0$). For a better comparison we show data for a SDL and a DL in the same disorder. Note that as the same disorder was used the velocities are very similar, but not identical. All system parameters but the temperature are the same as for Fig. 49.

Direct computation of threshold force – Middleton's theorems

In the study of the depinning of directed lines two important properties have been found [103]: a) the "no-passing" theorem, which states that two lines in the same disorder realisation that do not cross each other at a given time will never cross each other; b) if each segment of the line has at some point in time a non-negative velocity the velocity will remain non-negative for all times; this has been referred to as "no-return" property [148]. The no-passing theorem is believed to hold for every convex next-neighbour elastic energy. The combination of these properties allows for a fast and precise algorithm to determine the threshold force directly [143].

With regard to the no-passing theorem we consider the following situation: two lines z_1, z_2 in the same medium that touch each other at exactly one

point, that is there is one x with $z_1(x) = z_2(x)$ and $z_1(x') > z_2(x')$ for $x \neq x'$. For the DL, it follows that $v_1(x) > v_2(x)$. As both lines touch each other in x a possibly differing velocity of the two lines is due to the elastic forces. In the discrete version we then have $v_1(x) > v_2(x)$, because $(z_1(x-1) - z_2(x-1)) + (z_1(x+1) - z_2(x+1)) > 0$. This does not work for the SDL, because the difference in velocity[132] can take any value. We visualise this in Fig. 56.

Therefore, the SDL does not necessarily explore "new" regions of the disorder potential. A line that moves back and forth "knows" essentially the whole potential at any point. This could be an explanation for the two distinct correlation length exponents ν and ν_{FS} that we found for the SDL, see eq. (47). The fact that Middleton's theorems guarantee that $u(x)$ is a monotonic function of time is also used in the evaluation of ambiguous vertices within the FRG treatment in Ref. [70]. However, we feel that coming from a moving line with $v > 0$ the quasistatic depinning limit is still well defined for the SDL, because the long time limit of the roughness is (for finite L) finite and, therefore, all segments will eventually move on average with the same velocity. The agreement of the FRG with our numerical results supports that there is no fundamental problem with the applicability of the FRG for the SDL. Still, there is definitely room and need for a more rigorous analysis.

[132] This difference can be written as

$$\begin{aligned} &v_1(x) - v_2(x) \\ &= -(z_1(x-2) - z_2(x-2)) \\ &- (z_1(x+2) - z_2(x+2)) \\ &+ 4(z_1(x-1) - z_2(x-1)) \\ &+ 4(z_1(x+1) - z_2(x+1)). \end{aligned}$$

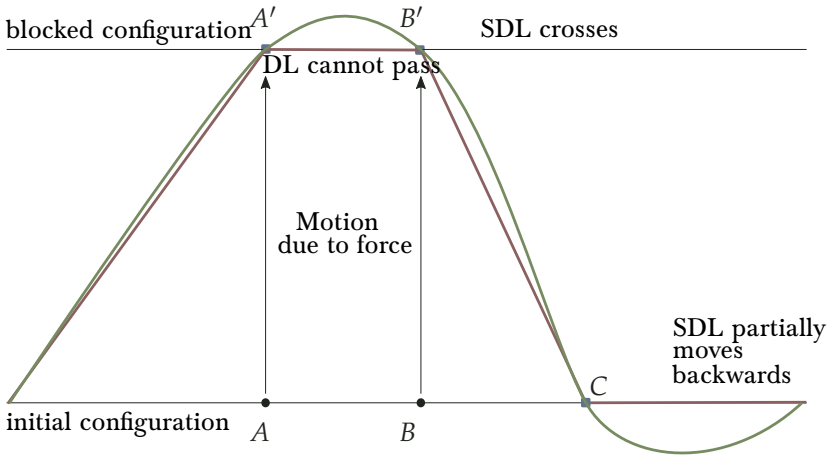

Figure 56: Cartoon exemplifying the difference in the evolution of a DL and a SDL starting from the lower horizontal conformation. Let the potential be such, that the line points at A and B are forced to move to A' and B', whereas the ends and the line point at C cannot move. The DL (red line) does not pass the blocked upper line and also does not cross the lower line. The SDL (green line) seeks to reduce the curvature and, consequently, does cross both lines.

Conclusion

We studied the depinning of SDLs from disorder (RF or RB) in $1+1$ dimensions due to a driving force. Using scaling arguments, analytical FRG calculations, and extensive numerical simulations, we characterised the critical behaviour at and around the depinning transition. Our study revealed some characteristic differences in depinning behaviour between SDLs and DLs governed by tension.

The resulting equation of motion for the SDL in disorder is equivalent to the Herring-Mullins equation for surface growth, which is governed by surface diffusion rather than surface tension, in quenched disorder. Our results also apply to semiflexible polymers with contour lengths smaller than their persistence length, which are pulled over a disordered surfaces or driven through a random medium.

We show that Middleton's theorems do not apply to SDLs. Nevertheless we find a well-defined threshold force F_T for depinning. Likewise, critical exponents characterising roughness and the dynamics of depinning can be

defined and numerically determined for the SDL as for the DL. The SDL represents an own dynamical universality class with a different set of exponents. Our extensive numerical data is best described by the set (47) of critical exponents which is also consistent with scaling relations, see section starting on page 63. We also investigated the behaviour of the SDL persistence length, which exhibits a characteristic non-monotonous force-dependence through the depinning transition (see Fig. 51).

We transferred functional renormalisation group results to the elasticity of stiff interfaces, which allows us to derive analytical results or bounds for critical exponents. We find satisfying agreement of these analytical predictions with our numerical work. Our results indirectly imply that the depinning threshold is associated with two distinct correlation length exponents ν and ν_{FS}. To our knowledge this would be the first occurrence of such behaviour in a non-periodic system. This result could be linked to the non-validity of Middleton's no-passing theorem.

Our findings for the critical exponents at the threshold force disagree in parts with previous numerical work, which suggests that further work, especially on much larger systems, might be helpful to settle these exponents.

For finite temperatures, the depinning of a SDL is an interesting problem because, at equilibrium (no pulling force), the problem features a disorder-driven localisation transition at a finite temperature. Such a transition is absent for the DL, which remains in a localised disorder-dominated phase for all temperatures. Surprisingly, the numerical results for a comparison of the thermal rounding of the force-driven depinning transition do not show any qualitative difference between DLs and SDLs, see Fig. 55. In a renormalisation group sense, this supports the notion that the force-driven depinning and the temperature-driven delocalisation are not described by the same fixed point.

Appendix

Details of the numerical FRG calculation

In this section we present the numerical solution of the FRG flow equation, following Ref. 58. We want to find the stationary solution of the two-loop flow equation (9)

$$\left.\frac{\partial R}{\partial l}\right|_{\text{two loop}} = (\varepsilon - 4\zeta)R + \zeta z R' + \frac{1}{2}R''^2 - R''R''(0) + \frac{X_\vartheta}{2}\left[R'' - R''(0)R'''^2 - R'''(O^+)^2 R''\right]$$

with the initial conditions

$$R(0) = \varepsilon \quad \text{and} \quad R'(0) = 0$$

where the former is a choice of scale and the latter is due do the inversion symmetry mentioned in main text. As before we omit arguments of the functions whenever unambiguously possible. Expanding in a way that already incorporates the elasticity dependence

$$R = \varepsilon R_1 + \varepsilon^2 X_\vartheta R_2 + \mathcal{O}(\varepsilon^3) \quad \text{and} \quad \zeta = \varepsilon\zeta_1 + \varepsilon^2 X_\vartheta \zeta_2 + \mathcal{O}(\varepsilon^3)$$

we find

$$0 = (1 - 4\zeta_1)R_1 + \zeta_1 z R_1' + \frac{1}{2}R_1'' - R_1''R_1''(0)$$
$$0 = R_2 - 4\zeta_2 R_1 - 4\zeta_1 R_2 + \zeta_2 z R_1 + \zeta_1 z R_2 + R_1''R_2'' - R_1''(0)R_2'' - R_1''R_2''(0) + (R_1'' - R_1''(0))R_1'''^2 - R_1''R_1'''(0^+)^2$$

with initial conditions $R_1(0) = 1$, $R_1'(0) = 0$, $R_2(0) = 0$ and $R_2'(0) = 0$. This system of equations has to be solved in order, that is R_1 as a solution of the first equation is needed to solve the second equation for R_2. The dependence on the values of the derivatives at zero impedes a solution by direct integration starting from zero. We therefore expand again, this time in z,

$$R_1 = 1 + \sum_{i=2}^{\infty} a_i z^i \quad \text{and} \quad R_2 = \sum_{i=2}^{\infty} b_1 z^i.$$

The expansion coefficients are given by the equations

$$0 = (1 - 4\zeta_1)a_i + \zeta_1 i a_i + \frac{1}{2}\sum_{k=0}^{i}\left((i-k+2)(i-k+1)(k+2)(k+1)a_{n-k+2}a_{k+2}\right) - 2(i+2)(i+1)a_{i+2}a_2 = g_1(i)$$

$$\begin{aligned}
0 = {} & (1 - 4\zeta_1)b_i - 4\zeta_2 a_i + \zeta_2 i a_i + \zeta_1 i b_i + \sum_{k=0}^{i}\left[(n-k+2)(n-k+1)(k+1)(k+2)a_{n-k+2}b_{k+2}\right] \\
& - 2(i+2)(i+1)(a_{i+2}b_2 + a_2 b_{i+2}) \\
& + \frac{1}{2}\sum_{k=0}^{i}\left[\sum_{l=0}^{i-k}(i-k-l+3)(i-k-l+2)(i-k-l+1)(l+3)(l+2)(l+1)a_{n-k-l+3}a_{l+3}\right](k+2)(k+1)a_{k+2} \\
& - a_2\sum_{k=0}^{i}(i-k+3)(i-k+2)(i-k+1)(k+3)(k+2)(k+1)a_{n-k+3}a_{k+3} - 18(i+2)(i+1)a_3 a_3 a_{i+2} = g_2(i).
\end{aligned}$$

Here, a_{i+1} (b_{i+1}) is in general inferred from $g_{1(2)}(i) = 0$, with the exception of a_2 (b_2) that is fixed by $g_{1(2)}(0) = 0$.

The solution of this is

$$\begin{aligned}R_1(z) = 1 &- 0.288797z^2 + 0.0967487z^3 - 0.0109959z^4 + 0.000197282z^5 + 0.0000162077z^6 + 1.37054\cdot 10^{-6}z^7\\ &+ 1.06127\cdot 10^{-7}z^8 + 5.84538\cdot 10^{-9}z^9 - 1.50021\cdot 10^{-10}z^{10} - 1.19821\cdot 10^{-10}z^{11} - 2.52931\cdot 10^{-11}z^{12}\\ &- 3.93584\cdot 10^{-12}z^{13} - 4.90717\cdot 10^{-13}z^{14} - 4.49155\cdot 10^{-14}z^{15} - 1.21758\cdot 10^{-15}z^{16} + 6.7758\cdot 10^{-16}z^{17}\\ &+ 2.11465\cdot 10^{-16}z^{18} + 4.19348\cdot 10^{-17}z^{19} + 6.49483\cdot 10^{-18}z^{20} + 7.78044\cdot 10^{-19}z^{21} + 5.52691\cdot 10^{-20}z^{22}\\ &- 4.37559\cdot 10^{-21}z^{23} - 2.72231\cdot 10^{-21}z^{24} - 6.74332\cdot 10^{-22}z^{25} - 1.23417\cdot 10^{-22}z^{26} - 1.77913\cdot 10^{-23}z^{27}\\ &- 1.83328\cdot 10^{-24}z^{28} - 4.51243\cdot 10^{-26}z^{29} + 3.86106\cdot 10^{-26}z^{30} + \mathcal{O}(z^{31})\end{aligned}$$

and for the two-loop contribution

$$\begin{aligned}R_2(z) = &-0.060496z^2 + 0.034528z^3 - 0.00628098z^4 + 0.000239627z^5 + 0.0000198228z^6 + 1.42201\cdot 10^{-6}z^7\\ &+ 5.17932\cdot 10^{-8}z^8 - 8.64457\cdot 10^{-9}z^9 - 2.72753\cdot 10^{-9}z^{10} - 4.78603\cdot 10^{-10}z^{11} - 6.23523\cdot 10^{-11}z^{12}\\ &- 5.49529\cdot 10^{-12}z^{13} - 8.77227\cdot 10^{-15}z^{14} + 1.30233\cdot 10^{-13}z^{15} + 3.60567\cdot 10^{-14}z^{16} + 6.72385\cdot 10^{-15}z^{17}\\ &+ 9.51287\cdot 10^{-16}z^{18} + 9.0609\cdot 10^{-17}z^{19} - 9.09186\cdot 10^{-20}z^{20} - 2.59564\cdot 10^{-18}z^{21} - 7.67912\cdot 10^{-19}z^{22}\\ &- 1.53921\cdot 10^{-19}z^{23} - 2.36567\cdot 10^{-20}z^{24} - 2.56697\cdot 10^{-21}z^{25} - 6.75627\cdot 10^{-23}z^{26} + 5.76328\cdot 10^{-23}z^{27}\\ &+ 1.98332\cdot 10^{-23}z^{28} + 4.34841\cdot 10^{-24}z^{29} + 7.31116\cdot 10^{-25}z^{30} + \mathcal{O}(z^{31}).\end{aligned}$$

The reproduced solutions are already for the best values for ζ_1, ζ_2. The proper process is the following: starting from a "guessed" pair ζ_1,ζ_2 we find the solution for the Taylor expansion and then we determine $R_{1,2}(z_{init})$ and $R'_{1,2}(z_{init})$ as well as the needed values $R''_1(0)$, $R''_2(0)$ and $R'''_1(0)$ and integrate the flow equations from $z_{init} = 0.5$ to $z_{max} = 25$. We are looking for an exponentially fast decaying solution that has no roots on the real axis. This turns out to fix $\zeta_{1,2}$ to the lowest value for which $R_{1,2}$ does not pass through zero. In this way we reproduce the values of Ref. 58 which are

$$\zeta_1 = 0.20829804 \quad \text{and} \quad \zeta_2 = 0.006858.$$

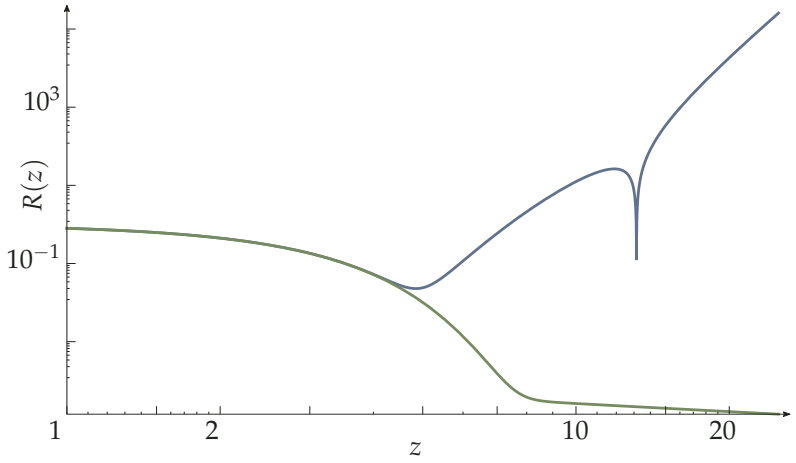

Figure 57: Log-log plot of the found solution for $d = 0.84$. The blue line is the approximative solution by a Taylor expansion which coincides with the solution found by integration (green line) pretty well up to $z \approx 5$. This is more than sufficient as we only evaluate it at $z = 0$ and $z = 0.5$. The actual solution decays fast to zero (the tail looks algebraic in this presentation, which is due to the finite precision in ζ).

For $d \neq 1$ the numerical scheme is completely analogous, but starting from the generalised equations[71] derived assuming a spherical symmetry of $R(\boldsymbol{z}) = R(z)$. Here, we only use the elasticity-independent one-loop contributions

$$\left.\frac{\partial R}{\partial l}\right|_{\text{one loop}} = (\varepsilon - 4\zeta)R + \zeta z R' + \frac{1}{2}R''^2 - R''R''(0) + \frac{d-1}{2}\frac{R'}{z}\left(\frac{R'}{z} - 2R''(0)\right).$$

However, this equation does not allow for an iterative determination of the expansion coefficients and we have to solve the full linear system, which substantially increases the numerical effort needed and we limit ourselves to the order $\mathcal{O}(z^{12})$ and lower. For $d = 0.84$ we find in the same manner as before $\zeta = 0.21421\varepsilon \approx \zeta_{th}$ and for the Taylor expansion of the correlator

$$\begin{aligned}R_{d=0.84} = 1 &- 0.291915z^2 + 0.0982641z^3 - 0.0112128z^4 + 0.000200887z^5 + 0.000016632z^6 + 1.41913\cdot 10^{-6}z^7\\ &+ 1.11177\cdot 10^{-7}z^8 + 6.26618\cdot 10^{-9}z^9 - 1.35554\cdot 10^{-10}z^{10} - 1.24135\cdot 10^{-10}z^{11} + \mathcal{O}(z^{12})\end{aligned}$$

This approximate solution and the one found by numerical integration are shown in Fig. 57.

Derrida-Flyvbjerg-Singularities

We consider a simple random iterative process[83] (also illustrated in Fig. 58: Starting with an initial length (for simplicity we choose unity) we select in each time step a fragmentation point (using a given (up to rescaling) fixed distribution), keep everything left from it as the nth segment W_n and continue with the other part for the next step. This way we create a series of segments W_i whose properties are solely determined by the underlying statistics of the fragmentation point. We want to characterise the distribution of segments by the distribution of the largest segment w_1, the second largest segment w_2 (which for obvious reasons cannot be larger than one half) and the information entropy $s = -\sum_i W_i \ln W_i$.

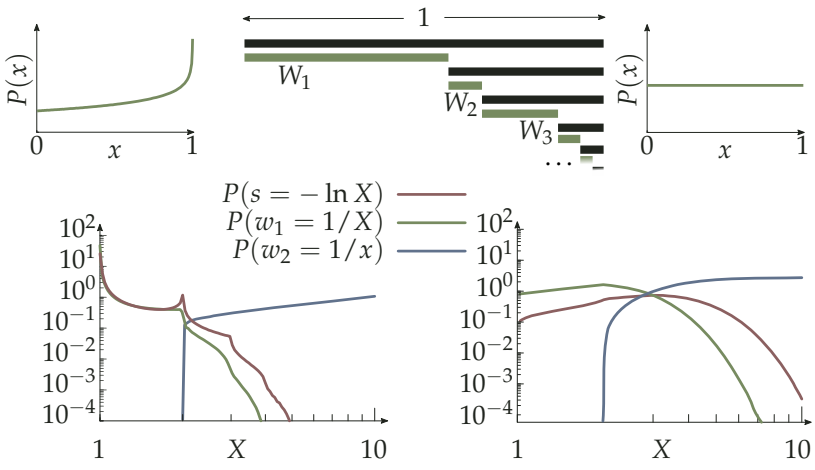

Figure 58: Derrida-Flyvbjerg-Singularities in a simple fragmentation process. The process is outlined in the upper middle. The interval of length 1 is iteratively fragmented. In each step the fragmentation point $x_i L$ for the remaining length L is randomly chosen using a fixed distribution $P(x)$. On the right side the results for a flat distribution are shown featuring hardly visible singularities. Once large steps are favoured as shown on the left side these singularities become more pronounced. The three curves depict the probability distributions for the entropy s of the fragmentation sequence, the largest segment w_1 and the second largest segment w_2 in a way that the singularities occur at integer values of X. To infer the probability distributions in satisfying quality 10^9 single realisations of the process have been performed.

If we choose a flat fragmentation point distribution (right part of Fig. 58) these characteristics appear as exciting as one would suspect given the glamorous nature of the process considered here. However, there is a non-trivial feature, the so-called Derrida-Flyvbjerg singularities, appearing for fragmentation point distributions that favour drastically uneven fragmentation (left part of Fig. 58). Then, the probability of finding a largest segment w_1 with length $1/X$ becomes dependent of the number of segments X of this length that fit into unity, because X segments of roughly the same length are the realisation that allows for the biggest fragmentation steps. Thus, there is a kink in the distribution whenever X passes an integer value. This is also resembled in the distribution of the information entropy.

In the main text we consider the "fragmentation" of the total probability. The existence of Derrida-Flyvbjerg singularities in the disordered phase is evidence that this fragmentation of the probability is of the latter kind. Physically, this is because of a free energy landscape whose valleys have significantly differing heights.

Multifractal measures

We can introduce the concept of a multifractal measure with a process similar to the process before. However, here we will take a more geometrical perspective. This is meant to serve as evidence that multifractal properties arise in very simple processes. Again we consider a fixed quantity of value 1 (the total probability), which is given by a measure on a given interval, say $0 \leq x \leq 1$. Now, we halve this interval and weight the left half by $1 - \delta$ and the right half by $1 + \delta$, and continue this on the created segments, see Fig. 59. After a sufficient number of iterations this creates a very ragged measure, the binomial multifractal measure[86, 87], which we could consider to be a simple measure on a complex, fractal geometry. However, if we try to quantitatively describe this geometry by means of say a fractal geometry, we notice that different moments of this measure (or distribution) are dominated by subsets of the fractal landscape that have different geometry.

This perspective perceives non-trivial distributions as measures of strange sets[87] and its moment as a tool to explore different fractal subsets. Each of this fractal subsets has a fractal dimension, which leads to the introduction of generalised dimensions (as introduced in the main text) or their Legendre transform, the singularity spectrum, respectively, see Fig. 59 (bottom).

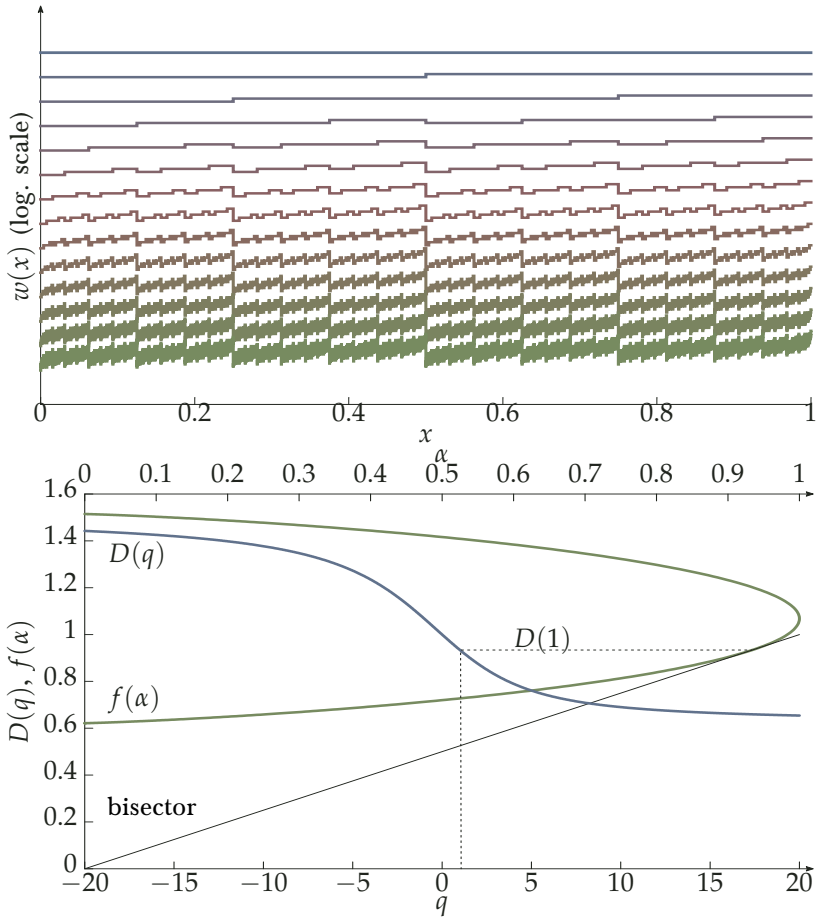

Figure 59: Top: The generation of the binomial multifractal measure. In each time step (from top to bottom, shifted for clarity) the measure on each "segment" is redistributed with unequal weight to its right and left half. This simple process can be very efficiently calculated as the weight of each segment is given by the number of zeros in the binary representation of its index and creates a multifractal measure, due to the different geometry of contributions of various heights (for $q \to \infty$ large contributions dominate the moments, whereas for $q \to -\infty$ small contributions dominate). The figure shows the measure up to time-step $n = 13$ on a logarithmic scale. Bottom: Generalised Dimensions $D(q)$ and singularity spectrum $f(\alpha)$ (q is shown on the lower, α on the upper horizontal axis) as introduced in the main text for the binomial multifractal measure at time-step $n = 24$. We also included the bisector which touches the singularity spectrum at $D(1)$ due to relation of the spectrum and the generalised dimensions via Legendre transform, see main text.

The Herring-Mullins equation

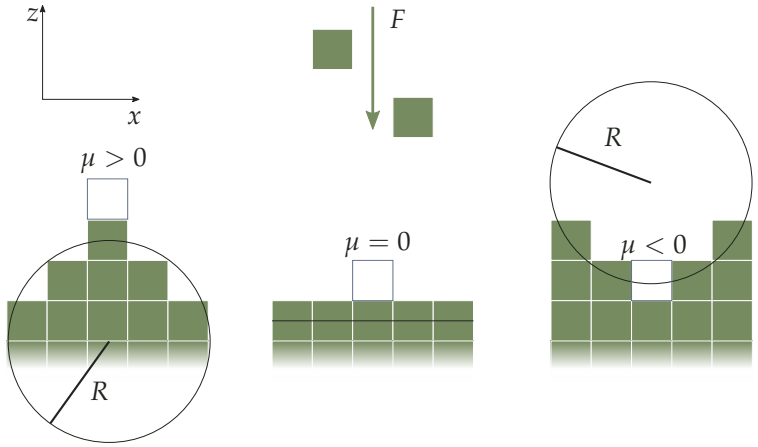

Figure 60: Sketch to elucidate the relation between the chemical potential and the local surface curvature as indicated by the best fitting circle (the discrete analogon of an osculating circle). The figure shows the three possible scenarios in $1+1$ dimensions (the adsorption site under consideration is the hollow square), which are from left to right: a concave surface (negative curvature), a flat surface (zero curvature) and a convex surface (positive curvature). It is clear that adsorption at sites with positive local curvature, i.e. in "valleys"a, leads to high coordination numbers and is thus favourable, corresponding to a negative chemical potential. Adsorption onto a site with negative local curvature is unfavourable, as surface diffusion in any direction would lead to higher coordination number, hence $\mu > 0$ here. A flat surface is translationally invariant and no site is distinguished, thus $\mu = 0$. Additionally shown is the deterministic deposition flux F, leading to surface growing in positive z-direction. This figure is adapted from Ref. 50.

We briefly derive the Herring-Mullins-equation[114, 115] in the context of surface growth. Without external deposition the evolution of an interface $h(x,t)$ is governed by mass conservation or the continuity equation

$$\frac{\partial h}{\partial t} = -\nabla \cdot \boldsymbol{j}.$$

We consider an interface with *surface diffusion*, that is a mass element in the uppermost layer is mobile and free to explore other sites. The long-time statistics will be given by the thermodynamical equilibrium distribution, that is by the chemical potential μ to adsorb at the respective site, thus the flux is

given by *Fick's law*

$$j \propto -\nabla\mu.$$

The chemical potential for adsorption is governed by the local geometry, see Fig. 60. Adsorption is favourable in regions where the interface has a negative local curvature as an adsorbed element here would have a high number of near neighbours. The simplest way to account for this, is to identify (up to factors) the chemical potential with the curvature

$$\mu \propto -\nabla^2 h.$$

Combining these three equations gives the Herring-Mullins equation for an interface with surface diffusion

$$\frac{\partial h}{\partial t} = -\nabla^4 h$$

where (stochastic or deterministic) deposition terms are easily added. The Herring-Mullins universality class is characterised by its thermal exponents $\zeta = 3/2$, $z = 4$. One important class of systems that is believed to be described by this equation is the growth of tumours[122], which has been rationalised by the observation of surface diffusion of tumour cells[149].

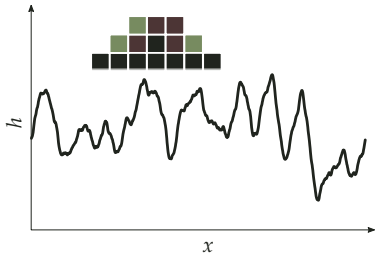

Figure 61: Height profile of an interface grown using a solid-on-solid random deposition model that is within the Herring-Mullins universality class. The model is sketched in the upper part: in each time-step one site is chosen and its height is increased or decreased $h_i \to h_i \pm 1$. Here, we do not restrict the slopes, as in Fig. 10, but the curvature. This allows for adsorption on the green sites and desorption from the red sites in the sketch.

Details of the FRG calculation in the dynamic case

(Functional) renormalisation is a technique for statistical systems as in the static case where we computed the partition function, which allowed us to determine order by order the feedback to the disorder correlator. In the dynamic case we have a (stochastic) equation of motion. However, we can employ the so-called Martin-Siggia-Rose[150] formalism to transfer the problem from a equation of motion into a statistical system that is closer to the static case.

We start from the equation of motion, which for the SDL in $1+1$ dimensions can be written as

$$0 = \partial_t u + \partial_x^4 u - \eta - F - \tau$$

where we remind ourselves that η is the (quenched) random disorder force and τ is the (thermally fluctuating) random thermal force. The key idea is now to recognise that we are little interested in individual solutions of this equation of motion per se, but in *averaged* observables measured along a solution, that is

$$\overline{X}_T = \overline{\int \mathcal{D}u\, X \delta(\partial_t u + \partial_x^4 u - \eta - F - \tau)}_T$$

where the T-subscripted over-line shall indicate averaging over realisations of η and τ. The delta-function guarantees that we only consider actual solutions, but operating with delta-functions tends to be rather cumbersome, which is why we expand the delta-function introducing an auxiliary field h

$$\overline{X}_T = \overline{\iint \mathcal{D}u\mathcal{D}h\, \mathcal{X}\, \mathrm{e}^{-\mathrm{i}\iint \mathrm{d}t\mathrm{d}x\, h(\partial_t u + \partial_x^4 u - \eta - F - \tau)}}_T.$$

We perform the average using that the forces are Gaussian with zero mean and known correlators[133] yielding

$$\overline{\mathcal{X}}_T = \iint \mathcal{D}u\mathcal{D}h\, \mathcal{X}\, \mathrm{e}^{-\mathcal{S}}$$

with the *averaged dynamical action* $\mathcal{S}[u,h]$

$$\mathcal{S} = \mathrm{i}\iint \mathrm{d}t\mathrm{d}x\, h(\partial_t u + \partial_x^4 u - F) - T\iint \mathrm{d}t\mathrm{d}x\, h^2 - \frac{1}{2}\iiint \mathrm{d}t\mathrm{d}t'\mathrm{d}x\, h(x,t)h(x,t')\Delta(u(x,t) - u(x,t')).$$

[133] As a quick reminder

$$\overline{\eta(x,u)\eta(x',u')} = \Delta(u-u')\delta(x-x')$$

$$\langle \tau(x,t)\tau(x',t')\rangle_T = 2T\delta(x-x')\delta(t-t').$$

This dynamical action plays the same essential role for the computation of averages as the reduced energy βH and is the starting point for the renormalisation programme. We do not reproduce the diagrammatics of Ref. [70] here, but simply give the resulting stationary flow-equation to two-loop order

$$0 = (\varepsilon - 2\zeta)\Delta + \zeta u \Delta' - \frac{1}{2}\left[(\Delta - \Delta(0))^2\right]'' + \frac{X_\vartheta}{2}\left[([\Delta - \Delta(0)]\Delta'^2)'' + \Delta'(0^+)^2\Delta''\right].$$

or with $\Delta(u) = R''(u)$

$$\left.\frac{\partial R}{\partial l}\right|_{\text{two loop}} = (\varepsilon - 4\zeta)R + \zeta z R' + \frac{1}{2}R''^2 - R''R''(0) + \frac{X_\vartheta}{2}\left[R'' - R''(0)R'''^2 + R'''(O^+)^2 R''\right]$$

where the only difference to the static equation, eq. (9) is the sign of the $R'''(0^+)$-term, which is the only difference between the static and the quasi-static ($v \to 0^+$) formulation. It is this sign that breaks the *potentiality*, that is the solutions R are not exponentially fast decaying (as in the statics, which corresponds to $\int \Delta = 0$), but show random-force behaviour $R(u) \propto |u|$ ($\int \Delta = \text{const} \neq 0$) at large u due to the motion of the line. Integrating the full flow equation we find

$$\partial_l \int \Delta = (\varepsilon - 3\zeta)\int \Delta - X_\vartheta \Delta'(0^+)^3.$$

To one-loop order, $X = 0$, this implies that the flow for $\int \Delta$ is easily fixed by $\zeta = \varepsilon/3$ (the random force solution) or $\int \Delta = 0$ (the static random potential solution). To two loops we can expand Δ and ζ in powers of ε and find that we can write the latter as

$$\zeta = \frac{\varepsilon}{3} - \frac{X_\vartheta \Delta_1'(0^+)^3}{3\int \Delta_1},$$

where Δ_1 is the one-loop solution. The one-loop solution can be found analytically (as we know the roughness exactly), which has been done in Refs. [70, 104].

Bounds for the dynamical exponent z

In Ref. [70] the dynamical exponent z has been found to be to two-loop order

$$z = 4 - 2/9\varepsilon + \varepsilon^2\left(\frac{\zeta_2}{3} - \frac{2X_\vartheta}{27} + \frac{Y_\vartheta}{54}\right)$$

with ζ_2, $X^{(2\vartheta)}$ the same as in the main text and

$$Y_\vartheta = X_\vartheta + \varepsilon\left(\frac{2I_\eta}{(\varepsilon I_1)^2} - \frac{1}{\varepsilon}\right),$$

where we use I_η as shorthand notation for the aforementioned correction to friction for the SDL

$$I_\eta = I_\eta^{(4)} = \int_{q_1,q_2} \frac{1}{\left(q_1^2 + m^2\right)^2 \left(q_2^2 + m^2\right)^4} \frac{1}{\left(\left(q_2^2 + m^2\right)^2 + \left(\left(\boldsymbol{q}_1 - \boldsymbol{q}_2\right)^2 + m^2\right)^2\right)}$$

and I_1 is the one-loop integral given by

$$I_1 = m^{-\varepsilon}\frac{\Gamma(\varepsilon/2)}{\Gamma(4)}\left(\int_q \mathrm{e}^{-q^2}\right).$$

Using $I_\eta \geq 0$ we find the lower bound

$$z \geq 1.8607.$$

For an upper bound we note that in any dimension (any value of ε) the following inequality holds ($\boldsymbol{q}_3 = \boldsymbol{q}_1 - \boldsymbol{q}_2$)

$$I_\eta \leq J_\eta = \int_{q_1,q_2} \frac{1}{(q_1^2 + m^2)^2 (q_2^2 + m^2)^4 (q_3^2 + m^2)^2}$$

and J_η can be evaluated to leading order in ε via Laplace transforms[134]

$$J_\eta = \frac{1}{\Gamma(4)} \int\limits_{\substack{s_1,s_2,s_3>0\\ q_1,q_2}} s_1 s_2^3 s_3 \mathrm{e}^{-s_1(q_1^2+m^2)-s_2(q_2^2+m^2)-s_3(q_3^2+m^2)}$$
$$= \frac{\left(\int_q \mathrm{e}^{-q^2}\right)^2}{\Gamma(4)} \int\limits_{s_1,s_2,s_3>0} \frac{s_1 s_2^3 s_3 \mathrm{e}^{-m^2(s_1+s_2+s_3)}}{(s_1s_2+s_1s_3+s_2s_3)^{D/2}}$$

Substituting $s_2 \to s_1 s_2$, $s_3 \to s_1 s_3$ gives

$$J_\eta = \frac{\left(\int_q \mathrm{e}^{-q^2}\right)^2}{\Gamma(4)} \int\limits_{s_1,s_2,s_3>0} \frac{s_1^{7-D} s_2^3 s_3 \mathrm{e}^{-m^2 s_1(1+s_2+s_3)}}{(s_2+s_3+s_2s_3)^{D/2}}$$
$$= \frac{\left(\int_q \mathrm{e}^{-q^2}\right)^2}{\Gamma(4)} \Gamma(\varepsilon) m^{-2\varepsilon} \int\limits_{s_2,s_3>0} \frac{s_2^3 s_3}{(s_2+s_3+s_2s_3)^{D/2}} \frac{1}{(1+s_2+s_3)^\varepsilon} = \frac{\left(\int_q \mathrm{e}^{-q^2}\right)^2}{\Gamma(4)} \Gamma(\varepsilon) m^{-2\varepsilon} J$$

$$J = \int\limits_{s_2,s_3>0} \frac{s_2^3 s_3}{(s_2+s_3+s_2s_3)^4} \frac{(s_2+s_3+s_2s_3)^{\varepsilon/2}}{(1+s_2+s_3)^\varepsilon} = \int\limits_{s_2,s_3>0} \frac{s_2 s_3}{(1+s_3+s_2s_3)^4} \frac{s_2^{\varepsilon/2}(1+s_3+s_2s_3)^{\varepsilon/2}}{(1+s_2+s_2s_3)^\varepsilon} = J_1 + J_2 + J_3$$

In the second to last step we substituted $s_3 \to s_2 s_3$. We have divided the integration in three terms to isolate the (important) divergent part.

$$J_1 = \int_1^\infty \mathrm{d}s_2 \int_0^\infty \mathrm{d}s_3 \frac{s_2 s_3}{(1+s_3+s_2s_3)^4} \frac{s_2^{\varepsilon/2}(1+s_3+s_2s_3)^{\varepsilon/2}}{(1+s_2+s_2s_3)^\varepsilon} = -\frac{1}{12} + \frac{\ln 2}{6} + \mathcal{O}(\varepsilon)$$
$$J_2 = \int_0^\infty \mathrm{d}s_3 \int_0^1 \mathrm{d}s_2 \left[\frac{s_2 s_3}{(1+s_3+s_2s_3)^4} \frac{s_2^{\varepsilon/2}(1+s_3+s_2s_3)^{\varepsilon/2}}{(1+s_2+s_2s_3)^\varepsilon} - \frac{s_2^{1+\varepsilon/2} s_3}{(1+s_2s_3)^{4+\varepsilon/2}}\right] = -\frac{1}{12} - \frac{\ln 4}{6} + \mathcal{O}(\varepsilon)$$
$$J_3 = \int_0^\infty \mathrm{d}s_3 \int_0^1 \mathrm{d}s_2 \frac{s_2^{1+\varepsilon/2} s_3}{(1+s_2s_3)^{4+\varepsilon/2}} = \frac{1}{3\varepsilon} - \frac{5}{18}$$

Thus collecting all terms we find

$$J_\eta = \frac{\left(\int_q \mathrm{e}^{-q^2}\right)^2}{\Gamma(4)} \Gamma(\varepsilon) m^{-2\varepsilon} (J_1+J_2+J_3) = \frac{6}{4}(J_1+J_2+J_3)(\varepsilon I_1)^2$$

and

$$Y_4 \leq X_4 + \varepsilon\left(\frac{2J_\eta}{(\varepsilon I_1)^2} - \frac{1}{\varepsilon}\right) \leq -\frac{1}{6} + \mathcal{O}(\varepsilon),$$

which ultimately yields

$$z \leq 2.76811,$$

i.e., eq. (39) in the main text (page 66).

[134] A different approach leading to the same integrals would be to Laplace transform the original integral

$$I_\eta = \int\limits_{\substack{s_1,s_3>0\\ q_1,q_2}} \frac{s_1 \sin\left((q_2^2+m^2)s_3\right)}{(q_2^2+m^2)^5} \times \mathrm{e}^{-s_1(q_1^2+m^2)}\, \mathrm{e}^{-s_3(q_3^2+m^2)}$$
$$\leq \int\limits_{\substack{s_1,s_3>0\\ q_1,q_2}} \frac{s_1 s_3}{(q_2^2+m^2)^4} \times \mathrm{e}^{-s_1(q_1^2+m^2)}\, \mathrm{e}^{-s_3(q_3^2+m^2)}$$
$$= \frac{1}{\Gamma(4)} \int\limits_{\substack{s_1,s_2,s_3>0\\ q_1,q_2}} s_1 s_2^3 s_3 \times \mathrm{e}^{-s_1(q_1^2+m^2)-s_2(q_2^2+m^2)-s_3(q_3^2+m^2)}$$

Bibliography

[1] Boltz, H.-H. and Kierfeld, J. (2012). *Phys. Rev. E*, **86**:060102(R)

[2] Boltz, H.-H. and Kierfeld, J. (2013). *Phys. Rev. E*, **88**:012103

[3] Boltz, H.-H. and Kierfeld, J. (2014). *Phys. Rev. E*, **90**(1):012101

[4] Boltz, H.-H. (2011). *Semiflexible Polymere in ungeordneten Potentialen*. Diplomarbeit, TU Dortmund

[5] Jenkins, A. et al. (1996). *Pure and applied chemistry*, **68**(12):2287–2311

[6] Chaikin, P. M. and Lubensky, T. C. (2000). *Principles of condensed matter physics*, Vol. 1. Cambridge University Press

[7] Deserno, M. *Notes on differential geometry with special emphasis on surfaces in* $\mathbb{R}^3$. as of writing available under `http://www.cmu.edu/biolphys/deserno/pdf/diff_geom.pdf`

[8] Mandelbrot, B. B. (1985). *Physica Scripta*, **32**(4):257

[9] Landau, L. and Lifshitz, E. (1986). *Theory of Elasticity*, Vol. 7. Pergamon, New York

[10] Harris, R. and Hearst, J. (1966). *J. Chem. Phys.*, **44**:2595

[11] Kratky, O. and Porod, G. (1949). *Recl. Trav. Chim. Pays-Bas*, **68**:1106

[12] Kleinert, H. (2006). *Path Integrals in Quantum Mechanics, Statistics, Polymer Physics, and Financial Markets*. World Scientific, Singapore

[13] Dua, A. and Vilgis, T. (2004). *J. Chem. Phys.*, **121**:5505

[14] Käs, J. et al. (1996). *Biophysical journal*, **70**(2):609

[15] Kirchhoff, G. (1897). *Vorlesungen über Mechanik*, Vol. 1. BG Teubner

[16] Gutjahr, P., Lipowsky, R. and Kierfeld, J. (2006). *Europhys. Lett.*, **76**:994

[17] Kierfeld, J. et al. (2008). In Garay, O. J., Garciá-Rió, E. and Vázquez-Lorenzo, R. (Hg.), *AIP Conference Proceedings*, Vol. 1002, 151

[18] Bundschuh, R., Lässig, M. and Lipowsky, R. (2000). *Eur. Phys. J. E*, **3**:295

[19] Kierfeld, J. and Lipowsky, R. (2005). *J. Phys. A*, **38**:L155

[20] Fisher, M. (1984). *J. Stat. Phys.*, **34**:667

[21] Gompper, G. and Burkhardt, T. (1989). *Phys. Rev. A*, **40**:6124

[22] Roberts-Austen, W. C. and Neville, F. H. (1911). In *Encyclopaedia Britannica Eleventh Edition*. Article: Alloys

[23] Wang, X., Havlin, S. and Schwartz, M. (2000). *J. Phys. Chem. B*, **104**:3875

[24] Halpin-Healy, T. and Zhang, Y.-C. (1995). *Phys. Rep.*, **254**(4)

[25] Kardar, M., Parisi, G. and Zhang, Y. (1986). *Phys. Rev. Lett.*, **56**:889

[26] Corwin, I. (2012). *Random Matrices: Theory and Applications*, **01**(01):1130001

[27] Hairer, M. (2011). *arXiv preprint arXiv:1109.6811*

[28] Krug, J. (1997). *Adv. Phys.*, **46**:139

[29] Blatter, G. et al. (1994). *Rev. Mod. Phys.*, **66**:1125–1388

[30] Nattermann, T. and Scheidl, S. (2000). *Adv. Phys.*, **49**:607

[31] Imbrie, J. and Spencer, T. (1988). *J. Stat. Phys.*, **52**:609

[32] Kim, J. M. and Kosterlitz, J. (1989). *Phys. Rev. Lett.*, **62**(19):2289

[33] Derrida, B. and Golinelli, O. (1990). *Phys. Rev. A*, **41**:4160

[34] Kim, J., Bray, A. and Moore, M. (1991). *Phys. Rev. A*, 44:R4782
[35] Kim, J., Moore, M. and Bray, A. (1991). *Phys. Rev. A*, 44:2345
[36] Monthus, C. and Garel, T. (2006). *Eur. Phys. J. B*, 53:39
[37] Monthus, C. and Garel, T. (2006). *Phys. Rev. E*, 74:011101
[38] Monthus, C. and Garel, T. (2006). *Phys. Rev. E*, 74:051109
[39] Monthus, C. and Garel, T. (2007). *Phys. Rev. E*, 75:051122
[40] Monthus, C. and Garel, T. (2007). *J. Stat. Mech.: Theory Exp.*, P03011
[41] Monthus, C. and Garel, T. (2007). *Markov Processes Relat. Fields*, 13:731
[42] Monthus, C. and Garel, T. (2008). *J. Stat. Mech.: Theory Exp.*, P01008
[43] Schwartz, M. and Perlsman, E. (2012). *Phys. Rev. E*, 85:050103(R)
[44] Mezard, M. (1990). *J. Phys. France*, 51:1831
[45] Mukherji, S. (1994). *Phys. Rev. E*, 50:R2407
[46] Comets, F., Shiga, T. and Yoshida, N. (2003). *Bernoulli*, 9:705
[47] Pagnani, A. and Parisi, G. (2013). *Phys. Rev. E*, 87:010102(R)
[48] Bundschuh, R. and Lässig, M. (1996). *Phys. Rev. E*, 54:304
[49] Mukherji, S. and Bhattacharjee, S. (1996). *Phys. Rev. B*, 53:R6002
[50] Barabasi, A. and Stanley, H. (1995). *Fractal Concepts in Surface Growth*. Cambridge University Press, Cambridge
[51] Arthur, J. R. (2002). *Surface science*, 500(1):189–217
[52] Das Sarma, S., Ghaisas, S. and Kim, J. (1994). *Phys. Rev. E*, 49(1):122
[53] Racz, Z. and Plischke, M. (1994). *Phys. Rev. E*, 50(5):3530
[54] Deker, U. and Haake, F. (1975). *Phys. Rev. A*, 11(6):2043
[55] Fisher, D. S. and Huse, D. A. (1991). *Phys. Rev. B*, 43:10728
[56] Engel, A. (1993). *Nucl. Phys. B*, 410:617
[57] Villain, J. (1982). *Journal de Physique Lettres*, 43(15):551–558
[58] Le Doussal, P., Wiese, K. J. and Chauve, P. (2004). *Phys. Rev. E*, 69:026112
[59] Dotsenko, V. (2001). *Introduction to the Replica Theory of Disordered Statistical Systems*. Cambridge University Press, Cambridge
[60] Kardar, M. (1987). *Nucl. Phys. B*, 290:582
[61] Kardar, M. (2007). *Statistical physics of particles*. Cambridge University Press
[62] Lieb, E. H. and Liniger, W. (1963). *Phys. Rev.*, 130:1605–1616
[63] Feynman, R. P. (1982). *Statistical Mechanics – A Set of Lectures*. W.A. Benjamin
[64] Feynman, R. P. und Hibbs, A. R. (1965). *Quantum Mechanics and Path Integrals*. McGraw-Hill
[65] Mezard, M. and Parisi, G. (1991). *J. Physique I*, 1:809
[66] Mezard, M., Parisi, G. und Virasoro, M. A. (1986). *Spin Glass Theory and Beyond*. World Scientific
[67] Fisher, D. S. (1986). *Phys. Rev. Lett.*, 56:1964–1967
[68] Balents, L. and Fisher, D. (1993). *Phys. Rev. B*, 48:5949
[69] Chauve, P., Le Doussal, P. and Wiese, K. J. (2001). *Phys. Rev. Lett.*, 86:1785
[70] Le Doussal, P., Wiese, K. J. and Chauve, P. (2002). *Phys. Rev. B*, 66:174201
[71] Doussal, P. L. and Wiese, K. J. (2005). *Phys. Rev. E*, 72:035101(R)
[72] Schulz, U. et al. (1988). *Journal of statistical physics*, 51(1-2):1–27
[73] Abramowitz, M. and Stegun, I. (1972). *Handbook of Mathematical Functions*. Applied Mathematics Series – 55. National Bureau of Standards, Washington
[74] *NIST Digital Library of Mathematical Functions*. http://dlmf.nist.gov/, Release 1.0.9 of 2014-08-29
[75] Olver, F. W. J. et al. (Hg.) (2010). *NIST Handbook of Mathematical Functions*. Cambridge University Press, New York, NY
[76] Ala-Nissila, T. et al. (1993). *J. Stat. Phys.*, 72:207
[77] Marinari, E. et al. (2000). *J. Phys. A: Math. Gen.*, 33:8181

[78] Marsaglia, G. and Tsang, W. W. (2000). *J. Stat. Soft.*, 5:1

[79] Doty, C. and Kosterlitz, J. (1992). *Phys. Rev. Lett.*, **69**:1979

[80] Giamarchi, T. and Le Doussal, P. (1995). *Phys. Rev. B*, **52**:1242

[81] Schöbl, S. et al. (2014). *Phys. Rev. Lett.*, **113**:238302

[82] Kierfeld, J. and Lipowsky, R. (2003). *Europhys. Lett.*, **62**:285

[83] Derrida, B. and Flyvbjerg, H. (1987). *J. Phys. A: Math. Gen.*, **20**:5273

[84] Jensen, M. H., Kadanoff, L. P. and Procaccia, I. (1987). *Phys. Rev. A*, **36**:1409

[85] Riedi, R. H. (2003). In Doukhan, P., Oppenheim, G. and Taqqu, M. S. (Hg.), *Theory and applications of long-range dependence*. Springer Science & Business Media

[86] Mandelbrot, B. B. (1974). *Journal of Fluid Mechanics*, **62**:331–358

[87] Tél, T. (1988). *Z. Naturforsch.*, **43a**:1154

[88] Bhattacharjee, S. M. and Seno, F. (2001). *Journal of Physics A: Mathematical and General*, **34**(33):6375

[89] Huckestein, B. (1995). *Rev. Mod. Phys.*, **67**:357

[90] Evers, F. and Mirlin, A. D. (2008). *Rev. Mod. Phys.*, **80**:1355–1417

[91] Chhabra, A. and Jensen, R. V. (1989). *Phys. Rev. Lett.*, **62**:1327

[92] Dotsenko, V. S. (2011). *Physics - Uspekhi*, **54**:259

[93] Lässig, M. (1998). *Phys. Rev. Lett.*, **80**(11):2366

[94] Kolokolov, I. and Korshunov, S. (2007). *Phys. Rev. B*, **75**:140201

[95] Kolokolov, I. and Korshunov, S. (2008). *Phys. Rev. B*, **78**:024206

[96] Krug, J. and Meakin, P. (1990). *J. Phys. A: Math. Gen.*, **23**:L987

[97] Gumbel, E. J. (1954). *Statistical theory of extreme values and some practical applications*. Applied Mathematics Series – 33. National Bureau of Standards, Washington

[98] Kampmann, T. A. private communication

[99] Marinari, E. et al. (2002). *Phys. Rev. E*, **65**:026136

[100] Paczuski, M., Maslov, S. and Bak, P. (1996). *Phys. Rev. E*, **53**:414–443

[101] Feigel'man, M. (1983). *Sov. Phys. JETP*, **58**(5):1077

[102] Sneddon, L., Cross, M. and Fisher, D. S. (1982). *Phys. Rev. Lett.*, **49**(4):292

[103] Middleton, A. (1992). *Phys. Rev. Lett.*, **68**:670

[104] Chauve, P., Giamarchi, T. and Le Doussal, P. (2000). *Phys. Rev. B*, **62**(10):6241

[105] Duemmer, O. and Krauth, W. (2005). *Phys. Rev. E*, **71**:061601

[106] Le Doussal, P. and Wiese, K. J. (2007). *EPL (Europhysics Letters)*, **77**(6):66001

[107] Middleton, A. A., Le Doussal, P. and Wiese, K. J. (2007). *Phys. Rev. Lett.*, **98**:155701

[108] Rosso, A., Le Doussal, P. and Wiese, K. J. (2007). *Phys. Rev. B*, **75**:220201

[109] Ferrero, E. E., Bustingorry, S. and Kolton, A. B. (2013). *Phys. Rev. E*, **87**(3):032122. A detailed description of the numerical implementation can be found in the supplemental material at `http://link.aps.org/supplemental/10.1103/PhysRevE.87.032122`. See also Ref. 151

[110] Giamarchi, T., Kolton, A. and Rosso, A. (2006). In *Jamming, Yielding, and Irreversible Deformation in Condensed Matter*, 91–108. Springer

[111] Narayan, O. and Fisher, D. S. (1992). *Phys. Rev. B*, **46**(18):11520

[112] Narayan, O. and Fisher, D. S. (1992). *Phys. Rev. Lett.*, **68**(24):3615

[113] Nattermann, T. et al. (1992). *J. Phys. Paris*, **2**(8):1483–1488

[114] Herring, C. (1951). In Kingston, W. E. (Hg.), *The Physics of Powder Metallurgy*, 143. McGraw-Hill, New York

[115] Mullins, W. W. (1957). *J. Appl. Phys.*, **28**:333

[116] Park, K. and Kim, I.-M. (2000). *Phys. Rev. E*, **61**:4606–4609

[117] Lee, C. and Kim, J. M. (2006). *Phys. Rev. E*, **73**(1):016140

[118] Liu, H. et al. (2008). *Physics Letters A*, **372**:7077

[119] Song, H. S. and Kim, J. M. (2006). *J. Korean Phys. Soc.*, **49**(4):1520

[120] Kierfeld, J. et al. (2006). *J. Comput. Theor. Nanosci.*, 3(6):898–911
[121] Bundschuh, R. and Lässig, M. (2002). *Phys. Rev. E*, 65:061502
[122] Brú, A. et al. (1998). *Phys. Rev. Lett.*, 81(18):4008
[123] Edwards, S. F. and Wilkinson, D. R. (1982). *Proc. Roy. Soc. London, Ser. A*, 381(1780):17–31
[124] Belanger, D. and Young, A. (1991). *J. Magn. Magn. Mater.*, 100(1):272–291
[125] Seppälä, E. T., Petäjä, V. and Alava, M. J. (1998). *Phys. Rev. E*, 58:R5217–R5220
[126] Lee, J. H., Kim, S. K. and Kim, J. M. (2000). *Phys. Rev. E*, 62:3299–3302
[127] Narayan, O. and Fisher, D. (1993). *Phys. Rev. B*, 48(10):7030
[128] Bolech, C. J. and Rosso, A. (2004). *Phys. Rev. Lett.*, 93:125701
[129] Middleton, A. A. and Fisher, D. S. (1991). *Phys. Rev. Lett.*, 66:92–95
[130] Chayes, J. et al. (1986). *Phys. Rev. Lett*, 57:2999
[131] Larkin, A. I. (1970). *Sov. Phys. JETP*, 31(4)
[132] Leschhorn, H. (1993). *Physica A*, 195(3):324–335
[133] Ioffe, L. B. and Vinokur, V. M. (1987). *J. Phys. C*, 20(36):6149
[134] Nattermann, T., Shapir, Y. and Vilfan, I. (1990). *Phys. Rev. B*, 42:8577–8586
[135] Lemerle, S. et al. (1998). *Phys. Rev. Lett.*, 80:849–852
[136] Anderson, P. W. and Kim, Y. B. (1964). *Rev. Mod. Phys.*, 36:39–43
[137] Kes, P. et al. (1989). *Supercond. Sci. Tech.*, 1(5):242
[138] Kolton, A. B. et al. (2009). *Phys. Rev. B*, 79:184207
[139] Tang, L. H. and Stepanow, S. Unpublished, as cited in [104]
[140] Bustingorry, S., Kolton, A. B. and Giamarchi, T. (2008). *EPL (Europhysics Letters)*, 81(2):26005
[141] Bustingorry, S., Kolton, A. B. and Giamarchi, T. (2012). *Phys. Rev. E*, 85:021144
[142] NVIDIA Corporation. *CUDA C Programming Guide*. Available online: `http://docs.nvidia.com/cuda/cuda-c-programming-guide/`
[143] Rosso, A. and Krauth, W. (2002). *Phys. Rev. E*, 65:025101
[144] Press, W. H. et al. (1992). *Numerical recipes in C*. Cambridge University press, Cambridge
[145] Kolton, A. B. et al. (2006). *Phys. Rev. B*, 74:140201
[146] Le Doussal, P. (2006). *EPL (Europhysics Letters)*, 76(3):457
[147] Dong, M., Marchetti, M. C. and Middleton, A. A. (1993). *Phys. Rev. Lett.*, 70(5):662
[148] Kolton, A. B. et al. (2006). *Phys. Rev. Lett.*, 97:057001
[149] Brú, A. et al. (2003). *Biophysical journal*, 85(5):2948–2961
[150] Martin, P. C., Siggia, E. and Rose, H. (1973). *Phys. Rev. A*, 8(1):423
[151] Ferrero, E. E., Bustingorry, S. and Kolton, A. B. (2013). *Phys. Rev. E*, 87:069901

Part II

ELASTIC CAPSULES IN LINEARISED VISCOUS FLOW

Preface to this part

Tempora mutantur, nos et mutamur in illis or *times change and we change with them.* In less cryptical terms, parts[135] of the following have meanwhile (in between handing in this thesis and publishing it) been published, see Ref. 1, and I therefore feel obliged to inform you, the reader of the future, of this. Not much more to see here, let us go on with the the text.

Horst-Holger Boltz, October 2015

HHB

[135] These parts are ©2015 American Physical Society

Introduction

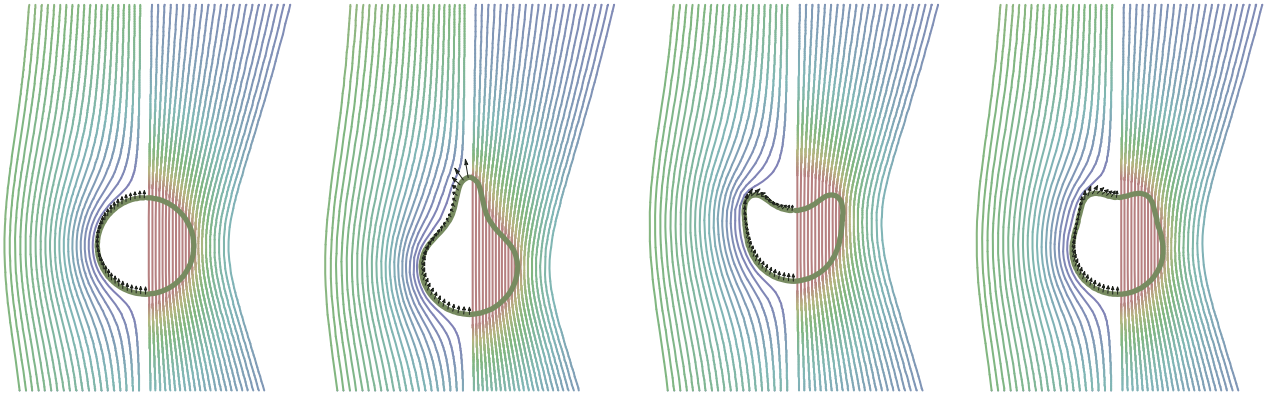

Figure 62: Velocity of the surrounding fluid in the resting frame of the immersed capsule (left half) and in the lab frame (right half) reconstructed from the surface forces found by the outlined boundary integral method for the four shape types found under sedimentation with volume control, which are from left to right pseudospherical, pear shape, strongly buckled and weakly buckled. We show streamlines to indicate the flow. Additionally, the absolute value of the velocity is colour-coded in the stream lines and the hydrodynamic surface forces are shown as dark arrows on the surface.

On the microscale, the motion and deformation of closed soft elastic objects through a viscous fluid, either by a driving force or in a hydrodynamic flow, represents an important problem with numerous applications, for example, for elastic microcapsules [2], red blood cells [3, 4] or vesicles moving in capillaries, deforming in shear flow, or sedimenting under gravity [5, 6]. Another related system are droplets moving in a viscous fluid [7, 8].

The analytical description and the simulation are challenging problems as the hydrodynamics of the fluid is coupled to the elastic deformation of the capsule or vesicle. It is important to recognise that this coupling is mutual: On the one hand, hydrodynamic forces deform a soft capsule, a vesicle, or a droplet. On the other hand, the deformed capsule, vesicle or droplet changes the boundary conditions for the fluid flow. As a result of this interplay, the soft object deforms and takes on characteristic shapes; eventually there are transitions between different shapes as a function of the driving force or flow velocity. Such shape changes might have important consequences for applications or biological function, for example, if we consider red blood cells or microcapsule containers moving in narrow capillaries. Shapes can also exhibit additional dynamic features such as tank-treading or tumbling, as it has been shown experimentally and theoretically for vesicles or elastic capsules in shear flows [2, 5].

In the following, we investigate stationary shapes of elastic capsules sedimenting in an otherwise quiescent incompressible fluid, either by gravity or by the centrifugal force in a centrifuge. Possible shapes and the nature of dynamic transitions between them are only poorly understood for sedimenting capsules. We will always consider the microscale, where Reynolds numbers are small and fluid flows can be assumed to be viscous. We will also consider elastic capsules, i.e. closed elastic membranes. As opposed to fluid vesicles, which are governed by bending elasticity and are bounded

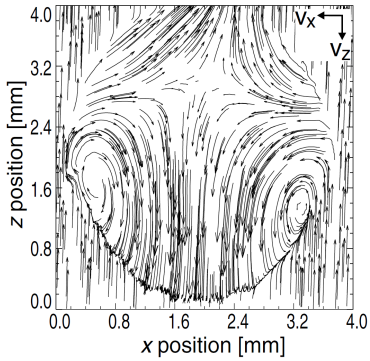

Figure 63: Two-dimensional cross-section of the flow in- and outside of a falling (in negative z-direction) water droplet as inferred from NMR imaging[10]. There is a jump in the normal velocities at the droplet's surface and the emerging toroidal flow inside the capsule is identifiable by two clearly visible vortices. Reprinted figure with permission from (Ref. 10): S.-I. Han, S. Stapf, B. Blümich, Physical Review Letters **87**, 144501 (2001). Copyright (2001) by the American Physical Society.

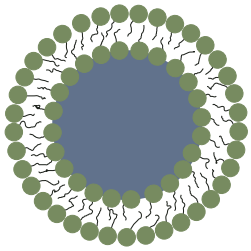

Figure 64: Schematic depiction of the structure of a vesicle. The aqueous interior (blue) is surrounded by a lipid bilayer that assembles to screen the hydrophobic tails of the lipids. The two layers are free to move against each other thus allowing for surface flows but are virtually unstretchable. Therefore, a vesicle filled with an incompressible liquid needs excess area (more area than a sphere of same encapsulated volume) to be able to deform.

by two-dimensional fluid surfaces (lipid membranes) [9], capsules are closed elastic shells, i.e., two-dimensional solids, which can support in-plane shear stresses and inhomogeneous stretching stresses with respect to their equilibrium configuration. Whereas the rest shape of vesicles is determined by a few global parameters such as fixed area and spontaneous curvature, elastic capsules can be produced with arbitrary rest shapes, in principle. We focus on elastic microcapsules with a spherical rest shape, which are moving in a quiescent fluid, driven by a homogeneous external body force, as it is realised in sedimentation by gravity or in a centrifuge. We use this problem to introduce a new iterative method to calculate efficiently axisymmetric stationary capsules shapes, which iterates between a boundary integral method to solve the viscous flow problem for given capsule shape and capsule shape equations to calculate the capsule shape in a given fluid velocity field. The method does not capture the dynamic evolution of the capsule shape but directly converges to its stationary shape.

There are various theoretical and simulation approaches to capsules [2, 11], vesicles [5], red blood cells [3, 4] or liquid droplets [7, 8, 11] moving in viscous fluids, some of which have also been applied to sedimentation problems.

Sedimenting liquid droplets in a viscous fluid [7, 8, 12] develop an internal toroidal circulation (see Fig. 63), which is increasing with the sedimenting velocity [7]. For a spherical droplet, its steady state sedimenting velocity and the fluid velocity field is given by the Hadamard-Rybczynski solution, which is obtained by solving the Stokes equation both inside and outside the droplet, along with boundary conditions of continuity of velocity and tangential stress [8]. The spherical shape remains a solution of the Stokes equations for arbitrary surface tension; this solution becomes unstable, however, for vanishing surface tension [13–15]. Then, a tail forms for infinitesimal prolate perturbations, whereas a dimple or cavity forms for oblate perturbations. For non-zero surface tension, a critical perturbation amplitude is needed to destabilise the spherical shape [14, 15]. If the unstable drop develops a tail, this tail will grow and eventually break up.

Sedimenting vesicles are less prone to shape instabilities than droplets as their shapes are stabilised by the additional two-dimensional liquid membrane, which has a fixed area and bending rigidity [9]. Sedimenting vesicles have also been investigated numerically [16–18] using boundary integral methods for the fluid and triangulation of the surface and experimentally [6]; sedimenting charged vesicles have been investigated in Ref. 19. For sedimenting vesicles, pear-like and egg-like shapes are observed experimentally [6] in the quasi-spherical low velocity limit. At sufficiently high velocities, tethering instabilities occur both in experiments [6] and simulations [18].

There are important differences between vesicles and elastic capsules, which will give rise to qualitatively different sedimenting shapes. Vesicles, see Fig. 64, are virtually unstretchable and have a fixed area. Therefore, excess area (which could be "hidden" in thermal fluctuations) is needed in order to deform an initially spherical vesicle during sedimentation. Elastic capsules, on the other hand, can change their area by local stretching. Therefore, also an initially spherical capsule can deform into non-spherical shapes during sedimentation. Spherical elastic capsules will not be able to develop tethers, however, because this involves strong stretching with respect to their equilibrium configuration. Vesicles are 2D fluids and can, therefore, exhibit surface flows, whereas elastic capsule surfaces could only rotate rigidly, as is the case for the tank-treading motion in a shear flow [2]. For sedimenting vesicles,

surface flows have been found for the banana shape in Refs. 16, 17.

Shape transitions of sedimenting spherical elastic capsules have not yet been studied. From the comparison with sedimenting fluid vesicles [16–18], we can expect to find such classes of sedimenting shapes, which do not involve surface flows. Following Refs. 16, 17 (cf. Fig. 65), these are axisymmetric prolate pear-like or oblate parachute-like capsules shapes, whereas the non-axisymmetric banana-shape of vesicles involves surface flows. Tether formation starting from pear-shaped capsules should be strongly suppressed by stretching elasticity. Also, non-axisymmetric banana shapes should be suppressed because they involve surface flows, which cannot be supported by an elastic capsule. Red blood cells have similar elasticity properties as elastic capsules, but elastic deformation happens with respect to the peculiar biconcave rest shape. This gives rise to non-axisymmetric fin-tailed and tear drop shapes in sedimentation [20]. We will focus on the simpler spherical rest shape of capsules, which is also prepared more easily in applications involving synthetic microcapsules, and on axisymmetric sedimenting shapes.

Another important property is the relation between the sedimenting driving force, i.e., a homogeneous gravitational force or a centrifugal force, and the resulting velocity of the sedimenting elastic objects. For strictly spherical shapes this relation is easily obtained both for droplets [8] and vesicles [17], and also for spherical elastic capsules, which simply sediment as a solid sphere following Stokes' law. Shape transformations of a deformable sedimenting object should, however, reflect in qualitative changes or even bifurcations in the force-velocity curves. This important aspect has only been poorly studied for droplets, vesicles and red blood cells. Some results have been obtained for quasispherical vesicles in Ref. 17. MPCD simulations for red blood cells (see Fig. 66) showed no specific signs of shape transitions in the force-velocity relations [20], experimental measurements for vesicles [6] are also not precise enough to find such features. We will calculate the force-velocity relation for sedimenting elastic capsules with high accuracy, such that we can address this issue for sedimenting spherical capsules.

There are many simulation methods which have been applied to the dynamics of vesicles or capsules in viscous fluids, either particle based hydrodynamic simulation techniques such as MPCD [21], dissipative particle dynamics [22], and Lattice Boltzmann simulations [23], or boundary integral methods [2]. These techniques simulate the full time-dependent dynamics using a triangulated representation of vesicles or capsules; stationary states are obtained in the long-time limit. Here, we introduce an iterative boundary integral method coupled to shape equations for axisymmetric shapes, which directly converges to stationary shapes without simulation of the real dynamics. Instead, we exploit axisymmetry to avoid triangulated representations and get an efficient iterative method based on boundary integrals for the fluid and shape equations for the capsule.

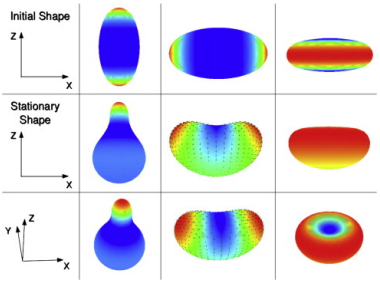

Figure 65: Stationary shapes (middle row and tilted in the last row) of sedimenting vesicles as a function of the initial shape (top row) as found from an integration of the equations of motion. The color represents the mean curvature and arrows (if present) surface flows. (Right) An oblate vesicle with symmetry axis aligned with gravity converges toward a "parachute-like" shape. Reprinted from (Ref. 16) Journal of Computational Physics, 230(1), G. Boedec,M. Leonetti,M. Jaeger, 1020–1034, Copyright (2011), with permission from Elsevier.

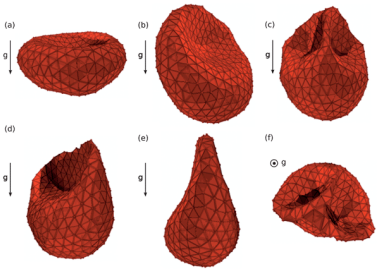

Figure 66: Snapshots of the MPCD simulation of a sedimenting red blood cell. The shapes with an extrusion (b-e) are the result of a reorientation of the cell, such that the identations of the biconcave resting shape that originally were on the two intersections with the axis of symmetry are located on the flanks of the extrusion. This figure is adapted from Ref. 20 with permission from the Royal Society of Chemistry.

Methods

We limit ourselves to axisymmetric capsule[136] shapes resulting also in axisymmetric viscous fluid flows. Then, the elastic surface of the sedimenting capsule has to be at rest in its stationary shape without any surface flows. Therefore, also the fluid inside the capsule will be at rest (in the frame moving with the capsule). We will obtain the stationary capsule shape by solving a shape equation in curvilinear cylindrical coordinates and solve for the Stokes flow of the surrounding fluid by applying boundary integral methods adapted to the axisymmetric symmetry. In an iterative procedure we converge to the stationary shape, where the fluid forces onto the capsule and the boundary conditions for the fluid flow posed by the capsule shape are consistently incorporated. We perform this iterative procedure for a given capsule sedimenting velocity and obtain the corresponding driving gravitational force from the condition of force balance with the total fluid force onto the capsule surface.

Geometry

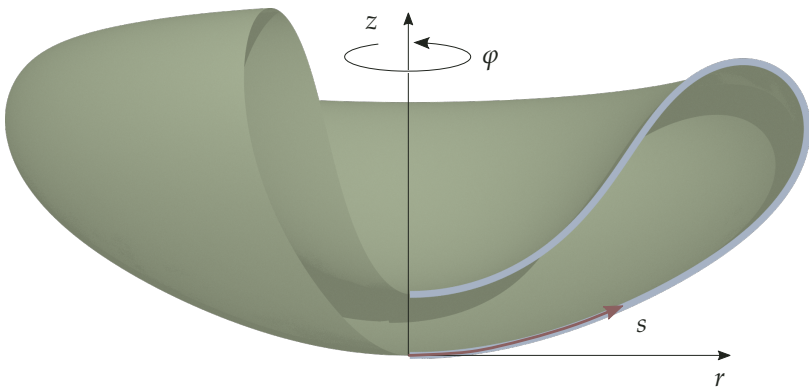

For the parametrisation of the capsule shape, we want to directly exploit the axisymmetry. Thus, we work in cylindrical coordinates. The axis of symmetry is called z, the distance to this axis r and the polar angle φ, see Fig. 67. The shell (which provides the boundary condition for the Stokes equation) is given by the generatrix $(r(s),z(s))$ which is parametrised in arc-length s (starting at the lower apex with $s = 0$ and ending at the upper apex with $s = L$). The unit tangent vector $\boldsymbol{e}_s$ to the generatrix at $(r(s),z(s))$ defines an angle ψ via $\boldsymbol{e}_s = (\cos\psi, \sin\psi)$, which can be used to quantify the orientation of a patch of the capsule relative to the axis of symmetry.

[136] One of the technical advantages of demanding axisymmetry is that the principal curvatures are known. Suppose we have a surface of revolution parametrised by

$$\boldsymbol{r} = \begin{pmatrix} r(s)\cos\varphi \\ r(s)\sin\varphi \\ z(s) \end{pmatrix}.$$

The principal curvatures are then given by the first and second fundamental form of this surface[24]. We can write the former (the symmetry follows from Schwarz' (or Clairaut's) theorem) as

$$\mathrm{I} = \begin{pmatrix} E & F \\ F & G \end{pmatrix}$$

with $E = \partial_s\boldsymbol{r}\cdot\partial_s\boldsymbol{r} = r'^2 + z'^2$, $F = \partial_\varphi\boldsymbol{r}\cdot\partial_s\boldsymbol{r} = 0$ and $G = \partial_\varphi\boldsymbol{r}\cdot\partial_\varphi\boldsymbol{r} = r^2$. Analogously, we find for the second fundamental form

$$\mathrm{II} = \begin{pmatrix} e & f \\ f & g \end{pmatrix}$$

with

$$e = \boldsymbol{v}\cdot\partial_s^2\boldsymbol{r} = \sqrt{E}^{-1}(r'z'' - z'r'')$$
$$f = \boldsymbol{v}\cdot\partial_\varphi\partial_s\boldsymbol{r} = 0$$
$$g = \boldsymbol{v}\cdot\partial_p^2 hi\boldsymbol{r} = \sqrt{E}^{-}1(r'z')$$
$$\boldsymbol{v} = \frac{\partial_t\boldsymbol{r}\times\partial_\varphi\boldsymbol{r}}{|\partial_t\boldsymbol{r}\times\partial_\varphi\boldsymbol{r}|}$$

whose eigenvectors are the directions of principal curvature. As both forms are diagonal in our parametrisation, we find the principal curvatures

$$\varkappa_s = e/E = \frac{r'z'' - z'r''}{(r'^2 + z'^2)^{3/2}}$$
$$\varkappa_\varphi = g/G = \frac{z'}{r(r'^2 + z'^2)^{1/2}}.$$

Figure 67: Example of an axisymmetric shell with a section cut out to clarify the cylindrical geometry used here, the coordinate along the axis of symmetry is called z, the distance to this axis r and the remaining polar angle φ. The shell is generated by revolution of the generatrix (blue) that is subject of the shape equations.

Cauchy momentum equation

This is not the place for a comprehensive account of the topic, but seeing that the unifying concept of both the shape of an elastic capsule and the motion of a viscous fluid is *continuum mechanics* there might be some value to the reader in a minimal introduction. Furthermore, this sets the framework to present both aspects on equal footing.

The fundamental equation (for computations at least) in point (or particle) mechanics is Newton's second law

$$\frac{\mathrm{d}\boldsymbol{p}}{\mathrm{d}t} = \boldsymbol{F},$$

that is the change in momentum[137] $\boldsymbol{p}$ is given by the acting net force $\boldsymbol{F}$. Together with Newton's third law, $\boldsymbol{F}_{A\to B} = -\boldsymbol{F}_{B\to A}$, it establishes the conservation of momentum. We want to formulate the equivalent equation for a continuous medium. For this purpose we consider a volume element $\mathrm{d}V$ with mass $\rho \mathrm{d}V$ moving with velocity $\boldsymbol{u}(\boldsymbol{r},t)$. We explicitly state the functional dependence to stress the fact that $\boldsymbol{u}$ is a field variable, there is a velocity for every point $\boldsymbol{r}$ in the total volume, Ω, considered (and every time). We are interested in the change of the momentum of a specific volume element, that moves in time, we therefore have to track its motion, that is we compute the total time derivative of $\boldsymbol{u}(\boldsymbol{r}(t),t)$ along the path of its motion[25], that is with $\partial_t \boldsymbol{r}(t) = \boldsymbol{u}$, which is called the *material derivative*

$$\frac{\mathrm{D}(\rho\boldsymbol{u})}{\mathrm{D}t} \equiv \frac{\partial(\rho\boldsymbol{u})}{\partial t} + \rho\boldsymbol{u}\cdot\nabla(\rho\boldsymbol{u}).$$

There can in principle be two types of force acting upon the volume element, interface forces $\boldsymbol{f}_i$ due to the interaction with other volume elements acting at the element's surface and body forces $\boldsymbol{b}$ acting on the volume and we can adapt Newton's law to

$$\int_\Omega \mathrm{d}V \,\frac{\mathrm{D}(\rho\boldsymbol{u})}{\mathrm{D}t} = \int_{\partial\Omega} \mathrm{d}A \boldsymbol{f}_i + \int_\Omega \mathrm{d}V\, \boldsymbol{b}.$$

We write $\boldsymbol{f}_i = \sigma\cdot\boldsymbol{n}$ with $\boldsymbol{n}$ the surface normal and call σ the *stress tensor*. Applying Stokes' theorem (also known as (Ostrogradsky-)Gauss theorem) we find

$$\int_\Omega \mathrm{d}V \,\frac{\mathrm{D}(\rho\boldsymbol{u})}{\mathrm{D}t} = \int_\Omega \mathrm{d}V\, \left[\nabla\cdot\sigma + \boldsymbol{b}\right].$$

This holds regardless of the choice of Ω and we can therefore infer equality of the integrands, which yields the *Cauchy momentum equation*

$$\frac{\mathrm{D}(\rho\boldsymbol{u})}{\mathrm{D}t} = \nabla\cdot\sigma + \boldsymbol{b}. \tag{49}$$

In the following we basically consider a complex version of this equation, where the so-called *constitutive relations*, i.e. the prescription on how to compute σ given the configuration of the medium (stress-strain-relation), changes depending on whether one deals with a volume element of fluid or of the capsule. The left-hand side of this equation will be zero in both cases as we consider the stationary ($\boldsymbol{u} = 0$) in one case and a stationary, incompressible (or solenoid, if you will) flow at low Reynolds number. In an attempt to reduce obfuscation to the reader we will only write the Stokes equation in this form throughout the main text, that is we reserve σ for the stress tensor of the liquid.

[137] In light of the following it is unfortunate to call the momentum $\boldsymbol{p}$, because this symbol will be used for the pressure later on. The author has confidence in the reader's ability to limit the scope of this definition to precisely this one equation.

Equilibrium shape of capsule

As already mentioned the stationary shape of an elastic capsule due to hydrodynamic forces is a joint problem: any change of shape is associated with a change in the flow and the accompanying forces and vice versa. We will however not try to achieve a joint solution, but instead find the solution by solving a series of separated problems, i.e. the stationary capsule shape for a given flow field around it and the flow field for a given capsule shape, whose solution will then converge to the solution of the joint problem. We are ultimately interested in the shape of the capsule, it is therefore straightforward to start at this sub-problem. Also, this will allow us insight into what information we actually need from the hydrodynamic sub-problem.

The shape of a thin axisymmetric shell of thickness H can be derived from non-linear shell theory [26, 27]. A known reference shape $(r_0(s_0),z_0(s_0))$ (a subscript zero refers to a quantity of the reference shape; $s_0 \in [0,L_0]$ is the arc length of the reference shape) is deformed by hydrodynamic forces exerted by the viscous flow. Each point $(r_0(s_0),z_0(s_0))$ is mapped onto a point $(r(s_0),z(s_0))$ in the deformed configuration, which induces meridional and circumferential stretches, $\lambda_s = ds/ds_0$ and $\lambda_\varphi = r/r_0$, respectively. The arc length element $\mathrm{d}s$ of the deformed configuration is $\mathrm{d}s^2 = (r'(s_0)^2 + z'(s_0)^2)\mathrm{d}s_0^2$.

The shape of the deformed axisymmetric shell is given by the solution of a system of first-order differential equations, henceforth referred to as the shape equations. Using the notation of Refs. 28, 38 these can be written as

$$s'(s_0) = \lambda_s \tag{50a}$$
$$r'(s_0) = \lambda_s \cos\psi \tag{50b}$$
$$z'(s_0) = \lambda_s \sin\psi \tag{50c}$$
$$\psi'(s_0) = \lambda_s \varkappa_s \tag{50d}$$
$$\tau_s'(s_0) = \lambda_s \left(\frac{\tau_\varphi - \tau_s}{r} \cos\psi + \varkappa_s q + p_s \right) \tag{50e}$$
$$m_s'(s_0) = \lambda_s \left(\frac{m_\varphi - m_s}{r} \cos\psi - q + l \right) \tag{50f}$$
$$q'(s_0) = \lambda_s \left(-\varkappa_s \tau_s - \varkappa_\varphi \tau_\varphi - \frac{q}{r} \cos\psi + p \right). \tag{50g}$$

The additional quantities appearing in these shape equations are shown in Figs. 68 and 69 and defined as follows: The angle ψ is the slope angle between the tangent plane to the deformed shape and the r-axis, $\varkappa_\varphi$ is the circumferential curvature, $\varkappa_s$ the meridional curvature; τ_s and τ_φ are the meridional and circumferential stresses, respectively; q is the transverse shear stress, p the total normal pressure, p_s the shear pressure, and l the external stress couple. The first equation defines λ_s, the next three equations follow from geometry, and the last three express force and torque equilibrium. For a derivation of these equations[138] we refer to Refs. 26, 27, 38.

Whereas the curvatures and circumferential strains are known from the geometrical relations $\varkappa_\varphi = \frac{\sin\psi}{r}$, $\varkappa_s = \frac{\mathrm{d}\psi}{\mathrm{d}s}$ and $\lambda_\varphi = \frac{r}{r_0}$, the normal pressure

$$p = p_0 + p_n - g_0 \Delta\rho z, \tag{51}$$

the shear-pressure p_s, and the stress couple[139] $l = p_s H/2$ are given externally by hydrodynamic and gravitational forces[140]. Note that we measure the gravitational hydrostatic pressure $-g_0\Delta\rho z$ relative to the lower apex, for which we can always choose $z(0) = 0$.

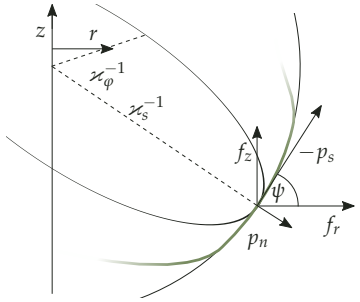

Figure 68: Part of the generatrix (green) with the external surface force densities, decomposed into the coordinate components (f_r, f_z) as well as into normal and tangent components (p_n, p_s). Also shown are the two principal curvature radii $\varkappa_s^{-1}$ and $\varkappa_\varphi^{-1}$ alongside the respective osculating circles.

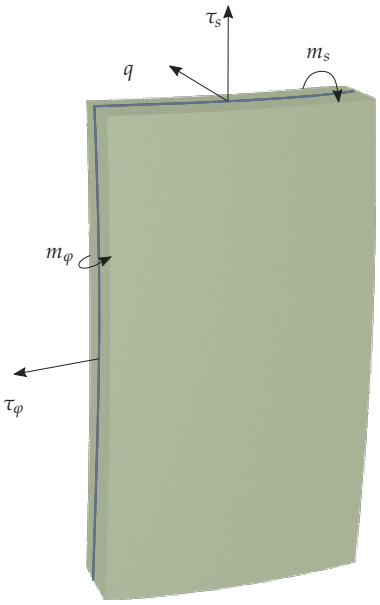

Figure 69: Slab of the shell (finite thickness H) with acting tensions τ_s (meridional),τ_φ (circumferential), q (transverse shear stress) and bending moments m_s, m_φ.

[138] We add our personal take on the derivation in the appendix starting on page 125.

[139] The fluid inside the capsule is assumed to be at rest.

[140] Here, g_0 is the gravitational acceleration and $\Delta\rho = \rho_{\text{in}} - \rho_{\text{out}}$ the density difference between the fluids inside and outside the capsule.

The pressures p_n and p_s are the normal and tangential forces per area which are generated by the surrounding fluid. For the latter it would usually be more natural to give express stresses in terms of their radial and axial contributions. The vector[141]

$$\boldsymbol{p}_H = p_n \boldsymbol{n} - p_s \boldsymbol{e}_s$$

with $\boldsymbol{n}$ and $\boldsymbol{e}_s$ the normal and tangent unit vectors to the generatrix

$$\begin{aligned}\boldsymbol{n} &= -\cos\psi \boldsymbol{e}_z + \sin\psi \boldsymbol{e}_r \\ \boldsymbol{e}_s &= \sin\psi \boldsymbol{e}_z + \cos\psi \boldsymbol{e}_r\end{aligned}$$

equals the surface force density vector

$$\boldsymbol{f} = f_z \boldsymbol{e}_z + f_r \boldsymbol{e}_r,$$

which will be calculated in the following section. Re-decomposing $\boldsymbol{f}$ into its normal and tangential components p_n and p_s we find

$$\begin{aligned}p_n &= f_r \sin\psi - f_z \cos\psi \\ p_s &= -f_r \cos\psi - f_z \sin\psi.\end{aligned}$$

This is also illustrated in Fig. 68.

All remaining quantities in the shape equations (50) follow from *constitutive (stress-strain) relations* that depend on the elastic law, which will be discussed later. In addition to the elastic law, there might be global constraints. We consider here only one geometric constraint to the shape, namely a fixed volume $V = V_0$ (due to an incompressible fluid inside the closed capsule). We introduce the conjugated Lagrange parameter p_0, the static pressure difference between the interior and exterior fluids, which also enters the pressure p in eq. (51). Additionally, the shape has to be in global force equilibrium, to which the velocity of the capsule is the conjugated parameter. The latter is a crucial constraint to the external loading we prescribe (as manifested by p,p_s). The *equilibrium* equations are derived from local force and torque balance and therefore intrinsically only allow for solutions that are in *global force balance*[142]. This is connected to a first integral of the shape equations that we derive in the appendix, see page 126.

[141] The subscript H indicates that this only incorporates the hydrodynamic contributions. We do not consider cases with a static shear-pressure, but as is apparent from eq. (51) there are static contributions to the normal pressure.

[142] Global torque balance follows from the rotational symmetry.

Elastic law and reference shapes.

To keep things simple for now we use a Hookean energy density with a spherical rest shape[143] to model soft, deformable capsules. As a measure for the deformation of the capsule we introduce the meridional and circumferential strains $e_s = \lambda_s - 1$ and $e_\varphi = \lambda_\varphi - 1$ as well as the meridional and circumferential bending strains $K_s = \lambda_s \varkappa_s - \varkappa_{s0}$ and $K_\varphi = \lambda_\varphi \varkappa_\varphi - \varkappa_{\varphi_0}$. The elastic law we use is Hookean in the sense that it is a quadratic form in these strains. More precisely, the surface energy density w, which measures the elastic energy of an infinitesimal patch of the (deformed) surface divided by the area of this patch in the undeformed state, is given by

$$w_s = \frac{1}{2}\frac{Y_{2D}}{1-\nu^2}\left(e_s^2 + 2\nu e_s e_\varphi + e_\varphi^2\right) + \frac{1}{2}E_B\left(K_s^2 + 2\nu K_s K_\varphi + K_\varphi^2\right) \qquad (52)$$

with the two-dimensional Young's modulus Y_{2D}, which defines the tension (energy per surface) scale, the bending modulus E_B and the (two-dimensional) Poisson ratio[144] ν. We already introduced the (homogeneous) thickness H

[143] We briefly discuss non-spherical rest shapes in the appendix, see page 128.

[144] We assume equal Poisson ratios for bending and stretching, which is the result starting from an elastically isotropic (three-dimensional) membrane material.

of the membrane, with the help of which we can relate the two-dimensional Young modulus to its three-dimensional counterpart $Y_{2D} = EH$ if we assume that the shell is a thin plate made from an isotropic elastic material. The second fundamental length scale is the radius R_0 of the spherical rest shape (with $R_0 = \varkappa_{s_0}^{-1}$ and $L_0 = \pi R_0$)

$$r_0(s_0) = R_0 \sin(s_0/L_0)$$
$$z_0(s_0) = R_0(1 - \cos(s_0/L_0)).$$

For Hookean elasticity and a spherical rest shape the resulting set of shape equations has been given and solved for a pure hydrostatic pressure $p = p_0$, $p_s = 0$ in Ref. 38.

The Hookean elastic model for a spherical rest shape contains five parameters Y_{2D}, R_0, E_B, ν, and[145] H. We will eliminate two parameters, Y_{2D} and R_0, by choosing our scales of energy (or tension) and length appropriately. The two-dimensional Poisson ratio is bounded by $\nu \in [-1; 1]$, and we reduce our parameter space by always using $\nu = 1/2$. This way our Hookean energy density has the same behaviour for small stresses as the more complex Mooney-Rivlin functional [26]. Assuming that the shell can be treated as thin plate made from an isotropic elastic material, the bending modulus is directly related to the shell thickness H by

$$E_B = \frac{Y_{2D}H^2}{12(1-\nu^2)} = \frac{1}{9}Y_{2D}H^2. \tag{53}$$

Thus, we have one remaining free parameter to change the elastic properties, the bending modulus E_B, which is related to the dimensionless Föppl-von-Kármán number [26] γ_{FvK} via

$$\gamma_{FvK} \equiv \frac{Y_{2D}R_0^2}{E_B} = 9\frac{R_0^2}{H^2}.$$

The Hookean elastic energy law we use here is well suited to describe the deformation behaviour of soft elastic capsules. For other systems different energies (e.g. Helfrich bending energy and a locally inextensible surface for vesicles) might be more adequate. As pointed out before, a different choice of elastic law enters the formalism through the constitutive relations and, thus, does not require changes in our method on the conceptual level.

[145] H enters the shape equation via the stress couple l

Hydrodynamics

Let us stop the discussion of the capsule shape for a while to switch over to our second branch: we want to calculate the flow field of a viscous incompressible fluid around an axisymmetric capsule of given fixed shape. We chose to separate the problems, which allows us to state that for the calculation of the flow field the deformability of the capsule is not relevant, and the capsule can be viewed as a general immersed body of revolution $\mathfrak{B}$. For the calculation of the capsule shape, which is addressed in the following section, and for the determination of its sedimenting velocity, we only need to calculate the surface forces onto the capsule which are generated by the fluid flow.

Stokes equation

We start with the fundamental notion that the mass of the fluid should be conserved under its flow $\boldsymbol{u}$ giving rise to the *continuity equation*

$$\frac{\partial \rho}{\partial t} = -\nabla \cdot (\rho \boldsymbol{u})$$

with ρ being the local mass density. Furthermore, we only consider incompressible fluids, thus the density of a volume element of the fluid cannot changer under its motion due to the flow or

$$\frac{D\rho}{Dt} = \frac{\partial\rho}{\partial t} + \boldsymbol{u}\cdot\nabla\rho.$$

We combine these two equations and apply an appropriate vector calculus identity to find the result

$$\nabla\cdot\boldsymbol{u} = 0, \tag{54}$$

which is commonly referred to as the continuity equation for an incompressible flow. Setting the incompressibility equation, eq. (54), into the Cauchy momentum equation, eq. (49), gives[146] for a *stationary flow* with $\partial_t\boldsymbol{u} = 0$

$$\rho\boldsymbol{u}\cdot\nabla\boldsymbol{u} = \nabla\cdot\sigma. \tag{55}$$

[146] We omit the external force as they do not change any of the following in a non-trivial manner.

To reduce this equation further, we have to formulate a constitutive relation for the liquid. Demanding Galilean invariance of σ we see that σ can only depend on spatial derivatives of the velocity and from conservation of angular momentum we know that σ is symmetric[147]. Based on experimental evidence we further demand that there are no shear stresses in a quiescent fluid, that σ is isotropic and that stresses grow linearly with the velocity, which allows us to write

[147] This is sometimes referred to as Cauchy's second law of motion (the first one being the momentum equation).

$$\sigma = -p\mathbb{1} + \mu\left(\nabla\boldsymbol{u} + (\nabla\boldsymbol{u})^T\right).$$

or in Cartesian coordinates

$$\sigma_{ij} = -p\delta_{ij} + 2\mu e_{ij}$$

with the pressure p, the viscosity μ and the *rate of deformation* (or rate of strain) tensor for the flow velocity $\boldsymbol{u}$

$$e_{ij} = \frac{1}{2}\left(\frac{\partial u_i}{\partial x_j} + \frac{\partial u_j}{\partial x_i}\right).$$

A liquid for which our assumptions hold is called a *Newtonian fluid*. This constitutive relation, the incompressibility equation and the Cauchy momentum equation give rise to the famous *Navier-Stokes equation*. Going back to eq. (55) we rescale velocities, lengths and stresses by their respective typical scales u, R, $\mu v/L$ (as inferred from the constitutive relation) to find

$$\mathrm{Re}\,\tilde{\boldsymbol{u}}\cdot\tilde{\nabla}\tilde{\boldsymbol{u}} = \tilde{\nabla}\cdot\tilde{\sigma}$$

with a tilde marking a rescaled quantity and the *Reynolds number*[29]

$$\mathrm{Re} = \frac{\rho u L}{\mu}.$$

Thus we can neglect the so-called advective term on the left hand-side of our equation of motion, if the Reynolds number is sufficiently low, that is for small, slowly moving particles in a medium of high viscosity.

All in all, in the limit of small Reynolds numbers the stress tensor σ in a stationary fluid on which no external body forces are exerted is given by the *stationary Stokes equation* [30]

$$\nabla\cdot\sigma = 0.$$

Solution of the Stokes equation in an axisymmetric domain

In the rest frame of the sedimenting axisymmetric capsule and with a "no-slip" condition at the capsule surface $\partial\mathfrak{B}$, we are looking for axisymmetric solutions that have a given flow velocity $\boldsymbol{u}^\infty$ at infinity and vanishing velocity on the capsule boundary. In the lab frame, $-\boldsymbol{u}^\infty$ is the sedimenting velocity of the capsule in the stationary state. Therefore, $\boldsymbol{u}^\infty$ has to be determined by balancing the total gravitational pulling force and the total hydrodynamic drag force on the capsule.

For the calculation of the flow field the deformability of the capsule is not relevant and the capsule can be viewed as a general immersed body of revolution B. For the calculation of the total hydrodynamic drag force and for the calculation of the capsule shape we need the surface force field $\boldsymbol{f} = \sigma \cdot \boldsymbol{n}$ generated by the flow, where $\boldsymbol{n}$ is the local surface normal. This is the only property of the fluid flow entering the shape equations for the capsule and the equation for the sedimenting velocity $|\boldsymbol{u}^\infty|$.

In the lab frame we are looking for solutions with vanishing pressure and velocity at infinity. The Green's function for these boundary condition is the well-known Stokeslet[148] (also called Oseen-Burgers tensor), that is the fluid velocity $\boldsymbol{u}$ at $\boldsymbol{y}$ due to a point-force $-\boldsymbol{F}_p$ at $\boldsymbol{x}$

$$\boldsymbol{u}(\boldsymbol{y}) = -\frac{1}{8\pi\mu}\mathsf{G}(\boldsymbol{y}-\boldsymbol{x})\cdot\boldsymbol{F}_p$$

with the Stokeslet G whose elements are in Cartesian coordinates ($x = |\boldsymbol{x}|$)

$$\mathsf{G}_{ij}(\boldsymbol{x}) = \frac{\delta_{ij}}{x} + \frac{x_i x_j}{x^3}.$$

This is the basis of the boundary integral approach for a solution of the Stokes equation, where we want to find the correct distribution of point forces to match the "no-slip" condition on the capsule surface.

Due to the axisymmetry we can integrate over the polar angle and find the velocity due to a ring of point forces with a local force density[149] $-\boldsymbol{f}$ as

$$\boldsymbol{u}(\boldsymbol{y}) = -\frac{1}{8\pi\mu}\mathsf{M}(\boldsymbol{y},\boldsymbol{x})\cdot\boldsymbol{f},$$

with a matrix M, which can be calculated by integration of the Stokeslet G with respect to the polar angle. Integrating over all point forces on the surface, we find the general solution[150] of the Stokes equation for an axisymmetric point force distribution on the surface of the body of revolution $\mathfrak{B}$,

$$u_\alpha(\boldsymbol{y}) = -\frac{1}{8\pi\mu}\int_C \mathrm{d}s(\boldsymbol{x})\mathsf{M}_{\alpha\beta}(\boldsymbol{y},\boldsymbol{x})f_\beta(\boldsymbol{x}). \tag{56}$$

Here, Greek indices denote the component in cylindrical coordinates, i.e. $\alpha,\beta = r,z$ (with $u_\varphi = f_\varphi = 0$ for symmetry reasons and hereafter omitted). The integration in eq. (56) runs along the path C given by the generatrix, i.e., the cross-section of the boundary $\partial\mathfrak{B}$, with arc length $s(\boldsymbol{x})$.

This representation of a Stokes flow in terms of a *single-layer potential* (using only the Stokeslet and not the Stresslet) is possible as long as there is no net flow through the surface of the capsule[31]

$$\int \mathrm{d}A\,(\boldsymbol{u}-\boldsymbol{u}_0)\cdot\boldsymbol{n} = 0$$

which is reasonable for the motion of a closed capsule (or even a porous one without sinks or sources in the interior).

[148] We are looking for solutions of

$$0 = \nabla\cdot\sigma + \boldsymbol{F}_p\delta(\boldsymbol{x}).$$

Taking the divergence of this equation we see (since $\nabla\cdot\boldsymbol{u} = 0$)

$$\Delta p = -\boldsymbol{F}_p\cdot\nabla\delta(\boldsymbol{x})$$

or (say from electrostatics)

$$p = \frac{\boldsymbol{F}_p\cdot\boldsymbol{r}}{4\pi|\boldsymbol{x}|^3}$$

which gives the Stokeslet, when set into the Stokes equation.

[149] The sign convention is such that (by virtue of Newton's third law) the force on the surface of the capsule is $\boldsymbol{f}$.

[150] The elements of the matrix kernel M are given in the appendix.

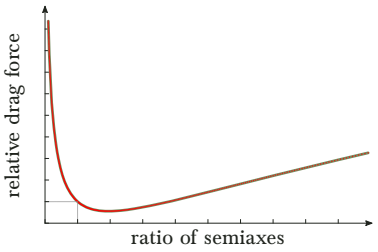

Figure 70: Perrin factors, i.e. the drag of a spheroid with radial semiaxes a and axial semiaxis b relative to a sphere of same volume moving with the same velocity, computed with our numerical method (red dots). For comparison we show the analytical result (green line) with which our results agree very well. The scale of the axes is indicated by the thin grey lines which correspond to a sphere.

According to the "no-slip" condition we have (working in the lab frame) $\boldsymbol{u} = -\boldsymbol{u}^\infty$ at every point $\boldsymbol{y} \in \partial\mathfrak{B}$ on the surface, this results in the equation

$$u_\alpha^\infty = \frac{1}{8\pi\mu} \int_C \mathrm{d}s(\boldsymbol{x}) \mathsf{M}_{\alpha\beta}(\boldsymbol{y},\boldsymbol{x}) f_\beta(\boldsymbol{x}) \qquad (\text{for } \boldsymbol{y} \in \partial\mathfrak{B}), \tag{57}$$

which can be used do determine the surface force distribution.

To numerically solve the integral for the surface force $f(\boldsymbol{x}_i)$ at a given set of points $\{\boldsymbol{x}_i\}$ $(i = 1, \ldots, N)$ we employ a simple collocation method, i.e., we choose a discretized representation of the function $f_\beta(\boldsymbol{x})$ and approximate the integral in (57) by the rectangle method.

This leads to a system of linear equations

$$\boldsymbol{U} = \tilde{\mathsf{M}}\boldsymbol{F}$$

with the "super-vectors"

$$\boldsymbol{U} = (u^\infty(\boldsymbol{y}_1)_r, u^\infty(\boldsymbol{y}_1)_z, \ldots, u^\infty(\boldsymbol{y}_N)_r, u^\infty(\boldsymbol{y}_N)_z) = (0, u^\infty, \ldots, 0, u^\infty)$$
$$\boldsymbol{F} = (f(\boldsymbol{x}_1)_r, f(\boldsymbol{x}_1)_z, \ldots, f(\boldsymbol{x}_N)_r, f(\boldsymbol{x}_N)_z)$$

and a matrix (using numbered indices $r \widehat{=} 0$, $z \widehat{=} 1$ for a more compact notation)

$$\tilde{\mathsf{M}}_{2i+\alpha-1,2j+\beta-1} = \frac{1}{8\pi\mu}(s(\boldsymbol{x}_{j+1}) - s(\boldsymbol{x}_j))\mathsf{M}_{\alpha\beta}(\boldsymbol{y}_i,\boldsymbol{x}_j).$$

Due to singularities[151] in the diagonal components of M, the two sets of points, the nodes of the collocation scheme $\{\boldsymbol{x}_i\}$ and the points at which the velocity is evaluated $\{\boldsymbol{y}_i\}$ must be distinct (or M otherwise regularised), so that $2N$ points of the surface are needed and the solution is the surface force at every other point. For use in the shape equations we then decompose this surface force into one component acting normal to the surface, the hydrodynamic pressure p_n, and another component acting tangential to the surface, the shear-pressure p_s.

We note that we usually restrict our computations to the bare minimum, i.e., the surface forces needed for the calculation of the capsule shape but, thereby, have all necessary information to reconstruct the whole velocity field in the surrounding liquid as shown in Fig. 62. The possibility to limit the computation to the needed surface forces is the great advantage of our approach to the solution of the Stokes equation in comparison to other approaches that rely on the velocities or the stream function in the whole domain[30, 32].

We validated our algorithm and implementation using exactly known results as for example the Perrin factors[30, 33] for the total drag of a spheroid[152] with given semiaxes (a in radial direction and b axially). Denoting the ratio of total drag of the spheroid and the drag of a sphere of same volume moving with the same velocity by Ξ and the ratio of semiaxes $b/a = \xi$, one can (e.g. by solving the stream function in ellipsoidal coordinates) derive the following result

$$\Xi = \begin{cases} \xi^{-1/3} \left(\frac{3}{4}\sqrt{\xi_p^2 - 1}(-\xi_p + (\xi_p^2 + 1)\,\mathrm{artanh}(\xi_p^{-1})) \right)^{-1} & \xi \geq 1 \\ \xi^{-1/3} \left(\frac{3}{4}\sqrt{\xi_o^2 + 1}(\xi_o - (\xi_o^2 - 1)\,\mathrm{atan}(\xi_o^{-1}) \right)^{-1} & \xi < 1 \end{cases}$$

with the short-hand notations

$$\xi_p = \sqrt{1 - \xi^{-2}}^{-1}$$
$$\xi_o = \sqrt{\xi^{-2} - 1}^{-1}.$$

[151] There is a logarithmic singularity, that is integrable. One might feel that there are more elaborate ways to handle such a singularity than simply integrating over it. However, these errors are of order $h \sim L/N$ at worst and we checked that our number of collocation points is sufficiently large by doubling it and finding no evidence for different results (usually we use $N = 10^3$).

[152] By the term spheroid we refer to an ellipsoid with two degenerate semiaxes, i.e. the body whose surface can be parametrised by

$$\boldsymbol{r} = \begin{pmatrix} a\cos\theta\sin\varphi \\ a\sin\theta\sin\varphi \\ b\cos\theta \end{pmatrix}$$

with the semiaxes $a,b \in \mathbb{R}^+$, the polar angle $0 \leq \varphi \leq 2\pi$ and the parametric latitude $0 \leq \theta \leq \pi$.

We compare our results to this analytical expression in Fig. 70.

Here, we used a "no-slip"-condition, that is the velocity directly at the surface of the immersed body vanishes in its resting frame. This is easily extended to the case of a non-vanishing tangential slip velocity[153]. This will allow us to generalise the approach to model *active* swimmers [34, 35] whose active locomotion can be captured by means of an effective flow field which is called the *squirmer model*[36, 37].

[153] A normal velocity on the surface in the capsule's resting frame would conflict with its impenetrability and could also lead to a net flux of fluid through the capsule, which we cannot incorporate using only the single-layer potential.

Solution of the shape equations.

The boundary conditions for a shape that is closed and has no kinks at its poles are

$$r(0) = r(L_0) = \psi(0) = \pi - \psi(L_0) = 0, \tag{58}$$

and we can always choose[154] $z(0) = 0$. For the solution of the shape equations it is important that there is no net force on the capsule as the shape equations are derived from force equilibrium. Therefore, the total hydrodynamic drag force and the total gravitational force have to be equal, which determines the resulting sedimenting velocity for a given strength of gravity. If hydrodynamic drag and gravitational pull cancel each other in a stationary state, there is no remaining point force at the poles needed to ensure equilibrium and, thus,

[154] In the presence of gravity there is no translational symmetry along the axial direction, but shifting the capsule as a whole just adds a constant to the hydrostatic pressure $-g\Delta\rho z \to -g\Delta\rho(z + z_0)$ which is absorbed into the static pressure p_0 under volume control. This becomes relevant when considering capsules under pressure control.

$$q(0) = q(L_0) = 0. \tag{59}$$

The shape equations have (removable) singularities at both poles; therefore, a numerical solution has to start at both poles requiring 12 boundary conditions [155] out of which we know 7 (by eqs. (58) and (59) and $z(0) = 0$). The 5 remaining parameters[156] can be determined by a shooting method using that the solution starting at $s_0 = 0$ and the one starting at $s_0 = L_0$ have to match continuously in the middle, which gives 6 matching conditions (r, z, ψ, τ, m, q). This gives an over-determined non-linear set of equations which we solve iteratively using linearisations. However, as in the static case [38], the existence of a solution to the resulting system of linear equations (the matching conditions) is ensured by the existence of a first integral (see appendix) of the shape equation. In principle, this first integral could be used to cancel out the matching condition for one parameter (e.g. q), and, thus, we have 5 independent equations to determine 5 parameters, and the system is not genuinely over-determined. We found the approach using an over-determined system to be better numerically tractable, where we ultimately used a multiple shooting method including several matching points between the poles. For the data presented in the following we used a fourth-order Runge-Kutta scheme with step-width $\Delta s_0 = 5 \cdot 10^{-5} R_0$.

[155] These are

$$\left.\begin{pmatrix} r \\ z \\ \psi \\ \tau_s \\ m_s \\ q \end{pmatrix}\right|_{s=0} \text{and} \left.\begin{pmatrix} r \\ z \\ \psi \\ \tau_s \\ m_s \\ q \end{pmatrix}\right|_{s=L}.$$

[156] These are

$$\left.\begin{pmatrix} \tau_s \\ m_s \end{pmatrix}\right|_{s=0} \text{and} \left.\begin{pmatrix} z \\ \tau_s \\ m_s \end{pmatrix}\right|_{s=L}.$$

Using these boundary conditions, it is straightforward to see that the shape equations do not allow for a solution whose shape is the reference shape, unless there are no external loads ($p_s = p = l = 0$).

Iterative solution of shape and flow, determination of sedimenting velocity

We find a joint solution to the shape equations and the Stokes equation by solving them separately and iteratively, as illustrated in the scheme in Fig. 71, to converge to the desired solution: We assume a fixed axisymmetric shape

and calculate the resulting hydrodynamic forces on the capsule for this shape. Then, we use the resulting hydrodynamic surface force density to calculate a new deformed shape. Using this new shape we re-calculate the hydrodynamic surface forces and so on. We iterate until a fixed point is reached. At the fixed point, our approach is self-consistent, i.e., the capsule shape from which hydrodynamic surface forces are calculated is identical to the capsule shape that is obtained by integration of the shape equation under the influence of exactly these hydrodynamic surface forces.

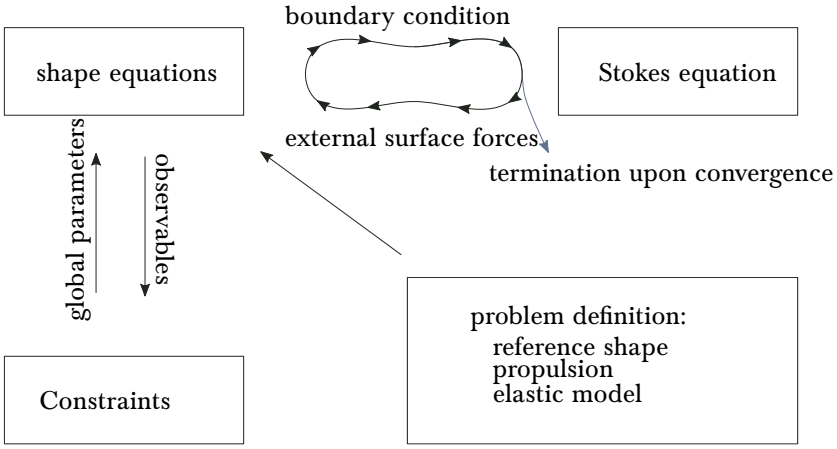

Figure 71: Iterative scheme for the solution to the problem of elastic capsules in Stokes flow. Details of the iterative scheme are given in the main text.

For each capsule shape during the iteration, we can determine its sedimenting velocity $u = |\boldsymbol{u}^\infty|$ by requiring that the total hydrodynamic drag force equals the total gravitational force,

$$g_0 \Delta\rho V_0 = -\int_C \mathrm{d}s(\boldsymbol{x}) 2\pi r(\boldsymbol{x}) f_z(\boldsymbol{x}) \tag{60}$$

The integration runs along the path C given by the generatrix, i.e., the cross section of the boundary $\partial\mathfrak{B}$, with arc length $s(\boldsymbol{x})$. By changing $u = |\boldsymbol{u}^\infty|$ we can adjust the hydrodynamic drag forces on the right hand side to achieve equality for a given capsule shape during the iteration. During the iteration u will converge to the proper sedimenting velocity for the stationary state.

The Stokes equation is linear in the velocity, and we can just scale the resulting surface forces accordingly, if we change the velocity parameter u. In this way, the global force balance can be treated the same way as other possible constraints like a fixed volume. Numerically, it is impossible to ensure the exact equality of the drag and the drive forces in eq. (60). Demanding a very small residual force difference makes it difficult to find an adequate velocity, a too large force difference makes it impossible to find a solution with small errors at the matching points. Global force balance (60) is equivalent to the condition[157]

$$X(L) = -2\pi \int_0^L \mathrm{d}s\, r(p\cos\psi + p_s \sin\psi) = 0,$$

for the parameter $X(L)$, which is related to the first integral of the shape equations, see eq. (63).

The iteration starts with a given (arbitrary) stress, e.g., one corresponding to the flow around the reference shape. For the resulting initial capsule shape, the Stokes flow is computed and the resulting stress is then used to start the iteration. If, during the iteration, the new and old stress differ strongly it might

[157] To monitor global force balance numerically, we use a criterion $|X(L)| < 10^{-5}$, which turns out to be a good compromise for a numerical force balance criterion.

be difficult to find the new shooting parameters for the capsule shape and the right sedimenting velocity starting at their old values. To overcome this technical problem, we use a convex combination $\sigma = \alpha\sigma_{\text{new}} + (1-\alpha)\sigma_{\text{old}}$ of the two stresses and slowly increase the contribution α of the new stress until it reaches unity. The resulting capsule shape for $\alpha = 1$ is used to continue the iteration. The iteration continues until the change[158] within one iteration cycle is sufficiently small. If there are multiple stationary solutions at a given gravitational strength the iterative procedure will obviously only find one. Therefore we also use continuation of solutions to other parameters (different gravitational strength or bending modulus) to get closer to the full set of solutions.

In total, this allows for a joint solution of the shape equations and the Stokes equation to find the stationary shape and the sedimenting velocity at rather small numerical cost.

[158] We monitor the convergence of our iteration in the global parameters, i.e. the pressure and velocity, and the global geometrical quantities contour length of the generatrix, surface area, volume (if not fixed). These are computed with little overhead (volume and length have to be integrated) and allow for a effective measurement of convergence.

Control parameters and non-dimensionalisation

In order to identify the relevant control parameters and reduce the parameter space, we introduce dimensionless quantities by measuring lengths in units of the radius R_0 of the spherical rest shape of the capsule, energies in units of $Y_{2D}R_0^2$ (i.e., tensions in units of Y_{2D}) and times in units of $R_0\mu/Y_{2D}$ in the remainder of the paper. This results in the following set of control parameters for the capsule shape:

1. Our elastic law is fully given by the dimensionless bending modulus

$$\tilde{E}_B \equiv \frac{E_B}{Y_{2D}R_0^2}. \tag{61}$$

   In general, elastic properties also depend on the Poisson ratio ν but we limit ourselves to $\nu = 1/2$ as explained above. Using the thin-shell result (53) the dimensionless bending modulus $\tilde{E}_B = (H/9R_0)^2$ also determines the shell thickness H for an isotropic shell material.

2. The gravitational (or centrifugal) pull $g_0\Delta\rho$ is measured in units of Y_{2D}/R_0^2 in the following. The dimensionless parameter g then takes the form of a Bond (or Eötvös) number[39],

$$g = \text{Bo} \equiv \frac{g_0\Delta\rho R_0^2}{Y_{2D}}, \tag{62}$$

   where the elastic tension Y_{2D} is used instead of a liquid surface tension.

3. The static pressure p_0 within the capsule is measured in units of Y_{2D}/R_0.

4. The resulting sedimenting velocity u is measured in units of Y_{2D}/μ.

We conclude that the resulting stationary sedimenting shapes of the capsule are fully determined by two dimensionless control parameters if the capsule volume is fixed: (i) the dimensionless bending modulus $\tilde{E}_B$ or its inverse, the Föppl-von-Kármán number $\gamma_{\text{FvK}} = 1/\tilde{E}_B$ characterises the elastic properties of the capsule (by the typical ratio of bending to stretching energy) and (ii) the Bond number describes the strength of the driving force (relative to elastic deformation forces). If the capsule pressure is controlled rather than its volume, the dimensionless pressure p_0 provides a third parameter, see appendix starting on page 129. Because stationary shapes are independent of time, they do not depend on the solvent viscosity.

Results for passive sedimentation

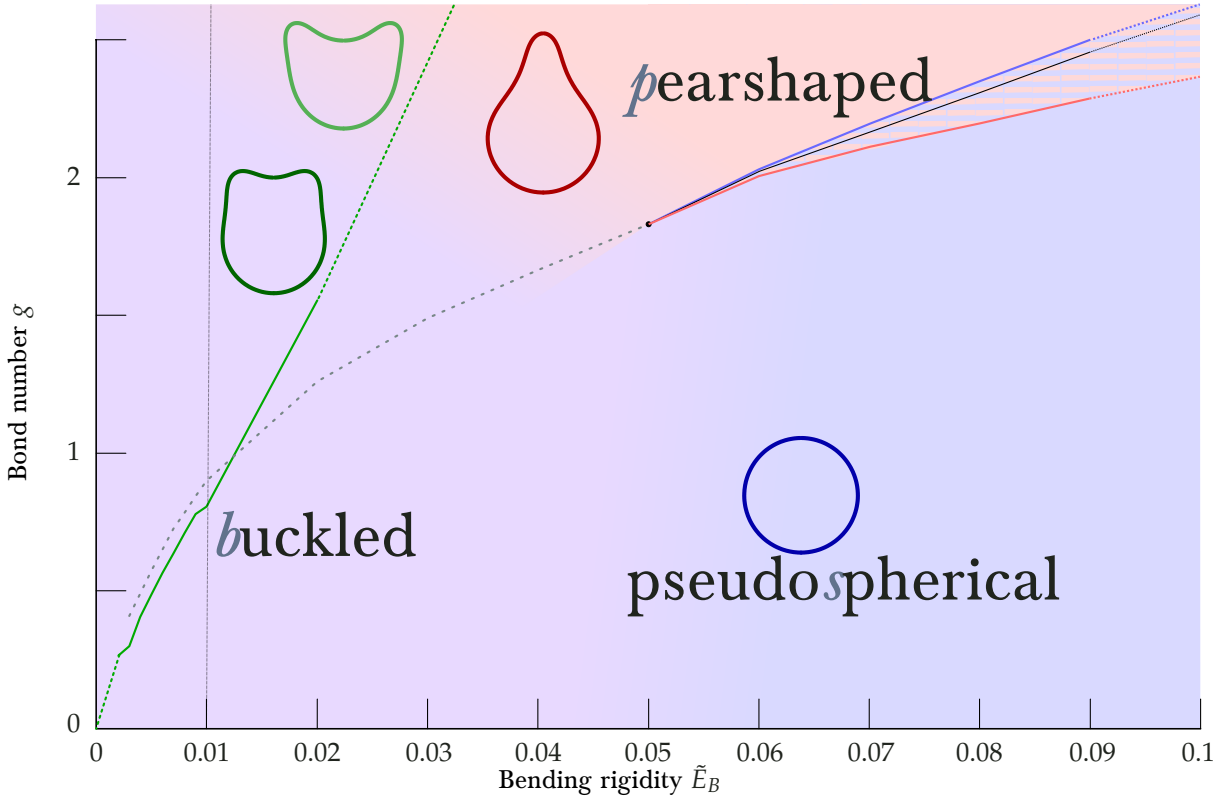

Figure 72: Stationary axisymmetric shapes for a sedimenting Hookean capsule with spherical reference shape in the parameter plane of the two control parameters, the dimensionless bending modulus $\tilde{E}_B$ (the inverse of the Föppl-von-Kármán number γ_{FvK}) and the dimensionless gravity g (the Bond number Bo). We find pseudospherical (blue), pear-shaped (red), and a pair of strongly (light green) and weakly (dark green) buckled shapes. The black line is a line of discontinuous shape transitions between pear and pseudospherical shape which terminates in a critical point beyond which a sphere transforms smoothly into the pear shape. The blue and red lines are spinodals indicating the limits of stability of the pseudospherical and pear-shaped shapes, respectively. Above the solid green line the pair of buckled shapes occur in a bifurcation; the dotted continuation of the solid line signals numerical difficulties in following this bifurcation line.

In this section we present the results for stationary axisymmetric sedimenting shapes and stationary sedimenting velocities as obtained by the fixed point iteration method. We focus on elastic capsules with spherical rest shape and address the sedimentation of capsules under volume control ($V = V_0 = \text{const}$) and under pressure control ($p_0 = \text{const}$). Additionally, we show the results for a capsule that is driven (or pulled) by a localised force rather than a homogeneous acceleration. In accordance with common experience, all our figures are oriented so that gravity acts “downward”, i.e., in negative z-direction.

Volume control

For a spherical rest shape of the capsule the prescribed dimensionless volume is $V = 4\pi/3$. Under volume control we also use this value as the prescribed fixed volume $V_0 = 4\pi/3$. In principle, it is also possible to prescribe volumes different from the rest shape volume. This will be done using pressure control in the appendix below. For the static case, the only stationary shape at fixed volume is the strictly spherical shape, regardless of the bending modulus. This is different for a sedimenting capsule, which displays various shape

transitions already at fixed volume.

Shape diagram.

To alleviate the numerical search for a solution under volume control, we use a finite target interval ($\Delta V = 5 \cdot 10^{-3}$) for the capsule volume. Every shape obtained in this way has slightly different volume, and we have to rescale the shape (and, accordingly, every quantity that scales with the shape) to the volume of the reference shape to eliminate the noise induced by the varying volume. As we are interested in strict volume control, we will apply this rescaling procedure where necessary without explicitly stating it.

We investigated stationary axisymmetric capsule shapes for gravity strengths (Bond numbers) up[159] to $g = g_{\max} = 2.5$ and bending moduli $\tilde{E}_B \in [10^{-3}, 10^{-1}]$ corresponding to Föppl-von-Kármán numbers $\gamma_{\mathrm{FvK}} = [10, 1000]$. For high Bond and Föppl-von-Kármán numbers, the iteration procedure becomes numerically more demanding[160], but remains possible in principle.

[159] Usually using a resolution of $\Delta g = 0.005$.

[160] Higher forces ask for finer discretisation of the shape equations, smaller distances between solutions in parameter space ask for a more thorough fixed point search.

We summarise our findings regarding the axisymmetric sedimenting shapes in the shape diagram Fig. 72 in the plane of the two control parameters $(\tilde{E}_B, g)$. Overall, we identify three classes (also shown in Fig. 62) of axisymmetric shapes:

1. Pseudospherical shapes. For shapes very close to the reference sphere we find[161] $u \approx 2g/9$. Additionally, the pressure due to gravity is then $p_0 = g\langle z \rangle \approx g$.

2. Pear shapes, which have a convex upper apex but develop an axisymmetric indentation at the side of the capsule. For high gravitational driving force (high sedimentation velocities) the pear shape resembles a tether with a high curvature at the upper apex.

3. Buckled shapes, which develop a concave axisymmetric indentation at the upper apex of the capsule. For fixed capsule volume, these buckled shapes always occur in pairs of a weakly buckled shape with a shallow and narrow indentation and a strongly buckled shape with a deep and wide indentation at the upper apex.

[161] We can use Stokes' law $F = 6\pi\mu R u$ and $F = 4/3\pi R^3 g_0 \Delta\rho$, which yields the stated result in reduced units.

Our solution method allows us to identify bifurcations or transitions between these classes of shapes as shown in Fig. 72. Upon increasing the gravity g or decreasing the bending rigidity $\tilde{E}_B$, the stationary sedimenting pseudospherical shape transforms into a pear shape. The black line in Fig. 72 is a line of *discontinuous* shape transitions between pseudospherical and pear shape, which terminates in a critical point at $g_c \simeq 1.85$ and $\tilde{E}_{B,c} \simeq 0.05$. At the discontinuous shape transition we find hysteresis with two spinodal lines (red and blue lines) indicating the limits of stability of pseudospherical and pear-shape shapes. For smaller dimensionless bending rigidities $\tilde{E}_B < \tilde{E}_{B,c}$, the spherical shape transforms *smoothly* into the pear shape upon increasing gravity. Discontinuous buckling transitions are also known from static spherical shells [40, 41], for example as a function of the external static pressure or an osmotic pressure [42]. That a line of discontinuous buckling transitions terminates in a critical point as a function of the elastic properties of the capsules is, however, unknown from static buckling transitions.

Within this smooth crossover regime between sphere and pear shapes at small bending rigidities, the pair of buckled shapes occurs in a bifurcation

for higher gravity strengths g above the solid green green line in Fig. 72. The spherical/pear shape also remains a stable solution above the green line, such that we have three possible stationary sedimenting shapes in this parameter regime. Which of these shapes is dynamically selected in an actual experiment, depends on the initial conditions. The dotted continuation of the solid line only signals numerical difficulties in following this bifurcation line. Likewise, above the upper dotted green line, numerical difficulties in tracing the buckled shapes occurred. We will investigate the nature of these shape bifurcations in more detail in the following.

The shape bifurcations into the pair of buckled shapes (upon crossing the solid green line in Fig. 72) can be identified by monitoring the pressure p_0 (the Lagrange parameter associated with the volume constraint) and the resulting sedimenting velocity u of the capsule as a function of the control parameters g or $\tilde{E}_B$. In Fig. 73, we show results for u and p_0 as a function of the control parameter g for fixed $\tilde{E}_B = 0.01$, i.e., along the vertical black dotted line in Fig. 72. Above a critical gravity threshold, velocity u and pressure p_0 bifurcate into three "solution branches" (indicated by different colours in Fig. 73): a continuous line that corresponds to a shape evolution from a pseudospherical to pear-shaped form and ultimately to a long extruded tether, and a pair of buckled shapes that have smaller (ultimately negative) curvature at the upper apex. To visualise the changes in the stationary states that occur along these branches with increasing gravity strength g, we show corresponding snapshots of the sedimenting shapes in Fig. 74.

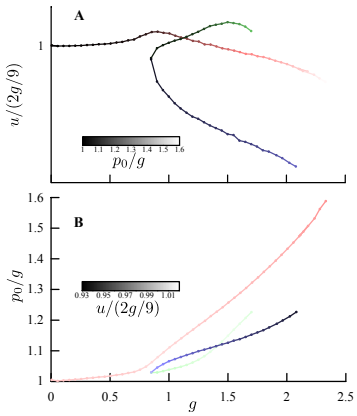

Figure 73: (A) Sedimentation velocity u and (B) dimensionless pressure p_0 for varying gravity g (at fixed bending modulus $\tilde{E}_B = 0.01$) rescaled relative to the result for a sphere. Above a critical gravity threshold g, we find a bifurcation into three branches: The red branch corresponds to pseudospherical shapes which smoothly develop into pear shapes. The blue and green branches represent the pair of buckled shapes: the blue line corresponds to the wide, strongly buckled shape, the green line to the narrow, weakly buckled shape. The colour hue identifies the different branches, whereas their lightness indicates the missing third parameter (see legends).

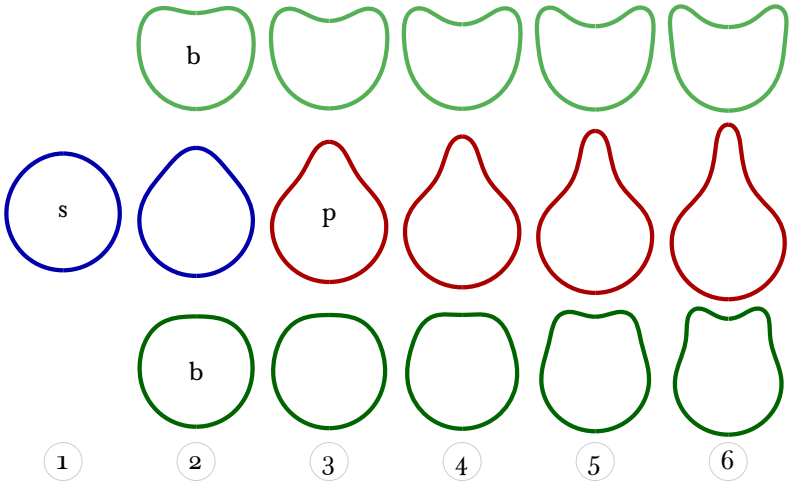

Figure 74: The generatrices of stationary sedimenting axisymmetric shapes for $\tilde{E}_B = 0.01$, corresponding to the dotted line in Fig. 72, in the range $g \in [0.7,1.7]$. The gravity strength g increases from left to right in steps of $\Delta g = 0.2$. The numbers allow for a localisation of these shapes in the force-velocity relation shown in Fig. 75.

Qualitatively, the shape transformations from a spherical shape into a pear shape or into buckled shapes are a result of buckling instabilities of a hydrodynamically stretched capsule at the upper part of the capsule. Starting from a spherical rest shape and increasing the gravitational force g the capsule acquires a higher sedimenting velocity and, thus, the fluid velocities increase (in the frame of the capsule). This stretches the capsule along the z-direction. The numerical results show, that the fluid flow generates a positive contribution p_n to the interior pressure at the bottom part of the capsule and a negative contribution at the upper part for all types of stationary shapes. The gravitational hydrostatic pressure contribution $-g_0\Delta\rho z$, on the other hand, generates a negative contribution on the upper part as compared to a vanishing contribution on the lower apex (by choice of the z-coordinate). Together with the positive volume pressure p_0, this results in a negative total normal pressure at the upper part and positive total pressure at the lower

part. Both for pear and buckled shapes, the negative total normal pressure at the upper part of the capsule, which is mainly caused by the gravitational hydrostatic pressure contribution, is the reason to develop indentations. In the transition from pseudospherical to pear-shapes capsules an axisymmetric indentation develops at the side of the capsule (see the shapes in the middle row in Fig. 74), because for an elongated stretched capsule, this part of the capsule has lower curvature and, thus, less stability with respect to buckling. At higher driving force g and sedimenting velocities, the indentation can also form at the upper apex (see top and bottom rows in Fig. 74), and the pair of buckled configurations become stable solutions.

Force-velocity relation

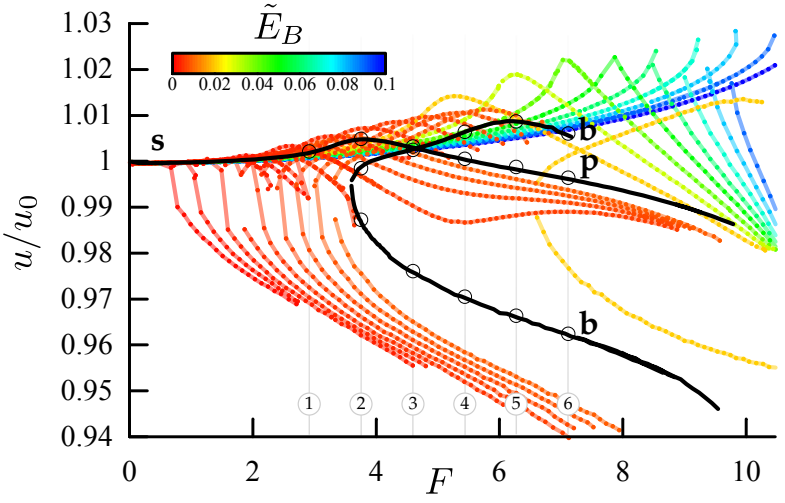

Figure 75: Force-velocity relations for sedimenting capsules under volume control. The plot shows the velocity relative to the (dimensionless) velocity $u_0 = 2g/9$ of a perfect sphere with the same volume (Stokes' law) as a function of the (dimensionless) total external force $F = 4\pi g/3$. The bending modulus $\tilde{E}_B$ is colour-coded. Two distinct branches can be distinguished: the solution branches corresponding to pseudospherical and pear shapes start at zero force. A pair of solution branches for strongly or weakly buckled shapes starts at a nonzero threshold force. The branches for $\tilde{E}_B = 0.01$ are marked in black as a typical example. The capsule shapes 1–6 in Fig. 72 are realised at the points marked by circles. It is also apparent that the transition from pseudospherical to pear shapes is continuous for $\tilde{E}_B \lessapprox 0.05$ and becomes discontinuous for $\tilde{E}_B \gtrapprox 0.05$.

All dynamic shape transitions reflect in bifurcations in the force-velocity relations. In Fig. 75, we show the force-velocity relations between sedimenting velocity u and gravity g for all stationary axisymmetric shapes and for a colour-coded range of bending rigidities $\tilde{E}_B = 10^{-3}$ to 10^{-1}. The total driving force F can be computed using the total drag from the fluid corresponding to the right hand side of eq. (60)) or as the product of the total mass difference and the sedimenting acceleration $F = g_0 \Delta\rho V_0$ or $F = 4\pi g/3$ (in dimensionless form) corresponding to the left hand side of eq. (60). The leading contribution of the force-velocity relation is given by the force-velocity relation of a perfect sphere, which is Stokes' law $u = u_0 = F/6\pi = 2g/9$ (in dimensionless form). To eliminate this leading contribution, we show the relative velocity u/u_0 in Fig. 75. By definition, the relative velocity is also proportional to the *sedimentation coefficient*, which is defined as v/g_0 and a standard quantity in centrifugation and sedimentation experiments [43].

Fig. 75 clearly shows two qualitatively different types of force-velocity curves. The force-velocity curves corresponding to pseudospherical or pear shapes with positive curvature at both apexes start at zero force, whereas the solution curves corresponding to the weakly and strongly buckled shapes bifurcate at a nonzero threshold force with a vertical tangent and have two branches: The weakly buckled shapes with a narrow indentation have a higher sedimenting velocity and correspond to the upper branch, the strongly buckled shapes have a lower sedimenting velocity and correspond to the

lower branch.

We note that, because of the g-dependence of u_0, the absolute sedimenting velocities u are increasing with the gravity for both buckled shapes, although u/u_0 is decreasing for the strongly buckled shapes. Above the threshold force for the buckled shapes, three different axisymmetric sedimenting capsule shapes can occur with different sedimenting velocities for the same gravitational driving force. Which of these shapes is dynamically selected in an actual experiment, depends on the initial conditions.

The force-velocity curves for the pseudospherical or pear shapes allow us to detect how the transition between spherical and pear shapes evolves into a discontinuous transition: Fig. 75 shows that these force-velocity curves develop a *cusp* close to the critical point for $\tilde{E}_B \approx E_{B,c} \simeq 0.05$, whereas they remain smooth for $\tilde{E}_B < E_{B,c}$. For $\tilde{E}_B > E_{B,c}$, we find two overlapping and intersecting velocity branches, which corresponds to the characteristic hysteretic velocity switching in a discontinuous transition. In fact, we identify the discontinuous transition line in Fig. 72 by these velocities: if the two branches coexist we localise the transition at the crossing of the two $u(g)$ curves. For $\tilde{E}_B < E_{B,c}$, the velocity curve still exhibits a maximum, which we can use to define the crossover line between the pseudospherical and pear shape as it is shown in the shape diagram Fig. 72. The discontinuous nature of the sphere-pear transition is confirmed by monitoring other quantities, such as the capsule area, as a function of the gravity g. As illustrated in Fig. 76, the area clearly exhibits hysteretic switching at the transition. The pair of weakly and strongly buckled solutions appears in a bifurcation above a critical driving force. Also this bifurcation reflects in a corresponding bifurcation of the capsule area as shown in the inset of Fig. 76.

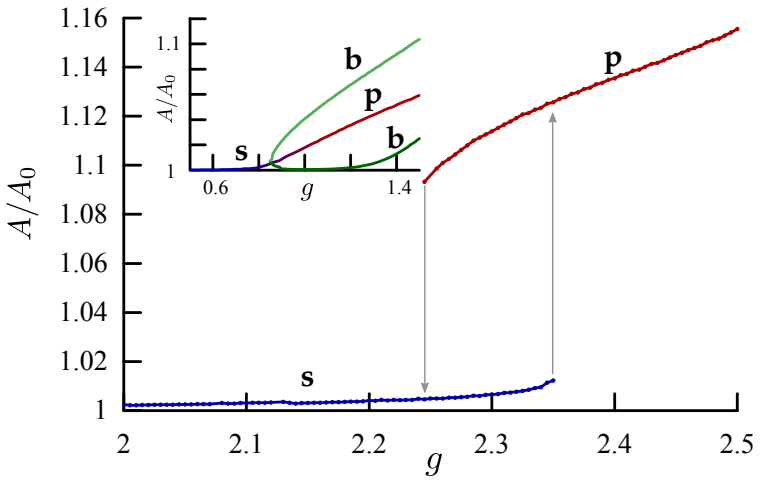

Figure 76: Reduced capsule area as a function of the dimensionless gravity strength g for a high bending modulus $\tilde{E}_B = 0.08$. There is an interval where pseudospherical and pear-shaped solutions with different area coexist with hysteretic switching upon increasing and decreasing g. Inset: For $\tilde{E}_B = 0.01$, the area changes continuously from pseudospherical to pear shapes. For the pair of weakly and strongly buckled solutions the area bifurcates at a critical g.

Transition mechanism

Qualitatively, the shape transformations from a spherical shape into a pear shape or into buckled shapes are a result of buckling instabilities of a hydrodynamically stretched capsule at the upper part of the capsule. Upon increasing the gravitational force g the capsule acquires a higher sedimenting velocity and stretches along the z-direction. This stretching is essential as it provides the excess area necessary for a shape transformation out of a spherical rest shape, which has the minimal area for the fixed volume.

The numerical results show that the fluid flow generates a negative (com-

pressive) contribution p_n to the interior pressure at the bottom part of the capsule and a positive (dilatational) contribution at the upper part for all types of stationary shapes (see orange arrows in Fig. 62). The gravitational hydrostatic pressure contribution $-g_0\Delta\rho z$, on the other hand, generates a negative contribution on the upper part as compared to a vanishing contribution on the lower apex [162]. Together with the positive volume pressure p_0, this results in a compressive negative total normal pressure at the upper part and dilatational positive total pressure at the lower part. Both for pear and buckled shapes, the negative total normal pressure at the upper part of the capsule, which is mainly caused by the gravitational hydrostatic pressure contribution, is the reason to develop indentations. In the transition from pseudospherical to pear-shaped capsules an axisymmetric indentation develops at the side of the capsule [163], because for an elongated stretched capsule, this part of the capsule has lower curvature and, thus, less stability with respect to buckling. At higher driving force g and sedimenting velocities, the indentation can also form at the upper apex[164], and the pair of buckled configurations become stable solutions.

[162] This is by choice of the z-coordinate.

[163] See the shapes in the middle row in Fig. 72.

[164] See top and bottom rows in Fig. 72.

An approximative limit for the stability of the spherical shape can be given in terms of the classical buckling pressure [26, 40, 41] $p_c = -4\sqrt{\tilde{E}_B}$ in dimensionless units. We first note that the height of a sphere is $z_{\max} \approx 2$ and that the static pressure contribution needed to maintain a constant volume against the hydrostatic pressure is $p_0 \approx g\bar{z}$, where $\bar{z} \approx 1$ is the z-component of the centre of mass. This gives an effective compressive pressure $p_0 - gz_{\max} \approx -g$ at the upper apex[165]. If this compressive pressure exceeds the classical buckling pressure, i.e., $g \gtrsim |p_c|$ the spherical shape is unstable with respect to indentations at the upper side of the capsule, which leads to the pear shape. A parameter dependence $g \propto \sqrt{\tilde{E}_B}$ describes the boundary between spherical and pear-shape in the shape diagram Fig. 72 well.

[165] The compressive hydrodynamic contribution $p_n > 0$ is smaller and can be neglected compared to relative to hydrostatic and static pressure.

The termination of the line of discontinuous transitions between sphere and pear shapes terminating in a critical point is a result of the deformation of the capsule by the fluid flow prior to the shape transition: Increasing the gravity g gives rise to a hydrodynamic stretching of the upper part of the capsule. The smaller the dimensionless bending rigidity $\tilde{E}_B$, the smaller is the meridional curvature $\varkappa_s$ in the upper part. For soft capsules, the meridional curvature vanishes *before* the effective compressive pressure becomes comparable to the buckling pressure. (see, for example, the second shape in the middle row in Fig. 72 for $\tilde{E}_B = 0.01$). For a flat shell segment, however, buckling becomes continuous and does not require a threshold normal pressure. Rigid capsules, on the other hand, remain curved upon increasing the gravity g up to the discontinuous buckling induced by the normal pressure in the upper part of the capsule.

For the bifurcation line of the two buckled shapes in the shape diagram Fig. 72, we find an approximately linear dependence $g \propto \sqrt{\tilde{E}_B}^{1.7}$ from fitting our numerical results. Currently, we have no simple explanation for this result.

Rotational stability

We always assumed axisymmetric shapes that perform a rotation-free sedimentation, i.e., stability with respect to rotation or tilt of the shape. The question whether the sedimentation motion of an axisymmetric rigid body is rotationally stable can be reduced [30] to the question whether the so-called

centre of hydrodynamic stress lies above or below the centre of mass; both points have to be on the symmetry axis. In general, sedimenting bodies will tilt in a way that aligns the connection vector of the centres of mass and hydrodynamic stress with the direction of gravity [44] or start to rotate. The centre of hydrodynamic stress is the point about which the translational and rotational motions decouple. Thus, the computation of the centre of hydrodynamic stress requires additional information not available within our approach, e.g., the rotational resistances for swirling motions around axes perpendicular to the axis of symmetry [45].

In the appendix, see page 129, we present a stability argument that only uses the information available to us. The result of this analysis is exemplarily shown in Fig. 77 for $\tilde{E_B} = 0.01$. We find that the centre of hydrodynamic stress z_0 lies almost always below the centre of gravity z_{cm} for all three classes of shapes, pseudospherical, pear-shaped and buckled such that the shapes are linearly stable against out-of-axis rotations. Only solutions in the pear-shape class for very high gravity forces $g \gtrsim 2.2$ are unstable. These shapes exhibit a very pronounced tether-like extrusion.

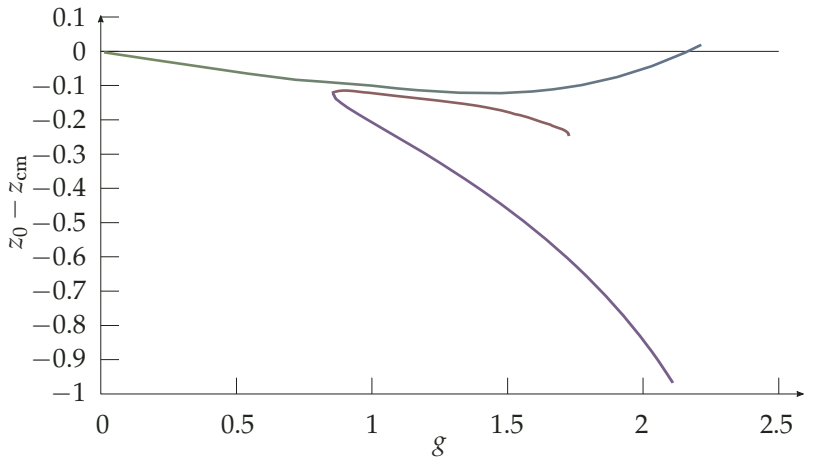

Figure 77: Linear analysis concerning rotational stability for $\tilde{E_B} = 0.01$. We show the difference $z_0 - z_{\mathrm{cm}}$ between the centre of hydrodynamic stress z_0 and the centre of gravity z_{cm} as a function of the dimensionless gravity strength g for all three solution branches (green to blue: pseudospherical to pear-shaped, red, violet: buckled). For $z_0 - z_{\mathrm{cm}} < 0$, i.e., below the gray line, the shape is linearly stable against out-of-axis rotations. Only solutions with a very pronounced tether extrusion at high g are unstable.

Accessible parameter space

With the shape diagram in Fig. 72 we have a complete overview of theoretically possible shapes and transitions between them in the plane of the two control parameters, the dimensionless bending rigidity $\tilde{E}_B$ or its inverse, the Föppl-von-Kármán number $\gamma_{\mathrm{FvK}} = 1/\tilde{E}_B$, and the Bond number $\mathrm{Bo} = g$. There are three limitations, however, to the accessible parameter range.

First, our analysis is limited to the regime of low Reynolds numbers because we used the Stokes equation to describe the fluid flow. The Reynolds number for the sedimenting capsule is given by $\mathrm{Re} = v\rho R_0/\mu$. To leading order the sedimenting velocity is given by Stokes' law $v = g_0\Delta\rho V/6\pi\mu R_0$ resulting in $\mathrm{Re} = 2g_0\Delta\rho\rho R_0^3/9\mu^2$. A criterion $\mathrm{Re} < 1$ limits the accessible Bond numbers to $g < g_{\mathrm{max,\,Re}} \sim 9\mu^2/2\rho R_0 Y_{2\mathrm{D}}$. For water as solvent we have $g_{\mathrm{max,\,Re}} \sim 5 \times 10^{-9} R_0^{-1} Y_{2\mathrm{D}}^{-1}$ N. This can be easily increased by a factor of 100 in a more viscous solvent. For a capsule of size $R_0 \sim 10\mu$m in water, the criterion $g < g_{\mathrm{max,\,Re}}$ corresponds to a condition that the acceleration should remain smaller than 5000 times the standard gravity.

Second, the sedimenting force is very small for gravitation; it is much larger for a centrifuge but also modern ultracentrifuges are limited to accelerations about 10^6 times the standard gravity [43]. With a typical density difference of

$\Delta\rho = 10^2\,\mathrm{kg/m^3}$ (10% of the density of water) we find that the Bond number is limited in available centrifuges to $g < g_{\max,\,\mathrm{cf}} \sim 10^9 R_0^2 Y_{2D}^{-1}\,\mathrm{N/m^3}$.

Both of these constraints give an upper bound for the accessible Bond number range. The constraints are size-dependent, however: For small capsule sizes $R_0 \lesssim 1\,\mu\mathrm{m}$, for example for viruses, the centrifuge constraint is more restrictive, whereas for larger capsule sizes $R_0 \gtrsim 1\,\mu\mathrm{m}$, the low Reynolds number constraint is more restrictive. The latter case is typical for all synthetic capsules, red blood cells or artificial cells consisting of a lipid bilayer and a filamentous cortex, which all have capsule sizes in the range $R_0 \gtrsim 10$ to $1000\mu\mathrm{m}$.

Third, it is not possible to realise arbitrarily large dimensionless bending rigidities $\tilde{E}_B$ or small Föppl-von-Kármán numbers in experimentally available capsules. For isotropic elastic shell materials the relative shell thickness determines this parameter, $\tilde{E}_B \sim (H/R_0)^2$, see eq. (53), and values $\tilde{E}_B \gtrsim 0.01$ are difficult to realise with synthetic capsules. Also viruses follow this law (with a shell thickness $H \sim 2\mathrm{nm}$) resulting in Föppl-von-Kármán numbers $\gamma_{\mathrm{FvK}} \gtrsim 60$ or $\tilde{E}_B \lesssim 0.02$ with $\tilde{E}_B$ decreasing with increasing virus size [46]; small viruses with $R_0 \sim 15\mathrm{nm}$ realise the largest values of $\tilde{E}_B$.

Also red blood cells have similar values of $\tilde{E}_B$ although they are elastically strongly anisotropic because they consist of a lipid bilayer and a spectrin cytoskeleton. The liquid lipid bilayer dominates the bending modulus $E_B \sim 50 k_B T$, whereas the shear modulus is determined by the filamentous spectrin cortex or skeleton. Filamentous networks typically have low shear moduli, for example $G_{2D} \sim \mu\mathrm{N/m}$ for the spectrin skeleton of a red blood cell [47]. Using $Y_{2D} \sim 4G_{2D}$ for the red blood cell, because the lipid bilayer has a much higher area expansion modules $K_{2D} \sim 0.3\mathrm{N/m}$, we obtain $\tilde{E}_B \sim 0.005$ for a size $R_0 \sim 3\mu\mathrm{m}$. Larger values of $\tilde{E}_B$ could be realised in artificial cells consisting of a lipid bilayer and a cortex from filamentous proteins for low filament densities in the cortex. These estimates of $\tilde{E}_B$ for red blood cells or artificial cells might be misleading because the relevant elastic modulus in the elastic energy (52) is actually $Y_{2D}/(1-\nu^2)$ rather than Y_{2D}, which is used in the standard definition of the Föppl-von-Kármán number and $\tilde{E}_B$, see eq. (61). Because of their lipid bilayer, red blood cells or artificial cells are in the unstretchable limit $K_{2D} \gg G_{2D}$, where ν approaches unity, and we obtain $Y_{2D}/(1-\nu^2) \approx K_{2D}$. Using this modulus in a definition of $\tilde{E}_B$ (i.e., in the non-dimensionalisation) leads to much smaller values $\tilde{E}_B \sim 10^{-9}$.

The discontinuous sphere-pear transition happens beyond a critical point, $\tilde{E}_B > \tilde{E}_{B,c} \simeq 0.05$, see Fig. 72. Therefore, this peculiar transition is not accessible for typical synthetic capsules. To observe this transition an elastically very anisotropic capsule shell material with high bending and low stretching moduli would be needed. The transition into buckled shapes, however, should be well accessible with generic soft synthetic capsules.

The softness of the shell material is also important if high Bond numbers $\mathrm{Bo} \sim 1$ are to be realised in the shape diagram Fig. 72. In the presence of the above low Reynolds number constraint, very soft shell materials with a small two-dimensional Young modulus $Y_{2D} \lesssim 5 \times 10^{-4}\mathrm{N/m}$ for a capsule of size $R_0 \sim 10\mu\mathrm{m}$ are needed to reach such Bond numbers in water. Typical soft synthetic capsules such as OTS capsules have much larger moduli $Y_{2D} \sim 0.1\mathrm{N/m}$ [28]. Red blood cells or artificial cells with shear moduli governed by a soft filamentous network have small moduli $Y_{2D} \sim 10^{-6}\mathrm{N/m}$, which will allow to reach high Bond numbers. Again, these estimates might be misleading because the relevant elastic modulus in the elastic energy

is actually $Y_{2D}/(1-\nu^2)$ rather than Y_{2D}. If this modulus is used in the non-dimensionalisation and the definition of the Bond number in eq. (62), Bond numbers become much smaller because red blood cells or artificial cells are hardly stretchable.

Localised driving forces

There are other possible external driving forces and self-propulsion mechanism [35, 48]. One extreme case is a very localised external force. We study this case by employing a driving pressure that acts on a small patch on one apex (we used the criterion $s_0 \leq 0.1$ or $L - s_0 \leq 0.1$, respectively; even more localised pressures would have to be higher and, thus, require smaller integration steps). For a pushing force, i.e., a force that acts on the stern of the capsule, this gives rise to strongly indented shapes. They have a higher drag than a spherical shape such that the driving force has to be higher than in Stokes' law $u \approx F/6\pi$ (in dimensionless form) resulting in $F_{\text{drive}} > 6\pi u$, whereas for pulling forces (acting on the bow) the drag is lower as compared to a sphere. We show force-velocity relations with some exemplary shapes for these two types of external driving forces in Fig. 78. As can clearly be seen in the force-velocity relations, there are *no* shape bifurcations for elastic capsules driven by localised forces. One way to apply a localised force experimentally is to attach beads to the capsule that can be manipulated via optical tweezers, as it has been done with giant vesicles[49].

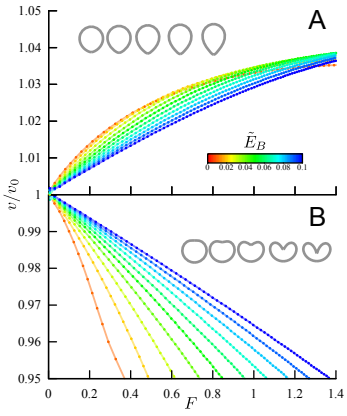

Figure 78: Force-velocity relations for a capsule with fixed volume driven by (A) a localised *pulling* force and (B) a localised *pushing* force. The plots show the velocity relative to the (dimensionless) velocity $u_0 = F/6\pi$ of a hard sphere with the same volume as a function of the total external force. The insets show exemplary capsule shapes for $\tilde{E}_B = 0.01$.

Discussion and Conclusion

We introduced a new iterative solution scheme to find stationary axisymmetric shapes and velocity of a deformable elastic capsule driven through a viscous fluid by an external force at low Reynolds numbers. We focused on sedimenting capsules in gravitation or in a centrifuge, but also demonstrated that other force distributions, such as localised forces, can be studied.

The iterative method is sufficiently accurate and fast to identify all branches of different shapes and to resolve dynamic shape transitions. We find a rich dynamic bifurcation behaviour for sedimenting elastic capsules, even at fixed volume, see Fig. 72 with three types of possible axisymmetric stationary shapes: a pseudospherical state, a pear-shaped state, and buckled shapes. The capsule can undergo shape transformations as a function of two dimensionless parameters. The elastic properties are characterised by a dimensionless bending rigidity $\tilde{E}_B$ (see eq. (61)), the driving force is characterised by the dimensionless Bond number (see eq. (62)).

The transition between pseudospherical and pear shape is a discontinuous transition with shape coexistence and hysteresis for large bending rigidity or large Bond number. The corresponding transition line terminates in a critical point if the bending rigidity is lowered. Parameter estimates show that this transition cannot be observed with standard synthetic capsules because it requires a rather large bending rigidity or low Föppl-von-Kármán number, which cannot be realised for thin ($H/R_0 < 0.1$) shells of an isotropic elastic material. Observation of this discontinuous transition requires a material, which combines high bending rigidity while it remains highly stretchable.

We find an additional bifurcation into a pair of buckled shapes at small bending rigidities upon increasing the gravitational force. All shape bifurcations can be resolved in the force-velocity relation of sedimenting capsules,

where up to three capsule shapes with different velocities can occur for the same gravitational driving force, see Fig. 75. In an experiment, these shapes are selected depending on the initial conditions. We also confirmed the stability of all axisymmetric shapes with respect to rotation around an axis perpendicular to the axis of symmetry, see Fig. 77. We find more stationary buckled shapes if we consider sedimenting capsules where we vary the volume by changing the pressure[166]. These additional shapes are higher order buckled shapes with more indentations.

[166] It is explained in more detail in the appendix, see page 129

It is instructive to discuss our results in comparison with sedimenting vesicles [16–18] and sedimenting red blood cells [20]. Vesicles are bounded by a two-dimensional fluid lipid bilayer rather than a two-dimensional solid membrane or shell and are virtually unstretchable, i.e., they have a fixed area. Therefore, shape transitions out of a spherical shape with the minimal area for given volume require excess area. For the sedimenting capsules this additional area is generated by hydrodynamic stretching. For vesicles, excess area can be "hidden" in thermal fluctuations. A spherical vesicle without such excess area cannot undergo any shape transitions during sedimentation. The pear shape for elastic capsules at high Bond numbers is similar to the "tether" formation by sedimenting vesicles [18]. However, there are two important differences. First, the stretching energy of capsules penalises deformations from the resting shape[167], which leads to less extreme and pronounced tethers. Moreover, cylindrical tethers are an actual equilibrium shape of a membrane under tension, which can coexist with a spherical vesicle [50]. This is not the case for an elastic capsule. Secondly, we do not find a bulge or "droplet" forming at the upper end, by which we mean an increase in the width of the extrusion near the end of the tether. This is rooted in the different bending energies: using a Helfrich bending energy that is quadratic in the mean curvature $w_B \sim (\varkappa_s + \varkappa_\varphi)^2$, the negative meridional curvature needed to form a drop at the end of the tether is energetically favourable, whereas it is not with the Hookean bending energy (52) we employ. Moreover, elastic capsules cannot develop shapes with circulating surface flows because of their solid membrane. Therefore, there is no analogue of the banana shape with surface flows that has been found in Refs. 16, 17 for vesicles.

[167] Vesicles have a liquid surface that allows any shape with the correct area.

Also sedimenting red blood cells exhibits different shapes; in MPCD simulations transitions between tear drop shapes, parachute (or cup-shaped) blood cells and fin-tailed shapes [20] have been found. Red blood cells have a non-spherical discocyte rest shape, which already provides some excess area as compared to the minimal area of a sphere. Therefore, stretching is not essential for dynamic shape transitions. The initial discocyte shape of red blood cells also gives rise to a strong tendency to tilt, which is absent for our initially spherical capsules. The parachute shape also tilts by almost 90 degrees during transformation into a tear drop [20]. All transitions observed in Ref. 20 did not show any signatures in the force-velocity relation or the bending or shear energies. For spherical capsules we find clear signatures of all transitions in the force-velocity relation in Fig. 75. It remains to be clarified in future work, whether the MPCD technique is not accurate enough or exhibits too many fluctuations to resolve these signatures or whether the dynamic transitions of sedimenting red blood cells are qualitatively different, for example, because tilt plays such a prominent role.

Additionally, we studied capsules driven by localised force. For such localised driving forces, we always find shapes to transform smoothly without any shape bifurcations, see Fig. 78.

Outlook – further applications

Finally, we want to lay out how to extend our iterative method, primarily to actively swimming capsules[35]. One possible swimming mechanism[51], for example in squirmer type swimmer models [36, 37, 52], is a finite velocity field at the capsule surface in its rest frame. Our solution technique remains still applicable as long as there is no net velocity normal to the surface.

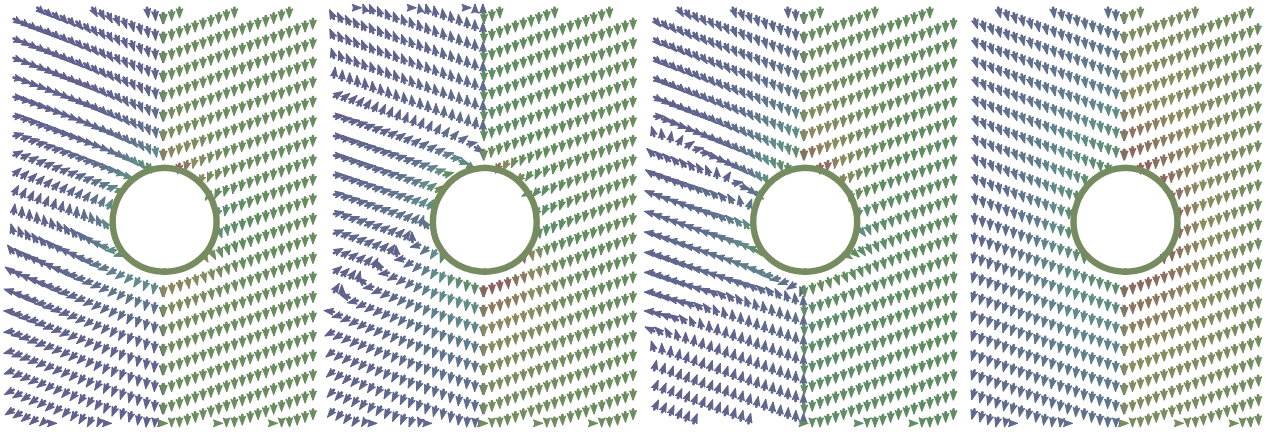

Figure 79: The flow field around three types of squirmers – from left to right $\alpha = 0$ (neutral), $\alpha = -1$ (puller), $\alpha = 1$ (pusher) – and a passive particle for comparison. The left half of each diagram depicts the flow in the resting frame of the immersed particle, whereas the flow in the lab frame is shown in the right half.

The squirmer model for a spherical capsule corresponds to a decomposition of the slip velocity into Legendre polynomials. We restrict ourselves to the first two modes and write the tangential slip velocity as

$$u_s \propto \sin(s_0) + \alpha/2 \sin(2s_0).$$

The first mode corresponds to a "force" velocity field (resembling a dipole field in standard multipole expansions) and the latter to a "force dipole" field (a quadrupole contribution). For $\alpha > 0$ there is a flow towards the middle, the thrust comes from the bow of the capsule, this case is therefore commonly referred to as a *pusher*. The case $\alpha < 0$ is referred to as a *puller* as the flow is directed away from the middle and the thrust comes from the stern of the capsule. The velocity a rigid sphere assumes due to the finite slip velocity is independent from α and depends only on the omitted prefactor[168].

The justification of a slip velocity of any kind is that this allows us to incorporate the effect of some underlying propulsion mechanism that we do not model explicitly. A large variety of propulsion mechanisms have been studied. However, we are interested in deformable swimmers and in general quantifying the change of the effective slip velocity with the deformation would require a profound knowledge of the underlying mechanism. Usually this would increase the complexity of the problem by coupling to a third system of differential equations for the drive, for example a heat equation for thermophoretic particles[54] or a diffusion equation for diffusiophoretic particles[55, 56]. One rather generic possibility would be a propulsion by cilia (biological or artificial) on the surface, we would then assume that there

[168] Generally, the resulting velocity of a rigid sphere due to a given slip velocity distribution is given by the *average slip velocity*. This follows[53] from an application of Lorentz' reciprocal theorem[30]. For a general body of revolution we can analogously relate the translational velocity $\boldsymbol{u}_\infty$ and the slip velocity $\boldsymbol{u}_s$ if we know the surface forces $\widetilde{\boldsymbol{f}}$ for a rigid, passive translation of this body by $\left(\int_C \mathrm{d}s\, r \sin\psi\, \widetilde{\boldsymbol{f}}\right) \cdot \boldsymbol{u}_\infty = -\int_C \mathrm{d}s\, r \sin\psi\, \widetilde{\boldsymbol{f}} \cdot \boldsymbol{u}_s$ or $u_\infty \int_C \mathrm{d}s\, r \sin\psi\, \widetilde{f}_z = \int_C \mathrm{d}s\, r \sin\psi\, \widetilde{p}_s u_s$.

Figure 80: Generatrices of a neutrally squirming (g_s increases from left to right) for $\tilde{E}_B = 0.001$. The deformation is dominated by the tangential stress.

is a given density of cilia of a given strength on any surface element of the undeformed capsule. As the cilia number is fixed and the cilia itself are immotile this constitutes a model where we are able to give the slip velocity for the deformed capsule as well. We call the previously omitted proportionality factor g_s and can then give the slip velocity on the surface of the capsule at any state of deformation $u_s(s_0) = \frac{g_s}{\sqrt{\lambda_s \lambda_\varphi}} (\sin(s_0) + \alpha/2 \sin(2s_0))$. By including the local area dilatation $\lambda_s \lambda_\varphi$ the power density (and hence the total propulsion power) is conserved $P \propto \int \mathrm{d}A u_s^2(s) \propto \int \mathrm{d}A_0 \lambda_s \lambda_\varphi u_s^2(s_0)$. As stated before the initial force-velocity relation (for a spherical resting shape) is only dependent on g_s and one finds[37] that the stationary velocity is given by $u = 2/3 g_s$. On the technical level the additional slip velocity adds little overhead and some results are shown in Fig. 80. The slip velocity enters on the level of the boundary conditions, that is the left hand side of eq. (56). As it is more efficient to adapt the velocity of the capsule u, while computing the deformation of the capsule[169], we want to separate the flow and the stresses into the contributions from the motion of the capsule ($\propto u$) and the contributions from the propulsion ($\propto g_s$). We are free to do this since the Stokes equation is linear. We therefore solve two versions of eq. (57), one with the same boundary condition as for sedimentation and one with the slip velocity as boundary condition on the capsule surface. A variation to the fixed "squirming pattern" considered before would be to search for the *optimal* slip velocity distribution. As we separated the two hydrodynamics and the capsule deformability, we can directly[170] adapt the approach for rigid bodies of Ref. 63.

A more direct approach to swimming would be to consider a direct deformation of the capsule. To avoid subtleties[57] let us assume that the deformation is given by a deformation velocity $\boldsymbol{u}_D$ describing the time evolution of each surface segment. The resulting motion of the entire capsule leads to a velocity boundary condition $\boldsymbol{u} + \boldsymbol{u}_D(s)$ on the surface of the capsule. The correct value of the swimming velocity is fixed by the absence of a net force and therefore easily computed as we can separate the two contributions (translation, deformation) due to the linearity of the Stokes equation [171]. However, the very nature of this locomotion procedure rules out the existence of a *steady state* and thus the incorporation of elasticity would have to be dynamic in nature and thus out of the scope of the method presented here.

Aside from actively swimming capsules there are also a number of interesting problems with externally controlled flow fields[172], which one can employ to probe elastic properties of the capsule. For example, we could prescribe an extensional flow[31] $\boldsymbol{u}_{\text{ext}} = -\varepsilon r \boldsymbol{e}_r + 2\varepsilon(z - z_{\text{cm}})$. This is the most general form of an axisymmetric extensional flow, the factor two guarantees compatibility with incompressibility. We are generally interested in stationary solutions, but this flow field has broken symmetry along the (axial) direction of motion, hence we can only consider a capsule that is localised (with vanishing centre of mass velocity) around the centre of mass. We already took this into account by centring the flow around the centre of mass of the capsule z_{cm}. Stationary shapes in this flow are not only axisymmetric, but also have a fore-aft symmetry, as this is needed to establish the absence of a net force. An experimentally important setup is a capsule inside a (rigid) spherical tube, that is in a Poiseuille flow[25]. However, the inclusion of additional walls alters the boundary conditions at infinity, hence we can no longer use the free propagator to find an exact solution[173].

[169] This is a technical subtlety. At any stage of the iterative process (except for the initial iteration) we use the flow corresponding to the shape of the previous iteration in the solution of the shape equations. However, we cannot deduce the absence of a net flow on the new shape based upon the previous shape, thus violating global force balance, which severely afflicts the ability to find a solution of the shape equations. Our approach to this is to adapt the velocity in the solution of the shape equations (using a convex combination of old and new stresses, as stated before). The alternative would be to compute u based upon the old shape at the level of the solution of the Stokes equation. For the finally found stationary solution these approaches coincide.

[170] However, this renders the remark of sidenote 169 mute, as we now do compute the force and velocity based upon the old shape, but as stated before this is a minor technicality.

[171] The deformation pattern has to be cyclic to sustain prolonged locomotion (and reasonably be called swimming), but must not be reciprocal[58] as the absence of a direct time dependence in the Stokes equation leads to an invariance under (nonlinear) reparametrisation of time (including time reversal). This is commonly referred to as the *scallop theorem*.

[172] In light of the nature of the developed method, we only consider arrangements that lead to a non-trivial hydrodynamic stress. For example, we could also compute the deformation of a capsule inside a spinning drop apparatus, but this only amounts for adding a pressure contribution $\boldsymbol{p} \propto sin(\psi) r^3 \boldsymbol{e}_r$.

[173] Sadly, the only representation[31, 59] of the propagator for Poiseuille boundary conditions known to the author in Fourier space is exceptionally badly fit for a numerical approach. However, we can try to find an approximate solution in a way that has been shown to work for the deformation of vesicles[60]: we ignore the influence of the walls and reduce the problem to a prescribed parabolic velocity profile

$$\boldsymbol{u}_{\text{poi}} = g_p (1 - (r/d)^2) \boldsymbol{e}_z.$$

Here, g_p quantifies the strength of the Poiseuille flow (given by the pressure gradient along the tube without the capsule in it) and d is the radius of the "phantom tube". A different approach with more effort, but better control of the error would be to consider[61] the motion in a finite tube. After separating the problem into a capsule with free boundary conditions and a tube with given velocity on its surface, we can solve both subproblems using our standard boundary integral formalism.

Appendix

Derivation of the shape-equations

In the following we present a "quick-and-dirty" derivation of the shape equations. We refer the reader to the literature stated in the main text for a clearer, more careful, better thought through derivation. From the Cauchy momentum equation we gather that the equilibrium is given by[174] $\nabla \cdot \sigma = 0$.

[174] External forces are easily added and actually necessary for the existence of non-trivial solutions.

We will not use Cartesian coordinates here, but curvilinear coordinates that are better suited to the capsule geometry. In the vicinity of the capsule we can parametrise space by the set of coordinates n,s,φ and

$$\boldsymbol{r}(n,s,\varphi) = \begin{pmatrix} r(s)\cos\varphi \\ r(s)\sin\varphi \\ z(s) \end{pmatrix} + n \begin{pmatrix} \sin\psi\cos\varphi \\ \sin\psi\sin\varphi \\ -\cos\psi \end{pmatrix}$$

which corresponds to a local tripod of orthogonal vectors[175]

[175] Identifying $\tilde{\boldsymbol{n}}$ and $\boldsymbol{n}$ corresponds to a rather sloppy notation that sets $\varphi \equiv 0$ if it is not needed (and subsequently ignores the y-component when operating in the cross-section plane of the generatrix).

$$\tilde{\boldsymbol{n}} = \boldsymbol{n} = \begin{pmatrix} \sin\psi\cos\varphi \\ \sin\psi\sin\varphi \\ -\cos\psi \end{pmatrix}, \quad \tilde{\boldsymbol{s}} = (1+n\psi') \begin{pmatrix} \cos\psi\cos\varphi \\ \cos\psi\sin\varphi \\ \sin\psi \end{pmatrix} \quad \text{and} \quad \tilde{\boldsymbol{\varphi}} = (r + n\sin\psi) \begin{pmatrix} \sin\varphi \\ -\cos\varphi \\ 0 \end{pmatrix}.$$

We want to derive equations for the elasticity of a *thin shell*, which we want to model as an effectively two-dimensional surface. This is done by restricting stresses to in-plane stresses and than integrating over the normal direction (the n-direction, $n \in [-H/2, H/2]$ with H being the thickness). Thus it is advantageous to define a projector $\mathsf{P} = \mathbb{1} - \boldsymbol{nn}$ that projects the stress onto the subspace of in-plane stresses. The tedious part is then to compute the tensor derivative in the defined curvilinear coordinates. We can use the general result (to be read with Einstein summation convention)

$$(\nabla \cdot \mathsf{A})_k = \frac{\partial \mathsf{A}_{ik}}{\partial i} - \mathsf{A}_{jk}\Gamma^j_{ii} - \mathsf{A}_{ij}\Gamma^j_{ik}$$

with $i,j,k \in n,s,\varphi$ and the Christoffel symbols of the second kind defined by $\frac{\partial \tilde{\boldsymbol{i}}}{\partial j} = \Gamma^k_{ij}\tilde{\boldsymbol{k}}$.

As we introduced $\tilde{\boldsymbol{i}}$ such that $\tilde{\boldsymbol{i}} = \partial_i \boldsymbol{r}$ we see that the Christoffel symbols of the second kind are symmetric in the lower indices. To get it over with we reproduce the non-vanishing symbols (at $n = 0$, i.e. on the surface, where we want to evaluate the stress)

$$\Gamma^s_{ns} = \varkappa_s = \Gamma^s_{sn}, \Gamma^\varphi_{n\varphi} = \varkappa_\varphi = \Gamma^\varphi_{\varphi n}, \Gamma^n_{ss} = -\varkappa_s, \Gamma^\varphi_{s\varphi} = \frac{\cos\psi}{r} = \Gamma^\varphi_{\varphi s}, \Gamma^n_{\varphi\varphi} = -r\sin\psi \text{ and } \Gamma^s_{\varphi\varphi} = -r\cos\psi.$$

Here we made use of the geometrical relations $\psi' = \varkappa_s$ and $\sin\psi = r\varkappa_\varphi$. From the given axisymmetry we can infer the following form of the projected stress

$$\mathsf{P}\sigma = \begin{pmatrix} 0 & 0 & 0 \\ \sigma_{sn} & \sigma_{ss} & 0 \\ 0 & 0 & \sigma_{\varphi\varphi} \end{pmatrix}$$

and computing the divergence (at $n = 0$) ultimately yields (remember $\partial_s r = \cos\psi$)

$$\nabla \cdot \mathsf{P}\sigma = \left(\frac{1}{r}\frac{\partial(r\sigma_{sn})}{\partial s} - \varkappa_s\sigma_{ss} - \sigma_{\varphi\varphi}\varkappa_\varphi \right)\boldsymbol{n} + \left(\frac{1}{r}\frac{\partial(r\sigma_{ss})}{\partial s} + \varkappa_s\sigma_{sn} - \sigma_{\varphi\varphi}\frac{\cos\psi}{r} \right)\boldsymbol{s}.$$

If we integrate over the small thickness and introduce (The sign of q might appear random and is such that the definition of q agrees with the literature)

$$\int_{-H/2}^{H/2} \mathrm{d}n\, \sigma_{ss} = \tau_s, \quad \int_{-H/2}^{H/2} \mathrm{d}n\, \sigma_{\varphi\varphi} = \tau_\varphi \quad \text{and} \quad \int_{-H/2}^{H/2} \mathrm{d}n\, \sigma_{sn} = -q.$$

this establishes two of the non-trivial shape equations. The final one is gathered from considering the acting torque. A shell of finite thickness is able to sustain finite bending moments $\boldsymbol{m}$, which in terms of basic physics means that there is an additional contribution to the torque balance. Arguing along the same lines as we did for the Cauchy momentum equation but starting from the principle of angular momentum

$$\frac{\mathrm{d}L}{\mathrm{d}t} = \boldsymbol{M}$$

yields (in equilibrium)

$$0 = \int \mathrm{d}V(\boldsymbol{r}' \times \boldsymbol{b}) + \int \mathrm{d}A(\boldsymbol{r}' \times \sigma \boldsymbol{n}_A + \boldsymbol{m})$$

where $\boldsymbol{r}'$ is the difference vector to the centre of mass of the patch. Now we introduce the *bending moment tensor* (also couple stress tensor) M by $\boldsymbol{m} = \mathsf{M}\boldsymbol{n}_A$ and the auxiliary tensor D by $\mathsf{D}\boldsymbol{n}_A = \boldsymbol{r}' \times \sigma \boldsymbol{n}_A$; after once again applying the divergence theorem we find in absence of body forces $\nabla \cdot (\mathsf{D} + \mathsf{M}) = 0$. We are interested in the case $\boldsymbol{n}_A = \tilde{\boldsymbol{n}}$ and (after projection to in-plane stresses) see that $\sigma\tilde{\boldsymbol{n}} = \sigma_{sn}\tilde{\boldsymbol{s}}$. We consider a small patch such that we can write $\boldsymbol{r}' = s\tilde{\boldsymbol{s}} + n\tilde{\boldsymbol{n}} + \varphi\tilde{\boldsymbol{\varphi}}$: after projection to in-plane-torques and using that the internal bending moments act along the directions of principal curvature, i.e.

$$\mathsf{PM} = \begin{pmatrix} 0 & 0 & 0 \\ 0 & M_{ss} & 0 \\ 0 & 0 & M_{\varphi\varphi} \end{pmatrix},$$

we find (for $n = 0$)

$$0 = \frac{1}{r}\frac{\partial r M_{ss}}{\partial s} + \sigma_{sn} - \frac{\cos\psi}{r} M_{\varphi\varphi}$$

which gives the final equation after renaming

$$\int_{-H/2}^{H/2} \mathrm{d}n\, M_{ss} = m_s \quad \text{and} \quad \int_{-H/2}^{H/2} \mathrm{d}n\, M_{\varphi\varphi} = m_\varphi.$$

First Integral of the shape equations

Inspired from the known first integral in the static problem (cf. eqs. (17), (22) in Ref. 38) we make the following Ansatz for a first integral of the shape equations

$$U(s) = 2\pi r \cos\psi q + 2\pi r \sin\psi \tau_s + X = \text{const.}$$

We are also assuming that the pressure p and the shear pressure p_s can be written as functions solely dependent on the arc length s. The calculation is rather straightforward, we differentiate and get

$$\begin{aligned}
0 = U'(s) &= 2\pi\cos^2\psi q - 2\pi r \sin\psi \varkappa_s q + 2\pi r \cos\psi(-\varkappa_s\tau_s - \varkappa_\varphi\tau_\varphi - \cos\psi\frac{q}{r} + p) + 2\pi\cos\psi\sin\psi\tau_s \\
&\quad + 2\pi r\cos\psi\varkappa_s\tau_s + 2\pi r\sin\psi(\cos\psi\frac{\tau_\varphi - \tau_s}{r} + \varkappa_s q + p_s) + X' \\
&= 2\pi\cos^2\psi q - 2\pi r\sin\psi\varkappa_s q \; + 2\pi r\cos\psi(-\varkappa_s\tau_s - \varkappa_\varphi\tau_\varphi - \cos\psi\frac{q}{r} + p) \\
&\quad + 2\pi\cos\psi\sin\psi\tau_s + 2\pi r\cos\psi\varkappa_s\tau_s + 2\pi r\sin\psi\left(\cos\psi\frac{\tau_\varphi - \tau_s}{r} + \varkappa_s q + p_s\right) + X' \\
&= 2\pi r p\cos\psi + 2\pi r p_s \sin\psi + X' = 0
\end{aligned}$$

In the second to last step most terms cancel each other out. Thus we have found an ordinary differential equation for X, which we can integrate directly

$$\begin{aligned} X' &= -2\pi r(p\cos\psi + p_s\sin\psi) \\ X &= -2\pi\int_0^s \mathrm{d}x\, r(p\cos\psi + p_s\sin\psi) \end{aligned} \tag{63}$$

Inspecting the behaviour at $s = 0$ we then deduce

$$0 = 2\pi r\cos\psi q + 2\pi r\sin\psi\tau_s - 2\pi\int_0^s \mathrm{d}x\, r(p\cos\psi + p_s\sin\psi)$$

This is indeed a generalisation of the static quantity, as we see by setting $p_s = 0$, $p = \text{const.}$

$$X = -2\pi p\int_0^s \mathrm{d}x\, r\cos\psi = -\pi p r^2$$

and thus the first integral is (up to the choice of constant prefactors) identical to the one given in Ref. 38.

The physical interpretation of this first integral is that the capsule has to be in global force balance. By symmetry there can be no net force in radial direction, but the external forces can lead to net force in axial direction. The quantity X contains the contribution to the net force in z-direction and thus a shape with the desired features (namely $q = 0$ at the apexes) must have $X(L) = 0$ and thus be in global force balance.

Single-layer potential solution of the Stokes equation in an axisymmetric domain

To make our presentation self-contained, we give the analytical expressions for the elements of the matrix kernel M that relates the forces and the velocities on the surface of the capsule via

$$u_\alpha^\infty = -\frac{1}{8\pi\mu}\int_C \mathrm{d}s(\boldsymbol{x})\mathsf{M}_{\alpha\beta}(\boldsymbol{y},\boldsymbol{x})f_\beta(\boldsymbol{x}) \quad (\text{for } \boldsymbol{y}\in\partial\mathfrak{B}),$$

see eq. (57). The derivation of this matrix kernel is briefly outlined in the main text and can also be found in Ref. 31. As we are working in cylindrical coordinates (r,z,φ) and the problem is axisymmetric, the matrix has four elements ($\alpha,\beta = r,z$) which can be explicitly written as

$$\begin{aligned} \mathsf{M}_{zz}(\boldsymbol{y},\boldsymbol{x}) &= 2k\sqrt{\frac{r_x}{r_y}}\left(F + \hat{z}^2E\right) \\ \mathsf{M}_{zr}(\boldsymbol{y},\boldsymbol{x}) &= \frac{k\hat{z}}{\sqrt{r_xr_y}}\left(F - (r_y^2 - r_x^2 + \hat{z}^2)E\right) \\ \mathsf{M}_{rz}(\boldsymbol{y},\boldsymbol{x}) &= -k\frac{\hat{z}}{r_y}\sqrt{\frac{r_x}{r_y}}\left(F + (r_y^2 - r_x^2 - \hat{z}^2)E\right) \\ \mathsf{M}_{rr}(\boldsymbol{y},\boldsymbol{x}) &= \frac{k}{r_xr_y}\sqrt{\frac{r_x}{r_y}}\left[(r_y^2 + r_x^2 + 2\hat{z}^2)F - (2\hat{z}^4 + 3\hat{z}^2(r_y^2 + r_y^2) + (r_y^2 - r_x^2)^2)E\right] \end{aligned}$$

using the abbreviations

$$\hat{z} \equiv z_x - z_y, \quad k^2 \equiv \frac{4r_xr_y}{\hat{z}^2 + (r_x + r_y)^2}, \quad E \equiv \frac{E(k)}{\hat{z}^2 + (r_x - r_y)^2} \quad \text{and} \quad F \equiv K(k)$$

and the complete elliptic integrals of first and second kind [62]

$$K(k) = \int_0^{\pi/2}\frac{\mathrm{d}x}{\sqrt{1 - k^2\cos^2 x}} \quad \text{and} \quad E(k) = \int_0^{\pi/2}\mathrm{d}x\,\sqrt{1 - k^2\cos^2 x}$$

For the numerical computation of M elliptic integrals of the first and second kind we use polynomial approximants as given in Ref. 62, that is we approximate (with a deviation of less than $2 \cdot 10^{-8}$) the elliptic integral of the first kind by

$$K(k) = \sum_{i=0}^{4} a_i (1-k^2)^i - \ln(1-k^2) \sum_{i=0}^{4} b_i (1-k^2)^i$$

with

$$a_0 = 1.38629436112, a_1 = 0.09666344259, a_2 = 0.03590092383, a_3 = 0.03742563713 \text{ and } a_4 = 0.01451196212$$
$$b_0 = .5, \quad b_1 = 0.12498593597, \quad b_2 = 0.06880248576, \quad b_3 = 0.03328355346 \quad \text{and} \quad b_4 = 0.00441787012$$

and the elliptic integral of the second kind by

$$K(k) = \sum_{i=0}^{4} c_i (1-k^2)^i - \ln(1-k^2) \sum_{i=0}^{4} d_i (1-k^2)^i$$

with

$$c_0 = 1, \quad c_1 = .44325141463, \quad c_2 = .06260601220, \quad c_3 = .04757383546 \quad \text{and} \quad c_4 = .01736506451$$
$$d_0 = 0, \quad d_1 = 0.24998368310, \quad d_2 = 0.09200180037, \quad d_3 = 0.04069697526 \quad \text{and} \quad d_4 = 0.00526449639.$$

Non-spherical reference shapes

Throughout the main text we restricted our discussion to the case of spherical rest shapes. Clearly, this is a simplification and a broader range of rest shapes might be desirable in applications (whilst still adhering to the underlying premise of axisymmetry). In the presented numerical scheme the geometry of the rest shape enters in three quantities: the radial coordinate $r_0(\theta)$, the circumferential curvature or the slope angle $\sin\psi_0(\theta) = r_0\varkappa_{\varphi,0}$ and the circumferential curvature $\varkappa_{s,0}(\theta)$. Here, we opened the formalism up towards the possibility that there might be a more suitable parametrisation θ of the resting shape than the undeformed arc length s_0. However, this comes at the cost that we have to replace any occurrence of λ_s in the shape equations by $\lambda_s\lambda_\theta$ with $\lambda_\theta = \partial_{s_0}\theta$. These can all easily be added numerically (e.g. by means of splines through given points). However, we can give the needed quantities analytically for a slightly more general class of resting shapes, namely spheroids (axisymmetric ellipsoids). We use the standard parametrisation with θ being the parametric latitude of an ellipsoid whose lower apex is at $z = 0$

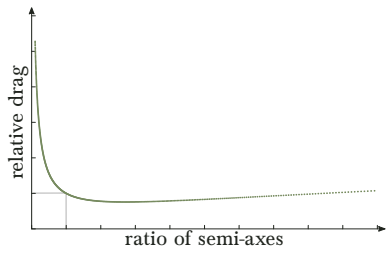

Figure 81: The drag of a squirming spheroid with radial semiaxes a and axial semiaxis b relative to a sphere of same volume. Here, we consider optimal squirmers.[63] Propulsion by tangent slip-velocity is obviously more efficient for prolate spheroids ($b/a > 1$). However, an increased area also increases the friction, which gives rise to a non-trivial minimum. As in Fig. 70 we give the scale of the axes by comparison to the case of a sphere (grey lines).

$$\boldsymbol{r}(\theta,\varphi) = \begin{pmatrix} a\sin\theta\cos\varphi \\ a\sin\theta\sin\varphi \\ b(1-\cos\theta) \end{pmatrix}$$

and find

$$r_0(\theta) = a\sin\theta$$
$$\varkappa_{\varphi,0} = \frac{b}{a\lambda_\theta}$$
$$\varkappa_{s,0} = \frac{ab}{\lambda_\theta^3}$$
$$\lambda_\theta = \sqrt{a^2 + (b^2-a^2)\sin\theta^2}.$$

Considering rigid body motion, distinguished values for the ratio of semiaxes other than unity (the case of a sphere), are the spheroid with minimal friction under passive motion (see Fig. 70) with $b/a \approx 1.9$ or the spheroid that is optimal for squirming propulsion (see Fig. 81) with $b/a \approx 2.7$.

Rotational stability

We want to study the change in the torque due to a infinitesimally small rotation R of the velocity and the gravitational force vector. Geometrically, this is equivalent to rotating the capsule. A change of the velocity boundary condition $\boldsymbol{u}_0 \to \boldsymbol{u}_0' = \mathsf{R}\boldsymbol{u}_0$ leads to new hydrodynamic surface forces $\boldsymbol{f} \to \boldsymbol{f}'$. As we did not change the capsule we can employ the reciprocal theorem

$$\int \mathrm{d}A\, \boldsymbol{u} \cdot \boldsymbol{f}' = \int \mathrm{d}A\, \boldsymbol{u}_0' \cdot \boldsymbol{f}$$

and find $\boldsymbol{f}' = (\mathsf{R}^T)^{-1}\boldsymbol{f} = \mathsf{R}\boldsymbol{f}$. The new hydrodynamic torque is, thus,

$$\boldsymbol{T}_{\boldsymbol{u}}' = \int \mathrm{d}A\ (\boldsymbol{r} \times (\mathsf{R}\boldsymbol{f})) = \mathsf{R}\int \mathrm{d}A\ \left(\left(\mathsf{R}^{-1}\boldsymbol{r}\right) \times \boldsymbol{f}\right).$$

We limit ourselves to a linear analysis, that is, we perform an infinitesimal rotation around the y-axis by an angle $\mathrm{d}\alpha$, i.e., $\mathsf{R}^{\pm 1} = \mathsf{I} \pm \mathrm{d}\alpha \mathsf{J}_y$. Here, I is the unit matrix ($I_{ij} = \delta_{ij}$) and J_y generates a rotation around the y-axis with $\left(J_y\right)_{ij} = \delta_{i3}\delta_{j1} - \delta_{i1}\delta_{j3}$. Then, to linear order in $\mathrm{d}\alpha$

$$\boldsymbol{e}_y \cdot \boldsymbol{T}_{\boldsymbol{u}}' = -2\pi \mathrm{d}\alpha \int \mathrm{d}s\, r \left(\frac{1}{2} r f_r + (z - z_0) f_z\right).$$

Here, z_0 gives the pivot point of the rotation. Since we know that the centres of mass and hydrodynamic stress have to lie on the symmetry axis studying rotations about points on this axis suffices. Likewise, we can calculate the gravitational contribution to the new torque, which is (again to linear order in $\mathrm{d}\alpha$)

$$\boldsymbol{e}_y \cdot \boldsymbol{T}_{\boldsymbol{g}}' = \pi \mathrm{d}\alpha g \int \mathrm{d}s\, r^2 (z - z_0).$$

Equating these two gives the pivot point of the marginally stable infinitesimal rotation, i.e., the centre of hydrodynamic stress.

This argument does not account for a change of the capsule shape due to the altered stresses upon rotation, which means that a seemingly unstable capsule might be stabilised axially by a "wobbling" deformation leading to different hydrodynamic torques. In principle, this might also work the other way round (as for semiflexible cylindrical rods [64]), but we think is less relevant here, because of the typically large radius of curvature at the lower apex.

Pressure control

For volume control, we fixed $V_0 = 4\pi/3$ to the volume of the spherical rest shape and only explored the two parameters $\tilde{E}_B$ and g. The pressure p_0 served as Lagrange parameter to achieve the fixed volume V_0. To get a better understanding of the variety of shapes that are in principle possible, we study capsules with volumes other than that of the reference shape by controlling and changing the Lagrange parameter p_0. Thus, the explorable parameter space now consists of three parameters $\tilde{E}_B$, g, and p_0. As for volume control, the sedimenting velocity u is not a control parameter but determined from demanding a force free capsule.

With the additional pressure parameter p_0, we find more sedimenting shapes to be stable (with different volumes), in particular, more classes of buckled shapes. We tried to find solutions at $\tilde{E}_B = 0.01$ for pressures $p_0 \in [-0.95, 0.95]$ and $g \in [0, 1]$. As a consequence of the quadratic nature of the elastic law, see eq. 52, there is no solution for a resting capsule ($g = 0$) with $p_0 > 1$ [38]. For a cleaner comparison of different parameter sets (in particular for comparison of differently elongated shapes) it is helpful to not use p_0 but the pressure at the centre of mass, $p_{\mathrm{eff}} = p_0 - \langle z \rangle g$, as actual control parameter because we use a coordinate system that fixes $z = 0$ at the lower apex of the capsule. The possibility to explore a range of volumes allows for a greater variety of shapes. In Fig. 82, we show the pressure-volume relation for stationary axisymmetric shapes with a velocity close to $u = 0.07$ (which determines for each shape a certain gravity g). Solutions at lower velocities are typically easier to find, but very low velocities are rather atypical because one ultimately sees the variety of static solutions [38]. Each type of stable shape gives one pressure-volume branch in Fig. 82. Apart from pseudospherical, pear-shaped and the pair of weakly and strongly buckled solutions, we find additional branches, which correspond to higher order buckled shapes with three, four, or five indentations.

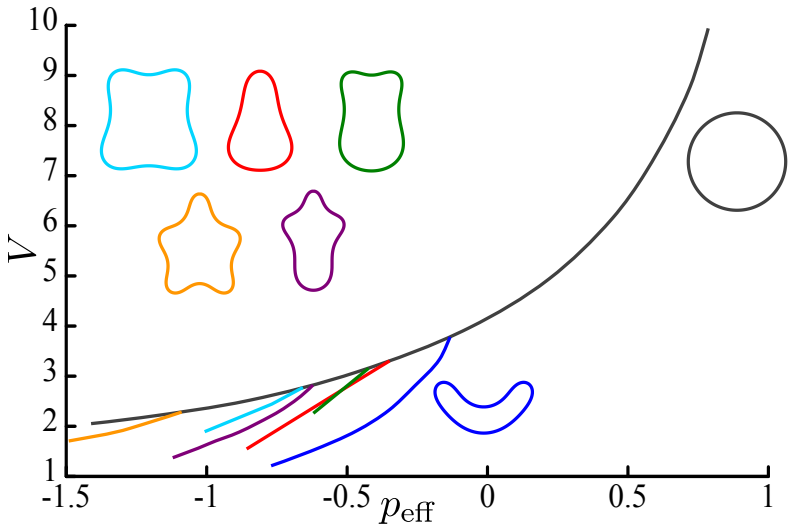

Figure 82: Volume V of the sedimenting elastic capsule as a function of the controlled pressure p_{eff} at the centre of mass at fixed bending rigidity $\tilde{E}_B = 0.01$ and for shapes moving at a velocity $u \approx 0.07$. Each type of stable shape gives one pressure-volume branch. We identified the branches by the shape of the generatrices. We show one representative generatrix for each branch in the colour of the branch. Please note that the generatrices are not drawn to scale. The pseudospherical branch is in good quantitative agreement with the static pressure-volume relation of eq. (64).

As for fixed volume, the main contribution to the shape is due to static pressure (differences). For the pseudospherical branch this can be seen by comparing the volume (in reduced units) with the known pressure-volume relation for a spherical capsule in the static ($g = 0$) case

$$V_{\mathrm{sphere}}(p) = \frac{4\pi}{3}\left(\frac{2}{p}\left(1-\sqrt{1-p}\right)\right)^3, \tag{64}$$

which fits our data rather well.

The higher order buckled shapes occur at small volumes or small effective pressure p_{eff}. We expect to find corresponding higher order buckled shapes also under volume control if we prescribe a corresponding small volume $V_0 \sim 1-2$. But also for higher prescribed volumes such as $V_0 = 4\pi/3 \simeq 4.19$, these shapes could become stable at very high g: Higher volumes require a larger pressure p_{eff} and, thus, also higher deformation forces to induce buckling. Such higher deformation forces can be achieved at high g.

Bibliography

[1] Boltz, H.-H. and Kierfeld, J. (2015). *Phys. Rev. E*, **92**:033003

[2] Barthès-Biesel, D. (2011). *Curr. Opin. Colloid Interface Sci.*, **16**(1):3–12

[3] Fedosov, D. A., Noguchi, H. and Gompper, G. (2014). *Biomech. Model. Mechanobiol.*, **13**(2):239–58

[4] Freund, J. B. (2014). *Annu. Rev. Fluid Mech.*, **46**(1):67–95

[5] Abreu, D. et al. (2014). *Adv. Colloid Interface Sci.*, **208**:129–41

[6] Huang, Z., Abkarian, M. and Viallat, A. (2011). *New J. Phys.*, **13**(3):035026

[7] Clift, R., Grace, J. and Weber, M. (1978). *Bubbles, Drops, and Particles*. Academic Press

[8] Stone, H. A. (1994). *Annu. Rev. Fluid Mech.*, **26**(1):65–102

[9] Seifert, U. (1997). *Adv. Phys.*, **46**(1):13–137

[10] Han, S.-I., Stapf, S. and Blümich, B. (2001). *Phys. Rev. Lett.*, **87**(14):144501

[11] Pozrikidis, C. (2001). *J. Comput. Phys.*, **169**(2):250–301

[12] Spells, K. E. (1952). *Proceedings of the Physical Society. Section B*, **65**(7):541

[13] Kojima, M., Hinch, E. J. and Acrivos, A. (1984). *Phys. Fluids*, **27**(1):19

[14] Koh, C. J. and Leal, L. G. (1989). *Phys. Fluids A*, **1**(8):1309

[15] Pozrikidis, C. (1990). *J. Fluid Mech.*, **210**:1

[16] Boedec, G., Leonetti, M. and Jaeger, M. (2011). *J. Comput. Phys.*, **230**(4):1020–1034

[17] Boedec, G., Jaeger, M. and Leonetti, M. (2012). *J. Fluid Mech.*, **690**:227–261

[18] Boedec, G., Jaeger, M. and Leonetti, M. (2013). *Phys. Rev. E*, **88**(1):010702

[19] Rey Suárez, I. et al. (2013). *PloS ONE*, **8**(7):e68309

[20] Peltomäki, M. and Gompper, G. (2013). *Soft Matter*, **9**(34):8346–8358

[21] Noguchi, H. and Gompper, G. (2005). *Proc. Natl. Acad. Sci. U.S.A.*, **102**(40):14159–64

[22] Fedosov, D. A. et al. (2011). *Proc. Natl. Acad. Sci. U.S.A.*, **108**(29):11772–7

[23] Dupin, M. et al. (2007). *Phys. Rev. E*, **75**(6):066707

[24] do Carmo, M. P. (1976). *Differential geometry of curves and surfaces*. Prentice Hall

[25] Batchelor, G. K. (2000). *An introduction to fluid dynamics*. Cambridge university press

[26] Libai, A. and Simmonds, J. (1998). *The nonlinear theory of elastic shells*. Cambridge University Press, Cambridge

[27] Pozrikidis, C. (2003). *Modeling and simulation of capsules and biological cells*. CRC Press

[28] Knoche, S. et al. (2013). *Langmuir*, **29**(40):12463

[29] Stokes, G. (1851). *Transactions of the Cambridge Philosophical Society*, **9**:8

[30] Happel, J. and Brenner, H. (1983). *Low Reynolds number hydrodynamics: with special applications to particulate media*, Vol. 1. Springer

[31] Pozrikidis, C. (1992). *Boundary integral and singularity methods for linearized viscous flow*. Cambridge University Press

[32] Langtangen, H. P., Mardal, K.-A. and Winther, R. (2002). *Advances in Water Resources*, **25**(8):1125–1146

[33] Perrin, F. (1936). *J. Phys. Radium*, **7**(1):1–11

[34] Lauga, E. and Powers, T. R. (2009). *Rep. Prog. Phys.*, **72**(9):096601

[35] Degen, P. (2014). *Curr. Opin. Colloid Interface Sci.*, **19**(6):611–619

[36] Lighthill, M. (1952). *Communications on Pure and Applied Mathematics*, 5(2):109–118
[37] Blake, J. (1971). *Journal of Fluid Mechanics*, 46(01):199–208
[38] Knoche, S. and Kierfeld, J. (2011). *Phys. Rev. E*, 84:046608
[39] Kuneš, J. (2012). *Dimensionless physical quantities in science and engineering*. Elsevier
[40] Landau, L. and Lifshitz, E. (1986). *Theory of Elasticity*, Vol. 7. Pergamon, New York
[41] Pogorelov, A. V. (1988). *Bendings of surfaces and stability of shells*, Vol. 72. American Mathematical Soc.
[42] Knoche, S. and Kierfeld, J. (2014). *Soft Matter*, 10(41):8358–69
[43] Planken, K. L. and Cölfen, H. (2010). *Nanoscale*, 2(10):1849–1869
[44] ten Hagen, B. et al. (2014). *Nat. Commun.*, 5:4829
[45] Dote, J. L. and Kivelson, D. (1983). *J. Phys. Chem.*, 87(20):3889–3893
[46] Lidmar, J., Mirny, L. and Nelson, D. R. (2003). *Phys. Rev. E*, 68:051910
[47] Lenormand, G. et al. (2001). *Biophys. J.*, 81(1):43–56
[48] Ebbens, S. J. and Howse, J. R. (2010). *Soft Matter*, 6(4):726–738
[49] Dasgupta, R. and Dimova, R. (2014). *J. Phys. D: Appl. Phys.*, 47(28):282001
[50] Lipowsky, R. et al. (2005). *J. Phys.: Condens. Matter*, 17(9):S537–S558
[51] Pak, O. S. and Lauga, E. (2015). *Chapter in: C. Duprat and H. A. Stone (Eds.), Low-Reynolds-Number Flows: Fluid-Structure Interactions (RSC publishing)*
[52] Downton, M. T. and Stark, H. (2009). *Journal of Physics: Condensed Matter*, 21(20):204101
[53] Stone, H. A. and Samuel, A. D. T. (1996). *Phys. Rev. Lett.*, 77:4102–4104
[54] Bickel, T., Majee, A. and Würger, A. (2013). *Phys. Rev. E*, 88(1):012301
[55] Michelin, S., Lauga, E. and Bartolo, D. (2013). *Physics of Fluids (1994-present)*, 25(6):061701
[56] Michelin, S. and Lauga, E. (2014). *Journal of Fluid Mechanics*, 747:572–604
[57] Evans, A. A., Spagnolie, S. E. and Lauga, E. (2010). *Soft Matter*, 6(8):1737–1747
[58] Purcell, E. M. (1977). *Am. J. Phys*, 45(1):3–11
[59] Tözeren, H. (1984). *International Journal for Numerical Methods in Fluids*, 4(2):159–170
[60] Coupier, G. et al. (2012). *Phys. Rev. Lett.*, 108:178106
[61] Zhu, L., Lauga, E. and Brandt, L. (2013). *J. Fluid Mech.*, 726:285–311
[62] Abramowitz, M. and Stegun, I. A. (1972). *Handbook of mathematical functions: with formulas, graphs, and mathematical tables*. 55. Courier Dover Publications
[63] Vilfan, A. (2012). *Phys. Rev. Lett.*, 109(12):128105
[64] Manghi, M. et al. (2006). *Soft Matter*, 2(8):653

Part III

HARD SPHERES IN MONTE-CARLO SIMULATIONS

Preface to this part

The following presents work that was done in collaboration with *Tobias Alexander Kampmann*. It has already been published[176] in Refs. [1, 2]. In a collaboration it is often difficult to separate individual contributions. Furthermore, an isolated presentation of parts of this materials would hardly be followable for the reader. In mutual agreement with Tobias I declare my contribution to this material amounts for 25% of the work.

[176] Therefore this part of this thesis contains parts that are reprinted from Journal of Computational Physics, Volume 281, Tobias A. Kampmann, Horst-Holger Boltz and Jan Kierfeld, Parallelized event chain algorithm for dense hard sphere and polymer systems, 864 – 875, Copyright (2015), with permission from Elsevier.

HB

Introduction

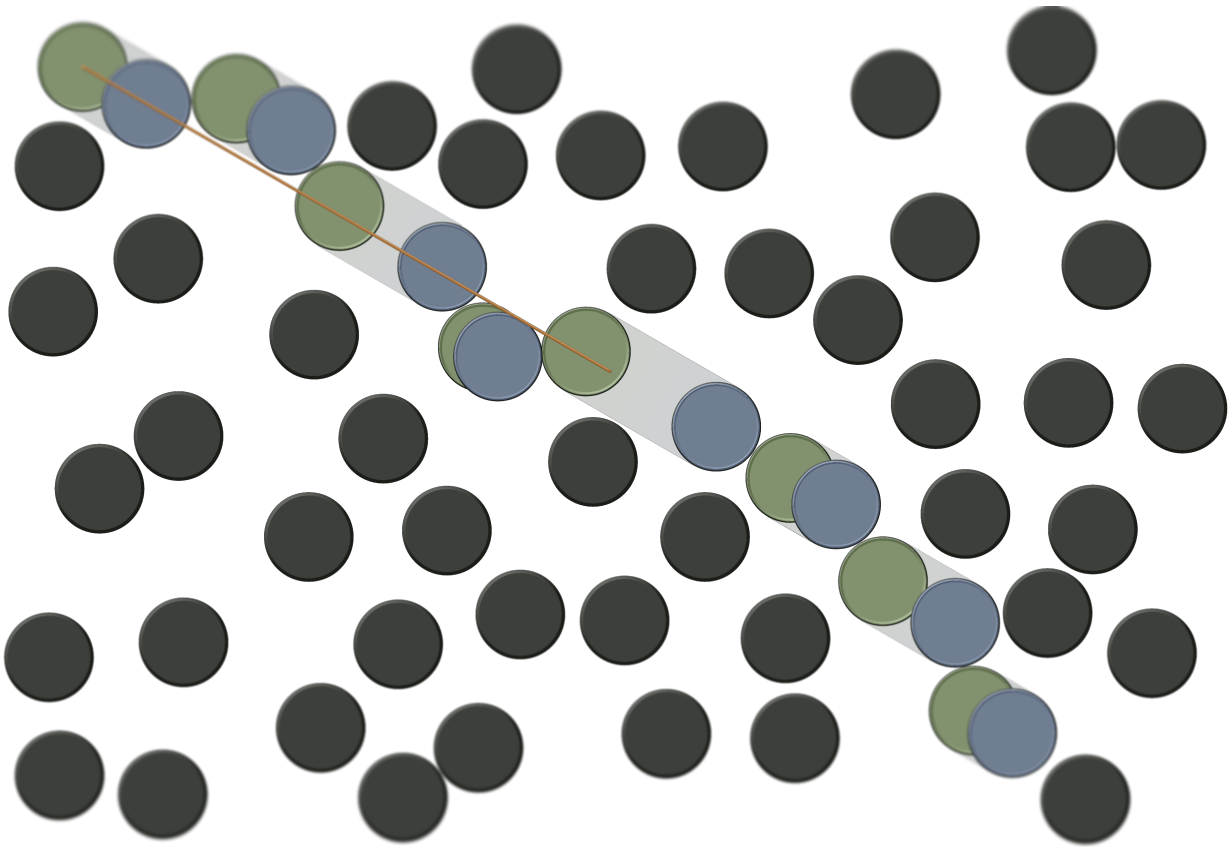

Figure 83: Visualisation of an event-chain cluster update of a system of impenetrable disks. The disks that are part of the moved cluster are green and their final position is blue. The orange line depicts the total displacement distributed upon the cluster in the update.

Since their first application to a hard disk system [3], (Markov-Chain) Monte Carlo (MC) simulations have been applied to practically all types of models in statistical physics, both on-lattice and off-lattice. MC samples microstates of a thermodynamic ensemble statistically according to their Boltzmann weight. In its simplest form, the Metropolis MC simulation [3, 4], a MC simulation is easily implemented for any system by offering a new microstate to the system and accepting or rejecting according to the Metropolis rule, which is based on the Boltzmann weights. The Metropolis rule guarantees *detailed balance*[177]. Typical local MC moves, such as single spin flips in spin systems or single particle moves in off-lattice systems of interacting particles, are often motivated by the actual dynamics of the system. Sampling with local moves can become slow, however, under certain circumstances, most notably, close to a critical point, where large correlated regions exist, or in dense systems, where acceptable moves become rare.

The strategy to improve these MC simulations is essentially the same two-headed hydra that is omnipresent in any field of scientific computation:

algorithmic research and an increase in computational power[178]. For MC simulations this means to address the issues of critical slowing down and dense systems by means of *cluster algorithms* and (massive) *parallelization*:

(i) One route for improvement is *cluster algorithms*, which go beyond local Metropolis MC. Such methods construct MC moves of large *non-local* clusters. Ideally, clusters are generated in a way that the MC move of the cluster is performed *rejection-free*. Clusters have to be sufficiently large and cluster building has to be sufficiently fast to gain performance. For lattice spin systems, the Swendsen-Wang [5] and Wolff [6] algorithms are the most notable cluster algorithms with enormous performance gains close to criticality, where they reduce the dynamical exponent governing the critical slowing down.

For off-lattice interacting particle systems, the simplest of which are dense hard spheres, cluster algorithms have been proposed based on different types of cluster moves[7–11]. In Ref. 7, a cluster algorithm based on pivot moves has been proposed, which was applied to different hard core systems [8, 9], and variants formulated for soft core systems [10]. In Ref. 11, the event chain (EC) algorithm has been proposed, which generates large clusters of particles in the form of a chain of particles, which are moved simultaneously and rejection-free. ECs become long in the dense limit, which significantly reduces autocorrelation times.

(ii) The other route is *parallelization*, as multi-processor computing has become widely available both in the form of multiple CPUs and, in recent years, in the form of graphic processing units (GPUs). On GPUs, "massively" parallel algorithms can significantly improve performance of simulations. For massively parallel computation on GPUs, the algorithm has to be data-parallel to gain performance, i.e., the simulation system has to be dividable into pieces, which can be updated independently accessing a limited shared memory. This has been achieved very efficiently for molecular dynamics (MD) simulations [12, 13] and MC simulations [14].

It seems attractive to combine both strategies and search for parallelization options for cluster algorithms. For conventional Metropolis MC based on single spin/particle moves or MD simulations with finite range of interactions, the parallelization strategy typically consists in spatial partitioning of the system into several domains, on which the algorithm works independently in a data-parallel manner. Such algorithms can also be massively parallelized for GPUs. For cluster algorithms the suitable parallelization strategy is less clear. There is an inherent conflict at hand here as it is not without compromise possible to divide the system into a large number (of necessarily small) *independent* subsystems and also perform *coherent* updates on a large number of particles in the system. If a spatial decomposition strategy is to be used, it must be applied to the cluster selection and cluster identification. This has been achieved for Swendsen/Wang and Wolff algorithms for lattice spin models recently [15, 16], and these algorithms have been implemented with efficiency gains on GPUs.

The EC algorithm for dense hard sphere system[11], see Fig. 83, relies on a sequential selection of a chain of particles as the cluster to be updated (and will be explained in more detail below), which makes massive parallelization difficult. We want to investigate a strategy to apply spatial partitioning into independent simulation cells as parallelization technique to the EC algorithm for hard sphere systems in order to combine performance gains from cluster algorithm and parallelization. A similar approach has been proposed in Ref. 33. Here, we also systematically test parallelized EC algorithms for

[177] A Markov-chain is said to be in detailed balance (or reversible), if the transition rates $\omega_{i\to j}$ between any two states i,j are such that there is no net flux between these two states in equilibrium (as represented by the equilibrium distribution P_i), i.e.

$$\omega_{i\to j}P_i = \omega_{j\to i}P_j.$$

This is a stricter requirement than *global balance*, which is to demand the absence of net fluxes from (or to) any state in equilibrium,

$$\sum_j \omega_{i\to j}P_i = \sum_j \omega_{j\to i}P_j.$$

Obviously, the latter suffices for a stationary distribution. Detailed balance is usually enforced because, for one, it guarantees global balance on the most fundamental level and, secondly, corresponds to microscopic time-reversal invariance, which should hold in any autonomous physical system.

[178] In the light of "Moore's law" the latter could almost certainly be achieved by waiting for better machines, but who has the time?

correctness and efficiency using the well-studied example of two-dimensional hard disks. As a result, we find that for the parallel EC algorithm to work correctly it is crucial how the starting points of ECs are selected during a sweep in a simulation cell.

Moreover, the most efficient parallelization will not be massive; the scalability will be limited by the nature of the EC algorithm itself. The EC algorithm is most efficient if EC clusters have an optimal size [11], which is related to the particle density. If simulation cells become too small compared to the typical size of EC clusters, parallelization becomes inefficient. The parallel EC algorithm will, therefore, be best suited to multicore CPUs with shared memory.

We present and systematically test the parallel EC algorithm in detail in the context of the hexatic to liquid transition in two-dimensional melting of a system of hard disks and consider applications in polymer systems later on.

Two-dimensional melting

Model

We use the simplest possible (non-trivial[17]) system of particles with a hard-core interaction to introduce our parallel event-chain cluster algorithm: the two-dimensional hard-disk gas.

Two-dimensional melting[18], especially in the simplest formulation of a system of hard (impenetrable) disks, is a fascinating example of a classical phase transition. Hard disks are an epitome of a system that is easily described and quickly implemented in a (naive) simulation, but very hard to tackle analytically. Hard disks have been subject of computational studies ever since the seminal works of Metropolis *et al.* [3], which can be regarded as a starting point for MC simulations and of the area of computational physics as a whole.

For two-dimensional melting, there has been a long debate on the nature of the phase transitions leading from the liquid to the solid phase. In two dimensions genuine long-range positional order is not possible because of thermal fluctuations, but a two-dimensional fluid with short-range interactions can only condense into a solid phase with algebraically decaying positional correlations. The KTHNY-theory [19–21] describes two-dimensional melting as defect-mediated two-step melting process (cf. Fig. 84): Starting from the quasi-ordered solid in a first transition dislocations unbind, which destroys the translational order [19] resulting in a so-called hexatic liquid, which remains orientationally ordered. In a subsequent second transition, disclinations unbind destroying also the remaining orientational order [20, 21]. Both transitions are continuous phase transitions of Kosterlitz-Thouless type. Alternatively, a weak first order phase transition has been discussed, where a liquid phase with lower free energy appears before the instability of the ordered phase with respect to defect-unbinding sets in. Both phases then coexist in a region in parameter space. Simulations on hard disks in two dimensions gave indecisive results[22] regarding this issue for many years.

The EC algorithm helped to settle this issue for the two-dimensional hard disk system. The transition from the hexatic to the liquid phase is a first order transition[23, 24] by identifying a region of phase coexistence and a characteristic pressure loop[179] if the pressure p is measured as a function of the particle density. No such loop was detected between the hexatic and solid

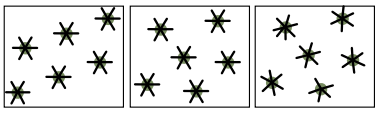

Figure 84: Schematic illustration of the two-step melting process in two-dimensions. Shown is a selection of disks (with large relative distances) with the directions towards their next neighbours the density (including omitted disks) decreases from left to right. Left: Crystalline phase, the disks are orientationally and positionally ordered. Middle: Hexatic phase, the disks do no longer possess long-ranged positional order but are orientationally ordered. Right: Liquid phase without any long-ranged order (and only on average six next neighbours).

[179] The mere existence of a loop in the pressure gathered from a finite-size simulation does not allow for the conclusion that one observes a first-order transition as finite-size effects can also induce a (Mayer-Woods)-loop even at a higher-order transition[25–27]. However, the scaling of the "amplitude" of the loop with the system sizes distinguishes these and this is the way how the order of transition for the hard-disk system has been established.[24].

phase with quasi-long-range positional order indicating that the hexatic to solid transition is continuous. These results were corroborated by massively parallel local MC and MD simulations[24].

We simulate a gas of N hard disks of diameter σ in an $L \times L$ box with periodic boundary conditions. As velocities trivially decouple from positions, we restrict ourselves to the latter. Hard disks are an athermal system and the particle density $\rho = N/L^2$ or the occupied volume fraction η defined as

$$\eta = N\pi\sigma^2/4L^2 = \pi\sigma^2\rho/4.$$

is the only control parameter for the phase behaviour of the system[180].

We will explore the new parallelized version of the EC algorithm using the example of the liquid to hexatic transition following Refs. 24, 32. The hexatic phase is characterized by *bond-orientational order*, which gives rise to a finite absolute value of the hexatic order parameter Ψ given by

$$\Psi = N^{-1}\sum_k \Psi_k \qquad \text{with } \Psi_k = \sum_{\langle k,l\rangle} \frac{\mathrm{e}^{\left(6\mathrm{i}\varphi_{k,l}\right)}}{n_k},$$

where the first summation extends over all particles k and the second one over all of their n_k next neighbours l. The angle $\varphi_{k,l}$ is the orientational angle between the vector from the particle k to its neighbour l and a fixed reference axis (the x-axis in our implementation).

To decide which particle pairs constitute next neighbours a Delaunay triangulation (the dual graph of the Voronoi diagram) is used[181]. The hexatic order parameter Ψ is very useful to quantitatively track the change in the state of the system during the simulation. For this purpose we define the autocorrelation time τ as characteristic time scale in the exponential decay of the Ψ-autocorrelation

$$C(\Delta t) = \frac{\langle \Psi^*(t)\Psi(t+\Delta t)\rangle}{\langle \Psi^*(t)\Psi(t)\rangle} \sim \mathrm{e}^{(-\Delta t/\tau)}.$$

Note that the phase of Ψ for a given state depends on the choice of the arbitrary reference axis and therefore the average $\langle\Psi\rangle$ should be zero[182], which we already incorporated in the definition of the autocorrelation. This is a useful check to decide if the measurement was performed over sufficiently long time[183] or, correspondingly, a large enough ensemble of systems.

We use τ as a measure for the speed of the simulation and the efficiency of the sampling. To precisely check for the correctness of the simulation we measure the pressure P as a function of the occupied volume fraction η. Close to melting, the pressure is extremely sensitive to problems in the algorithm and, therefore, very suitable to test new algorithms[184]. The pressure in this hard sphere system is given by the value of the pair correlation at contact distance [3],

$$\beta p\sigma^2 = \sigma^2\rho\left(1 + \frac{\pi}{2}\sigma^2\rho \lim_{r\to\sigma+} g(r)\right), \tag{65}$$

where $\beta = 1/k_BT$ denotes the inverse temperature, $\rho = N/V = 4\eta/\pi\sigma$ the density, and $g(r)$ the pair correlation function. We measure $g(r)$ using a histogram $n(r_i)$ which counts all pair distances[185] d with $|d - r_i| \le \delta_r/2$,

$$g(R_i) = \frac{\langle n(r_i)\rangle}{N\rho 2\pi R_i\delta_r} \qquad \text{with } R_i = \frac{2\left(r_{i+1}^3 - r_i^3\right)}{3\left(r_{i+1}^2 - r_i^2\right)},$$

and follow the procedure laid out in Ref. 24 to extrapolate $\lim_{r\to\sigma+} g(r)$.

[180] The system is[23, 24] in a disordered liquid phase for $\eta < \eta_{lh} \approx 0.7$, in a hexatic phase for $\eta_{lh} < \eta < \eta_{hs} \approx 0.72$ and, finally, in an ordered phase for $\eta_{hs} < \eta < \eta_{hcp} = \pi/2\sqrt{3} \approx 0.9069$, where the upper bound η_{hcp} corresponds to a hexagonal close packaging of disks[28].

[181] The computation of either (the Delaunay triangulation or the Voronoi diagram) is rather intricate[29]. In the implementation we made use of the CGAL library [30]. Still the triangulation leads to a high computational cost for the measurement of Ψ in a simulation, which we therefore avoid as far as possible.

[182] This holds also for the ordered phase, in which $|\Psi|$ is non-zero. The phase of the complex quantity ψ then rotates about 2π on timescales of the correlation time τ.

[183] There are multiple concepts of time here. We refer to the "number of steps in our MC simulation" as *time* for the sake of conceptual simplicity, and to the actual time a simulation runs on a computer as *wall time* (as it is the time difference one would infer from a clock on a wall next to the computer whilst waiting for it to finish the simulation).

[184] Also, from a thermodynamical point of view one could not ask for more information: As we are looking at a system with athermal interactions the caloric equation of state is trivially $E = {}^{k_BT}/_2 2N$ stemming from the completely decoupled velocity degrees of freedom. Furthermore, we only consider the canonic ensemble with a fixed number of particles, whence it follows that the thermal equation of state $f(p,N,V) = 0$ suffices to completely describe the system.

[185] We stress the importance of the binning rule, as we experienced that a different binning rule (e.g. $d - r_i \le \delta_r$) leads to differing results for $g(r)$ with errors of the order of δ_r, which give important deviations in the pressure on the scale discussed here. This dependence has not been seen in Refs. 32 and 24, where it is stated that different binning lead to quantitatively similar results.

Algorithm

Traditional local displacement Monte Carlo

The local displacement MC algorithm is the simplest way to implement a Markov chain MC simulation for hard disks. Particles are moved by an isotropically distributed random vector $\boldsymbol{r}$ whose length is uniformly distributed between 0 and $\ell_{\max}$. The maximal displacement length $\ell_{\max}$ determines the acceptance rate of the simulation. Optimal performance is usually obtained for an acceptance rate around $20\% - 50\%$ (for a Gaussian move distribution there is an exact result of an optimal acceptance rate 23% [31]), which means in the case of hard disks that $\ell_{\max}$ is of the order of the mean free path of the particle. Compared to an MD simulation this method leads to very large autocorrelation times[24] and, therefore, is not very suitable to equilibrate larger systems, in particular, for higher densities.

Event chain algorithm

The EC algorithm introduced by Krauth *et al.* [11] has been developed to decrease the autocorrelation time of a system of hard disks or spheres. It performs rejection-free displacements of several spheres in a single MC move. The basic idea is to perform a large displacement ℓ, the chainage of the update, in a "billiard" fashion, transferring the displacement to the next disk upon collision (cf. Fig. 83). First, an initial pivot particle of the EC and a random direction are chosen. The pivot particle is then moved in this direction until it is tangent to another particle; the displacement ℓ_1 of the first particle is subtracted from the initial total displacement length and the remaining displacement $\ell - \ell_1$ is carried over to the tangent particle, which is the new pivot particle. This procedure continues[186] until no displacement length is left. The total displacement length ℓ is an adjustable algorithm parameter. In principle, ℓ should be as large as possible; however, there is a finite ℓ beyond which there is no substantial gain[11] from simulating longer ECs.

For collision detection a decomposition into square cells with a lattice constant of the order of the mean free path is used. Each disk is assigned to one square cell and collision tests are limited to neighbouring squares, which leads to a complexity of $O(1)$ for each trial move.

The most performant version of the straight EC algorithm, the so called *xy*-version or irreversible straight EC algorithm, uses only displacements along coordinate axes and only in positive direction, thus simplifying various computations, but also breaking the detailed balance condition (ergodicity is preserved through periodic boundary conditions). Our parallel EC algorithm will rely on a partition of the system into simulation cells, such that we have fixed rather than periodic boundary conditions for each simulation cell. In this situation abandoning detailed balance is no longer possible, and we only use ECs that fulfil the detailed balance condition[187].

For optimal parameters the EC algorithm achieves a speed up by a factor of roughly 16 compared to local MC [11]. This algorithmic improvement has facilitated the extensive study of large (up to $N = 1024 \times 1024$) systems and, thus, the clear identification of the two-dimensional melting process [23].

[186] There are (at least) two versions of this algorithm which differ in the direction of the displacement of the hit disk. The hit disk is either displaced in the original direction which is called *straight event chain* algorithm or in the direction reflected with respect to the symmetry axis of the collision which is called *reflected event chain* algorithm. The straight EC variant has been found to sample more efficiently, as it achieves a larger change in the system state with the same computational effort thus featuring a smaller autocorrelation time. We only consider the straight variant here.

[187] The additional pain of less performant sampling does not come without gain. Enforcing detailed-balance ensures microreversibility and this leads to the correct dynamic behaviour of the system on coarse time-scales (see below).

Massively parallel MC simulation

A different approach to overcome the limitations of the local MC is to increase the number of processing units used in the simulation. As seen before, the number of CPUs commonly available in standard workstations would not suffice to increase the performance to the level reached by the EC algorithm, even if ideal scaling is assumed. However, modern GPUs can execute several thousands threads simultaneously and, therefore, allow for a massively parallel simulation accessing a limited shared memory. Such a parallelization comes with its own peculiarities, in particular, it has to be taken care that no concurrent memory changes occur.

The massively parallel MC algorithm (MPMC) by Engel *et al.* [24, 32] relies on the spatial decomposition into a chequerboard where four "cells" forming a 2×2 square belong to one thread to ensure independent areas for each thread as in Fig. 85 (left). In every sweep the chequerboard is shifted by a random vector to ensure ergodicity and a list of all particles in each cell is created and shuffled. This step is essential to ensure detailed balance, because in every cell a fixed number n_m of particle moves are suggested to balance the work load[188]. A thread works on the four cells in a chosen sequential order; while working on one cell, positions of particles in the other cells are frozen. If a particle attempts to leave a cell the corresponding move is rejected.

The additional rejection lowers the effectiveness of the sampling, but due to the massive parallelization the simulation runs several orders faster than a simple sequential local MC algorithm: for optimal parameters a speed up[189] by a factor[32] of roughly 148.

[188] The other possibility would be to draw a random sequence of disks to move. However, moving the same disk multiple times slows down the sampling of the phase space as the disks cannot leave their cell and therefore have very limited space to explore.

[189] This has been done using a TESLA K20 GPU with 2496 arithmetic logic units.

Parallel event chain algorithm

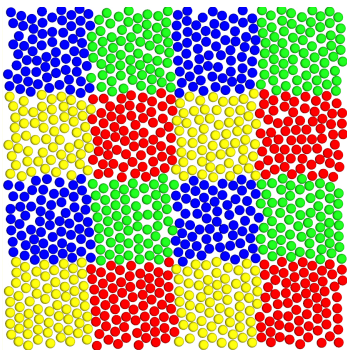

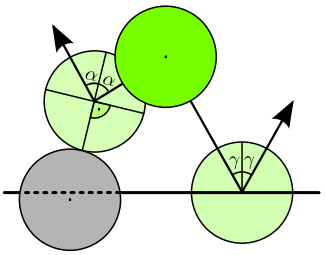

Figure 85: Left: Scheme of the cell decomposition. To ensure independence of each thread only beads in cells with the same colours are movable at the same time. In every sweep the chequerboard is shifted by a random vector to ensure ergodicity. Right: Scheme of event chain reflections to handle cell boundary events, whenever a disk moved by an EC would move outside the current cell or hit an inactive frozen disk. The angle of reflection of the EC equals the angle of incidence.

Our goal is to formulate a parallel event-chain (PEC) algorithm that uses commonly available resources (4 to 16 CPUs on a current multi-processor machine[190]) which combines aspects from the EC algorithm and the massively parallelized local MC algorithm.

For the two-dimensional hard disk system our PEC algorithm for n parallel threads consists of the following steps in each MC sweep:

1. Decompose the system into $4n$ square[191] cells; the square lattice is shifted by a random vector.

2. Form n blocks of 2×2 square cells (cells with different colours in Fig. 85).

[190] Thus there are of the order of 10 event-chains evaluated at any time. However, the denomination event-furlong has as of now sadly not caught on.

[191] The description focuses on the method used for the data presented below. For the general purpose applications we have in mind (see below), it is favourable to use an isotropic distribution of displacement directions, which basically eliminates the striped geometry proposed in Ref. 33 because displacements transverse to the stripe direction will either be rejected or reflected with very little net displacement. However, there are more efficient decompositions that allow for larger cell sizes, one of which (tile-joint scheme) we will use below.

3. Randomly shuffle the order of cells in the blocks (select one series of colours in Fig. 85, e.g. blue, yellow, green, red)

4. Fork into n threads, each of which acts on one block.

5. Create a list with n_m EC pivot disks for each of the four cells in the block by drawing *with replacement*.

6. Start one EC at each of the n_m disks in the list. While working on one cell, particle positions in the other cells are frozen. Synchronise threads when list is done and repeat for all four cells in the block.

7. Go to step 1. and generate a new decomposition.

The generalisation to higher-dimensional hard sphere systems is obvious.

Less obvious are some technical aspects: *(a)* How are collisions of the event-chains with the introduced boundaries (be it the boundary of the cell or a frozen disk from an adjacent cell) handled and *(b)* Why are n_m chains started in each cell and why did we stress that the pivot disks have to be drawn with replacement?

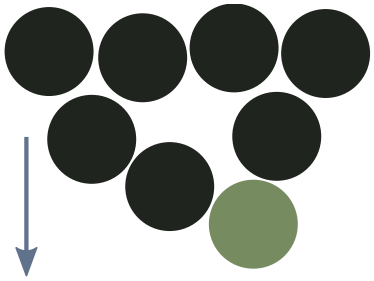

Figure 87: An extreme case of end-particle statistics i: Any sufficiently long event-chain whose pivot disk is one of the shown moving in the shown direction will end at the green disk.

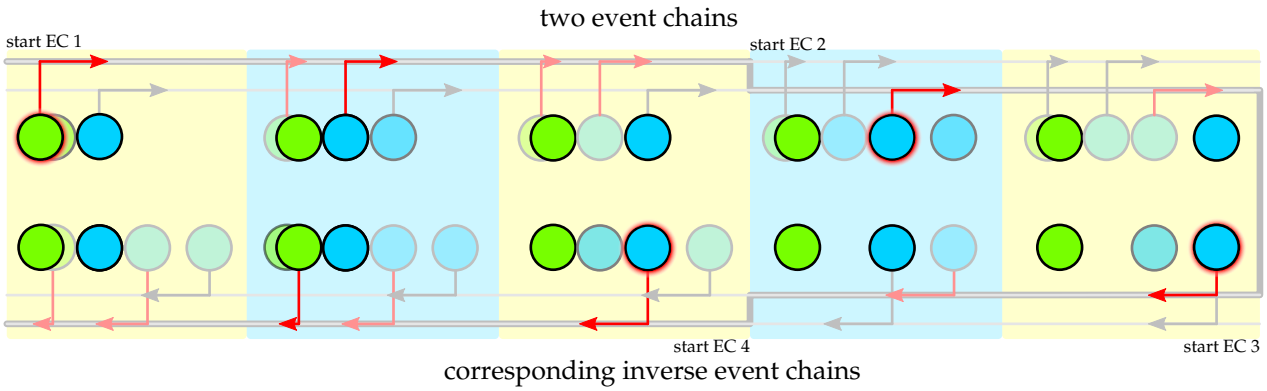

Figure 86: Influence of event chain starting point distribution on detailed balance. For the sake of simplicity we show a one-dimensional system containing only two disks. A MC sweep then consist of two ECs (1, 2): EC 1 starts at the green disk, EC 2 at the blue disk (upper row). The starting points of event chains are highlighted by a red halo. The inverse sweep (lower row) also consists of two ECs (ECs 3, 4). Both EC 3 and EC 4 have to start at the blue disk (the end disks of EC 1 and EC 2): Although the starting points of the sweep are distinct, for the inverse sweep the event chains need to start on the same disk. To ensure detailed balance on the sweep level both sweeps need to be suggested with the same probability. Therefore a shuffled list with distinct starting points will lead to an incorrect sampling, because the inverse sweep cannot be suggested in every case.

Regarding *(a)*, we note that, in the actual EC step, the EC must *not* leave the cell, otherwise detailed balance and independence of the parallelly working threads are not guaranteed. This means that whenever a disk moved by an EC would move outside the current cell or hit a disk that is outside the current cell, a separate treatment is required. In both cases we think it is most effective to *reflect* the EC at the cell wall or an inactive frozen disk at the cell wall with the angle of incidence equal to the angle of reflection as shown in Fig. 85 (right). In this way, detailed balance is still guaranteed and no rejections are introduced. It has been proposed[33] to *reject* ECs reaching the cell wall or an inactive disk at the cell wall. In principle, rejections are also suited to handle these situations but will slow down the sampling and also ask for additional memory overhead, because only a rejection-free cluster update can be performed in-situ without separately storing the original positions.

Regarding point *(b)*, the creation of the list of n_m starting particles for ECs is a subtle issue. At first, naive sight, it seems favourable to shuffle a list containing n_m *distinct* particles in the cell (as in the MPMC algorithm) for a given cell decomposition. Then the maximally possible number of distinct EC pivot particles is guaranteed, which seems to promise more efficient sampling. However, this use of a shuffled list of distinct pivot particles violates detailed balance on the sweep level and gives rise to incorrect results (unless $n_m = 1$). To see this we note that the inverse of an EC with displacement

ℓ starting at disk a with direction $\boldsymbol{r}$ and ending at disk b is an EC with the same displacement ℓ and the inverse direction $-\boldsymbol{r}$ starting at b and ending at a. Alas, the distribution of ending disks is unclear, see Fig. 87, and we can therefore not guarantee the identical statistics of pivot and ending disks. For a sweep with multiple ECs starting this means that the sets of starting particles of the original and the inverse sweep need *not* to be permutations of each other. This is, however, what is assumed when using a shuffled list of distinct particles (and is valid for local displacement MC). For detailed balance, all n_m starting particles have to be selected with the same equal probability among *all* particles in the cell. Therefore, one has to create the list of starting particles by drawing *with* replacement (resulting in starting particles which are not necessarily distinct). We give a simple example for a situation where this becomes relevant in Fig. 86. The different statistics – either drawing with replacement or without replacement (shuffling) – of starting particles become more relevant the larger the list length n_m is and both list types become identical for $n_m = 1$.

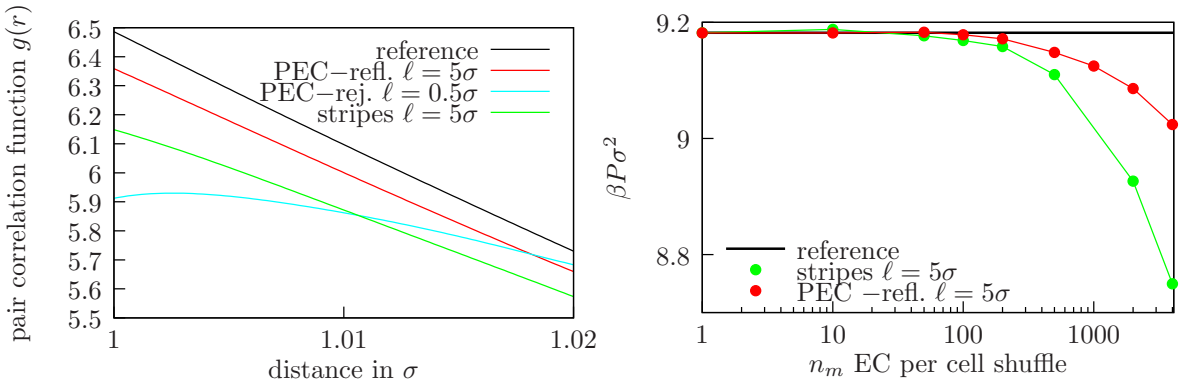

Figure 88: Left: Influence of the validity of detailed balance on the pair correlation function $g(r)$ for several incorrect simulation variants of the EC algorithm. As a reference, we show the correct $g(r)$ as obtained from a simulation with local MC moves (black). All variants of PEC algorithms using *shuffled lists of distinct EC starting particles* with list length $n_m > 1$ give incorrect results: "PEC-refl." uses EC reflection, "PEC-rej." uses EC rejection at the cell boundaries and a checkerboard decomposition; "stripes" uses EC rejection at the boundaries and a striped decomposition as in Ref. 33. On the other hand, *all* corresponding curves for algorithms with starting particle lists drawn with replacement lie strictly on top of the reference curve (and are not shown for clarity of the figure). Right: Pressure $\beta P\sigma^2$ as a function of the number n_m of started ECs per cell shuffle for different algorithms using shuffled lists for the starting particles. The colours correspond to the colours on the left. Only for $n_m = 1$, algorithms with shuffled lists become correct and the pressure assumes the reference value. All simulations are performed for $N = 256^2$ disks at occupied volume fraction $\eta = 0.708$.

In order to test the importance of the different statistics of starting particles for different list lengths n_m, we measure the pair correlation function $g(r)$ and obtain the pressure P using eq. (65) (for a system containing $N = 256^2$ disks at occupied volume fraction $\eta = 0.708$). Finally, we compare our results with standard MC simulations with local displacement moves as a reference. We compare PEC algorithms using shuffled lists of distinct EC starting particles with PEC algorithms using lists generated by drawing particles with replacement; for both types of algorithms we consider both variants with reflection and rejection of ECs at the cell boundaries.

We find that all PEC algorithms starting $n_m > 1$ ECs at particles drawn *without* replacement, i.e., by list shuffling give incorrect pair correlation functions $g(r)$. The pair correlations differ from the expected behaviour for small $r \approx \sigma$ both in their functional form, see Fig. 88 (left), and in the resulting value for P, see Fig. 88 (right), which is obtained from the limiting value of the pair correlation at $r \to \sigma+$ according to eq. (65). Differences in the pressure P increase with increasing n_m as shown in Fig. 88 (right). Only for the trivial list length $n_m = 1$, i.e., with only EC started in each cell, there is no difference between a list generated by drawing with replacement and generated a list generated by shuffling, and all algorithms converge to the reference result for P, see Fig. 88 (right).

For all list lengths $n_m > 1$, all PEC variants using starting particle lists generated *with* replacement yield the correct reference result for $g(r)$ from

the local MC simulation.

We also examined the importance of replacement in the starting particle list for a parallelization of the EC algorithm through a decomposition into striped cells as proposed in Ref. 33. Similar to the PEC with chequerboard cell decomposition we find that only drawing starting particles with replacement yields the correct pressure as also shown in Fig. 88.

The dependence of the pressure and pair correlation function on algorithmic details (choice of ℓ, reflection/rejection, squares/stripes) for the incorrect algorithms using shuffled lists stems from the different ending point statistics of the ECs and is not easily explained on a quantitative level.

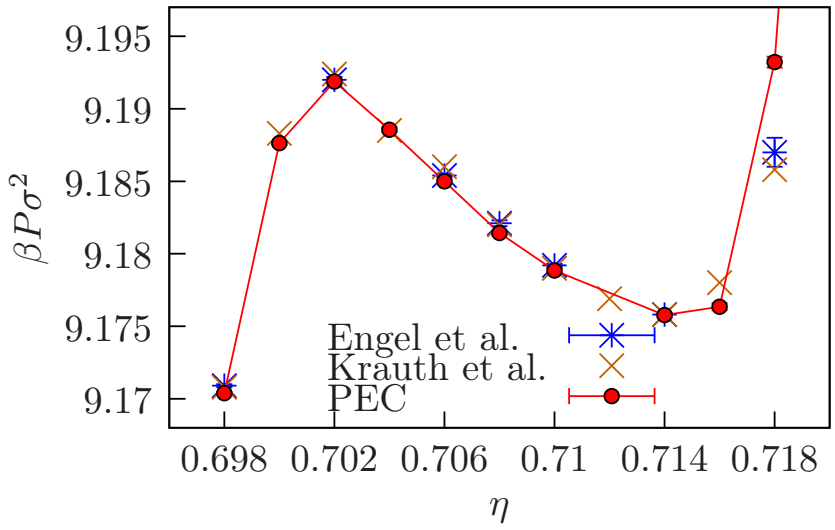

Figure 89: Phase diagram for the liquid-hexatic transition of hard spheres. We compare the results of the three algorithms MPMC (blue, data taken from Ref. 24), sequential EC (brown, data taken from Ref. 24) and PEC (red) for a system with $N = 256^2$ particles. Within the estimated simulation errors the algorithms yield the identical pressure density dependence. At large η, the PEC accuracy is limited by smaller running times. We run 30 independent simulations to estimate errors.

For a more extensive quantitative check of the correctness of our algorithm, we simulate a system with $N = 256^2$ particles in the range of occupied volume fractions $\eta = 0.698 \ldots 0.718$, which is the regime of coexisting densities at the transition between hexatic and liquid phase as reported in Refs. 23 and 24. We compare the measured pressure with literature values from these references in Fig. 89. We find good agreement with deviations only at the highest packing fractions η, which is not a problem of our PEC algorithm itself: For large η autocorrelation times become very large; simulations in Refs. 23 and 24 had significantly longer running times and, thus, give more accurate values.

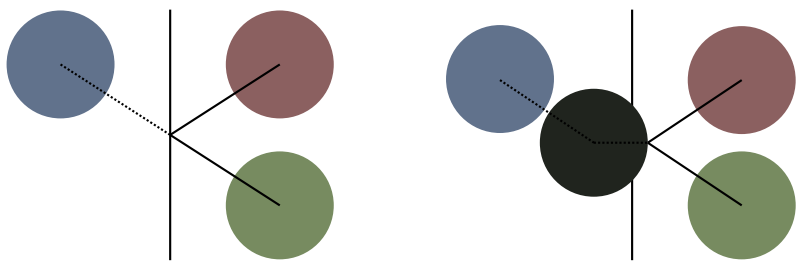

Figure 90: Sketch of the proposed method of images to extend the collision-rate based pressure measurement[34] to the parallel realm of the PEC. For a sequential EC it can be shown that the pressure can be computed from measuring the projection of the (vectorial) difference of starting and ending point onto the displacement direction for every event-chain. This can be extended to the PEC, if one does not consider the actual PEC (from green to red position), but a faux one (from green to blue), that accounts for the correction as shown in the left half. Due to reflections with frozen beads (dark), this is *not* the same as treating any reflection as the end (and beginning) of a event-chain with shorter effective displacement ℓ' as shown in the right half.

For sequential event chain implementations of hard disk systems there is a more effective way to calculate the pressure than by means of the pair correlation function and eq. (65), which uses a relation between the pressure and collision probabilities [34]. We chose to compute the pressure using the pair correlation function as this puts local MC and event chain data on

the same established footing and does not imply greater computational cost because we use the pair correlation as a source of additional information on the correctness of the sampling, especially with respect to detailed balance (see Fig. 88). We suggest that the pressure calculation of Ref. 34 could be extended to PEC sampling by treating reflected event chains using a method of images, see Fig. 90.

Efficiency of the parallel event chain

To optimise the efficiency of the PEC algorithm, we can adjust the degree of parallelization n, the number n_m of ECs started within each cell and the length of ECs via the total displacement length ℓ in the parallelization scheme. Parallelization of the EC algorithm will only offer an advantage over the sequential EC algorithm if the autocorrelation time τ in units of wall time decreases significantly with the number n of threads.

First we discuss efficiency as a function of the number n_m of ECs started within each cell. To sample efficiently there should be at least one displacement per particle which suggests

$$n_m \sim N/4nn_{\mathrm{EC}} \sim N\lambda_0/4n\ell, \tag{66}$$

where n_{EC} denotes the average number of disks per EC. On average, this number is given by the ratio of the total displacement length ℓ of the EC and the mean free path of disks λ_0 (approximately given by the free volume per particle $\lambda_0 \approx \sigma(\eta_{hcp} - \eta)/2\eta_{hcp}$ in the dense limit close to the close-packing density η_{hcp}),

$$n_{\mathrm{EC}} \sim \ell/\lambda_0.$$

For small values of n_m, the relative fraction of wall time spent on overhead (forking / synchronising / list creation) increases. Reducing the relative overhead by increasing n_m leads to the saturation of speed up (in terms of the number of MC moves per wall time) by parallelization to a maximal value close to n as shown in Fig. 91 (left). For values of n_m much larger than the value according to eq (66) finite size effects will increase as each decomposition into $4n$ cells persists for a long time[192]. Moreover, sampling small cells independently for a long time is inefficient in removing large scale correlations extending over several cells. Therefore, the autocorrelation time τ of the PEC algorithm (measured in wall time) increases for large n_m as shown in Fig. 91 (right). The optimal choice of n_m according to the results in Fig. 91 (right) agrees with the criterion (66).

[192] In the limit $n_m \to \infty$ the system consists of n (There would be $4n$ cells, but the computation would be limited to n systems.) entirely independent smaller systems.

Now we discuss efficiency in terms of the total displacement length ℓ and the degree of parallelization n. The efficiency of the EC algorithm in general depends crucially on the average number of disks per EC $n_{\mathrm{EC}} \sim \ell/\lambda_0$. In Ref. 11, it has been found that the straight EC algorithm has optimal efficiency for $\ell/\lambda_0 \sim 10^1 ... 10^3$ (for a system size $L \approx 34\sigma$). For smaller ℓ, the efficiency decreases and approaches traditional local MC (corresponding to $\ell < \lambda_0$). For very large ℓ, ECs comprise large parts of the system and give rise to motion similar to a collective translation of disks, which is also inefficient.

For the efficiency of the PEC algorithm, two additional competing effects are relevant to determine the optimal values for ℓ and the degree of parallelization n. On the one hand, it is obvious that the reflections at the cell walls in the PEC algorithm will impair the sampling of configuration space. Therefore, the autocorrelation time of the PEC algorithm can be significantly

increased for small cell sizes, which is equivalent to small system sizes for a fixed number $4n$ of simulation cells, or for long ECs, i.e., large total displacement lengths ℓ of the ECs. This leads to a decrease in efficiency if the EC length $L_{\mathrm{EC}} \sim \sigma n_{\mathrm{EC}} \sim \sigma\ell/\lambda_0$ is increased beyond the cell size $L/2\sqrt{n}$, see Fig. 92. On the other hand, the relative overhead in computation time from parallelization (due to forking/joining/synchronising threads) is larger for shorter chains. This leads to a decrease in efficiency for decreasing ℓ, see Fig. 91 (left).

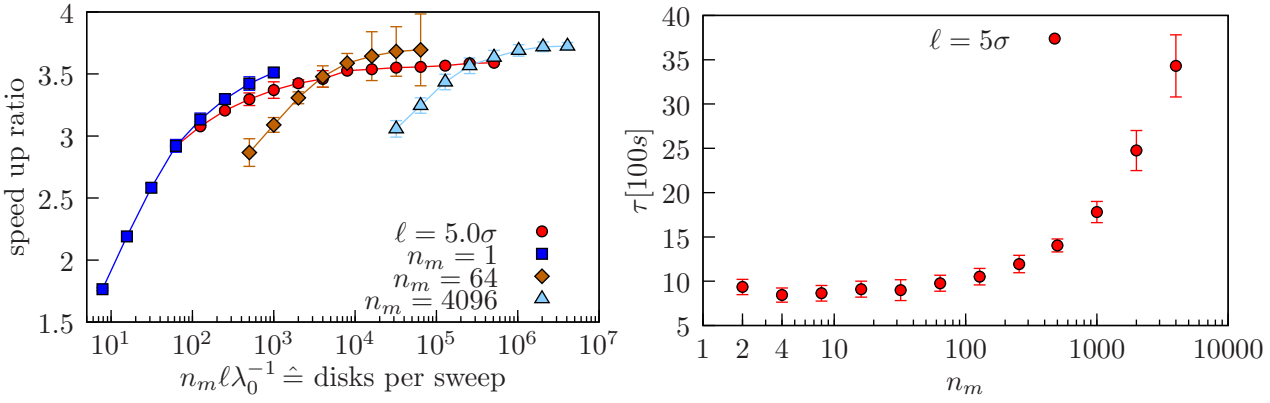

Figure 91: Left: Ratio of the number of moves per seconds (wall time) of the parallel and sequential EC algorithm as a function of the total displacement length ℓ and the number n_m of ECs started per cell configuration as a function of $n_m\ell/\lambda_0$ (for $N = 256^2$ disks at $\eta = 0.71$ using $n = 4$ blocks of 2×2 square cells). The speed up saturates to the maximal factor $n = 4$ both for large n_m and for large ℓ. Since the required computation time for the synchronisation overhead rises with n_m, it is more favourable to increase ℓ rather than n_m. The speed up should not depend on other simulation parameters such as η or N. Right: Autocorrelation time τ of the parallel EC algorithm measured in wall time as a function of the number n_m of started ECs per cell (for $N = 64^2$ disks at $\eta = 0.704$ using $n = 4$ blocks of 2×2 square cells). At $n_m \approx 5$, each disk in a cell is moved once per sweep on average according to eq. (66). If n_m increases the efficiency of the algorithm decreases strongly.

We conclude that ℓ should be chosen within the window $\ell \sim 10^1 ... 10^3\lambda_0$ of optimal values for the straight EC algorithm in general, on the one hand, and as large as the cell size permits, i.e., according to $L_{\mathrm{EC}}(\ell) \sim L/2\sqrt{n}$ or

$$\ell \sim \frac{L\lambda_0}{\sqrt{n}\sigma} \sim \lambda_0 \left(\frac{N}{\eta n}\right)^{1/2}, \tag{67}$$

on the other hand. If the number n of parallel threads is chosen too large, this choice for ℓ will drop below the optimal window $\ell < 10\lambda_0$ for straight EC algorithms and efficiency goes down. Therefore, we propose to adjust the degree of parallelization of the PEC algorithm according to the criterion (67) rather than massively parallelize.

In Fig. 92, we quantitatively investigate the optimisation of efficiency by adjusting ℓ or the EC length $L_{\mathrm{EC}} \sim \sigma\ell/\lambda_0$ according to the cell size for a degree of parallelization $n = 4$. In order to investigate how much the simulation can be accelerated by parallelization with $n = 4$, we measured the ratio of the autocorrelation time τ of sequential and parallel EC algorithm as a function of the number N of disks for $\ell = 5\sigma$ and a fixed particle density $\eta = 0.71$, see Fig. 92 (left). The number N of disks is related to the system size by $L = \sigma(N\pi/4\eta)^{1/2} \propto N^{1/2}$. Because we also work with a fixed number $n = 4$ of threads, $N^{1/2}$ is proportional to the system size L as well as the cell size $L/4$. For $\eta = 0.71$, the mean free path is $\lambda_0 \approx 0.08\sigma$ [11], such that $\ell = 5\sigma$ corresponds to $\ell/\lambda_0 \approx 62.5$, which is well within the window $\ell/\lambda_0 \sim 10^1 ... 10^3$ of optimal total displacement lengths for EC algorithms. In Fig. 92 (left), we show the autocorrelation time τ of the parallel and standard sequential EC algorithm in units of MC moves, where 20 MC moves correspond to one collision in the EC (using the same convention as in Ref. 11). We observe that for smaller systems $N < 128^2$ the autocorrelation time of the parallel EC algorithm exceeds the autocorrelation time of the sequential EC algorithm. First, this means that for smaller systems $N < 128^2$ corresponding to cell sizes $< 34\sigma$ the parallelized EC algorithm becomes less efficient. Because for $\ell = 5\sigma$ and $\lambda_0 \approx 0.08\sigma$, the typical EC length is

$L_{EC} \sim \sigma\ell/\lambda_0 \sim 62.5\sigma$, this marks also the range of cell sizes, which are comparable to or smaller than EC lengths. This supports our argument that EC lengths L_{EC} should be smaller than cell sizes for efficiency of the PEC algorithm.

The results in Fig. 92 (right) show explicitly that there exists an optimal ℓ for the PEC algorithm that minimises the autocorrelation time τ for a system with $N = 64^2$ disks. This minimum is attained for $\ell \gtrsim 10\lambda_0 \approx 0.8$ and $\ell \approx L\lambda_0/\sqrt{n}\sigma \approx 1.28$ in agreement with our criterion (67).

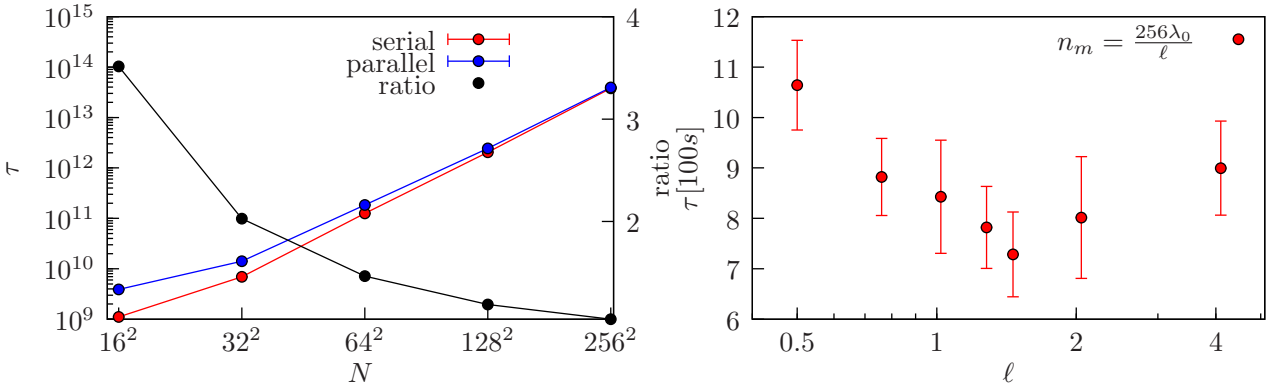

Figure 92: Left: Autocorrelation time of the order parameter Ψ for parallel and sequential EC algorithm (in units of effective local MC moves) as a function of the number of particles N for fixed volume fraction $\eta = 0.71$, total displacement length $\ell = 5\sigma$ and one EC per cell configuration $n_m = 1$. One collision in an EC is treated 20 effective local MC moves in a local displacement MC simulation [11]. For larger systems $N \geq 128^2$, the autocorrelation time differs only slightly between parallel and sequential algorithm. Therefore a good measurement for the efficiency of the algorithm is the mere increase in events per wall time shown in Fig. 91 (left). Right: Autocorrelation time of the parallel EC algorithm (in units of wall time) as a function of the total displacement length ℓ and with constant number of moved disks per sweep $n_m n_{EC}$=const for $N = 64^2$ and $\eta = 0.704$. The autocorrelation time exhibits a minimum for $\ell \gtrsim 10\lambda_0 \approx 0.8$ and $\ell \approx L\lambda_0/\sqrt{n}\sigma \approx 1.28$ in agreement with eq. (67).

Secondly, the results in Fig. 92 (left) show that for larger systems $N \geq 128^2$ the mere increase in MC moves per wall time is already a good measure for the efficiency of the PEC algorithm. Therefore, the ratio of the number of MC moves of the parallel and sequential EC algorithm, as shown in Fig. 91 (left) for a system of $N = 256^2$ disks, is also a measure of efficiency. In Fig. 91 (left), we show this ratio as a function of ℓ/σ and n_m. We find that the speed up ratio is an increasing function of both ℓ and n_m. For large values of ℓ/σ or n_m, the speed up ratio approaches ≈ 3.9 from below, which is remarkably close to the optimal speed up ratio 4 for $n = 4$ threads. We conclude that the PEC algorithm realises its efficiency gain by an approximately equal autocorrelation time as the sequential EC algorithm in units of MC moves but a significant increase in the speed up ratio, i.e., the number of MC moves per wall time with the degree of parallelization n.

In conclusion, we propose the following strategy of choosing the degree of parallelization n, the total displacement ℓ and the number n_m of ECs started within each cell to optimise efficiency:

1. Choose a degree of parallelization n such that $N/\eta n > 100$ such that $\ell > 10\lambda_0$ according to the criterion (67). We used $n = 4$ in our simulations.

2. Choose $\ell = \ell(n)$ according to the criterion (67) such that L_{EC} is comparable to the cell size.

3. Choose the number $n_m = n_m(n,\ell)$ according to (66).

Application of the Event-Chain Algorithm to Polymer Systems

An interesting (and large) class of systems to apply our (parallelized) event-chain algorithm to are polymer systems, which are commonly modelled by means of bead-spring models. Here and in many applications other than pure hard core systems, we have to deal with systems containing hard core repulsion (the steric interaction of the polymers that is captured by the impenetrability of the beads) alongside with other interactions (the bond energies) in a canonical ensemble. To account for these additional energies, one can in theory come up with two lines of strategy: Adapt the event-chain method to incorporate these energies (in a rejection-free manner) or take the point of view that the event-chain is an efficient way to generate updates (MC moves) that do not violate the hard-sphere constraint which are then accepted/declined according to a standard MC scheme (e.g. the Metropolis rule). Rejection-free extensions to the EC algorithm for continuous potentials have been presented using the concept of infinitesimal MC moves. However, the event-chain (and every adaptation) is on a very fundamental level meant to deal with *pair-interactions*. As seen before, bending energies do not fall under this category and can therefore not be treated in this manner. In the following section, where we study the formation of networks in systems of semiflexible polymers with a short-ranged attractive interaction, we will therefore take the simpler approach, i.e. we deal with the hard core repulsion using ECs and take into account the other interactions using the standard Metropolis algorithm. As this involves rejection and, thus, a slower sampling of the hard core degrees of freedom the need for parallelization is even larger than in a gas of hard disks/spheres. We will show that EC type MC moves not only improve the sampling of dense systems but can also give rise to a physically more correct "dynamics" in an equilibrium MC simulation of dense systems.

Networks of semiflexible Polymers

We will apply our algorithm to a system consisting of many semiflexible polymers, such as actin filaments, which are interacting via a short-range attractive potential in a flat simulation box in three dimensions. Under the influence of this attraction, semiflexible polymers tend to form densely packed bundles. Actin filament bundles consisting of many semiflexible actin filaments, which are held together by crosslinking proteins are a realisation of such a system and represent important cellular structures [35]. In vitro, F-actin bundles assemble both in the presence of crosslinking proteins and by multivalent counter ions. Theoretical work on crosslinker-mediated bundling of semiflexible polymers [36–39] and counterion-mediated binding of semiflexible polyelectrolytes [40]

show a discontinuous bundling transition above a threshold concentration of crosslinkers or counterions. Related bundling transitions have been found for crosslinker-mediated bundling [41], for counterion-mediated bundling [42] and for polyelectrolyte-mediated bundling [43].

It is an open question, both experimentally and theoretically, what the actual thermodynamic equilibrium state of the bundled system is and whether this state is kinetically accessible starting from a certain initial condition, for example, an unbundled polymer solution. Energetically, it is favourable to form a thick single bundle; entropically, a network of bundles (as shown in Figs. 93 B and C) might be advantageous. In both cases, the resulting bundles of semiflexible polymers are typically rather densely packed. This causes difficulties in equilibrating bundled structures in traditional MC simulations[38, 44] employing local moves. In Ref. 38 MC simulations showed evidence for kinetically arrested states with segregated sub-bundles, in Ref. 44 kinetically arrested bundle networks have been observed. Further numerical progress requires a faster equilibration of dense bundle structures. Ideally, the simulation reproduces the physically realistic centre of mass diffusion kinetics of whole bundles. Networks of bundles have also been observed experimentally in vitro for actin bundles with crosslinkers [45] and, more recently, in actin solutions where the counterion concentration has been increased in a controlled manner [46, 47].

Here we report a first application of the EC algorithm to a polymeric system of semiflexible harmonic chains (SHC) which are modelled as chains of hard spheres or beads of diameter σ connected by extensible springs[193] with rest length b_0 and spring constant k with an additional three bead bending energy characterised by a bending rigidity $\varkappa$ [48]. Beads in different chains also interact with a short-ranged attractive square well potential of strength g and range d. We choose the potential strength g well above the critical value for bundling [36, 38, 39].

The energy of this system[194] can be expressed as

$$H[t_i] = \sum_n \left[\varkappa \sum_{i=0}^{N-2} \left(1 - \frac{\boldsymbol{t}_{n,i}\,\boldsymbol{t}_{n,i+1}}{|\boldsymbol{t}_{n,i}||\boldsymbol{t}_{n,i+1}|} \right) + \frac{k}{2} \sum_{i=0}^{N-1} \left(\frac{|\boldsymbol{t}_{n,i}|}{b_0} - 1 \right)^2 - \sum_{\substack{\langle \{n,i\}, \\ \{m,j\} \rangle}} V_{n,m}^{i,j}(|\boldsymbol{r}_{n,i} - \boldsymbol{r}_{m,j}|) \right] , \tag{68}$$

where $\boldsymbol{t}_{n,i} = \boldsymbol{r}_{n,i+1} - \boldsymbol{r}_{n,i}$ denotes the tangent vector between the ith and $(i+1)$th bead of the nth chain and

$$V_{n,m}^{i,j}(x) = g(1 - \delta_{nm})\Theta(d - x) + (1 - \delta_{nm}\delta_{ij})\delta(\Theta(x - \sigma))$$

describes the pairwise attractive square-well potential and the hard sphere condition[195].

We consider an ensemble of many SHC in a flat box geometry of edge lengths $300\sigma \times 300\sigma \times 5\sigma$; this geometry is similar to what is used in microfluidic experimental setups in Ref. 47. For the chosen potential strength, the SHCs bind together and form a locally dense bundle resembling a dense hard sphere liquid. For systems containing *many* SHCs prepared in an initial state resembling a polymer solution (see Fig. 93 A), we obtain network bundle structures, which are very similar[196] to those seen in experiments for F-actin [46, 47], see Fig. 93 B and C. The network bundle structure is stationary or kinetically arrested on the accessible simulation time scales and characteristic

[193] The spring constant here has to be sufficiently large as to enforce the impenetrability of polymers and avoid unphysically large bond stretching. In principle, it would be possible to use very high spring constants approaching a fixed bond length, but this would diminish the simulation speed. A different approach that we also employed, but not for any of the data presented here, is the *fluctuating bond model* for hard sphere polymers, which has been used for melts, see for example in Ref. 57. In the fluctuating bond model, beads also interact via excluded volume only, but bonds are tethers with a maximal length rather than springs.

[194] We present simulation results for $k = 100k_BT$, $\varkappa = 20k_BT$ and $g = 1k_BT$. The range of the attractive square well potential is $d = 0.5\sigma$ and the resting length $b_0 = \sigma$.

[195] A less cumbersome way to define the hard sphere interaction is to simply state that there is an infinite energy penalty upon overlap (i.e. their mutual distance is smaller than σ of any two beads.

[196] A detailed quantitative investigation of these structures will follow in future publications/theses.

for the initial state of a homogeneous and isotropic polymer solution as it is also used in the experiments [46, 47].

To adapt the EC algorithm to the polymeric SHC system, the hard sphere repulsion is treated by an EC. The additional energies, such as bending, stretching and short-range inter-polymer attraction are treated conventionally employing Metropolis MC steps with rejections. First the entire EC is calculated as if we deal with a hard sphere system. After that the energy difference between the initial and final configuration determines if the whole EC move is accepted or rejected. This leads to a total displacement ℓ which determines the rejection rate. By adjusting the total displacement to an optimal value ℓ_{opt}, we can realise optimal acceptance rates around 50%.

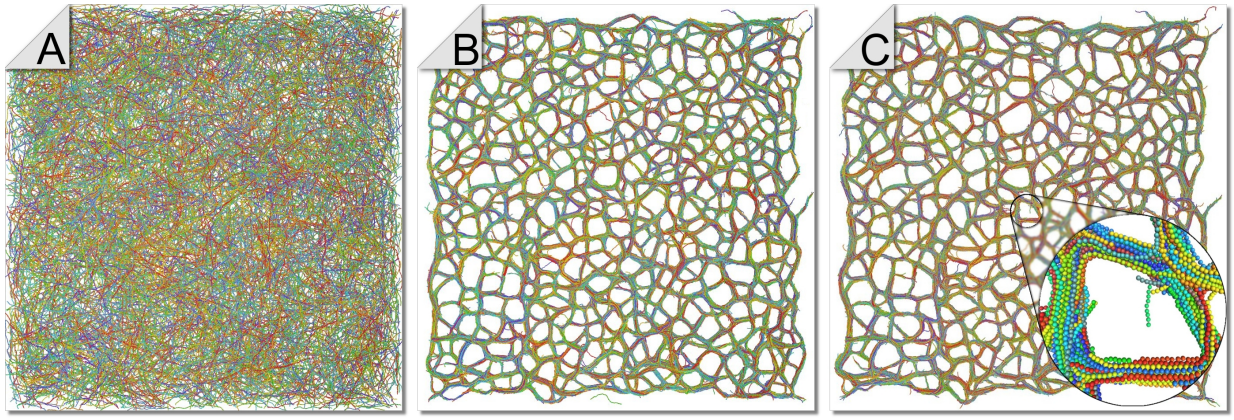

Figure 93: Three snapshots of polymer system with 10000 SHCs containing each 50 beads in a flat box of edge lengths $300\sigma \times 300\sigma \times 5\sigma$ with fixed boundaries. Chain colours are arbitrary and only to distinguish different chains. The initial state A of the simulation is prepared with homogeneously and isotropically distributed chains resembling a polymer solution state. Snapshot B is taken after $3.3 \cdot 10^6$ sweeps, snapshot C after $5.1 \cdot 10^6$ sweeps (in each MC sweep one event chain is started on each particle). Apparently, a stationary state is reached in snapshot B.

Our first simulation results show that such a dense polymeric system can also benefit from the EC algorithm. First, we measure the diffusion coefficient D for a bundle of polymers depending on the number of polymers N_p while interpreting the number of MC sweeps as time. The overdamped time evolution of the bundle (neglecting hydrodynamic effects) is described by Rouse dynamics[49], which gives a diffusion coefficient decreasing as $D \sim N_p^{-1}$. Applying single displacement local MC moves to such a system leads to an unphysically slow diffusion behaviour with $D \sim N_p^{-1.2}$, while the EC algorithm leads to the correct behaviour of the diffusion constant as shown in Fig. 94. This implies that the event chain as a cluster move not only allows for a more efficient sampling in this system, but also incorporates some essential features of the true dynamics, in that it allows (at least on a coarse scale) for an identification of "Monte Carlo time" (number of performed sweeps) and physical time. For the extraction of quantitative information a gauge would be needed, e.g. an otherwise measured (experiment, MD simulation) diffusion constant. The range d of the attractive square well potential is $d = 0.5\sigma$ and, therefore, rather large compared to the mean free path of densely packed disks examined before. For smaller potential ranges d we expect the bundle diffusion to exhibit a stronger slow down without EC moves.

Furthermore we determine how the optimal displacement length ℓ_{opt} depends on the number N_p of polymers in a bundle. For an efficient simulation, ℓ_{opt} should *not* depend on the thickness of a bundle. Figure 94 shows that ℓ_{opt} is drastically decreasing with N_p for local single displacement MC moves, whereas it is almost independent of N_p for the EC algorithm. For smaller potential ranges d we expect a faster decrease in ℓ_{opt}. Again, we expect the decrease to be much stronger without EC moves.

These two results can be interpreted such that local single displacement

moves do not produce a realistic Rouse dynamics including centre of mass diffusion of whole bundles and do not allow to interpret the MC sweep number as a realistic time. Furthermore, first simulations suggest that even if the EC length is not much longer than a single displacement the speed up in equilibration time can be very high.

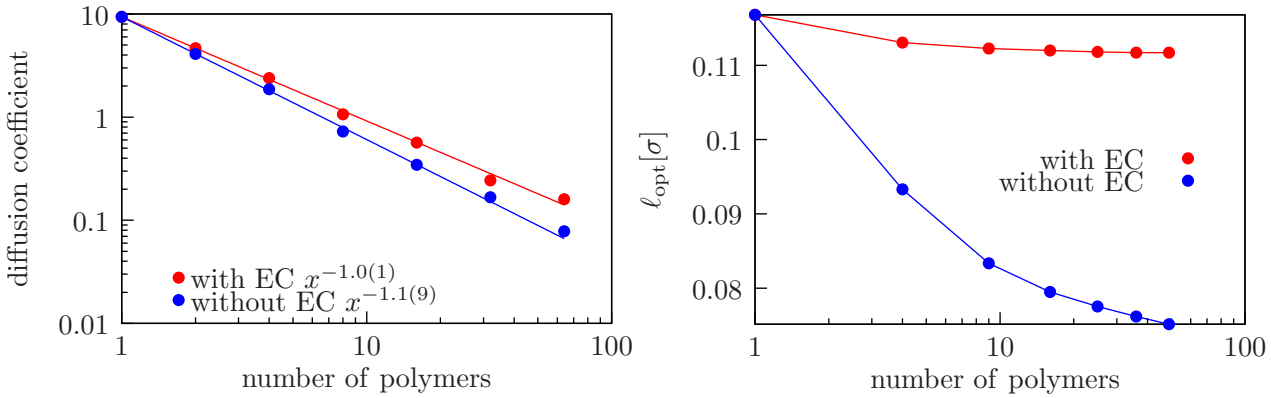

Figure 94: Left: Diffusion constant of the centre of mass of a polymer bundle consisting of N_p polymers. Using an EC algorithm, the result $D \sim N_p^{-1}$ characteristic for Rouse dynamics is reproduced, which allows for an identification of "Monte Carlo time" as physical time. Right: "Optimal move" length $\ell_{\rm opt}$ determined by adjusting the rejection rate to 0.5 as a function of the number N_p of polymers in a bundle. The acceptance probability is not reduced by the number of polymers if the event chain algorithm is used. This leads to a more effective sampling.

With the parallelized version of the EC algorithm it is possible to reach a stationary quasi-equilibrium state for large system sizes as shown in Fig. 93, which allows us to compare with experimental systems. The snapshot exhibits the same bundle network features as observed in experiments [46, 47], namely the formation of a network of bundles as the final state of the aggregation process. The network exhibits a polygonal cell structure, which is also observed in Refs. 46, 47. Further quantitative comparison between simulation and experiments will be performed in future investigations. The efficient sampling technique using the PEC will be useful to address the question whether the experimentally observed network states are true equilibrium states (due to their higher entropy in comparison to the energetically favourable single bundle) or are kinetically trapped metastable states and how the formation of a network depends on the global parameters (such as density and contour lengths of the polymer chains) and initial conditions.

Athermal melts of flexible, hard-sphere polymers

Polymer melts or polymer liquids are concentrated solutions of long chain molecules above their glass or crystallisation temperature. In a dense polymer melt long-range excluded volume interactions become screened and an individual polymer shows ideal behaviour [50]. Polymer melts exhibit a characteristic and complex dynamical and rheological behaviour because of entanglement effects, which impede chain diffusion and give rise to reptation dynamics of polymer chains [49–51]. The melt state is also most relevant for processing and manufacturing polymer materials [52].

The simulation of polymer melts by Molecular Dynamics (MD) or Monte-Carlo (MC) simulations usually comes at high numerical expense because of the slow reptation and entanglement dynamics. For chain molecules of length N the disentanglement time increases[49] $\propto N^3$, which impedes the equilibration of long chain molecules in a melt if only *local* displacement moves of polymer segments are employed as in a typical off-lattice MC simulation with fixed bond lengths [53–56] or fluctuating bond lengths [57], or in

MD simulations [58–60]. In MD simulations, reptation dynamics has been successfully identified in the entangled regime [58, 59]. In MC simulations, reptation dynamics has been first identified in lattice models [61] or fluctuating bond lattice models [62]. Reptation dynamics can also be introduced in a MC simulation as additional or alternative local MC reptation move [56, 63] (slithering snake moves) to obtain faster equilibration of a polymer melt. MC simulations have the general advantage that also *non-local* or *collective* MC moves can be introduced, for example, chain-topology changing double-bridging moves [60, 64–66], which speed up equilibration; dynamic properties, however, are no longer realistic in general if such collective MC moves are employed.

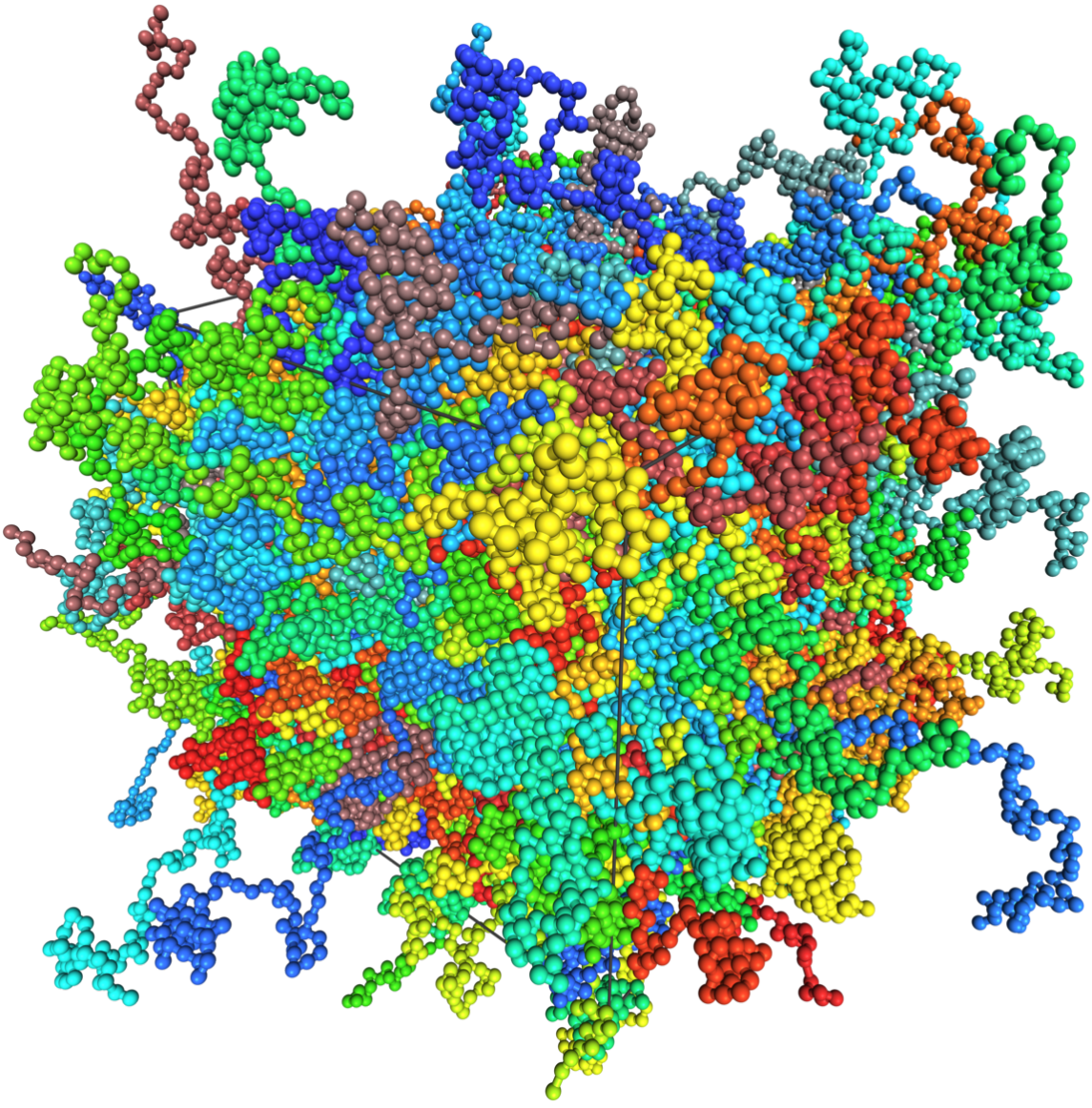

Figure 95: Exemplary snapshot of a polymer melt to illustrate the simulation geometry. The colour of the beads discriminates the individual polymers. Bonds are represented by cylinders. Although we employ periodic boundary conditions, we do not wrap the polymers periodically here, in an effort to give a better insight into the structure of polymers in a melt. The snapshot is taken at an occupied volume fraction of $\eta \approx 0.54$.

If polymers in a melt are modelled as bead-spring models with hard sphere beads [53, 55–57, 65, 66], an additional simulation problem arises, in particular in MC simulations. At high segment or monomer densities, the mean free path of segments is limited and local MC displacement moves are restricted to very small step-sizes[57].

The EC algorithm can be generalised from athermal hard sphere systems to spheres with interaction potentials [67, 68], which suggests that it can be

also used for polymer systems, where polymers are built from hard sphere beads bonded by spring potentials and eventually endowed with an additional bending rigidity. In Ref. 1, we showed that the EC algorithm can be used for simulations of semiflexible polymer systems.

We adapt the EC algorithm in the parallelized version presented before for the MC simulation of dense polymeric melts[197] consisting of flexible hard-sphere bead-spring polymers. We verify our algorithm by comparing the radius of gyration and inter- and intrapolymer diffusion to theoretical predictions and results using other MD and MC simulations. We benchmark the performance of this parallelized EC algorithm against standard local MC schemes and compare with state of the art MD simulations (using the LAMMPS package [69]), which we perform for a similar system.

[197] Again, it is with some grief for the author to have to acknowledge that the name *meltropolis algorithm* enjoys hardly any popularity.

Adaption of event chain algorithm

To simulate a polymer melt at a given density[198] $\rho = MN/L^3$, we generate a system of M polymers with polymerisation degree N in a cube of edge length[199] L, see Fig. 95 for a simulation snapshot. We employ periodic boundary conditions in all directions.

The polymers and their interaction are modelled the same way as before, see eq. (68). However, we are now interested in *flexible* polymers[200], rendering the appropriate value of the bending stiffness zero, $\varkappa = 0$. Furthermore, we restrict the inter-polymer interaction to the steric hard-sphere part, and thus, we also have the potential strength equal zero, $g = 0$. The remaining parameter in our model therefore is thus the spring constant k. For our system to have no explicit dependence from the temperature we set[201] $k \propto T$.

In this form all particles are now interacting solely via pair potentials and a completely rejection-free simulation solely based on EC moves is possible [67, 68]. For continuous interaction energies that only depend on the position of two beads, the EC move can be adapted by drawing an energy difference $\Delta E > 0$ according to the standard Boltzmann distribution for each move of the pivot bead. Every (partial) displacement of the pivot bead that reduces the interaction energy is accepted (as in the standard Metropolis algorithm), but energy increase is only accepted until the drawn energy difference ΔE is reached, or until the remaining EC displacement has been reached.

[198] The density and the packing fraction $\eta = 4\pi/3\sigma^3\rho$ are both often used ways to describe the filling of the system.

[199] The value used here is $L = 40\sigma$.

[200] Here, we refer to the mechanical stiffness. Due to the interactions in the melt the polymer acquires an effective stiffness that manifests itself in a finite tangent correlation, i.e. $\cos\theta \neq 0$ with θ being the bond angle between two adjacent tangents.

[201] In our simulations we chose bond stiffnesses ($k = 30k_BT$) such that bond stretching remains relatively weak with $\langle b_i \rangle \approx 1.1\sigma$.

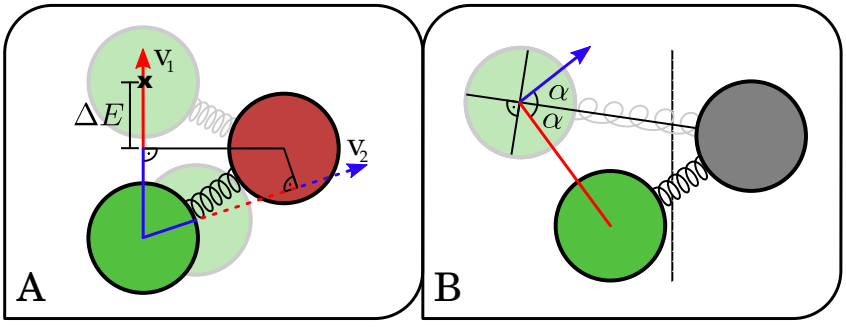

Figure 96: (A) Geometric considerations in the evaluation of the admissible EC displacements for the harmonic bond energy. Attempted EC displacements of the green bead are in one of two classes: (i) the beads do not collide along the path (for an EC move in direction v_1) or (ii) the beads do collide along the path (for an EC move in direction v_2). In both cases the energy stored in the bond reduces on the blue part of the trajectory, which, therefore, is always admissible, and increases on the red part, where the maximal admissible displacement is set by the drawn "consumable" energy ΔE. Thus, the bond-energy is only relevant for the maximal displacement when the beads do not collide, because the other case is dominated by the hard-sphere constraint. (B) Reflection of a spring-triggered EC necessary due to the parallelization. The Gray bead is rendered immotile due to the currently chosen spatial decomposition into parallel simulations cells. Therefore, the EC cannot be transferred to the Gray bead at the occurrence of a spring "collision". Thus, the pivot bead (green) does not change and the propagation direction is reflected as if there was a wall normal to the bond.

Next, we consider the general situation that the pivot bead has several pairwise interaction energies. For each interaction partner i, the energy difference ΔE then defines a maximal displacement of the pivot bead $x_i \leq x_{\max}(\Delta E)$. The largest possible displacement x of the pivot bead is the minimum of all x_i, i.e. $x = \min_i x_i$, which shall be realised for an interaction partner j, i.e., $x_j = \min_i x_i$. For interacting hard spheres, one of the interaction energies is

a hard-core interaction, such that x cannot become larger than the distance to the next collision event.

The EC is then continued at the other bead j involved in the most restrictive interaction energy, which becomes the next pivot bead. Here, it becomes obvious why this method is limited to pair-interactions. There is no uniquely defined "the other bead" when you consider a three-or-more-bead interaction (such as the bending-energy, which generally involves the position of five beads as moving the pivot beads changes three adjacent bond-angles). In case of a hard-core collision as the most restrictive interaction, the hit bead becomes the next pivot bead as in the hard sphere case.

In Fig. 96 A we show an example for polymer hard beads bonded by springs. The additional hard sphere constraint facilitates the evaluation of the admissible displacement for the spring energies, as also explained in Fig. 96 A.

Parallelization

We use a parallelized version of this event-chain algorithm and refer to our earlier exposition of the details and pitfalls of the parallelization. As discussed there, the parallelization requires a spatial decomposition of the system (which is changed in every sweep to ensure ergodicity) into simulation cells. This limits the displacement of each sphere to its respective simulation cell. For non-bonded hard spheres this can be treated by reflection of non-admissible ECs at the cell boundaries. If a spring-triggered event occurs, where the bonded bead which caused the event and would be the next pivot bead is lying outside the current simulation cell, we proceed in a very similar manner, i.e., by reflection at the plane normal to the bond of the two participating spheres as illustrated in Fig. 96 B.

In this work we used spatial decomposition scheme different from the chequerboard partition used before: we used a tile-joint partition, where large tiles are separated by small joints (areas which contain spheres that cannot move, see Fig. 97). As discussed in our previous work larger cells will lead to a more effective parallelization.

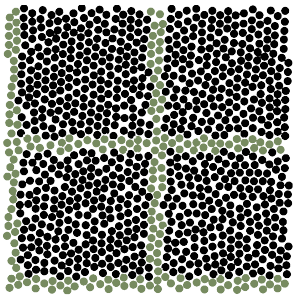

Figure 97: Exemplary visualisation of a tile-joint decomposition for the (two dimensional) hard-disk system. The green disks (joints) are frozen and separate areas of motile disks (black, tiles) which are concurrently worked upon.

As the beads in a polymer are bonded in a specific sequence, the hard spheres are not indistinguishable. On a very fundamental level, this is reflected by the fact that it makes sense, that in Fig. 83 the disks have one colour[202], whereas Fig. 95 covers a great range of colours. Thus, we have additional information about the system: *exchanging* the positions of *any two beads* generates a different system state. It appears more than reasonable to try to exploit this knowledge into a more efficient way of sampling.

Additional Bead Swapping

Typical conformations in a dense melt consist of highly entangled polymers. In the dense limit the ECs become very long, i.e., the rather large displacement of an EC is distributed on a lot of very small displacements of many beads participating in the EC move. This results in a small collective translation of all beads participating in an EC cluster move with only small changes to the topology of entanglements.

Topology changing MC moves such as the double-bridging (see Fig. 99) move [64] can speed up equilibration in polymer melts significantly [60, 65, 66]. Here, we improve sampling with EC moves further by introducing an additional swap MC move, which can locally change *the topology of entanglements*. For this purpose we modify the EC move so that the EC does not directly transfer to the next bead upon hard sphere contact but, instead, a *swap* of the two touching spheres is proposed, see Fig. 98. Such an additional swap move is MC specific[203] and allows for a local change of entanglements. The MC swap move is accepted according to the standard Metropolis algorithm. If

[202] Except for the highlights used there to explain the algorithm. It would not have been worth the paper to include a separate figure, just to make this point.

[203] Particle exchange can be and has been used to accelerate standard Metropolis MC schemes. However, for the EC this seems especially fruitful as a suitable pair of spheres to be exchanged is a ready by-product of the event-chain algorithm. Also, it allows for a rejection-free continuation in case the exchange is not performed.

the swap is rejected, the EC is transferred and the standard EC algorithm as described above is recovered. If it is accepted, the two beads are exchanged, and the EC continues without transferal (that is the pivot bead remains the same). The EC propagation due to the springs is not influenced by this change. The example of a swap move in Fig. 98 shows a situation where it might be energetically favourable to swap beads. Generally, the swap move is more useful if the directions of the involved bonds differ strongly, while it is more or less unphysical in a strictly two-dimensional setup (because then swapping gives rise to bonds crossing each other).

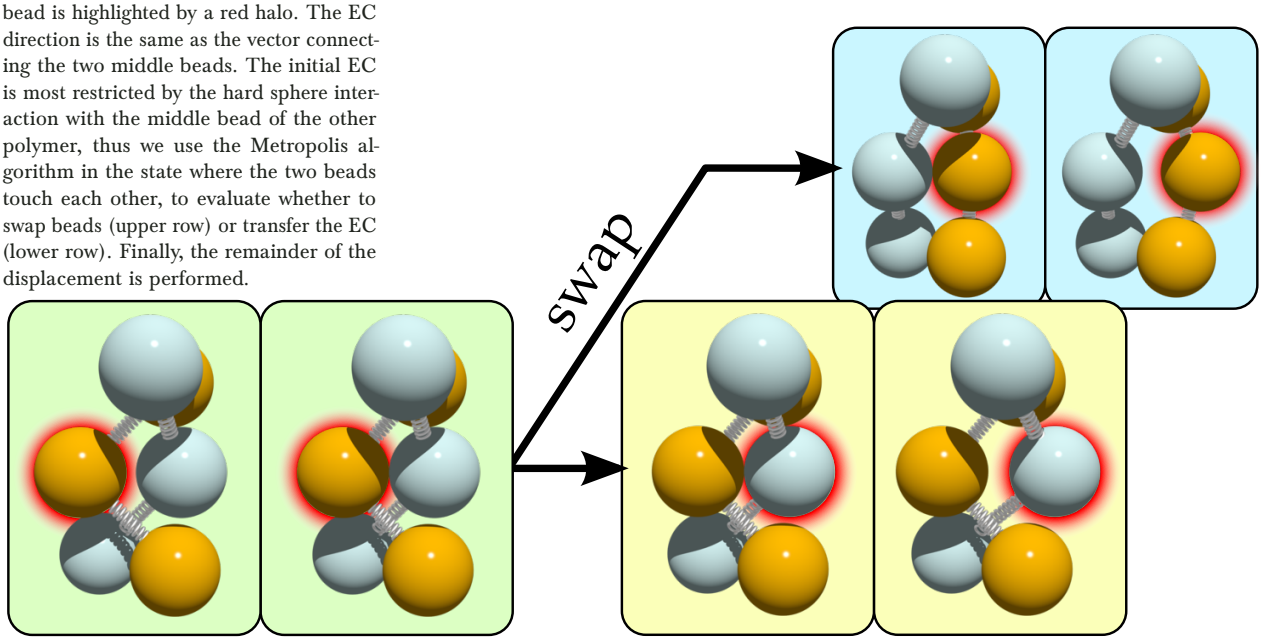

Figure 98: An EC move with/without bead swapping. We show the relevant steps in the computation of the swap move from left to right. The currently selected pivot bead is highlighted by a red halo. The EC direction is the same as the vector connecting the two middle beads. The initial EC is most restricted by the hard sphere interaction with the middle bead of the other polymer, thus we use the Metropolis algorithm in the state where the two beads touch each other, to evaluate whether to swap beads (upper row) or transfer the EC (lower row). Finally, the remainder of the displacement is performed.

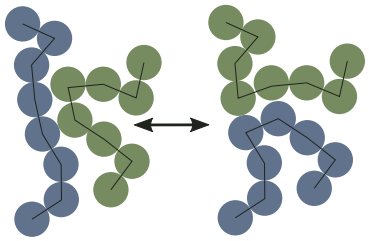

Figure 99: Sketch of the connectivity-changing double bridging move for polymeric systems. If two beads of a polymer (green in the left part) are close enough to another polymer (blue in the left part) a change of connectivity is proposed. This way entanglements can easily be overcome as they are resolved by changing the polymer affiliation of the involved beads. The double-bridging move generally induces a non-trivial length distribution among the polymers, when performed on non-centre segments, whereas our swap move conserves mono-dispersity in a melt. We note that double bridging (as any other additional MC move) could be added to the EC algorithm.

The entanglement of the polymers cause the reptation-like behaviour. Since the swap move efficiently de-entangles polymers, there is no detectable reptation regime, which is the reason for the accelerated equilibration of the melt. However, this move makes the resulting MC dynamics of the simulated melt unphysical on time scales smaller than the de-entanglement time.

This way we end up with a hybrid algorithm that features the EC, whose main idea is very close to an event-driven MD simulation, as well as particle exchange (swap moves) according to the Metropolis algorithm, standard concepts of MC simulations. We note that in the limit of vanishing bonds all beads become indistinguishable and the EC algorithms with and without bead swapping are identical up to book keeping differences.

The generation of a valid initial configuration, which is representative for an equilibrium configuration, is essential for short equilibration times but far from trivial at high monomer densities. We pursue an EC-based strategy that is conceptually similar to the slow push-off procedure in Ref. 60 for a Lennard-Jones melt.

The flexible polymers in the equilibrated melt are ideal but acquire an effective stiffness, which on the lowest level can be characterised by a finite value of $\langle \cos\theta \rangle$ with θ being the bond angle [60].

In order to capture the effective stiffness already at the level of the initial configurations, we set up a system with randomly placed phantom polymers with vanishing hard sphere diameter, which we grow by restricting

Initial configurations

subsequent (unit) tangents to $\boldsymbol{t}_i \cdot \boldsymbol{t}_{i+1} < \cos(\theta_{\max})$, see small symbols Fig. 101. For an otherwise uniform distribution of bond vectors, this leads to $\langle \cos\theta \rangle = \cos^2(\theta_{\max}/2)$, such that we can control the end-to-end-vector statistics of the phantom polymers by adjusting $\theta_{\max}$. We choose $\theta_{\max}$ such that $\langle R^2 \rangle / N \approx 1.90$ holds in accordance with our long-run simulation data, see Fig. 101.

This approach seems to suffer from circular reasoning as the value for c has been inferred from a long-run simulation and is then used in the initial configuration. However, we expect the effective stiffness to be only weakly dependent on the density (in the range we are interested in) and the length/number of the polymers. Thus we can shorten the equilibration of any simulation but one (from which we gathered c) using a more suitable estimate for the initial conformational statistics.

We then introduce a finite excluded volume, but with a hard sphere diameter that is only a fraction of the goal diameter σ. This generates some "conflicts", i.e., a number of overlapping spheres. We remove these conflicts from the initial configuration by repeatedly starting EC moves from the overlapping spheres only. From an overlapping bead we start EC moves into different directions until the conflicting overlap has been removed by creating enough space around the overlapping bead. In these ECs we ignore pre-existent overlaps so that the EC will only be transferred to a bead the current pivot bead is not overlapping with. This procedure corresponds to locally "rattling" in the hard sphere systems until enough space has been created around the overlapping bead to insert it, see Fig. 100.

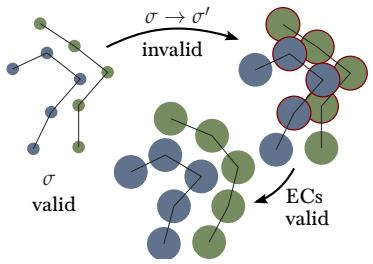

Figure 100: Sketch of the event-chain based procedure to generate valid configurations with mean-square displacement distribution in reasonable proximity with the equilibrated systems. Starting from a valid configuration with diameter σ (e.g. $\sigma = 0$) we increase the diameter to σ' which generally will lead to overlapping spheres (red contour), which we resolve by starting event-chains at the spheres that are afflicted by conflicts. This eventually results in a valid configuration.

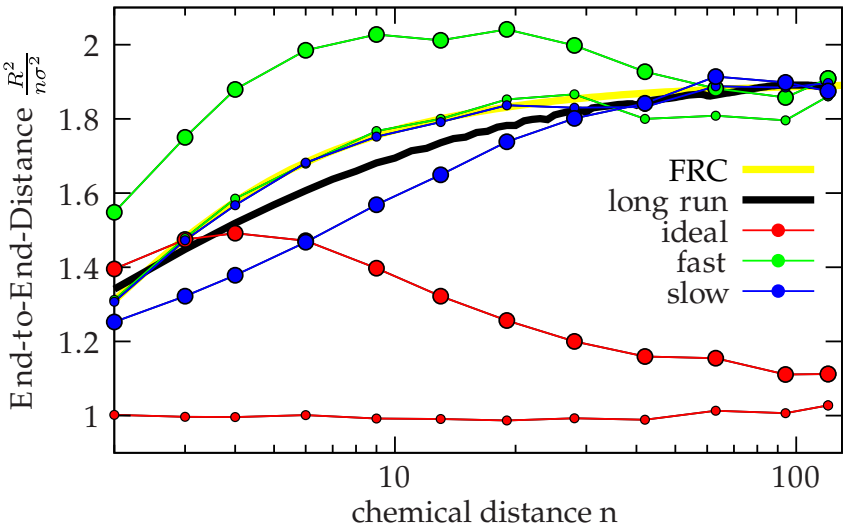

Figure 101: Mean-square (ensemble average in one sample) end-to-end vector $R^2(n)$ of initial condition for different initial condition generators. The small points are the end-to-end vector directly after setting up the phantom chains, the large points are the end-to-end vector after increasing the bead size to σ, either by a "slow push-off" (red and blue curves) or by a "fast push-off" (green curve). For comparison, the thermodynamic average result from a long run simulation, which serves as a target function and allows for a determination of the Kuhn length, and the R^2 of the initial phantom chains (freely rotating chains[49] with the same value of $\langle \cos\theta \rangle$) are shown. The initial configuration generated by the "slow push-off" scheme shows the least deviation to the target function. The simulation parameters were $N = 121, M = 500, L = 40\sigma$ resulting in a packing fraction $\eta = 0.495$.

Once all conflicts for a given diameter are solved we increase the diameter and continue iteratively until the goal diameter σ is reached. This way, we can generate initial configurations even for a very dense system with $\eta = 0.63995$, $N = 120$ and $M = 275$ in $\mathcal{O}(100h)$. However, this time only amounts for the generation of a *valid* configuration. For dense systems this configuration will usually be far from equilibrium, with very elongated bonds, and a thorough equilibration is necessary.

The iterative growth of sphere diameters (which we call "slow push-off" for conceptual analogy with a procedure of that name introduced in MD simulations[60].) leads to a smaller change in the initial distribution of end-to-vectors, see large symbols Fig. 101. For comparison we generate an initial condition without slowly increasing σ (which we call "fast push-off" [60]), see green curves in Fig. 101. The generated configuration should exhibit

an average mean-square end-to-end vector R^2 as close as possible to the equilibrium result as found by a long run simulation, see Fig. 101. The initial configurations generated with slow push-off and the optimal values $c \approx 1.9$ (blue lines in Fig. 101) are indeed similar to the long-run simulation results. The fast push-off configurations exhibit a maximum at intermediate N, which takes a long time to equilibrate due to the slow reptation dynamics [60]. Initial configurations generated from ideally flexible phantom chains (freely jointed chains[49]) differ considerably.

In this way we can initialise systems at (in principle) any (geometrically possible) density without resorting to configurations that are far from equilibrium (e.g., placing the beads on a lattice) in a reasonable amount of time (a couple of minutes wall-time for the system parameters below).

Results

We present numerical results of our proof-of-concept implementation of the outlined algorithms[204]. We demonstrate the massive gain in sampling efficiency due to EC moves in comparison with standard single move MC schemes and the additional performance gain by bead swapping moves.

Additionally, we compare our results to those from MD simulations performed using the highly optimised LAMMPS package [69]. As hard spheres cannot be used in a force-based MD simulation, we compare with beads that are interacting via the repulsive part of standard Lennard-Jones potentials (see Fig. 102), whereas the bonds remain Hookean springs. The identification of the effective hard sphere radius of such soft Lennard-Jones spheres has been subject of prior research [70]. However, our results will show that setting the Lennard-Jones length scale σ_{LJ} (defined by the zero of the Lennard-Jones potential, $V_{\mathrm{LJ}}(\sigma_{\mathrm{LJ}}) = V_{\mathrm{LJ}}(r \to \infty) = 0$) equal to the hard sphere diameter σ suffices for the purposes of this work. This comes with the great advantage that we can use the same initial configurations (generated by our EC-based procedure) for the MD and MC evolution.

In the following, we will compare these algorithms regarding different aspects of polymer behaviour in the melt, which have also been previously used in the literature to characterise polymer melts. We will address structural properties of chains in a polymer melt by investigating their typical shape as characterised by the moment of inertia tensor [72] and the distribution of end-to-end distance [72], and the pair correlation function [64–66, 72]. This will allow us to establish the correctness of the algorithm. Subsequently we will measure the sampling speed by means of a discussion of the dynamical behaviour of polymer chains in the melt using correlation functions that characterise the intra- and interpolymer diffusion [59].

We choose three different systems to investigate the influence of the occupied volume fraction η and the chain length for our analysis:

1. System I: $M = 400$, $N = 120$ and $\eta = 0.390$;
2. System II: $M = 500$, $N = 120$ and $\eta = 0.490$;
3. System III: $M = 250$, $N = 240$ and $\eta = 0.490$.

This means the volume fraction η increases from System I to System II, whereas the polymer length N increases when going from System II to System III.

The shape of a polymer in a dense melt is ellipsoidal rather than spherical, which can be shown by the distribution of beads in respect to the centre of

[204] For the comparison of the different algorithms, we distinguish algorithms by whether they use the EC or standard metropolis algorithm for (i) the hard sphere interactions and/or (ii) the bond spring interactions ("EC" for event chain, "MC" for standard metropolis) and (iii) if the algorithm is executed parallelly (par) or serially (ser) and (iv) if the swap move is used (swap). Accordingly, we introduce a naming scheme for algorithms where, for instance, "EC-MC-ser" refers to a sequentially executed simulation, where hard sphere interactions are handled by the EC, springs handled by standard metropolis algorithm, and the swap move is not used; "EC-MC-ser-swap" denotes the same algorithm with swap moves.

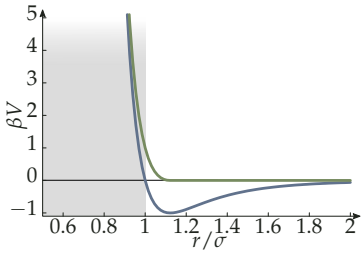

Figure 102: The standard Lennard-Jones potential (blue, using $\beta^{-1} = k_B T$ as energy scale and the hard-sphere diameter σ as length scale) and the truncated, shifted purely repulsive version we use to simulate hard-spheres (where the shaded area would correspond to an infinite energy penalty) in a MD simulation. This potential is also known as the (repulsive) Weeks-Chandler-Anderson (WCA) potential[71].

Equilibrium properties
Correctness of Sampling

mass in the coordinate system which is given by the eigenvectors $\boldsymbol{e}_i$ of the moment of inertia tensor $(\mathbf{I})_{ij} = \sum_k (\boldsymbol{r}_k^2 \delta_{ij} - r_{k,i} r_{k,j})$ of a polymer[72]. The sum runs over all beads of a polymer, where $r_{k,i}$ denotes the ith component of the kth bead coordinate.

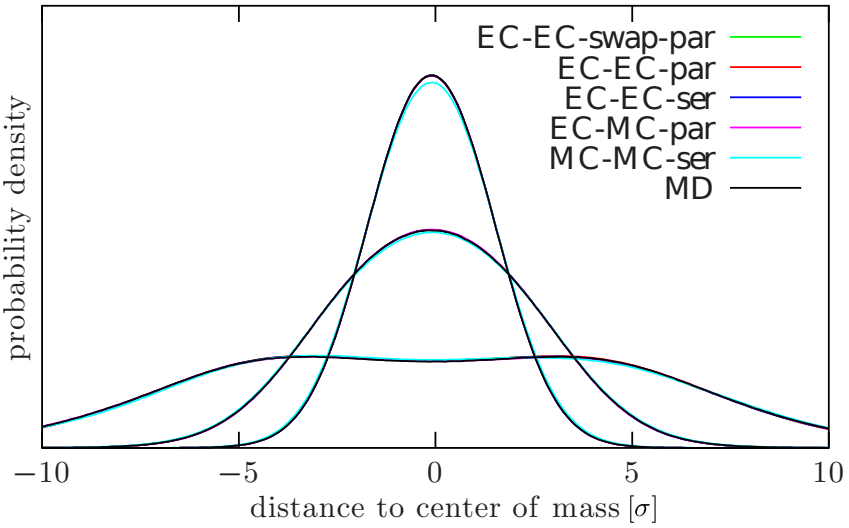

Figure 103: Bead distribution along the three principal axes of the moment of inertia tensor (for System I). The clear asymmetry along the principal axes shows that a polymer takes an ellipsoidal shape in a dense polymer melt. The distribution along the lowest eigenvalue axis becomes bimodal at high densities, which hints towards a dumbbell-like shape.

Following Ref. 72, we can use the eigenvalues $I_1 \leq I_2 \leq I_3$ of the moment of inertia tensor to characterise the shape in terms of its asphericity

$$\Delta_{\bigcirc} \equiv \frac{1}{2}(I_1 + I_2) - I_3,$$

acylindricity

$$\Delta_{\boxminus} \equiv I_1 - I_2$$

and shape anisotropy

$$\Delta_{\square} \equiv 4(1 - 3(I_2 I_3 + I_3 I_1 + I_1 I_2)/(\mathrm{Tr}\,\mathbf{I})^2.$$

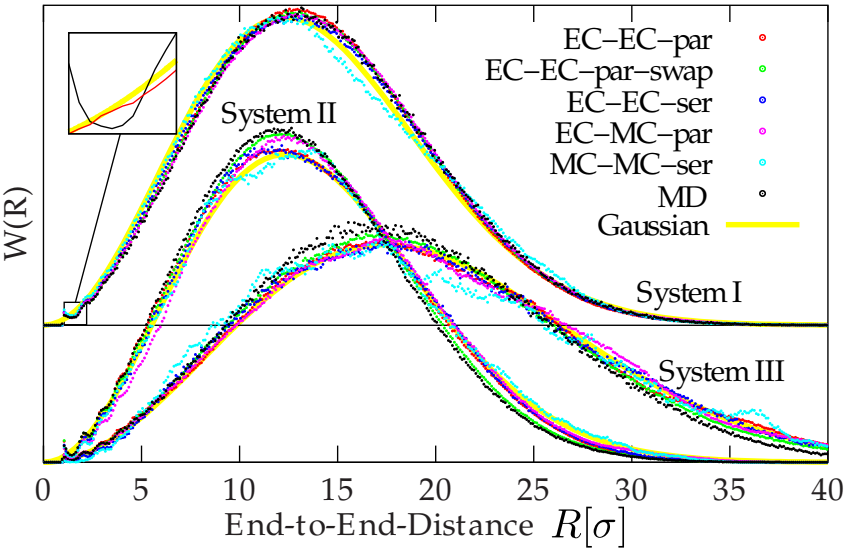

Figure 104: Distribution of the end-to-end distance $W(R)$. For clarity the results from System I are shifted by an offset. The algorithms are in good quantitative agreement with each other (apart from the MC-MC-ser variant which is not equilibrated due to its extremely slow sampling). For short distances the measured distribution shows oscillations arising from the dense structure. These oscillations can be explained by the influence of the pair correlation function $g(r)$ characterising the additional local liquid-like ordering of neighbouring polymer beads. The inset shows the ratio $W(R)/G(r)$ (red) of the end-to-end distance distribution and pair correlation which shows no oscillations.

Additionally, there exist several analytical predictions for an infinitely long

freely jointed chain [73, 74],

$$I_{4\bigcirc^2+3\square^2} = \lim_{N\to\infty} \frac{\langle 4\Delta_{\bigcirc}^2 + 3\Delta_{\square}^2\rangle}{\langle \mathrm{Tr}\,\mathbf{I}\rangle^2} = \frac{2}{3} \tag{69a}$$

$$I_{++-} = \lim_{N\to\infty} \frac{\langle I_1 + I_2 - I_3\rangle}{\langle \mathrm{Tr}\,\mathbf{I}\rangle} = 0.754 \tag{69b}$$

$$I_{+-+} = \lim_{N\to\infty} \frac{\langle I_1 - I_2 + I_3\rangle}{\langle \mathrm{Tr}\,\mathbf{I}\rangle} = 0.175 \tag{69c}$$

$$I_{-++} = \lim_{N\to\infty} \frac{\langle -I_1 + I_2 + I_3\rangle}{\langle \mathrm{Tr}\,\mathbf{I}\rangle} = 0.0646, \tag{69d}$$

which can be tested. In Fig. 103 we compare the distribution of beads of one polymer in the system spanned by the eigenvectors of the moment of inertia tensor for all algorithms (for System I). In Table 2, we compare the shape descriptors from our Monte-Carlo schemes and MD simulation with the theoretical expectations (69).

Furthermore, we check the distribution $W(R)$, see Fig. 104, of the end-to-end distances. For chains of length $L_c = Nb$ in a melt is approximately[205] given by a Gaussian distribution[49, 50]

$$G(R)\mathrm{d}R = 4\pi R^2 \left(\frac{3}{2\pi L_c b_k}\right)^{3/2} \mathrm{e}^{\left(-\frac{3R^2}{2L_c b_k}\right)}\,\mathrm{d}R,$$

where the Kuhn-Length $b_k = \langle R^2\rangle / L_c$ can be fixed via the second moment of this distribution.

[205] As discussed before, the polymers are ideal, meaning there is effectively no interaction that is long-ranged in chemical distance, however there is a short-ranged interaction, giving rise to the finite stiffness ($\langle\theta\rangle \neq 0$) and to deviations from results for freely jointed chains in general.

	MC-MC-ser			EC-EC-swap-par			MD			theo.
System	I	II	III	I	II	III	I	II	III	
$\langle\Delta_{\square}\rangle$	0.390	0.388	0.387	0.399	0.397	0.395	0.402	0.397	0.395	0.42
I_{++-}	0.763	0.758	0.757	0.765	0.764	0.766	0.765	0.767	0.763	0.754
I_{+-+}	0.173	0.178	0.177	0.172	0.173	0.172	0.172	0.170	0.173	0.175
I_{-++}	0.0642	0.0647	0.0654	0.0628	0.0631	0.0625	0.0623	0.0630	0.0643	0.0646
$I_{4\bigcirc^2+3\square^2}$	0.653	0.621	0.629	0.640	0.638	0.672	0.646	0.643	0.633	0.667

Table 2: Comparison of shape descriptors. For overview purposes we only show the results from MC-MC-ser, EC-EC-swap-par and MD algorithms, but the other variants do not differ in these results.

All curves and results coincide rather well, which proves the correctness of the novel MC algorithms and demonstrates that polymers in a melt exhibit ideal behaviour.

Dynamical Behaviour – Speed of sampling

Now that we can with confidence say that the event-chain algorithm in all its variants samples correctly, we can proceed to the next relevant attribute, the speed of sampling. We compare the speed of different algorithms in terms of wall time[206].

[206] Since the simulations ran on different CPUs all wall times were calibrated with short run simulations on one workstation.

An appropriate measure for the efficiency of the different algorithms can be seen in the dynamical behaviour of a polymer in a melt. Reptation dynamics in a dense melt slows down the diffusion of the polymer centre of mass beyond the entanglement time. The dynamics of a chain in the melt can be characterised by the intra- and interpolymer diffusion. For a chain with bead positions $\boldsymbol{r}_i$ ($i = 1,\ldots,N$) and centre of mass $\boldsymbol{R} = \frac{1}{N}\sum_{i=1}^{N} \boldsymbol{r}_i$, we measure the following time-dependent mean-square displacements [59],

$$g_{i,1}(\Delta t) = \langle [\boldsymbol{r}_i(t+\Delta t) - \boldsymbol{r}_i(t)]^2\rangle_t$$
$$g_{i,2}(\Delta t) = \langle [(\boldsymbol{r}_i(t+\Delta t) - \boldsymbol{R}(t+\Delta t)) - (\boldsymbol{r}_i(t) - \boldsymbol{R}(t))]^2\rangle_t.$$

The mean-square displacement $g_{i,1}$ describes the diffusion of a bead i and the mean-square displacement $g_{i,2}$ the diffusion of bead i relative to the centre of

mass of the polymer. For both quantities the average $\langle \ldots \rangle_t$ is an ensemble average and an average over the time t. We choose a middle bead $i = N/2$ in order to reduce the influence of finite chain lengths and measure $g_1 \equiv g_{N/2,1}$ and $g_2 \equiv g_{N/2,2}$ in the following.

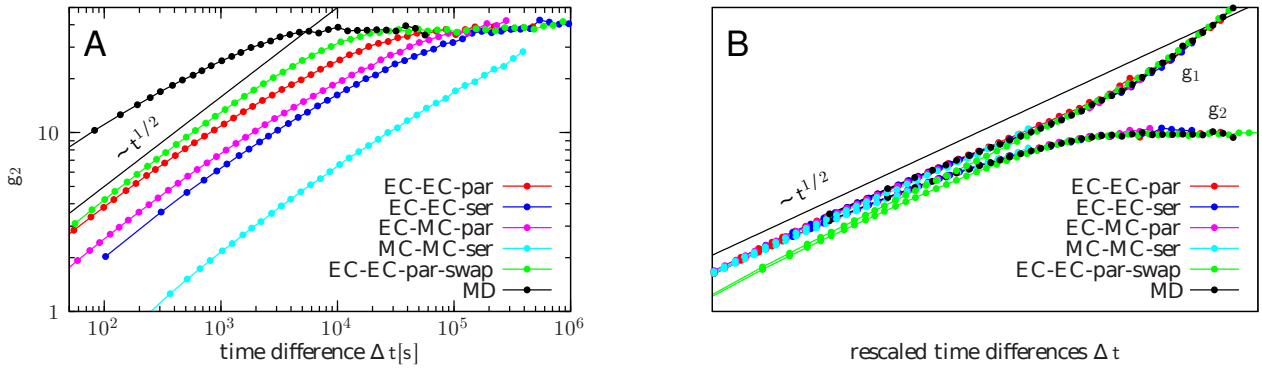

Figure 105: (A) Mean-square displacement (log-log plot) of the most inner bead in respect to the centre of mass of the entire polymer $g_2(\Delta t)$ for different algorithms against wall time [s]. We use this observable as measure of the efficiency of the tested algorithms. (B) The dynamical properties $g_1(\Delta t)$ and $g_2(\Delta t)$ (log-log plots) for different algorithms with time rescaled to collapse all curves and demonstrate that in all algorithms (except the one with swap moves) the polymers show the same behaviour. All simulations were performed for System I.

The time evolution is governed by a sequence of crossovers[49, 50]

$$g_1(t) \sim \begin{cases} t^{1/2} & \text{for } t < \tau_e \\ t^{1/4} & \text{for } \tau_e < t < \tau_R \\ t^{1/2} & \text{for } \tau_R < t < \tau_d \\ t & \text{for } \tau_d < t \end{cases}$$

with three different crossover time scales: the entanglement time scale τ_e, the Rouse time scale τ_R and the disentanglement time scale τ_d [59]. For all times scale $t > \tau_e$, reptation slows down the diffusional dynamics. The mean-square displacement g_2 exhibits the same regimes as g_1, but converges against the radius of gyration of a polymer $R_g^2(N) = N^{-1} \sum_{i=0}^{N} (\boldsymbol{r}_i - \boldsymbol{R})^2$ for $t > \tau_d$ giving rise to the plateau in the g_2-curves in Fig. 105. The reptation regime for $\tau_e < t < \tau_R$ is rather hard to observe for shorter chains and one expects a slightly increased exponent $g_1(t) \sim t^x$ with $0.25 \leq x < 0.4$ [75].

We focus our analysis on the plateau in g_2 as its existence is independent from the simulation method. In any (reasonable) simulation algorithm there is a time-scale of the order of the disentanglement τ_d on which the polymer explores the total conformational space, giving rise to $g_2 \to R_g^2$. Thus, we can determine a relative sampling speed by comparing τ_d (in wall-time) for different algorithms. We back this definition by the notion that τ_d is in fact the largest interesting time-scale. The two processes that happen on larger time-scales are the diffusion of polymers and the diffusion of the whole melt[207]. These two would be affected in a non-trivial manner only, if we considered moves of entire polymers (say exchanging polymer), but our moves perform only *local updates*[208].

In Fig. 105 A, we show the wall time evolution of the middle bead diffusion $g_2(t)$ relative to the centre of mass for different algorithms. We determine a speed-up factor for each algorithm by collapsing the plateaus (that is measure times in units of τ_d, the results are shown in Table 3.

Although the speed-up should be seen in a qualitative manner[209], there are some interesting conclusions to be drawn. The EC-MC algorithm gains some efficiency with respect to EC-EC algorithms with increasing η. In such dense systems the springs are strongly compressed, so the thermal/free bond length is much higher than in a melt. Therefore, the rejection rate caused

[207] The centre of mass is a conserved quantity in MD simulations, but in our MC simulations this only holds for its average.

[208] The entire event-chain is non-local, but every bead within it is only moved by a displacement of the order of the mean free path. The same goes for the bead swapping that only occurs if two beads are adjacent. Thus, the details of the sampling should become irrelevant for times much larger than τ_d and be completely determined by this time-scale.

[209] First, there are free parameters such as the initial displacement length ℓ, which could be optimised (see the discussion in the simpler hard-disk system). Second, the speed-up is system-dependent.

by the spring energy is rather low, such that the gain from the additional computational effort in the rejection-free treatment is small in denser systems. Since the disentanglement time $\tau_d \sim N^3$ is strongly influenced by the chain length N, the efficiency of the swap algorithm increases with longer chains. MD performance does not decrease with density, whereas local MC and also EC performance depends on the displacement length ℓ, which decreases with density. This explains the performance differences if the density η is increased. It is obvious, that all algorithms massively outperform the standard metropolis algorithm.

MC dynamics is not necessarily realistic depending on the choice of MC moves, whereas the MD dynamics provides realistic dynamics with a $t^{1/2}$-behaviour for short times and a crossover to the plateau $g_2 \approx R_g^2$ for $t > \tau_d$. Therefore, it is worth noting that both local MC dynamics and the cluster EC dynamics produce the same characteristic dynamic features with the characteristic $t^{1/2}$-behaviour and crossover to the plateau value. Only the swap MC moves, which are designed to allow unphysical disentanglement, give rise to an artificial MC dynamics with clear deviations for shorter time scales.

That both local MC dynamics and the cluster EC dynamics do indeed evolve the system in a way that allows for an identification of "Monte Carlo time" (i.e., number of moves) with physical time is corroborated in Fig. 105 B, where we show that the dynamical evolution gathered using the different algorithms can be collapsed onto one "master curve" upon a simple linear rescaling of the time with the corresponding speed-up factor.

Table 3: Comparison of relative speed-up compared to the standard local metropolis algorithm MC-MC-ser for different system parameters and algorithms. The EC-MC algorithm becomes more efficient as compared to EC-EC algorithms with increasing volume fraction η. For such dense systems, the springs are very compressed; therefore, rejections due to the spring energy are rare, such that the additional computational effort in the rejection-free treatment dominates in denser systems. The parallelization gives a factor of $a \approx 3.5 \ldots 3.9$ close to the theoretical limit of 4 (using 4 CPUs). For the local Monte-Carlo (MC-MC) variant the parallelization is straightforward and easily done in a strong-scaling fashion, which is why we omit stating the MC-MC-par case.

algorithm	System I	System II	System III
MC-MC-ser	1	1	1
EC-EC-ser	9	7	7
EC-MC-par	14	17	17
EC-EC-par	31	25	28
EC-EC-swap-par	230	115	423
MD (LAMMPS)	330	625	770

The LAMMPS implementation is the fastest, which should come as no surprise seeing that LAMMPS is under development since the mid 1990s[69] whereas our implementation, while adhering to general good practice rules for scientific computation, has no aspiration whatsoever to be optimised. However, given these preliminaries the performance difference between the MD LAMMPS simulation and our fastest EC variant seems very promising.

Conclusion

We presented a parallelization scheme for the EC algorithm and performed extensive tests for correctness and efficiency for the hard sphere system in two dimensions.

For parallelization we use a spatial partitioning approach into simulation cells. We find that it is crucial for correctness of the PEC algorithm that the starting particles for ECs in each sweep are drawn *with* replacement. We have shown implementations without replacement to give incorrect results for the pair correlation function and the resulting pressure, see Figs. 88. The reason for these incorrect results is the violation of detailed balance on the sweep level.

We analysed the performance gains for the PEC algorithm and find the criterion (67) for an optimal degree of parallelization. Because of the cluster nature of EC moves massive parallelization will not be optimal. The PEC algorithm will therefore be best suited for commonly available multicore CPUs with shared memory.

Finally, we discussed applications of the algorithm to dense polymer systems. Using ECs we simulated bundle formation in a solution of attractive semiflexible polymers. The EC moves give rise to a faster and much more realistic bundle diffusion behaviour. This allows us to simulate large systems, in particular, if the EC algorithm is parallelized. The simulation exhibits large-scale network bundle structures, see Fig. 93, which are very similar to structures observed in recent experiments [46, 47].

We also introduced our novel efficient MC algorithms for the simulation of dense polymer melts of hard sphere polymer. We generalise the algorithm to also handle the spring interactions in polymer bonds in a rejection-free manner. We suggest additional local topology-changing swap moves, see Fig. 98, to further increase simulation speeds in melts.

In addition, we introduce an efficient procedure to generate initial configurations, which are representative of typical equilibrated configurations in polymer melts. Using EC "rattling", we can generate initial configurations up to very high packing fractions (up to $\eta = 0.63995$).

We have shown that our EC algorithms produce the correct ideal behavior of polymer chains in the dense melt in equilibrium, as evidenced by the mean-square end-to-end distance (see Fig. 101) and the Gaussian distribution of end-to-end distances, see Fig. 104.

Moreover, the EC algorithm also captures the inter- and intrapolymer diffusion, i.e., essential features of the polymer dynamics in melts correctly, see Fig. 105. This allows us to used the actual polymer dynamics in the melt to quantify the speed-up achieved by EC algorithms.

We find that the combination of EC moves and parallelization can increase MC simulation speeds by factors up to 30 while it preserves a realistic polymer dynamics. The additional topology-changing swap moves give speed-up

factors up to 100-400 but make the polymer dynamics slightly artificial. With these speed-up factors, MC simulation speeds become comparable to optimised MD simulations that we performed with the LAMMPS package for comparison.

Although we only presented results for the most simple case of a melt of flexible polymers with no interpolymer interaction other than excluded volume, the added value of EC algorithms should persist in more complex systems. For (bond) interactions that are not pair interactions, e.g. bending energies, rejection-free sampling in the way presented here is not possible.

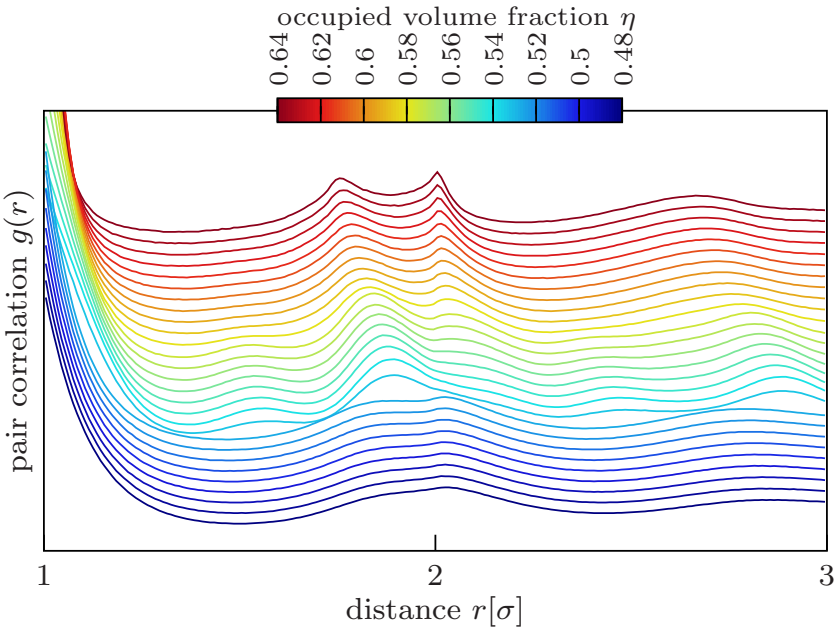

Figure 106: Pair correlation function for chain length of $N = 120$. The number of chains varies from $M = 400$ to $M = 640$ to match the desired occupied volume fraction η. At $\eta \approx 0.54$ there is abrupt change in the shape of $g(r)$ which we identify as the reported transition [57]. For the densest system of $\eta = 0.6283$ there are two sharp peaks at $r = \sqrt{3}$ and $r = 2$ which indicate a locally hexagonally packed structure. The presented data is based on simulations that were initially in a liquid-like state (without long-ranged positional order), thus there is a nucleation bias and the observed transition here is probably the end (increasing η) of the phase coexistence regime.

The presented algorithm offers the opportunity to study a broad range of systems with steric interactions. For the two presented exemplary applications a sufficiently fast Monte Carlo method offers a different approach to study the interesting emergent phenomena, such as the formation of networks in the system of semiflexible polymers that have steric repulsion and an additional short-ranged attractive interaction or the crystallisation of flexible polymers that only have steric repulsion.

The latter is evidenced for example by the pair correlation function, shown in Fig. 106. The pair correlation peaks of a dense system with $\eta = 0.6283$ are at $r = \sqrt{3}$ and $r = 2$, which can be identified as local tetrahedral order, where the beads are tangent to each other. At a packing fraction $\eta \approx 0.54$, a structural transition takes place, where the pair correlation function $g(r)$ strongly changes its shape. This feature could be identified with the glass transition that has been reported in Ref. 57 on the basis of MC simulations with local moves. The clear signature in $g(r)$ at $\eta \approx 0.54$ in our improved cluster EC simulations could also hint at the onset of crystallisation[210] rather than a glass transition. This touches the question of the existence of a glass transition with a thermodynamic signature in the polymer melt, which needs to and will be addressed in further simulations.

[210] Here, by crystallisation we refer to any solidification with long-ranged positional order, that is including the aperiodic "random hexagonally closed packed" (RHCP) order.

Bibliography

[1] Kampmann, T. A., Boltz, H.-H. and Kierfeld, J. (2015). *J. Comput. Phys.*, **281**:864–875

[2] Kampmann, T. A., Boltz, H.-H. and Kierfeld, J. (2015). *ArXiv e-prints*, 1502.06447. Accepted for publication by J. Chem. Phys.

[3] Metropolis, N. et al. (1953). *J. Chem. Phys.*, **21**(6):1087

[4] Hastings, W. K. (1970). *Biometrika*, **57**(1):97–109

[5] Swendsen, R. and Wang, J.-s. (1987). *Phys. Rev. Lett.*, **58**(2):86–88

[6] Wolff, U. (1989). *Phys. Rev. Lett.*, **62**(4):361–364

[7] Dress, C. and Krauth, W. (1995). *J. Phys. A: Math. and Gen.*, **28**(23):L597–L601

[8] Buhot, A. and Krauth, W. (1998). *Phys. Rev. Lett.*, **80**(17):3787–3790

[9] Santen, L. and Krauth, W. (2000). *Nature*, **405**(6786):550–1

[10] Liu, J. and Luijten, E. (2004). *Phys. Rev. Lett.*, **92**(3):035504

[11] Bernard, E. P., Krauth, W. and Wilson, D. B. (2009). *Phys. Rev. E*, **80**:056704

[12] Anderson, J. A., Lorenz, C. D. and Travesset, A. (2008). *J. Comput. Phys.*, **227**(10):5342–5359

[13] van Meel, J. et al. (2008). *Mol. Sim.*, **34**(3):259–266

[14] Preis, T. et al. (2009). *J. Comput. Phys.*, **228**(12):4468–4477

[15] Komura, Y. and Okabe, Y. (2012). *Comput. Phys. Comm.*, **183**(6):1155–1161

[16] Komura, Y. and Okabe, Y. (2014). *Comput. Phys. Comm.*, **185**(3):1038–1043

[17] Tonks, L. (1936). *Phys. Rev.*, **50**:955–963

[18] Strandburg, K. (1988). *Rev. Mod. Phys.*, **60**(1):161–207

[19] Kosterlitz, J. M. and Thouless, D. J. (1973). *J. Phys. C*, **6**(7):1181

[20] Halperin, B. and Nelson, D. (1978). *Phys. Rev. Lett.*, **41**(2):121–124

[21] Young, A. (1979). *Phys. Rev. B*, **19**(4):1855–1866

[22] Mak, C. (2006). *Phys. Rev. E*, **73**(6):065104

[23] Bernard, E. P. and Krauth, W. (2011). *Phys. Rev. Lett.*, **107**:155704

[24] Engel, M. et al. (2013). *Phys. Rev. E*, **87**:042134

[25] Mayer, J. E. and Wood, W. W. (1965). *The Journal of Chemical Physics*, **42**(12):4268–4274

[26] Furukawa, H. and Binder, K. (1982). *Phys. Rev. A*, **26**:556–566

[27] Schrader, M., Virnau, P. and Binder, K. (2009). *Phys. Rev. E*, **79**:061104

[28] Tóth, L. F. (1942). *Mathematische Zeitschrift*, **48**(1):676–684

[29] De Berg, M. et al. (2000). *Computational Geometry*. Springer, Berlin

[30] *CGAL, Computational Geometry Algorithms Library*. Http://www.cgal.org

[31] Roberts, G. O. et al. (1997). *Ann. Appl. Probab.*, **7**(1):110–120

[32] Anderson, J. A. et al. (2013). *J. Comput. Phys.*, **254**:27–38

[33] Kapfer, S. C. and Krauth, W. (2013). In *J. Phys.: Conf. Ser.*, Vol. 454, 012031. IOP Publishing

[34] Michel, M., Kapfer, S. C. and Krauth, W. (2014). *J. Chem. Phys.*, **140**:054116

[35] Bartles, J. R. (2000). *Curr. Opin. Cell Biol.*, **12**(1):72–78

[36] Kierfeld, J. and Lipowsky, R. (2003). *Europhys. Lett.*, **62**(2):285–291

[37] Kierfeld, J. and Lipowsky, R. (2005). *J. Phys. A: Math. Gen.*, **38**:L155–L161

[38] Kierfeld, J., Kühne, T. and Lipowsky, R. (2005). *Phys. Rev. Lett.*, **95**(3):038102
[39] Kampmann, T. A., Boltz, H.-H. and Kierfeld, J. (2013). *J. Chem. Phys.*, **139**(3):034903
[40] Borukhov, I. et al. (2001). *Phys. Rev. Lett.*, **86**(10):2182–2185
[41] Benetatos, P. and Frey, E. (2003). *Phys. Rev. E*, **67**(5):051108
[42] Shklovskii, B. (1999). *Phys. Rev. Lett.*, **82**(16):3268–3271
[43] DeRouchey, J., Netz, R. R. and Rädler, J. O. (2005). *Eur. Phys. J. E*, **16**(1):17–28
[44] Stevens, M. J. (1999). *Phys. Rev. Lett.*, **82**(1):101–104
[45] Pelletier, O. et al. (2003). *Phys. Rev. Lett.*, **91**(14):148102
[46] Huber, F., Strehle, D. and Käs, J. (2012). *Soft Matter*, **8**(4):931–936
[47] Deshpande, S. and Pfohl, T. (2012). *Biomicrofluidics*, **6**(3):034120
[48] Kierfeld, J. et al. (2004). *Eur. Phys. J. E*, **14**(1):17–34
[49] Doi, M. and Edwards, S. (1986). *The Theory of Polymer Dynamics*. Clarendon Press, Oxford
[50] de Gennes, P. (1979). *Scaling Concepts in Polymer Physics*. Cornell University Press, Ithaca and London
[51] Ferry, J. D. (1980). *Viscoelastic properties of polymers*. New York: Wiley, 3d ed Auflage
[52] Denn, M. M. (2008). *Polymer melt processing: foundations in fluid mechanics and heat transfer*. Cambridge University Press
[53] Curro, J. G. (1974). *J. Chem. Phys.*, **61**(3):1203
[54] Baumgärtner, A. (1981). *J. Chem. Phys.*, **75**(6):2994
[55] Khalatur, P., Pletneva, S. G. and Papulov, Y. (1984). *Chem. Phys.*, **83**(1-2):97–104
[56] Haslam, A. J., Jackson, G. and McLeish, T. C. B. (1999). *J. Chem. Phys.*, **111**(1):416
[57] Rosche, M. et al. (2000). *J. Chem. Phys.*, **112**(6):3051–3062
[58] Kremer, K. and Grest, G. S. (1990). *J. Chem. Phys.*, **92**(8):5057–5086
[59] Pütz, M., Kremer, K. and Grest, G. S. (2000). *EPL (Europhys. Lett.)*, **49**(6):735
[60] Auhl, R. et al. (2003). *J. Chem. Phys.*, **119**(24):12718–12728
[61] Kremer, K. (1983). *Macromolecules*, **16**(10):1632–1638
[62] Paul, W. et al. (1991). *J. Chem. Phys.*, **95**(10):7726
[63] Wall, F. T. and Mandel, F. (1975). *J. Chem. Phys.*, **63**(11):4592
[64] Karayiannis, N. C., Mavrantzas, V. G. and Theodorou, D. N. (2002). *Phys. Rev. Lett.*, **88**(10):105503
[65] Karayiannis, N. and Laso, M. (2008). *Phys. Rev. Lett.*, **100**(5):050602
[66] Karayiannis, N. C. and Laso, M. (2008). *Macromolecules*, **41**(4):1537–1551
[67] Michel, M., Kapfer, S. C. and Krauth, W. (2014). *J. Chem. Phys.*, **140**(5):054116
[68] Peters, E. et al. (2012). *Phys. Rev. E*, **85**(2):026703
[69] Plimpton, S. (1995). *J. Comput. Phys.*, **117**(1):1–19. LAMMPS can be found here `http://lammps.sandia.gov`
[70] Andersen, H. C., Weeks, J. D. and Chandler, D. (1971). *Phys. Rev. A*, **4**(4):1597
[71] Weeks, J. D., Chandler, D. and Andersen, H. C. (1971). *The Journal of Chemical Physics*, **54**(12):5237–5247
[72] Karayiannis, N. C., Foteinopoulou, K. and Laso, M. (2009). *J. Chem. Phys.*, **130**(16):164908
[73] Šolc, K. (1971). *J. Chem. Phys.*, **55**(1):335–344
[74] Koyama, R. (1968). *J. Phys. Soc. Japan*, **24**(3):580–588
[75] Ebert, U., Baumgärtner, A. and Schäfer, L. (1997). *Phys. Rev. Lett.*, **78**(8):1592

LISTS

List of Abbreviations

CPU central processing unit

DL directed line, line with elastic energy of the type of eq. (1) and $\zeta = 1$

DNA deoxyribonucleic acid

EC event-chain (algorithm)

F-actin filamentous form of actin

FRG functional renormalisation group

GPU graphics processing unit

HHB yours truly, Horst-Holger Boltz

KTHNY-theory Kosterlitz-Thouless-Halperin-Nelson-Young-theory of defect-mediated two-step melting

MBE molecular beam epitaxy

MC Monte-Carlo (algorithm)

MD molecular dynamics

MPCD multi-particle collision dynamics

PEC parallel event-chain (algorithm)

RB random-bond, as in random-bond disorder (also called random-potential disorder)

RF random-field (sometimes also random-force), as in random-field disorder

SDL stiff directed line, line with elastic energy of the type of eq. (1) and $\zeta = 2$

WLC worm-like chain

List of Symbols for Part I

List of Symbols for Part II

List of Symbols for Part III